THE NLO MULTILEG WORKING GROUP:
Summary Report

Convenors: Z. Bern[1], S. Dittmaier[2], L. Dixon[3], G. Heinrich[4], J. Huston[5], B. Kersevan[6,7], Z. Kunszt[8], D.E. Soper[9,10]

Contributing authors: Z. Bern[1], C. Bernicot[11], T. Binoth[12], F. Boudjema[11], R. Britto[13], J. Campbell[14], M. Czakon[15], A. Denner[16], G. Dissertori[8], S. Dittmaier[2], L. Dixon[3], G. Duplančić[17], R.K. Ellis[18], R. Frederix[19], T. Gehrmann[20], A. Gehrmann–De Ridder[8], W.T. Giele[18], E.W.N. Glover[4], J.P. Guillet[11], G. Heinrich[4], S. Kallweit[2], S. Karg[21], N. Kauer[15], D.A. Kosower[22], F. Krauss[4], Z. Kunszt[8], N.D. Le[11], P. Mastrolia[10,20], A. Mitov[23], S. Moch[24], S. Odaka[25], G. Ossola[26], C.G. Papadopoulos[26], E. Pilon[11], R. Pittau[27,28], T. Reiter[12], G. Sanguinetti[11], S. Schumann[12], C. Schwinn[21], P.Z. Skands[10], D.E. Soper[9,10], H. Stenzel[29], P. Uwer[30], S. Weinzierl[31], G. Zanderighi[32]

[1] Department of Physics and Astronomy, UCLA, Los Angeles, CA 90095-1547, USA
[2] Max-Planck-Institut für Physik (Werner-Heisenberg-Institut), D-80805 München, Germany
[3] Stanford Linear Accelerator Center, Stanford University, Stanford, CA 94309, USA
[4] Institute of Particle Physics Phenomenology, University of Durham, Durham, DH1 3LE, UK
[5] Michigan State University, East Lansing, Michigan 48824, USA
[6] Jozef Stefan Institute, Jamova 39, SI-1000 Ljubljana, Slovenia
[7] Faculty of Mathematicsand Physics, University of Ljubljana, Jadranska 19a, SI-1000 Ljubljana, Slovenia
[8] Institute for Theoretical Physics, ETH, CH-8093 Zurich, Switzerland
[9] University of Oregon, Eugene, Oregon 97403, USA
[10] CERN, CH-1211 Geneva 23, Switzerland
[11] LAPTH, CNRS and Université de Savoie, B.P. 110, Annecy-le-Vieux 74951, France
[12] The University of Edinburgh, J.C.M.B., The King's Buildings, Edinburgh EH9 3JZ, Scotland
[13] Institute for Theoretical Physics, University of Amsterdam, 1018 XE Amsterdam, The Netherlands
[14] Department of Physics and Astronomy, University of Glasgow, Glasgow G12 8QQ, UK
[15] Institut für Theoretische Physik und Astrophysik, Universität Würzburg, D-97074 Würzburg, Germany
[16] Paul Scherrer Institut, Würenlingen und Villigen, CH-5232 Villigen PSI, Switzerland
[17] Theoretical Physics Division, Rudjer Boskovic Institute, HR-10002 Zagreb, Croatia
[18] Theoretical Physics, Fermilab MS106, Batavia, IL 60510, USA
[19] CP3, Université catholique de Louvain, B-1348 Louvain-la-Neuve, Belgium
[20] Institut für Theoretische Physik, Universität Zürich, CH-8057 Zürich, Switzerland
[21] Institute for Theoretical Physics E, RWTH Aachen, D-52056 Aachen, Germany
[22] Institut de Physique Theorique, CEA-Saclay F–91191 Gif-sur-Yvette cedex, France
[23] Department of Mathematical Sciences, University of Liverpool, Liverpool L69 3BX, United Kingdom
[24] Deutsches Elektronensynchrotron DESY, Platanenallee 6, D-15738 Zeuthen, Germany
[25] High Energy Accelerator Research Organization (KEK), 1-1 Oho, Tsukuba, Ibaraki 305-0801, Japan
[26] Institute of Nuclear Physics, NCSR Demokritos, 15310 Athens, Greece
[27] Departamento de Física Teórica y del Cosmos, Centro Andaluz de Física de Partículas Elementales (CAFPE), Universidad de Granada, E-18071 Granada, Spain
[28] Dipartimento di Fisica Teorica, Università di Torino and INFN sezione di Torino, Torino, Italy
[29] II. Physikalisches Institut, Justus-Liebig Universität Giessen, D-35392 Giessen, Germany
[30] Institut für Theoretische Teilchenphysik, Universität Karlsruhe, D-76128 Karlsruhe, Germany
[31] Institut für Physik, Universität Mainz, D-55099 Mainz, Germany
[32] The Rudolf Peierls Centre for Theoretical Physics, University of Oxford, UK

Contents

1. INTRODUCTION

The LHC will be a very complex environment with most of the interesting physics signals, and their backgrounds, consisting of multi-parton (and lepton/photon) final states. The ATLAS and CMS experiments will measure these final states with negligible statistical error, even in the early running, and in many cases with systematic errors smaller than those achieved by the experiments at the Tevatron (see the contribution in these proceedings from G. Dissertori). The luminosity uncertainty and the uncertainty in the parton distribution functions (PDFs) can be minimized by the normalization of the physics process of interest to certain Standard Model (SM) benchmark processes, such as W, Z, and $t\bar{t}$ production. Thus, it is important to have theoretical predictions at the same or better precision as the experimental measurements. In many cases, SM backgrounds to non-SM physics can be extrapolated from background-rich to signal-rich regions, but a definite determination of the background often requires an accurate knowledge of the background cross sections. An accurate knowledge of a cross section requires its calculation to at least next-to-leading order (NLO).

There are many tools for constructing basically any complex final state at the LHC at leading order (LO). When interfaced to parton shower Monte Carlo programs, such predictions can provide a qualitative prediction of both inclusive and exclusive final states. There are several different interfaces between fixed order (both LO and NLO) matrix element and parton shower Monte Carlo programs, with a benchmark comparison reported in this workshop.

A realistic theoretical description of complex final states, though, exists only at NLO[1], with the current limit of such calculations being $2 \to 3$ and $2 \to 4$ processes (see below). At LO, calculations often have large scale dependence, a sensitivity to kinematic cuts, and a poor modeling of jet structure. These deficiencies are most often remedied at NLO. NLO parton level calculations can serve as useful benchmarks by themselves, as well as providing an even more complete event description when interfaced with parton shower Monte Carlo programs, or when resummation effects are included. For the crucial benchmark processes mentioned above (W, Z and $t\bar{t}$ production), it is useful to go beyond NLO to NNLO. This has been done for W and Z production, including the calculation of differential rapidity distributions, and is expected for $t\bar{t}$, Z/γ+jet and W+jet production in the near future. Progress towards $t\bar{t}$ is reported in the contributions from M. Czakon, A. Mitov and S. Moch.

Even at NLO, the calculation of $2 \to 3$ (and $2 \to 4$) processes is extremely time- and theorist-consuming, so clear priority needs to be established for those processes most needed for the LHC. In the 2005 Les Houches proceedings, such a realistic NLO wishlist was established (see Table 1). It is gratifying that 3 of the 8 processes (and some which were not listed, for example the one-loop interference between gluon fusion and weak boson fusion in Higgs plus dijet production [1, 2]), have been calculated in the intervening two years, but daunting to know that 5 remain and a new process has been added. As noted in the table, three groups have calculated WW+jet since Les Houches 2005 and a detailed comparison of the results is presented in these Les Houches proceedings. In addition to the new NLO calculation, several processes beyond NLO also have been added to the list.

The new processes that have been added are:

- $pp \to b\bar{b}b\bar{b}$
  There are several interesting physics signatures involving two b-pairs in the final state, such as $b\bar{b}H(\to b\bar{b})$ and hidden valley signatures where Z bosons may decay to multiple b-quarks. Related to this calculation is the production of 4jets, which is less interesting experimentally, but a benchmark calculation from a theoretical point of view.

The calculations beyond NLO added to the 2007 version of the list are:

- $gg \to W^*W^* \; \mathcal{O}(\alpha^2 \alpha_s^3)$
  This subprocess is important for understanding the backgrounds for $H \to W^{(*)}W^{(*)}$.
- NNLO $pp \to t\bar{t}$

---

[1]Unless otherwise stated, the terms LO, NLO , NNLO refer to the order in perturbative QCD only.

This process is important for the use of $t\bar{t}$ production at the LHC as a precision benchmark.

- NNLO to weak vector boson fusion (VBF) and Z/γ+jet
VBF production of a Higgs boson is essential for measuring the coupling of the Higgs to bosons. Z/γ+jet is an essential experimental process that is used to understand the jet energy scale. It will also be useful for PDF determination.

- In addition, to further reduce the theoretical uncertainty for the benchmark W/Z processes, a combined NNLO QCD and NLO electroweak (EW) calculation is needed. The cross sections are known separately to NNLO QCD and to NLO EW, but a combined calculation will improve the accuracy of the result.

It is also daunting to realize that all of the three finished calculations from the 2005 list remain private code. To be truly useful, such calculations need to be available in programs accessible to experimenters. Most useful is if the event 4-vectors and event weight outputs can be stored in ROOT n-tuple format, so that experimental analysis cuts can be easily applied in a manner similar to what is used for the actual data, and so that results do not have to be re-generated if the analysis cuts change. In such a format, it is also easy to store not only the nominal event weight, generated with the central PDF of a NLO set, but also the weights for the set of error PDFs as well. In such a manner, the PDF uncertainty for any event configuration can be easily established, at the expense of a larger n-tuple size. Such a modification is being carried out for the MCFM program.

The calculation of complex multi-parton final states results in the generation of many subtraction terms for soft and/or collinear real radiation (e.g. Catani-Seymour dipole or antenna subtraction terms), and each of these in turn requires a counter-event to be generated for the Monte Carlo evaluation of the matrix element. Thus, for example, in MCFM for W+2jets (and for Higgs+2jets as well), there are 24 counter-term events for each real event. The net result is the requirement of a large amount of CPU time for computing such cross sections, and the need for many GB of disk space for storing the results in ntuples. These requirements will become even more extreme as the complexity of the calculations increases.

Although most of the NLO calculations for multi-particle production so far are private code tailored to the particular process at hand, there is a clear effort towards more automatisation and making results available to the community. Several agreements have been made during the workshop to facilitate comparisons and to make at least certain building blocks entering NLO calculations publicly available:

- Les Houches accord on master integrals: the aim is to have a library of one-loop integrals, finite as well as divergent ones, which can be used by anybody using a method which requires scalar master integrals. It has been agreed that the format for the labelling of the integrals respectively their arguments should follow the LoopTools [13, 14] conventions, as the infrared finite integrals are already available in LoopTools. The infrared divergent ones recently have been classified and listed in [15] and can be found in analytic form at `http://qcdloop.fnal.gov`. The final aim is a webpage containing
    1. a collection of scalar one-loop integrals in analytic form,
    2. benchmark points and comments which kinematic regions have been tested,
    3. code to calculate the Laurent series of each integral at points specified by the user,
    4. ideally also various codes for the reduction to master integrals.
This webpage is in Wiki format, such that contributions can be added easily. The location of the webpage is
`http://www.ippp.dur.ac.uk/LoopForge/index.php/Main_Page`, and input is eagerly awaited.

- If an amplitude is published in an analytic form, numerical values at some benchmark points should be given to facilitate cross-checks by other groups.

All of the 2005 NLO wishlist processes that have been completed to date relied on traditional Feynman diagrams for the loop amplitudes. On the other hand, as the complexity of the final-states

Process ($V \in \{Z, W, \gamma\}$)	Comments
Calculations completed since Les Houches 2005	
1. $pp \rightarrow VV$jet	WWjet completed by Dittmaier/Kallweit/Uwer [3]; Campbell/Ellis/Zanderighi [4] and Binoth/Karg/Kauer/Sanguinetti (in progress)
2. $pp \rightarrow$ Higgs+2jets	NLO QCD to the gg channel completed by Campbell/Ellis/Zanderighi [5]; NLO QCD+EW to the VBF channel completed by Ciccolini/Denner/Dittmaier [6,7]
3. $pp \rightarrow VVV$	ZZZ completed by Lazopoulos/Melnikov/Petriello [8] and WWZ by Hankele/Zeppenfeld [9]
Calculations remaining from Les Houches 2005	
4. $pp \rightarrow t\bar{t}b\bar{b}$	relevant for $t\bar{t}H$
5. $pp \rightarrow t\bar{t}$+2jets	relevant for $t\bar{t}H$
6. $pp \rightarrow VVb\bar{b}$,	relevant for VBF $\rightarrow H \rightarrow VV$, $t\bar{t}H$
7. $pp \rightarrow VV$+2jets	relevant for VBF $\rightarrow H \rightarrow VV$ VBF contributions calculated by (Bozzi/)Jäger/Oleari/Zeppenfeld [10–12]
8. $pp \rightarrow V$+3jets	various new physics signatures
NLO calculations added to list in 2007	
9. $pp \rightarrow b\bar{b}b\bar{b}$	Higgs and new physics signatures
Calculations beyond NLO added in 2007	
10. $gg \rightarrow W^*W^*$ $\mathcal{O}(\alpha^2\alpha_s^3)$	backgrounds to Higgs
11. NNLO $pp \rightarrow t\bar{t}$	normalization of a benchmark process
12. NNLO to VBF and Z/γ+jet	Higgs couplings and SM benchmark
Calculations including electroweak effects	
13. NNLO QCD+NLO EW for W/Z	precision calculation of a SM benchmark

Table 1: The updated experimenter's wishlist for LHC processes

grows further, it may prove necessary to adopt as well new approaches and methods. At the 2007 session of Les Houches, several such approaches were under discussion and development, primarily those based on the general analytic structure of amplitudes. These methods include recursive techniques at both tree and loop level; the use of (generalized) unitarity in four dimensions, and in $4 - 2\epsilon$ dimensions (the latter in the context of dimensional regularization); and automated solutions for coefficients of one-loop integrals, which is also connected with generalized unitarity. Complex final states possess intricate kinematic regions in which either the amplitude itself becomes singular, or a particular representation of it becomes numerically unstable. The general identification of such regions, and methods for dealing with potential instabilities, are also areas of active interest, which are not unrelated to the use of analyticity to construct loop amplitudes.

Even with the rapid progress we have been seeing in the last few years, there are NLO cross sections of interest that will not be completed in a timely manner for the LHC. One question is whether we can provide any approximations/estimates of the uncalculated NLO matrix elements based on experiences with simpler calculations. Table 2 shows the K-factors (NLO/LO) tabulated for some important processes at the Tevatron and LHC. Of course, K-factors are a simplified way of presenting the effects of NLO corrections (depending on both scale choice and PDF used for example), but the table provides some interesting insights. For example, it appears that processes that involve a large color annihilation (for example $gg \rightarrow$ Higgs) tend to have large K-factors for scales typically chosen to evaluate the matrix elements. The addition of extra legs in the final state tends to result in a smaller K-factor. For example, the K-factor for Higgs+2jets is smaller than for Higgs+1jet, which in turn is smaller than that for inclusive Higgs production. The same is true for the K-factor for W+2jet being less than that for W+1jet and the K-factor for $t\bar{t}$+1jet being less than that for $t\bar{t}$. Can we generalize this to estimate that the NLO corrections for W+3jets and $t\bar{t}$+2jets will be smaller still?

Process	Typical scales		Tevatron K-factor			LHC K-factor		
	μ_0	μ_1	$\mathcal{K}(\mu_0)$	$\mathcal{K}(\mu_1)$	$\mathcal{K}'(\mu_0)$	$\mathcal{K}(\mu_0)$	$\mathcal{K}(\mu_1)$	$\mathcal{K}'(\mu_0)$
W	m_W	$2m_W$	1.33	1.31	1.21	1.15	1.05	1.15
W+1jet	m_W	p_T^{jet}	1.42	1.20	1.43	1.21	1.32	1.42
W+2jets	m_W	p_T^{jet}	1.16	0.91	1.29	0.89	0.88	1.10
WW+jet	m_W	$2m_W$	1.19	1.37	1.26	1.33	1.40	1.42
$t\bar{t}$	m_t	$2m_t$	1.08	1.31	1.24	1.40	1.59	1.48
$t\bar{t}$+1jet	m_t	$2m_t$	1.13	1.43	1.37	0.97	1.29	1.10
$b\bar{b}$	m_b	$2m_b$	1.20	1.21	2.10	0.98	0.84	2.51
Higgs	m_H	p_T^{jet}	2.33	–	2.33	1.72	–	2.32
Higgs via VBF	m_H	p_T^{jet}	1.07	0.97	1.07	1.23	1.34	1.09
Higgs+1jet	m_H	p_T^{jet}	2.02	–	2.13	1.47	–	1.90
Higgs+2jets	m_H	p_T^{jet}	–	–	–	1.15	–	–

Table 2: K-factors for various processes at the Tevatron and the LHC calculated using a selection of input parameters. In all cases, the CTEQ6M PDF set is used at NLO. $\mathcal{K}$ uses the CTEQ6L1 set at leading order, whilst $\mathcal{K}'$ uses the same set, CTEQ6M, as at NLO. For most of the processes listed, jets satisfy the requirements $p_T > 15$ GeV/c and $|\eta| < 2.5$ (5.0) at the Tevatron (LHC). For Higgs+1,2jets, a jet cut of 40 GeV/c and $|\eta| < 4.5$ has been applied. A cut of $p_T^{\text{jet}} > 20 \ GeV/c$ has been applied for the $t\bar{t}$+jet process, and a cut of $p_T^{\text{jet}} > 50 \ GeV/c$ for WW+jet. In the W(Higgs)+2jets process the jets are separated by $\Delta R > 0.52$, whilst the VBF calculations are performed for a Higgs boson of mass 120 GeV. In each case the value of the K-factor is compared at two often-used scale choices, where the scale indicated is used for both renormalization and factorization scales.

The dream of experimentalists is for every NLO parton level calculation to come packaged with a complete parton shower for the partons produced in the NLO hard scattering process. So far, this exists for a few not-too-complicated processes, but it is not so easy to arrange this for each given NLO parton level calculation. To make this process easier, it will be useful to have a very systematic shower with a simple structure that can be matched to the structure of the NLO calculation. Two programs discussed at the workshop, and represented by contributions later in this section, may help. One would naturally match to a NLO calculation with antenna subtractions. The other would naturally match to a NLO calculation with the widely used Catani-Seymour dipole subtractions.

For many physics processes, though, we will have to continue to rely upon LO parton shower Monte Carlo programs (interfaced with exact LO matrix element calculations). In many instances, a large part of the difference between LO and NLO predictions is the use of LO PDFs for the former and NLO PDFs for the latter. Nominally, the choice indicated above is correct, but LO PDFs can differ from their NLO counterparts by a significant amount due to the influence of DIS data on the global fits. The LO PDFs often are changed in such a manner as to lead to significant deviations of LO predictions with LO PDFs from NLO predictions with NLO PDFs, in some kinematic regions. One solution that has been discussed is the use of NLO PDFs with LO Monte Carlos. This solves the problem mentioned above, but can lead to additional problems, for example with predictions for low mass objects at the LHC. The solution adopted by several groups, and presented at this workshop, is the development of *modified* LO PDFs, including the best features (for use in LO Monte Carlos) of the LO and NLO PDFs. It will be useful/important to tabulate the K-factors using these modified LO PDFs.

For the maximal exploitation of physics, there are also requirements on the experimental side. We suggest that cross sections at the LHC should be quoted at the hadron level, and where possible with the estimated parton-to-hadron corrections, so that any theoretical prediction (parton or hadron level) can easily be compared after the fact to the archived data [16]. Also, the experimental data needs to be quoted only for the range of measurement, rather than extrapolated to the full cross section; for example, measurements of $W \to e\nu$ should be quoted for the range of electron transverse momentum and rapidity and of missing transverse energy actually used in the triggering and analysis, rather than performing an extrapolation to the full W cross sections. Such recommendations were the exception (CDF W+jets) rather than the rule at the Tevatron and a clear model needs to be set for the LHC.

The structure of this report is as follows. First a review on expected cross sections and uncertainties at the LHC from an experimental point of view is given to set the stage. Then various new approaches to the calculation of tree-level and one-loop multi-leg amplitudes are presented, followed by a section on "improvements on standard techniques", with particular emphasis on the analysis of singularities which can create numerical instabilities when integrating multi-particle one-loop amplitudes. Section III contains various results, first a tuned comparison of different NLO calculations for $pp \to WW$+jet, then results pointing towards the $t\bar{t}$ cross section at NNLO, and finally NNLO predictions for hadronic event shapes in e^+e^- annihilation. The latter is not of direct relevance for the LHC, but is a benchmark calculation in what concerns the construction of NNLO Monte Carlo programs in the presence of a complicated infrared singularity structure. The report is closed by a section on parton showers, addressing the matching of parton showers with multi-leg LO matrix elements as well as the matching with partonic NLO calculations, which is of primordial interest at present and future TeV colliders.

2. MEASUREMENTS OF HARD PROCESSES AT THE LHC[2]

2.1 Introduction

We are approaching the start-up of the world's most powerful particle accelerator ever built. It is expected that CERN's Large Hadron Collider (LHC) will start its operation in 2008. Thanks to the unprecedented energies and luminosities, it will give particle physicists the possibility to explore the TeV energy range

---

[2]Contributed by: G. Dissertori

for the first time and hopefully discover new phenomena, which go beyond the so successful Standard Model (SM). Among the most prominent new physics scenarios are the appearance of one (or several) Higgs bosons, of supersymmetric particles and of signatures for the existence of extra spatial dimensions.

However, before entering the discovery regime, considerable efforts will be invested in the measurements of SM processes. We are sure that these have to be seen and thus they can serve as a proof for a working detector (a necessary requirement before any claim of discovery is made). Indeed, some of the SM processes are also excellent tools to calibrate parts of the detector. However, such measurements are also interesting in their own right. We will be able to challenge the SM predictions at unprecedented energy and momentum transfer scales, by measuring cross sections and event features for minimum-bias events, jet production, W and Z production with their leptonic decays, as well as top quark production. This will allow to check the validity of the Monte Carlo generators, both at the highest energy scales and at small momentum transfers, such as in models for the omnipresent underlying event. The parton distribution functions (pdfs) can be further constrained or measured for the first time in kinematic ranges not accessible at HERA. Important tools for pdf studies will be jet+photon production or Drell-Yan processes. Finally, SM processes such as W/Z+jets, multi-jet and top pair production will be important backgrounds to a large number of searches for new physics and therefore have to be understood in detail.

The very early goals to be pursued by the experiments, once the first data are on tape, are three-fold : (a) It will be of utmost importance to commission and calibrate the detectors in situ, with physics processes as outlined below. The trigger performance has to be understood in as unbiased a manner as possible, by analyzing the trigger rates of minimum-bias events, jet events for various thresholds, single and di-lepton as well as single and di-photon events. (b) It will be necessary to measure the main SM processes and (c) prepare the road for possible discoveries. It is instructive to recall the event statistics collected for different types of processes. For an integrated luminosity of $1\,\mathrm{fb}^{-1}$ per experiment, we expect about $10^7\ \mathrm{W} \to \mathrm{e}\nu$ events on tape, a factor of ten less $\mathrm{Z} \to \mathrm{e}^+\mathrm{e}^-$ and some $10^5\ \mathrm{t\bar{t}} \to \mu+X$ events. If a trigger bandwidth of about 10% is assumed for QCD jets with transverse momentum $p_\mathrm{T} > 150$ GeV, $\mathrm{b\bar{b}} \to \mu+X$ and minimum-bias events, we will write about 10^6 events to tape, for each of these channels. Also the existence of supersymmetric particles, for example gluinos with $m_{\tilde{\mathrm{g}}} \approx 1$ TeV, or a Higgs with $m_\mathrm{H} \approx 130$ GeV, would result in sizeable event statistics $(10^2 - 10^3)$. This means that the statistical uncertainties will be negligible after a few days, for most of the physics cases. The analysis results will be dominated by systematic uncertainties, be it the detailed understanding of the detector response, theoretical uncertainties or the uncertainty from the luminosity measurements.

Concerning the experimentally achievable precision, it is worth noting that the numerous quality checks during construction and beam tests of series detector modules let us conclude that the detectors as built should give a good starting-point performance. Furthermore, cosmic ray muons, beam-gas interactions and beam halo muons are available as commissioning and calibration tools already before the first real proton-proton collisions. Finally, with such first collisions in hand, the trigger and data acquisition systems will be timed-in, the data coherence checked, sub-systems synchronized and reconstruction algorithms debugged and calibrated. The electromagnetic and hadronic calorimeters will be calibrated with first physics events. For example, the initial crystal inter-calibration precision of about 4% for the CMS ECAL will be improved to about 2% by using the ϕ-symmetry of the energy deposition in minimum-bias and jet events. Later the ultimate precision ($\approx 0.5\%$) and the absolute calibration will be obtained using $\mathrm{Z} \to \mathrm{e}^+\mathrm{e}^-$ decays and the E/p measurements for isolated electrons, such as in $\mathrm{W} \to \mathrm{e}\nu$ decays [17]. The latter requires a well understood tracking system. The uniformity of the hadronic calorimeters can be checked with single pions and jets. In order to obtain the jet energy scale (JES) to a few per-cent precision or better, physics processes such as $\gamma + \mathrm{jet}$, $\mathrm{Z}(\to \ell\ell) + \mathrm{jet}$ or $\mathrm{W} \to 2$ jets in top pair events will be analyzed. Finally, the tracker and muon system alignment will be carried out with generic tracks, isolated muons or $\mathrm{Z} \to \mu^+\mu^-$ decays. Regarding all these calibration and alignment efforts, the ultimate statistical precision should be achieved very quickly in most cases. Then systematic effects have to be faced, which, eg., implies that pushing the tracker $R\phi$ alignment from an initial $100\,\mu$m to about $10\,\mu$m

8

might involve at least one year of data taking. More detailed reviews of the initial detectors and their performance can be found in Refs. [18] and [19].

The anticipated detector performance leads to the following estimates for the reconstruction precision of the most important physics objects :

- Isolated electrons and photons can be reconstructed with a relative energy resolution characterized by a stochastic term (which is proportional to $1/\sqrt{E}$) of a few per-cent and an aimed-for 0.5% constant term. Typically isolation requirements are defined by putting a cone around the electron/photon and counting the additional electromagnetic and hadronic energy and/or track transverse momentum within this cone. The optimal cone size in $\eta - \phi$ space[3] depends on the particular analysis and event topology. For typical acceptance cuts, such as a transverse momentum above 10-20 GeV and $|\eta| < 2.5$, electrons and photons can be expected to be reconstructed with excellent angular resolution, high efficiency ($\geq 90\%$) and small backgrounds. Again, the precise values depend very much on the final state topology and the corresponding tightness of the selection cuts. Most importantly, the systematic uncertainty on the reconstruction efficiency should be controllable at the 1-2% level, using in-situ measurements such $Z \rightarrow e^+e^-$ decays, with one of the electrons serving as tag lepton and the other one as probe object for which the efficiency is determined.

- Isolated muons, with similar acceptance cuts as mentioned above for electrons, should be reconstructed with a relative transverse momentum resolution of 1 - 5% and excellent angular resolution up to several hundreds of GeV. Again, a systematic uncertainty on the reconstruction efficiency of 1-2% appears to be achievable.

- Hadronic jets will be reconstructed up to pseudo-rapidities of 4.5 - 5, with good angular resolution. The energy resolution depends rather strongly on the specific calorimeter performance. For example, in the case of ATLAS (CMS) a stochastic term of the order of 50 - 60% (100 - 150%) is to be expected when energy deposits in projective calorimeter towers are used for the jet clustering procedure. Important improvements on the CMS jet energy resolution are expected from new approaches such as particle flow algorithms. Well above the trigger thresholds jets will be reconstructed with very high efficiency; the challenge is the understanding of the efficiency turn-on curves. In contrast to leptons, for jets the experimental systematic uncertainties are much more sizeable and difficult to control. A more detailed discussion will follow below.
A further important question is the lowest p_T threshold above which jets can be reconstructed reliably. Contrary to the naive expectation that only high-p_T objects (around 100 GeV and higher) are relevant, it turns out that many physics channels require jets to be reconstructed with rather low transverse momentum of $\sim 20 - 30$ GeV. One reason for this is the importance of jet veto requirements in searches for new physics, such as in the $H \rightarrow WW^* \rightarrow 2\ell \, 2\nu$ channel, where a jet veto is necessary to reduce the top background. The experimental difficulties related to the understanding of the low-p_T jet response[4], the thresholds due to noise suppression, the impact of the underlying event and additional pile-up events and ultimately the knowledge of the JES lead to the conclusion that it will be extremely challenging, if not impossible, to reliably reconstruct jets below a p_T of 30 GeV. In addition, also the theoretical predictions are challenged by very low-p_T effects, as for example induced by jet veto requirements. Here fixed-order calculations may have to be supplemented by resummations of large logarithms.

- Finally, the missing transverse energy will be a very important "indirect" observable, which is constructed from measurements of other quantities, such as all calorimeter energy deposits. Many searches for new physics, such as Supersymmetry, rely very much on this observable. However, it turns out that it is also an extremely difficult quantity to measure, since it is sensitive to almost every detail of the detector performance. Here it is even more difficult to give estimates of the

---

[3]Here η denotes the pseudo-rapidity and ϕ the azimuthal angle around the beam pipe.
[4]The jet response is defined as the ratio of the reconstructed and the "true" jet momentum.

expected systematic uncertainties. Also, the reconstruction performance depends very much on the details of the particular final state, such as the number of jets and/or leptons in the event, the existence of "true" missing energy, e.g. from neutrinos, the amount of pile-up events and in general the overall transverse energy deposited in the detector. The very first data will be of paramount importance for a timely understanding of this quantity.

More detailed discussions of the expected detector and reconstruction performance can be found in recent reviews ([18], [19]), for ATLAS in Ref. [20] and for CMS in its Physics Technical Design Reports (PTDR), Vol. 1 [17] and Vol. 2 [21].

In the following I will concentrate on the early physics reach of the LHC experiments, i.e. on measurements to be performed on the first few hundred pb^{-1} up to 1 fb^{-1} of integrated luminosity. Many reviews exist on this topic, such as Refs. [19,22–24] to mention only a few. Most of the results presented here are taken from the CMS PTDR Vol. 2 [21], because it represents the most recent comprehensive overview compiled by one of the LHC experiments.

2.2 Jet production

Because of its extremely large cross section, the inclusive dijet production (pp $\rightarrow$ 2 jets + anything) completely dominates over all other expected LHC processes with large momentum transfer. At lowest order in perturbative Quantum Chromodynamics (QCD), it is described as a $2 \rightarrow 2$ scattering of partons (quarks and gluons), with only partons in the initial, intermediate and final state. Depending on the exchanged transverse momentum (or generally the energy scale of the scattering process), the final state will consist of more or less energetic "jets" which arise from the fragmentation of the outgoing partons. Indeed, soft scattering processes, which give the largest contribution to the total inelastic proton-proton cross section, are most likely, leading to final states with hundreds of soft (i.e. below a few GeV) charged and neutral hadrons, uniformly distributed over most of the experimental acceptance in pseudo-rapidity. Since these are the most likely processes to occur, they are triggered on with the least stringent requirements and thus called "minimum-bias" events. For the same reason they also represent the typical pile-up events which can occur simultaneously with other triggered proton-proton collisions. Therefore very early measurements of the production rates[5] and the charged particle distributions will be extremely important, in particular for the tuning of the widely used Monte Carlo generators. Here I will not discuss further this class of measurements, but rather concentrate on the parton scattering at large transverse momentum. Examples of envisaged studies of minimum-bias events can be found in [21].

For outgoing partons with transverse momentum well above the QCD fragmentation scale ($\Lambda \sim$ 1 GeV) the picture of jet production arises, namely well collimated bundles of particles, leading to isolated clusters of deposited energy in the calorimeters. Several algorithms exist for the clustering of the final state objects (simulated particles, calorimeter towers, charged tracks) into jets with a well defined four-momentum, which in the optimal case closely matches the four-momentum of the original scattered parton. Examples of commonly used prescriptions are the Iterative Cone, Midpoint Cone, SISCone and k_T algorithms. In particular, the latter two algorithms recently receive a lot of theoretical and experimental attention, mainly because of their property of being infrared and collinear safe to all orders of perturbation theory. A detailed discussion of those jet algorithms is given elsewhere in these proceedings, as well as in [25–27] and references therein.

For the measurement of the inclusive jet cross section we simply count the number of jets inside a fixed pseudo-rapidity region as a function of jet p_T. For a second typical measurement, the dijet cross section, events are selected in which the two highest p_T jets, the leading jets, are both inside a specified pseudo-rapidity region and counted as a function of the dijet (invariant) mass. Both cases are inclusive processes dominated by the $2 \rightarrow 2$ QCD scattering of partons. The distinction between inclusive jets and

---

[5]Currently the extrapolations from the TEVATRON up to the LHC energies suffer from large uncertainties. For example, various Monte Carlo generators predict charged track multiplicities which differ by more than 30%.

dijets is only in a different way of measuring the same process. For a common choice of the η region, events selected by the dijet analysis are a subset of the events selected by the inclusive jet analysis, but the number of events in the two analyses coming from QCD is expected to be close at high p_T. The steeply falling cross sections are shown in Fig. 1. For the inclusive jet case, the spectrum roughly follows a power law, however, with increasing power for increasing p_T, ie., the power increases from about 6 at $p_T = 150$ GeV to about 13 at $p_T = 3$ TeV and keeps on increasing with jet p_T.
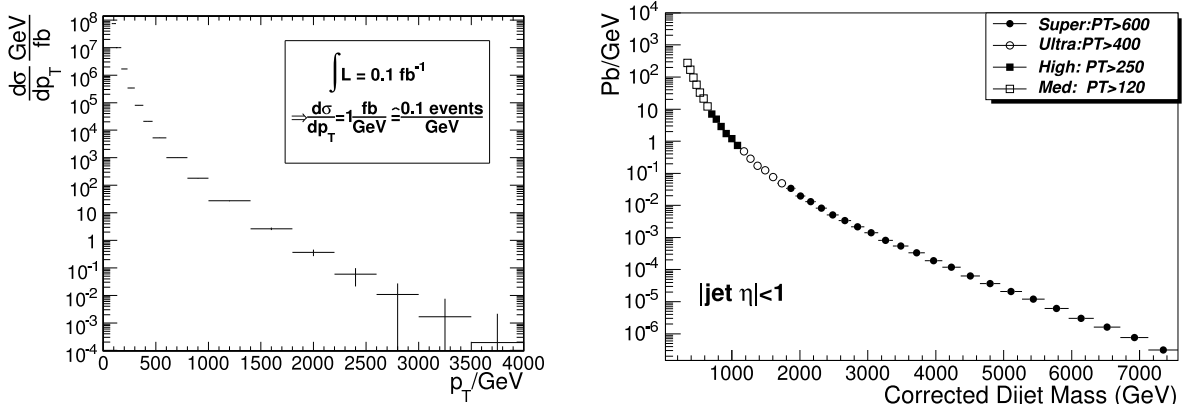

Fig. 1: Inclusive jet (left) and dijet (right) cross section measurements as foreseen by CMS [21]. The central cross section values are taken from a leading-order calculation in dependence of the transverse momenta of the hard interaction. The insert on the right plot indicates various trigger paths.

It can be seen that even for very small integrated luminosities the statistical uncertainties will be negligible, up to very high jet momenta. Thus the TEVATRON reach in terms of highest momenta and therefore sensitivity to new physics, such as contact interactions or heavy resonances, will be quickly surpassed. For 1 fb^{-1}, the inclusive cross section for central jet production (ie. jet pseudo-rapidities below ~ 1) will be known statistically to better than 1% up to a p_T of 1 TeV, and the statistical errors on the dijet cross section will be below 5% up to dijet masses of 3 TeV.

The real challenge for these measurements will be the determination and control of the jet energy scale. As mentioned above, the cross sections are steeply falling as a function of jet p_T. Therefore any relative uncertainty on the jet p_T will translate into a n-times larger relative uncertainty on the cross section, where n indicates the power of the spectrum in a specified p_T region, ie. $d\sigma/dp_T \propto p_T^{-n}$. For example, a 5% uncertainty on the energy scale for jets around 100-200 GeV of transverse momentum induces a 30% uncertainty on the inclusive jet cross section. This is also shown in Fig. 2 (left), here for the case of a 3% JES uncertainty. As a comparison, in Fig. 2 (right) we see the expected theoretical uncertainties on the inclusive jet cross section from the propagation of pdf uncertainties. These are below the 10% level up to a jet p_T of 1 TeV, thus much smaller than the experimental systematics from the JES. Therefore it is obvious that a measurement of the inclusive jet cross section will not allow to constrain the pdfs, unless the JES is known to 2% or better. This is definitely beyond reach for the early phase of the LHC, and might remain a huge challenge even later. Furthermore, because of these large experimental uncertainties, it might turn out that the currently known next-to-leading order (NLO) perturbative QCD calculation of the hard scattering process is precise enough for a comparison to data. However, with better experimental control at a later stage and/or other definitions of observables (see below) the need for going to next-to-next-to-leading order (NNLO) might arise.

Obviously, the knowledge of the JES also has a strong impact on the achievable precision of the dijet cross section measurement, as shown in Fig. 3 (left). However, the problem can be avoided by performing relative instead of absolute cross section measurements. A well suited observable is the dijet
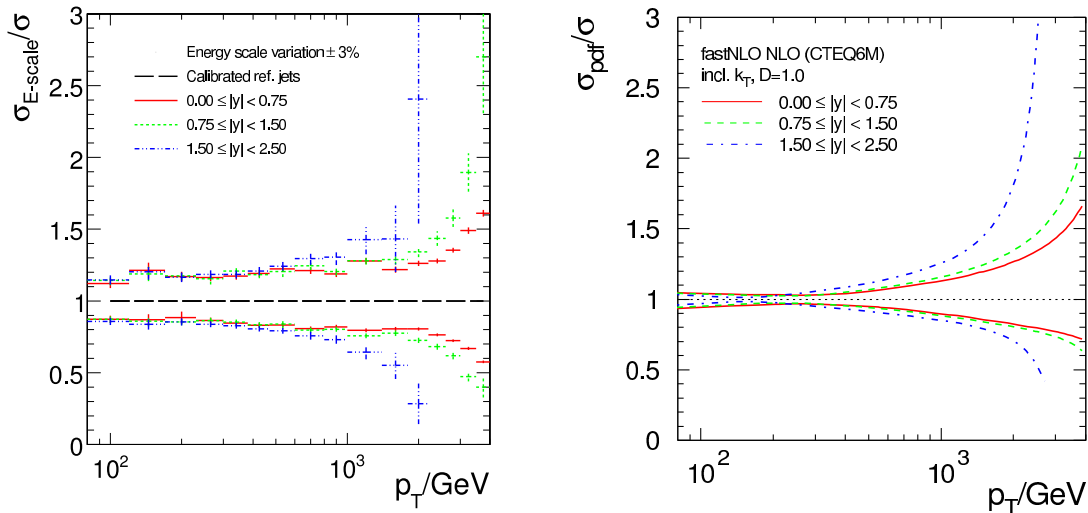
Fig. 2: Left: Relative systematic uncertainties of the inclusive jet cross sections for the k_T algorithm versus jet p_T due to a change in the JES of $\pm 3\%$ for three bins in rapidity, y. The error bars indicate the statistical uncertainty. Right: relative uncertainties propagated from the error sets of the CTEQ6M [28] pdfs, for the same regions in rapidity. Plots taken from [21].

ratio $N(|\eta| < |\eta_{\mathrm{in}}|)/N(|\eta_{\mathrm{in}}| < |\eta| < |\eta_{\mathrm{out}}|)$, ie., the ratio of the number of dijet events within an inner region $|\eta| < |\eta_{\mathrm{in}}|$ to the number of dijet events within an outer region $|\eta_{\mathrm{in}}| < |\eta| < |\eta_{\mathrm{out}}|$. Both leading jets of the dijet event must satisfy the $|\eta|$ cuts. In Ref. [21] the values chosen were $\eta_{\mathrm{in}} = 0.5$ and $\eta_{\mathrm{out}} = 1$, whereas in a recent update [29] of the CMS studies on inclusive and dijet production they have been increased to 0.7 and 1.3, respectively. The dijet ratio has two interesting features. First, it is very sensitive to new physics, such as contact interactions or the production of a heavy resonance, because those lead to jets at more central rapidities than in genuine QCD dijet events. Second, in the ratio we can expect many systematic uncertainties to cancel. For example, the luminosity uncertainty completely disappears in the ratio. More importantly, also the JES uncertainty is strongly reduced, since the dijet ratio is sensitive only to the relative knowledge of the scale as a function of rapidity, but not to the absolute scale any more. This is well illustrated in Fig. 3 (right), where the JES uncertainty is shown to be reduced to about 3%. In this figure also the sensitivity to new contact interactions at various scales is indicated. Hence we have a nice example of a ratio measurement where systematic uncertainties are reduced. Having an observable in hand with experimental systematic uncertainties at the level of 5% or less, it might become relevant to obtain a NNLO prediction for jet production.

As we have seen above, the JES is the dominant source of uncertainty in jet cross section measurements. Obviously, it is also important for many other analyses and searches which involve jet final states and possibly invariant mass reconstructions with jets. Therefore major efforts are devoted by the experimental collaborations to prepare the tools for obtaining JES corrections, both from the Monte Carlo simulations and, more importantly, from the data themselves. Currently approaches are followed which are inspired by the TEVATRON experience [30, 31]. The correction procedure is split into several steps, such as offset corrections (noise, thresholds, pile-up), relative corrections as a function of η, absolute corrections within a restricted η-region, corrections to the parton level, flavour-specific corrections etc. At the LHC startup we will have to rely on Monte Carlo corrections only, but with the first data coming in it will be possible to switch to data-driven corrections. At a later stage, after a lot of effort will have gone into the careful tuning of the Monte Carlo simulations, it might be feasible to use Monte Carlo corrections again. A rough estimate for the early JES uncertainty evolution in CMS is 10% at start-up, 7% after 100 pb^{-1} and 5% after 1 fb^{-1} [32]. Certainly it will be difficult and require time to obtain a detailed understanding of the non-Gaussian tails in the jet energy resolution.
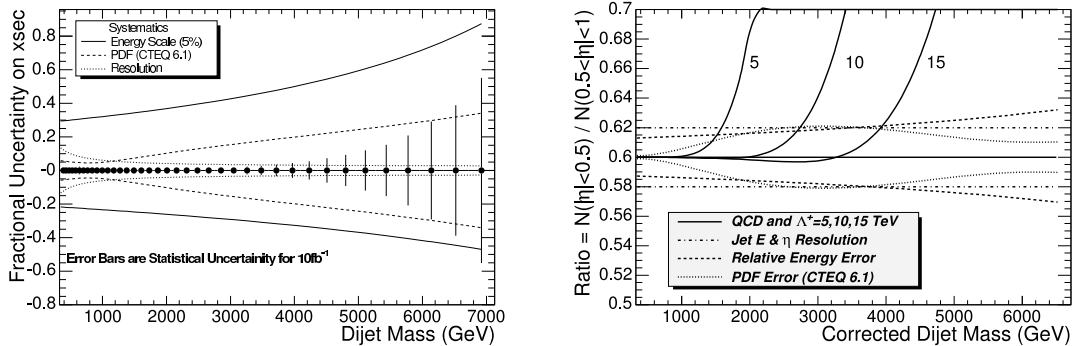
Fig. 3: Left : Systematic uncertainty on the dijet cross section due to JES (solid curve), parton distributions (dashed curve) and calorimeter energy and η resolution (dotted curve), compared to the statistical uncertainties for 10 fb^{-1} (errorbars). Right : Systematic bounds on the dijet ratio from uncertainties in the relative JES (dashed curve), parton distributions (dotted curve) and calorimeter energy and η resolution (dot dashed curve), compared to the expectations of QCD and three contact interaction scales (solid line and curves). Plots taken from [21].

Concerning data-driven JES corrections, one of the best channels is γ+jet production. At leading order, the photon and the jet are produced back-to-back, thus the precisely measured photon energy can be used to balance the jet energy. Real life is more difficult, mainly because of additional QCD radiation and the large background from jets faking a photon. These can be suppressed very strongly with tight selection and isolation cuts (eg., no additional third jet with a transverse energy beyond a certain threshold and tight requirements on additional charged and neutral energy in a cone around the photon). The need to understand well the photon-faking jet background and the photon fragmentation is avoided by using the channel $Z(\rightarrow \ell\ell)$+jet, with electrons or muons, however, at the price of a lower cross section.

Besides being a tool for obtaining JES corrections, both γ+jet and Z + jet processes will also be important handles for constraining the gluon pdf. It appears feasible to probe the gluon pdf at Bjorken-x values between about 0.0005 and 0.2 with a few per-cent statistical errors after only 1 fb^{-1} of integrated luminosity [33]. The x value is well determined using the lepton or photon kinematics only, thus it does not suffer from the less precise measurement of the jet momentum. Of course, in order to consistently constrain NNLO pdf sets (which should become more and more relevant with time), a NNLO calculation of the hard scattering part of the process is needed. Whereas this appears beyond reach for the γ+jet case, the Z+jet process might be tractable within the not-too-far future. As discussed below, Z+jet (as well as W+jet) production is a very important background to many searches, therefore having a NNLO prediction should be very valuable, also as a benchmark for Monte Carlo generators which combine leading order (LO) and/or NLO matrix elements with parton shower models.

2.3 Vector boson production

The production of vector bosons (W and Z), triggered on with their subsequent leptonic decays, will be among the most important and most precise tests of the SM at the LHC. The leptonic channels, mainly electrons and muons, can be reconstructed very cleanly, at high statistics, with excellent resolution and efficiency and very small backgrounds. At the same time, the theoretical predictions are known to high accuracy, as discussed in more detail below. This precision will be useful for constraining pdfs, by measuring the rapidity dependence of the Z production cross section, in particular when going to large rapidities and thus probing low x values. As proposed in [34], this process will serve as a standard candle for determining to high precision (at the few per-cent level) the proton-proton luminosity or alternatively the parton-parton luminosity. Finally, it will be attempted to improve on the current precision of the W mass. Besides that, W and Z production will be an important experimenter's tool. As mentioned already

earlier, Z and W decays to leptons will be used to understand and calibrate various sub-detectors, measure the lepton reconstruction efficiencies and control even the missing transverse energy measurement.

Below I will first discuss the inclusive case, concentrating on resonant production. Then I will highlight some issues for the W and Z production in association with jets. Although being highly interesting processes, di-boson production will not be discussed here, since for integrated luminosities up to 1 fb^{-1} the statistical precision will be the limiting factor for these measurements and only allow first proofs of existence and rough validations of the model expectations.

2.3.1 Inclusive W and Z production

Inclusive W and Z production currently is and probably will remain the theoretically best known process at the LHC. Predictions are available at NNLO in perturbative QCD, fully differential in the vector boson and even the lepton momenta [35]. Figure 4 (left) shows the Z rapidity distribution at various orders in perturbation theory. We see that the shape stabilizes when going to higher orders and that the NNLO prediction nicely falls within the uncertainty band of the NLO expansion, giving confidence in the good convergence of the perturbation series. More importantly, the renormalization scale uncertainty is strongly reduced at NNLO, to a level of about 1% for Z rapidities below 3. A renormalization scale uncertainty even below 1% can be obtained for ratio observables such as $\sigma(W^+)/\sigma(W^-)$ and $\sigma(W)/\sigma(Z)$, possibly as a function of rapidity. Again, ratio measurements are interesting also from the experimental point of few, since many systematic uncertainties cancel completely or to a large extend. The prospect of a precise measurement and knowing the hard scattering part of the process so well means that we have a tool for precisely constraining pdfs (or couplings and masses, in a more general sense). Indeed, when taking the full theoretical prediction for the W and Z production cross section, ie., the convolution of pdfs and hard scattering part, its uncertainty is dominated by the limited knowledge of the pdfs, currently estimated to be around 5-7% [36, 37]. This will then also limit the proton-proton luminosity to a precision of this size, unless the pdfs are further constrained, mainly by the rapidity dependence of the cross section, as for example shown in Ref. [36]. It is worth noting that at this level of precision also electro-weak corrections have to be considered [38–40].

An important point to make in this context is the importance of having differential cross section predictions. If we take resonant W and Z production at central vector boson rapidity, we probe x values of around 0.006, a region rather well constrained by the current pdf fits. However, for larger rapidities we probe more and more the small x region, which is less well known, eg., at leading order and for a Z rapidity of 3 we need (anti-)quark pdfs at $x = 0.12$ and $x = 0.0003$. Experimentally, because of the detector acceptance, we can only access a limited sub-region of the full phase space. This means that when measuring a total cross section, we have to extrapolate the measurement to the full acceptance (eg., full rapidity), which introduces a model dependence, especially on the poorly known low-x region. On the other hand, having differential predictions, we can compute exactly the same quantity as we measure, thus eliminating any extrapolation uncertainty. Similarly, for constraining NLO (NNLO) pdfs, exactly the same acceptance cuts (on the leptons) as in the data can now be applied on the available NLO (NNLO) predictions. Of course, with more and more differential higher-order predictions becoming available, this kind of argument applies to any cross section measurement (and/or deduced determination of physics quantities such as couplings, masses, pdfs), namely that we should compare the measurements and predictions for the experimentally accessible acceptance and avoid un-necessary extrapolations, which will not teach us anything new and only introduce additional uncertainties.

As mentioned above, the experimental reconstruction of W and Z production is rather straight forward. Leptons are required to have a minimum p_T of about 20 GeV, within a pseudo-rapidity of 2.5 (cf. Fig. 4, right). In the Z case the mass peak allows for further event selections and background estimations. However, the neutrino in the W decay leads to missing energy, which obviously is reconstructed less precisely. Instead of an invariant mass peak only the transverse W mass can be reconstructed, with larger backgrounds than for the Z. Here it is interesting to mention that a jet veto can help to control bet-
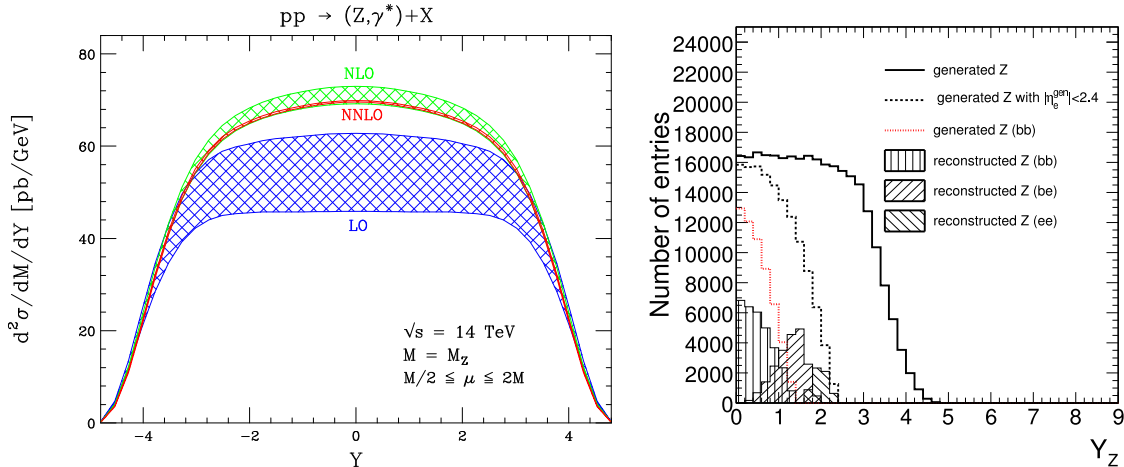
Fig. 4: Left : QCD predictions at various orders of perturbation theory for the Z rapidity distribution at the LHC. The shaded bands indicate the renormalization scale uncertainty. Plot taken from [41]. Right : Generated rapidity distribution for all Z candidates and for those where both electrons were generated within the geometrical acceptance of the CMS electromagnetic calorimeter (b=barrel, e=endcap). Also shown is the rapidity distribution of the finally accepted Z events. Plot taken from [21].

ter the QCD backgrounds and to improve the resolution of the missing transverse energy reconstruction. However, a jet veto introduces sensitivity to low-p_T QCD radiation, thus comparing the measurement to a calculation for the same acceptance cuts will only be meaningful if soft-p_T resummation effects are taken into account in the predictions. Fortunately, with the Z+jet process we have an experimental handle to study these issues rather precisely (see also below), since the radiation pattern in W+jet and Z+jet events is very similar. In Ref. [21] it has been shown that reconstruction efficiencies and ultimately cross section measurements with systematic uncertainties around 2% (or better) should be possible, excluding the luminosity uncertainty.

2.3.2   W/Z+jets production

Vector bosons produced in association with jets lead to final states with high-p_T leptons, jets and possibly missing transverse energy. Such a topology is also expected for many searches, in particular for squark and gluino production and subsequent cascade decays. Obviously it will be important to understand these SM processes as quickly as possible and validate the available Monte Carlo generators, which typically combine LO matrix elements with parton showers. A standard observable will be the W/Z cross section as a function of the associated leading jet transverse momentum or the number of additional jets. Obviously, such measurements will suffer from the same JES uncertainties as the QCD measurements discussed above, and thus constitute only limited calibration tools during the early data taking. The problem can be reduced by defining clever ratios of cross sections, involving different vector bosons and/or number of additional jets, or by normalizing the predictions to the data in limited regions of the phase space (eg. for small jet multiplicity and extrapolating to larger multiplicities). A completely different approach is to take a more inclusive look at this process, in the sense that the Z transverse momentum is measured from the lepton kinematics, which is possible at high statistical and, more importantly, high experimental accuracy (cf. Fig. 5). This distribution can be understood as the convolution of the Z+0/1/2/...jets distributions, therefore any model intended to describe Z+jets production has necessarily to reproduce the Z p_T distribution over its full range. As mentioned above, in this context it would be highly desirable to have a NNLO prediction, possibly matched with a resummation calculation, for a comparison to the precise data and as benchmark for other approximations, implemented in Monte Carlo simulations.
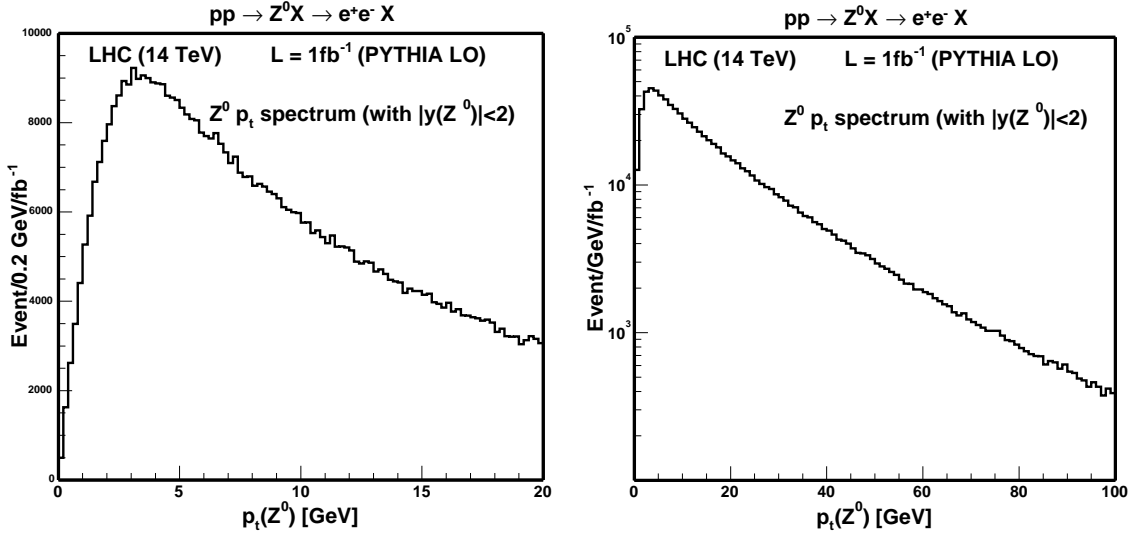
15

Fig. 5: Expected transverse momentum distribution for Z production at the LHC, for a p_T range up to 20 GeV (left) and 100 GeV (right). The p_T of the Z is reconstructed from the lepton kinematics. The fluctuations in the spectra indicate the statistical precision achievable with 1 fb^{-1} of integrated luminosity. Plots taken from [36].

2.4 Top pair production

The top quark is produced very abundantly at the LHC. With 1 fb^{-1} of integrated luminosity, we should already have a couple of thousand clean signal events on tape in the di-lepton channel, and a factor of 10 more in the single lepton channel (lepton+jets channel) [21]. The physics case for the study of top production is very rich and can not be discussed in detail here. For example, a recent review can be found in Ref. [42]. Combining many different channels, a top mass measurement with a precision of 1 GeV might be achieved, which together with a precise W mass measurement constitutes an important indirect constraint of SM predictions and its extensions. The production cross section (for single and top-pair production) will be an important measurement, again for testing the SM predictions and because top production is a copious background to a large number of new physics searches. In the single muon+X channel, the top-pair production cross section will soon (ie. with about 1 fb^{-1}) be measured with a statistical precision of 1%. The total uncertainty of 10-15% (excluding the luminosity uncertainty) will be dominated by systematics, most notably due to the knowledge of the b-tagging efficiency. At the moment it seems difficult to reduce this uncertainty to below 10% [21], even for much larger integrated luminosities. Therefore this should be seen as a benchmark value to be challenged by the theoretical predictions. Efforts are under way to compute the NNLO corrections to top-pair production and it will be interesting to compare the ultimately achievable theoretical precision to the experimental accuracy. Precise higher order predictions (possibly including resummation), both for inclusive top and top+jets production, should also be very valuable for obtaining precise background estimates, such as in Higgs searches. Although it will be tried to calibrate the backgrounds with the data themselves, by using background-enriched samples for the normalization [43, 44], the theoretical predictions are still needed for the extrapolation from the background-rich to the signal-enriched regions of phase space. A good theoretical precision will lead to reduced systematics on the background, which will be most relevant for searches with small signal-to-noise ratios. It is worth mentioning that for the measurement of the b-jet cross section similar observations hold as for the top, ie., the statistical error will soon be negligible, whereas the systematic uncertainty is expected to be around 15-20%, dominated by the JES.

Finally, top production will become an extremely valuable calibration tool. The mass peak can already be reconstructed with much less than 1 fb^{-1}, even without b-tagging requirements. With a clean sample in hand, it can be exploited for controlling the b-tagging efficiency and serve as a closure test for

the JES corrections determined from other processes. Concerning the JES, the mass of the hadronically decaying W serves as a calibration handle. CMS expects that for intermediate jet p_T values this sample could lead to JES uncertainties around or below 3% [21].

2.5   Conclusions

I have summarized the experimental and theoretical prospects for some of the most important measurements of SM processes at the LHC, namely jet, vector boson and top production. The early benchmark measurements will include the inclusive jet cross section, the dijet cross section and the dijet ratio, photon/Z plus jet production, the Z rapidity distribution, ratios of W and Z cross sections, the Z transverse momentum distribution and top pair production. I have indicated the expected uncertainties of the measurements and shown how these processes serve as tools for the understanding of the detector, for the control of backgrounds and for the validation and tuning of Monte Carlo generators. Particularly interesting are ratio measurements, because otherwise important systematic uncertainties cancel out in this case. With differential predictions at higher order in perturbation theory in hand, I have highlighted the importance of comparing theory and experiment for the same acceptance cuts, thus avoiding extrapolation errors. It is important to have (differential) NLO predictions, possibly combined with resummation calculations such as implemented in the Monte Carlo generator MC@NLO [45, 46], for as many processes as possible. For the cases where this appears to be difficult to achieve, LO plus parton shower approaches might still be very valuable tools. However, higher order predictions, up to NNLO, should be aimed for as benchmarks, at least in a few cases. I have identified dijet, Z+jet and top production as most interesting cases for investing the efforts towards NNLO calculations.

Acknowledgements

Part I
NEW APPROACHES

3.   ON-SHELL RECURSION RELATIONS[6]

3.1   Introduction

The efficient calculation of scattering amplitudes with many external legs is a challenging task and needed for phenomenological studies at TeV colliders. In the past years, various new methods for efficient calculations in QCD have been introduced, originally motivated by the relation of QCD amplitudes to twistor string theory [47]. These methods include the diagrammatic rules of Cachazo, Svrček and Witten (CSW) [48], where tree level QCD amplitudes are constructed from vertices that are off-shell continuations of maximal helicity violating (MHV) amplitudes [49], and the recursion relations of Britto, Cachazo, Feng and Witten (BCFW) [50, 51] that construct scattering amplitudes from on-shell amplitudes with external momenta shifted into the complex plane. These developments have triggered significant research and numerous applications towards Born amplitudes in QCD [52–73]. In addition, when combined with the unitarity method [74,75] the recursion relations have proven very useful for one-loop calculations in QCD [76–105]. Here, we would like to review the basics of the on-shell recursion relations for Born QCD amplitudes and the proof of its validity.

---

[6]Contributed by: C. Schwinn, S. Weinzierl

3.2 Helicity amplitudes and colour decomposition

It is a well-known fact that the complexity of a calculation based on Feynman diagrams grows factorially with the number of external particles. In order to keep the size of intermediate expressions under control, a divide-and-conquer strategy has been proven useful: One divides the quantity to be calculated into smaller pieces and calculates the small pieces separately.

One first observes that it is not necessary to square the amplitude and sum over the spins and helicities analytically. It is sufficient to do this numerically. This avoids obtaining $O(N^2)$ terms from an expression with $O(N)$ terms. The individual amplitudes have to be calculated in a helicity or spin basis. This is straightforward for massless fermions. The two-component Weyl spinors provide a convenient basis:

$$|p\pm\rangle = \frac{1}{2}\left(1 \pm \gamma_5\right)u(p). \tag{1}$$

In the literature there are different notations for Weyl spinors. Apart from the bra-ket-notation there is the notation with dotted and un-dotted indices: The relation between the two notations is the following:

$$|p+\rangle = p_B, \qquad \langle p+| = p_{\dot{A}}, \qquad |p-\rangle = p^{\dot{B}}, \qquad \langle p-| = p^A. \tag{2}$$

Spinor products are defined as

$$\langle pq \rangle = \langle p-|q+\rangle, \qquad [pq] = \langle p+|q-\rangle, \tag{3}$$

and take value in the complex numbers. It was a major break-through, when it was realised that also gluon polarisation vectors can be expressed in terms of two-component Weyl spinors [106–112]. The polarisation vectors of external gluons can be chosen as

$$\varepsilon_\mu^+(k,q) = \frac{\langle q-|\gamma_\mu|k-\rangle}{\sqrt{2}\langle q-|k+\rangle}, \qquad \varepsilon_\mu^-(k,q) = \frac{\langle q+|\gamma_\mu|k+\rangle}{\sqrt{2}\langle k+|q-\rangle}, \tag{4}$$

where k is the momentum of the gluon and q is an arbitrary light-like reference momentum. The dependence on the arbitrary reference momentum q will drop out in gauge invariant quantities.

The second observation is related to the fact, that individual helicity amplitudes can be decomposed into group-theoretical factors (carrying the colour structures) multiplied by kinematic functions called partial amplitudes [113–117]. These partial amplitudes do not contain any colour information and are gauge-invariant objects. In the pure gluonic case tree level amplitudes with n external gluons may be written in the form

$$\mathcal{A}_n(1,...,n) = g^{n-2} \sum_{\sigma \in S_n/Z_n} 2\,\mathrm{Tr}\left(T^{a_{\sigma(1)}}...T^{a_{\sigma(n)}}\right) A_n\left(\sigma(1),...,\sigma(n)\right), \tag{5}$$

where the sum is over all non-cyclic permutations of the external gluon legs and the normalisation of the colour matrices is $\mathrm{Tr}\,T^a T^b = \delta^{ab}/2$. The quantities A_n on the r.h.s. are the partial amplitudes and contain the kinematic information. They are colour-ordered, e.g. only diagrams with a particular cyclic ordering of the gluons contribute. In general, the colour factors are combinations of open strings $(T^{a_1}...T^{a_n})_{i_q j_{\bar{q}}}$ and closed strings $\mathrm{Tr}\left(T^{b_1}...T^{b_m}\right)$ of colour matrices. These building blocks form a basis in colour space. The choice of the basis for the colour structures is not unique, and several proposals for bases can be found in the literature [118–120].

3.3 Spinor space versus momentum space

It will be useful to discuss the relationship between spinor space and complexified momentum space. Let us first fix our conventions. The metric tensor is $g_{\mu\nu} = \mathrm{diag}(+1,-1,-1,-1)$. A null-vector satisfies

$$(p_0)^2 - (p_1)^2 - (p_2)^2 - (p_3)^2 = 0. \tag{6}$$

This relation holds also for complex p_μ. In complexified momentum space it is possible to choose a basis consisting only of null-vectors:

$$e_1 = (1,0,0,1), \quad e_2 = (0,1,i,0), \quad e_3 = (0,1,-i,0), \quad e_4 = (1,0,0,-1), \tag{7}$$

is an example of such a basis. Light-cone coordinates are defined as follows:

$$p_+ = p_0 + p_3, \quad p_- = p_0 - p_3, \quad p_\perp = p_1 + ip_2, \quad p_{\perp*} = p_1 - ip_2. \tag{8}$$

Note that $p_{\perp*}$ does not involve a complex conjugation of p_1 or p_2. A convenient representation for the Dirac matrices is the Weyl representation:

$$\gamma^\mu = \begin{pmatrix} 0 & \sigma^\mu \\ \bar{\sigma}^\mu & 0 \end{pmatrix}, \quad \gamma_5 = i\gamma^0\gamma^1\gamma^2\gamma^3 = \begin{pmatrix} 1 & 0 \\ 0 & -1 \end{pmatrix}, \quad \sigma^\mu_{A\dot{B}} = (1, -\vec{\sigma}), \quad \bar{\sigma}^{\mu\dot{A}B} = (1, \vec{\sigma}), \tag{9}$$

with $\vec{\sigma} = (\sigma_x, \sigma_y, \sigma_z)$ being the Pauli matrices. A Weyl spinor p_A is an element of a complex two-dimensional vector space S, and similar a spinor $p_{\dot{B}}$ is an element of (another) complex two-dimensional vector space S'. We will think of p_A and $p_{\dot{B}}$ as independent quantities. The dual space to S will be denoted by $\bar{S}$, its elements by p^A. Similarly, we denote the dual space to S' by $\bar{S}'$ and its elements by $p^{\dot{B}}$. The two-dimensional antisymmetric tensor provides an isomorphism between S and $\bar{S}$ as well as between S' and $\bar{S}'$:

$$p^A = \varepsilon^{AB} p_B, \quad p_B = p^A \varepsilon_{AB}, \quad p^{\dot{A}} = \varepsilon^{\dot{A}\dot{B}} p_{\dot{B}}, \quad p_{\dot{B}} = p^{\dot{A}} \varepsilon_{\dot{A}\dot{B}}. \tag{10}$$

We take the two-dimensional antisymmetric tensor as

$$\varepsilon^{AB} = \varepsilon_{AB} = \varepsilon^{\dot{A}\dot{B}} = \varepsilon_{\dot{A}\dot{B}} = \begin{pmatrix} 0 & 1 \\ -1 & 0 \end{pmatrix}. \tag{11}$$

Spinors are solutions of the Dirac equation, therefore we have for massless Weyl spinors

$$p_\mu \bar{\sigma}^\mu |p+\rangle = 0, \quad p_\mu \sigma^\mu |p-\rangle = 0, \quad \langle p+| p_\mu \bar{\sigma}^\mu = 0, \quad \langle p-| p_\mu \sigma^\mu = 0. \tag{12}$$

As normalisation we take for massless spinors

$$\langle p - |\sigma_\mu| p - \rangle = 2p_\mu, \quad \langle p + |\bar{\sigma}_\mu| p + \rangle = 2p_\mu. \tag{13}$$

The solutions to eqs. (12), (13) and (10) are

$$|p+\rangle = \frac{e^{i\left(\alpha - \frac{1}{2}\phi\right)}}{\sqrt{|p_+|}} \begin{pmatrix} -p_{\perp*} \\ p_+ \end{pmatrix}, \quad |p-\rangle = \frac{e^{-i\left(\alpha + \frac{1}{2}\phi\right)}}{\sqrt{|p_+|}} \begin{pmatrix} p_+ \\ p_\perp \end{pmatrix},$$

$$\langle p+| = \frac{e^{-i\left(\alpha + \frac{1}{2}\phi\right)}}{\sqrt{|p_+|}} (-p_\perp, p_+), \quad \langle p-| = \frac{e^{i\left(\alpha - \frac{1}{2}\phi\right)}}{\sqrt{|p_+|}} (p_+, p_{\perp*}). \tag{14}$$

Here α is an arbitrary phase and ϕ is the phase of $p_+ = |p_+| e^{i\phi}$. The spinors corresponding to a four-vector p_μ are only determined up to a phase. With these spinors we have

$$\langle pq \rangle [qp] = 2p \cdot q. \tag{15}$$

It is worth to note that the relation $\bar{u}(p) = u(p)^\dagger \gamma^0$, or equivalently

$$|p+\rangle^\dagger = \langle p+|, \quad |p-\rangle^\dagger = \langle p-|, \tag{16}$$

holds only for real p_μ and positive p_+ (e.g. $\phi = 0$), since

$$|p+\rangle^\dagger = \frac{e^{-i(\alpha - \frac{1}{2}\phi)}}{\sqrt{|p_+|}} \left((-p_{\perp *})^*, p_+{}^*\right), \qquad |p-\rangle^\dagger = \frac{e^{i(\alpha + \frac{1}{2}\phi)}}{\sqrt{|p_+|}} \left(p_+{}^*, p_\perp{}^*\right). \tag{17}$$

Here the upper asterisk denotes the usual complex conjugation. A pair of spinors $(p_{\dot{A}}, p_B)$ determines a (unique) null-vector through

$$p_\mu = \frac{1}{2} p_{\dot{A}} \bar{\sigma}_\mu^{\dot{A}B} p_B = \frac{1}{2} \langle p + |\bar{\sigma}_\mu| p+\rangle. \tag{18}$$

This is just eq. (13) written reversely. For arbitrary $p_{\dot{A}}$ and p_B the four-vector p_μ will be in general complex. While eq. (14) defines a map from complexified momentum space to the spinor space S and S', which is unique up to a phase, eq. (18) goes in the reverse direction: It defines a map from the space $S' \times S$ to complexified momentum space. In this context it is worth to observe that if we change $p_{\dot{A}}$ or p_B (but not both) by a linear transformation as

$$p_{\dot{A}} \to p_{\dot{A}} + z q_{\dot{A}} \quad \text{or} \quad p_B \to p_B - z q_B, \tag{19}$$

the resulting four-vector $p_\mu(z)$ will be a linear function of z. Note however that a linear change in p_μ as in $p_\mu \to p_\mu + z q_\mu$ with a subsequent application of eq. (14) will not result in a linear change in $p_{\dot{A}}$ nor p_B.

3.4   On-shell recursion relations

In the previous section we have seen that we can associate to any null-vector p_μ a pair of spinors $(p_{\dot{A}}, p_B)$. From this pair we can reconstruct the original four-vector through eq. (18). To state the on-shell recursion relations it is best not to view the partial amplitude A_n as a function of the four-momenta, but to replace each four-vector by a pair of two-component Weyl spinors. Therefore the partial amplitude A_n, being originally a function of the momenta k_j and helicities λ_j, can equally be viewed as a function of the Weyl spinors k_A^j, $k_{\dot{B}}^j$ and the helicities λ_j:

$$A_n(k_1, \lambda_1, ..., k_n, \lambda_n) = A_n(k_A^1, k_{\dot{B}}^1, \lambda_1, ..., k_A^n, k_{\dot{B}}^n, \lambda_n). \tag{20}$$

Let us now consider the n-gluon amplitude. For the recursion relation we single out two particles i and j. If $(\lambda_i, \lambda_j) \neq (-, +)$ we have the following recurrence relation:

$$A_n\left(k_A^1, k_{\dot{B}}^1, \lambda_1, ..., k_A^n, k_{\dot{B}}^n, \lambda_n\right) = \tag{21}$$

$$\sum_{partitions} \sum_{\lambda = \pm} A_L\left(..., \hat{k}_A^i, k_{\dot{B}}^i, \lambda_i, ..., i\hat{K}_A, i\hat{K}_{\dot{B}}, -\lambda\right) \frac{i}{K^2} A_R\left(\hat{K}_A, \hat{K}_{\dot{B}}, \lambda, ..., k_A^j, \hat{k}_{\dot{B}}^j, \lambda_j, ...\right).$$

where the sum is over all partitions such that particle i is on the left and particle j is on the right. The momentum K is given as the sum over all unshifted momenta of the original external particles, which are part of A_L. In eq. (21) the shifted spinors $\hat{k}_A^i$, $\hat{k}_{\dot{B}}^j$, $\hat{K}_A$ and $\hat{K}_{\dot{B}}$ are given by

$$\hat{k}_A^i = k_A^i - z k_A^j, \quad \hat{k}_{\dot{B}}^j = k_{\dot{B}}^j + z k_{\dot{B}}^i, \quad \hat{K}_A = \frac{K_{A\dot{B}} k_i^{\dot{B}}}{\sqrt{\langle i + |K| j+\rangle}}, \quad \hat{K}_{\dot{B}} = \frac{k_j^A K_{A\dot{B}}}{\sqrt{\langle i + |K| j+\rangle}}, \tag{22}$$

and

$$z = \frac{K^2}{\langle i + |K| j+\rangle}. \tag{23}$$

Here we shifted k_A^i and $k_{\dot{B}}^j$, while $k_{\dot{A}}^i$ and k_B^j were left untouched. We could equally well have used the other choice: Shifting $k_{\dot{A}}^i$ and k_B^j, while leaving k_A^i and $k_{\dot{B}}^j$ unmodified. In this case one obtains a recursion relation valid for the helicity combinations $(\lambda_i, \lambda_j) \neq (+, -)$. Therefore for all helicity combinations of (λ_i, λ_j) there is at least one valid recursion relation. Applying this recursion relation to the six-gluon amplitude $A_6(1^-, 2^-, 3^-, 4^+, 5^+, 6^+)$ with three positive and three negative helicities, we choose $(i, j) = (6, 1)$. In this case only two diagrams need to be calculated and we obtain the compact result

$$A_6(1^-, 2^-, 3^-, 4^+, 5^+, 6^+) =$$
$$4i \left[\frac{\langle 6 + |1 + 2|3 + \rangle^3}{[61][12]\langle 34 \rangle \langle 45 \rangle s_{126} \langle 2 + |1 + 6|5 + \rangle} + \frac{\langle 4 + |5 + 6|1 + \rangle^3}{[23][34]\langle 56 \rangle \langle 61 \rangle s_{156} \langle 2 + |1 + 6|5 + \rangle} \right]. \quad (24)$$

3.5 Quarks, massive or massless

QCD does not consist solely of gluons, but contains the quarks as well. Let us now discuss the general case of the inclusion of massive quarks. All formulae will have a smooth limit $m \to 0$, therefore the case of massless quarks will need no further discussion. For massive fermions we have to consider Dirac spinors. We can take them as

$$u(\pm) = \frac{1}{\langle p^\flat \mp | q \pm \rangle} (\not{p} + m) | q \pm \rangle, \quad \bar{u}(\pm) = \frac{1}{\langle q \mp | p^\flat \pm \rangle} \langle q \mp | (\not{p} + m),$$
$$v(\pm) = \frac{1}{\langle p^\flat \mp | q \pm \rangle} (\not{p} - m) | q \pm \rangle, \quad \bar{v}(\pm) = \frac{1}{\langle q \mp | p^\flat \pm \rangle} \langle q \mp | (\not{p} - m). \quad (25)$$

Here, p is the momentum of the fermion and $|q+\rangle$ and $\langle q + |$ are two independent Weyl spinors used as reference spinors. These two spinors define a light-like four-vector $q^\mu = \frac{1}{2} \langle q + |\gamma^\mu| q + \rangle$, which in turn is used to associate to any not necessarily light-like four-vector p a light-like four-vector $p^\flat$:

$$p^\flat = p - \frac{p^2}{2p \cdot q} q. \quad (26)$$

The reference spinors are related to the quantisation axis of the spin for the fermion, and the individual amplitudes with label $+$ or $-$ will therefore refer to this spin axis. From the Dirac spinors we can reconstruct the four-vector p^μ as follows:

$$p^\mu = \frac{1}{4} \sum_\lambda \bar{u}(\lambda) \gamma^\mu u(-\lambda). \quad (27)$$

For the recursion relation, we again single out two particles i and j, which need not be massless, with four-momenta p_i and p_j. To these two four-momenta we associate two light-like four-momenta l_i and l_j as follows [121, 122]:

$$l_i = \frac{1}{1 - \alpha_i \alpha_j} (p_i - \alpha_j p_j), \quad l_j = \frac{1}{1 - \alpha_i \alpha_j} (-\alpha_i p_i + p_j), \quad \alpha_k = \frac{2p_i p_j - \text{sign}(2p_i p_j)\sqrt{\Delta}}{2p_k^2}. \quad (28)$$

with $\Delta = (2p_i p_j)^2 - 4p_i^2 p_j^2$. These light-like four-vectors define massless spinors $|l_i+\rangle$, $\langle l_i + |$, $|l_j+\rangle$ and $\langle l_j + |$. If particle i is a massive quark or anti-quark, we use $|l_j+\rangle$ and $\langle l_j + |$ as reference spinors for particle i. If particle j is a massive quark or anti-quark, we use $|l_i+\rangle$ and $\langle l_i + |$ as reference spinors for particle j. We have the recursion relation

$$A_n \left(u_1(-), \bar{u}_1(+), \lambda_1, ..., u_n(-), \bar{u}_n(+), \lambda_n \right) = \quad (29)$$
$$\sum_{partitions} \sum_{\lambda = \pm} A_L \left(..., u_i'(-), \bar{u}_i(+), \lambda_i, ..., iv_K'(-), i\bar{v}_K'(+), -\lambda \right)$$
$$\times \frac{i}{K^2 - m_k^2} A_R \left(u_K'(-), \bar{u}_K'(+), \lambda, ..., u_j(-), \bar{u}_j'(+), \lambda_j, ... \right).$$

Here we denote by k the intermediate particle where we factorise the amplitude, and by K the off-shell four-momentum flowing through this propagator in the unshifted amplitude. We shift the Dirac spinors as follows:

$$u_i{}'(-) = u_i(-) - z|l_j+\rangle, \quad \bar{u}_j{}'(+) = \bar{u}_j(+) + z\langle l_i + |, \quad z = \frac{K^2 - m_k^2}{\langle l_i + |K|l_j+\rangle}. \tag{30}$$

For the intermediate particle k we define the polarisations with respect to the reference spinors $|l_j+\rangle$ and $\langle l_i + |$:

$$u_K{}'(-) = \frac{1}{\langle K^\flat + |l_i-\rangle} \left(K\!\!\!/' + m_k \right) |l_i-\rangle, \qquad \bar{u}'_K(+) = \frac{1}{\langle l_j - |K^\flat+\rangle} \langle l_j - | \left(K\!\!\!/' + m_k \right), \tag{31}$$

where

$$K'^\mu = K^\mu - \frac{z}{2}\langle l_i + |\gamma^\mu|l_j+\rangle, \qquad K^{\flat \mu} = K^\mu - \frac{1}{2}\frac{K^2}{\langle l_i + |K|l_j+\rangle}\langle l_i + |\gamma^\mu|l_j+\rangle. \tag{32}$$

The recursion relation is valid for $(\lambda_i, \lambda_j) \neq (-, +)$ with the following exceptions:

- Particles i and j cannot belong to the same fermion line.
- The combinations (q_i^+, g_j^+), $(\bar{q}_i^+, g_j^+)$, (g_i^-, q_j^-) and $(g_i^-, \bar{q}_j^-)$ are excluded.
- If i is massive, the combinations $(q_i^+, q_j'^+)$, $(q_i^+, \bar{q}_j'^+)$, $(\bar{q}_i^+, q_j'^+)$ and $(\bar{q}_i^+, \bar{q}_j'^+)$ are excluded.
- If j is massive, the combinations $(q_i^-, q_j'^-)$, $(q_i^-, \bar{q}_j'^-)$, $(\bar{q}_i^-, q_j'^-)$ and $(\bar{q}_i^-, \bar{q}_j'^-)$ are excluded.

Instead of shifting $u_i(-)$ and $\bar{u}_j(+)$, we can alternatively shift $\bar{u}_i(+)$ and $u_j(-)$:

$$\bar{u}_i{}'(+) = \bar{u}_i(+) - z\langle l_j + |, \quad u_j{}'(-) = u_j(-) + z|l_i+\rangle, \quad z = \frac{K^2 - m_k^2}{\langle l_j + |K|l_i+\rangle}. \tag{33}$$

For the intermediate particle k we define the polarisations now with respect to the reference spinors $|l_i+\rangle$ and $\langle l_j + |$:

$$u_K{}'(-) = \frac{1}{\langle K^\flat + |l_j-\rangle} \left(K\!\!\!/' + m_k \right) |l_j-\rangle, \qquad \bar{u}'_K(+) = \frac{1}{\langle l_i - |K^\flat+\rangle} \langle l_i - | \left(K\!\!\!/' + m_k \right), \tag{34}$$

where

$$K'^\mu = K^\mu - \frac{z}{2}\langle l_j + |\gamma^\mu|l_i+\rangle, \qquad K^{\flat \mu} = K^\mu - \frac{1}{2}\frac{K^2}{\langle l_j + |K|l_i+\rangle}\langle l_j + |\gamma^\mu|l_i+\rangle. \tag{35}$$

Doing so, we obtain a recursion relation valid for $(\lambda_i, \lambda_j) \neq (+, -)$ with the following exceptions:

- Particles i and j cannot belong to the same fermion line.
- The combinations (g_i^+, q_j^+), $(g_i^+, \bar{q}_j^+)$, (q_i^-, g_j^-) and $(\bar{q}_i^-, g_j^-)$ are excluded.
- If j is massive, the combinations $(q_i^+, q_j'^+)$, $(q_i^+, \bar{q}_j'^+)$, $(\bar{q}_i^+, q_j'^+)$ and $(\bar{q}_i^+, \bar{q}_j'^+)$ are excluded.
- If i is massive, the combinations $(q_i^-, q_j'^-)$, $(q_i^-, \bar{q}_j'^-)$, $(\bar{q}_i^-, q_j'^-)$ and $(\bar{q}_i^-, \bar{q}_j'^-)$ are excluded.

As we are free to choose the particles i and j, we can compute all Born helicity amplitudes in QCD with two-particle shifts via recursion relations, except the ones which involve only massive quarks or anti-quarks. Amplitudes consisting solely of massive quarks and anti-quarks and with more than six particles may be calculated recursively if one allows more general shifts, where more than two particles are shifted.

3.6 Proof of the on-shell recursion relations

For the proof [51, 55, 59–61, 72] of the on-shell recursion relation we discuss as an example the case of the holomorphic shift as in eq. (22) or eq. (30). One considers the function

$$A(z) = A_n \left(..., u_i{}'(-), \bar{u}_i(+), \lambda_i, ..., u_j(-), \bar{u}'_j(+), \lambda_j, ... \right) \tag{36}$$

of one variable z, where the z-dependence enters through

$$u_i{}'(-) = u_i(-) - z|l_j+\rangle, \qquad \bar{u}'_j(+) = \bar{u}_j(+) + z\langle l_i + |. \tag{37}$$

The function $A(z)$ is a rational function of z, which has only simple poles in z. This follows from the Feynman rules and the factorisation properties of amplitudes. Therefore, if $A(z)$ vanishes for $z \to \infty$, $A(z)$ is given by Cauchy's theorem as the sum over its residues. This is just the right hand side of the recursion relation. The essential ingredient for the proof is the vanishing of $A(z)$ at $z \to \infty$. If $(\lambda_i, \lambda_j) = (+, -)$ it can be shown that each individual Feynman diagram vanishes for $z \to \infty$. For the helicity combinations $(+, +)$ and $(-, -)$ one first constructs a supplementary recursion relation based on three-particle shifts and deduces from this representation the large z-behaviour of $A(z)$. This establishes the recursion relation for these helicity combinations with the exceptions indicated above. The proof for the anti-holomorphic shift as in eq. (33) proceeds analogously.

4. ON-SHELL RECURSION TO DETERMINE RATIONAL TERMS[7]

On-shell methods offer an auspicious approach for dealing with the rapid growth in complexity of loop amplitudes as the number of particles in the process increases. These methods rely on the unitarity of the theory [123, 124] which requires that the poles and branch cuts of amplitudes correspond to physical propagation of particles. On-shell methods are presently undergoing intense development for use at loop level (see, for example, refs. [86,87,89,95,97–104,125–127]). Their advantage lies in the relatively mild growth in complexity as the number of external particles increases, *effectively reducing loop calculations to tree-like calculations*.

On-shell methods fall into two basic categories: the unitarity method [74, 128] which constructs amplitudes based on their branch cuts, and on-shell recursion [50, 51] which constructs amplitudes from their poles. In this section we discuss using on-shell recursion as a means for computing rational terms of one-loop amplitudes. The loop-level construction is based directly on the construction of tree-level recursion relations by Britto, Cachazo, Feng and Witten (BCFW), though a number of new features are present. Further discussion of the unitarity method approach, as well as other new methods exploiting on-shell conditions on intermediate states [80, 89, 95, 98, 102, 104, 129] may be found in other sections of this report. Introductions to on-shell methods may be found in various reviews [130–132]. Earlier reviews of spinor methods, which are profitably used in conjunction with on-shell methods, may be found in refs. [133, 134].

In the context of the unitarity method, it is convenient to divide the amplitudes into pieces that contain branch cuts, plus rational (non-cut-containing) pieces. When using dimensional regularization, the branch-cut containing pieces may be computed by ignoring the distinction between $D = 4 - 2\epsilon$ dimensions and four-dimensions in the numerators of the loop-momentum integrands [74, 128]. This observation allows powerful four-dimensional spinor techniques to be used to greatly simplify the on-shell tree amplitudes appearing in the unitarity cuts. However, if one wants to obtain also the rational terms directly from the cuts [130, 135], then the (-2ϵ) dimensional contributions are crucial: dropping these pieces leaves undetermined additive rational terms. (The branch cuts can determine rational terms at $\mathcal{O}(\epsilon^0)$ because they develop branch cuts at $\mathcal{O}(\epsilon)$.) By using amplitudes valid in $D = 4 - 2\epsilon$ dimensions in the unitarity cuts, all rational terms are kept[8] but at the cost of more complicated expressions. It has

---

[7]Contributed by: Z. Bern, L.J. Dixon

[8]In the language of dispersion relations [136, 137], this reconstruction is possible because the dispersion integrals converge with dimensional regularization [138].
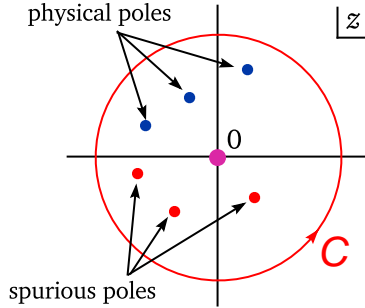
Fig. 6: Using Cauchy's theorem, rational terms in loop amplitudes can be reconstructed from residues at poles in the complex plane. The poles are of two types: physical and spurious. All pole locations are known *a priori*. Residues at physical poles follow from factorization onto lower-point amplitudes. Residues at spurious poles cancel against corresponding contributions from the cut parts, and so they can be inferred from four-dimensional cuts.

been pointed out [90–93] that the rational terms are relatively easy to obtain from Feynman diagrams because they do not require the full set of tensor integrals. In addition, Brandhuber *et. al.* have argued that the rational terms can be obtained from a set of counterterms [125]. Britto and Feng have recently given a complete set of formulæ for constructing loop amplitudes, including their rational terms [104], following earlier work [80, 89, 97–100, 129].

An early version of on-shell methods was used to compute the one-loop matrix elements needed for the NLO QCD corrections to $e^+e^- \to \gamma^*, Z \to 4$ jets and $pp \to W, Z + 2$ jets [139]. They have also been used to obtain analytic expressions for the complete one-loop six-gluon amplitude [74, 76, 78, 80, 86, 87, 89–92, 128] as well as a variety of helicity configurations for n-gluon amplitudes [82, 85–87, 101]. The results confirm the mild growth in complexity of these methods as the number of external particles grows.

A crucial next step for applying these methods to LHC physics is the construction of automated programs to compute the large number of phenomenologically interesting high-multiplicity processes. As discussed in other sections of this report, such automated programs are in the midst of being constructed [103, 126], using the integration machinery of Ossola, Papadopoulos, and Pittau [95]. The recent numerical implementation by Ellis, Giele and Kunszt [126] of the unitarity method presently makes use of $D = 4$ simplifications and hence does not contain rational terms. The program of Ossola, Papadopoulos, and Pittau [103] can be used to obtain the rational terms, but currently requires one-loop Feynman diagrams to capture these terms, instead of more efficient on-shell tree amplitudes.

On-shell recursion offers an efficient alternative for constructing one-loop rational terms directly from their known factorization properties, in much the same way as the BCFW recursion relations can be used to obtain tree-level amplitudes. However, a number of new issues arise at loop level that must be dealt with first to have a practical method. These issues include the appearance of branch cuts, spurious singularities, the behavior of loop amplitudes under large complex deformations and in some cases, 'unreal poles', which are present with complex but not real momenta. More practical issues are automation and numerical stability. Here we briefly summarize the construction of rational terms via on-shell recursion [81–83, 86, 87, 101], describing in particular a simple modification making it straightforward to automate.

In general, any one-loop amplitude can be divided into two pieces,

$$A_n^{(1)} = c_\Gamma \left[C_n + R_n \right], \tag{38}$$

where C_n are the 'cut-containing terms' possessing logarithms, polylogarithms, and associated π's. The
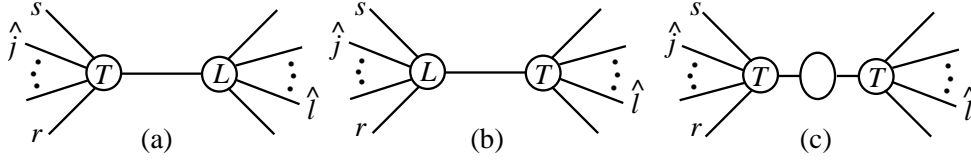
Fig. 7: Diagrammatic contributions to on-shell recursion at one-loop for a $[j, l\rangle$ shift. The labels 'T' and 'L' refer to tree and one-loop vertices corresponding to the rational parts of lower-point on-shell amplitudes.

rational terms, denoted by R_n, are defined by setting these (poly)logarithmic terms to zero,

$$R_n \equiv \frac{1}{c_\Gamma} A_n \bigg|_{\text{rat}} \equiv \frac{1}{c_\Gamma} A_n \bigg|_{\ln, \text{Li}_2, \pi \to 0} . \tag{39}$$

Let us assume that the cut-containing terms C_n of the particular amplitude under consideration have already been computed using four-dimensional unitarity. This leaves the problem of computing the rational terms R_n.

On-shell recursion relations can be derived by considering complex on-shell deformations of amplitudes $A(z)$, which are characterized by a single complex parameter z [51]. The z-dependence allows us to use standard complex variable theory to construct amplitudes via Cauchy's Theorem. To set up an on-shell recursion relation for R_n consider the effect of shifting some set of external momenta $k_i \to k_i(z)$, such that the on-shell conditions $[k_i(z)]^2 = m_i^2$ and the original momentum conservation are satisfied. In the massless case, it is particularly convenient to shift the momenta of two external legs, say, j and l,

$$\begin{aligned}
k_j^\mu &\to k_j^\mu(z) = k_j^\mu - \frac{z}{2} \langle j^- | \gamma^\mu | l^- \rangle, \\
k_l^\mu &\to k_l^\mu(z) = k_l^\mu + \frac{z}{2} \langle j^- | \gamma^\mu | l^- \rangle,
\end{aligned} \tag{40}$$

where z is a complex parameter and $|i^+\rangle$ and $|i^-\rangle$ are Weyl spinors of positive and negative chirality, following the notation of ref. [133]. In terms of these spinors, the shift is

$$|j^-\rangle \to |j^-\rangle - z\,|l^-\rangle, \qquad |l^+\rangle \to |l^+\rangle + z\,|j^+\rangle. \tag{41}$$

We denote the shift in eqs. (40) and (41) as a $[j, l\rangle$ shift.

The on-shell recursion relations follow from evaluating the contour integral,

$$\frac{1}{2\pi i} \oint_C dz \, \frac{R_n(z)}{z}, \tag{42}$$

where the contour is taken around the circle at infinity, as depicted in fig. 6, and $R_n(z)$ is R_n evaluated at the shifted momenta (40). If the rational terms under consideration vanish as $z \to \infty$, the contour integral vanishes and we obtain a relationship between the desired rational contributions at $z = 0$, and a sum over residues of the poles of $R_n(z)$, located at z_α,

$$R_n(0) = - \sum_{\text{poles } \alpha} \text{Res}_{z=z_\alpha} \frac{R_n(z)}{z}. \tag{43}$$

If $R_n(z)$ does not vanish as $z \to \infty$, then there are additional contributions. A systematic strategy for computing such large z contributions using auxiliary recursion relations was presented in ref. [86], to which we refer the reader.
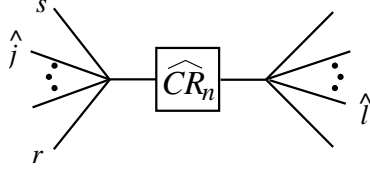
Fig. 8: Diagrammatic representation of one-loop overlap terms for a $[j, l\rangle$ shift. The channels correspond to physical poles and remove double counts induced by cut completion.

As illustrated in fig. 6, the poles in one-loop rational terms fall into two categories: the physical poles, which are present in the full amplitudes; and the spurious poles, which cancel against poles in the cut-containing terms.

Residues at physical poles are dictated by factorization onto lower-point amplitudes. They may be computed using the recursive diagrams[9] in fig. 7,

$$
\begin{aligned}
R_n^D \equiv & -\sum_{\text{phys. poles } \{r,s\}} \text{Res}_{z=z_{rs}} \frac{R_n(z)}{z} \\
= & \sum_{r,s,h} \left\{ A_L^{\text{tree}}(z = z_{rs}) \frac{i}{K_{r\cdots s}^2} R_R(z = z_{rs}) + R_L(z = z_{rs}) \frac{i}{K_{r\cdots s}^2} A_R^{\text{tree}}(z = z_{rs}) \right. \\
& \left. + A_L^{\text{tree}}(z = z_{rs}) \frac{iR_{\mathcal{F}}}{K_{r\cdots s}^2} A_R^{\text{tree}}(z = z_{rs}) \right\}.
\end{aligned}
\tag{44}
$$

The 'vertices' R_L and R_R in this recursion relation are the pure rational parts — using the definition (39) — of the lower-point, on-shell one-loop amplitudes. The 'vertices' A_L^{tree} and A_R^{tree} are on-shell tree amplitudes. The subscripts L and R on the vertices indicate their location to the left or right of the central propagator in fig. 7. In the vertices the shift variable z is frozen to the values

$$
z_{rs} = \frac{K_{r\cdots s}^2}{\langle j^- | \mathcal{K}_{r\cdots s} | l^- \rangle},
\tag{45}
$$

corresponding to the location of the poles in z, coming from shifted propagators. The rational part $R_{\mathcal{F}}$ of the factorization function $\mathcal{F}$ [140] only contributes in multi-particle channels, and only if the tree amplitude contains a pole in that channel. Generically we have a double sum, labeled by r, s, over recursive diagrams, with legs j and l always appearing on opposite sides of the pole. There is also a sum over the helicity h of the intermediate state. The superscript D on R_n^D indicates that this set of recursive diagrammatic contributions is not the whole rational part, as discussed below.

It is interesting to note the similarity of the one-loop recursion relation (44), to the corresponding tree-level recursion relation [51],

$$
A_n^{\text{tree}} = \sum_{r,s,h} A_L^{\text{tree}}(z = z_{rs}) \frac{i}{K_{r\cdots s}^2} A_R^{\text{tree}}(z = z_{rs}).
\tag{46}
$$

Thus loop-level recursive diagrams echo the simplicity of tree-level recursion.

One way to deal with the spurious poles is to start by finding a 'cut completion' $\hat{C}_n$ [83, 86, 87, 101, 132]. One adds certain rational terms $\widehat{CR}_n$ to C_n, such that the spurious poles in $\hat{C}_n(z)$ cancel entirely. Because physical amplitudes cannot have spurious singularities, the remaining rational terms,

---

[9]'Unreal' poles, which do not correspond to factorizations with real momenta, may be avoided by choosing appropriate shifts [86].
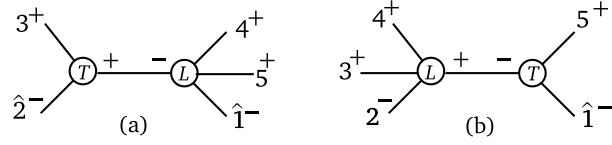
Fig. 9: Non-vanishing recursive diagrams for the rational terms of $A_5^{(1),s}(1^-, 2^-, 3^+, 4^+, 5^+)$, using a $[1, 2\rangle$ shift.

$\hat{R}_n(z)$, must also be free of these spurious singularities. This cut completion makes it unnecessary to compute residues at spurious poles. It is rather helpful when deriving compact analytic expressions for the amplitudes. It does introduce additional 'overlap diagrams', as depicted in fig. 8. These diagrams correct for the contributions of $\widehat{CR}_n$ in physical factorization limits. They are simple to compute from the residue of $\widehat{CR}_n$ at each physical pole z_{rs}.

Following the cut-completion procedure, a variety of rational terms with an arbitrary number of external legs have been constructed [85–87, 101], giving complete amplitudes when combined with the previously-computed cut-containing parts [74, 78, 79, 84, 101, 128]. More generally, it should be possible to form a set of cut completions using integral functions of the type given in ref. [141] to absorb the spurious singularities.

For the purposes of automation in a numerical program, another approach is preferable [142]. It is simpler to obtain the residues at the spurious poles directly from the cut parts, calculated from the four-dimensional unitarity method. Because a complete amplitude is free of spurious poles, any spurious pole found in the rational parts must cancel a spurious pole in the cut parts. To get the full rational part,

$$R_n = R_n^D + R_n^S, \tag{47}$$

we add to the recursive diagrams R_n^D some 'spurious' contributions R_n^S, evaluated by means of the cut terms $C_n(z)$,

$$R_n^S = - \sum_{\text{spur. poles } \beta} \text{Res}_{z=z_\beta} \frac{R_n(z)}{z} = \sum_{\text{spur. poles } \beta} \text{Res}_{z=z_\beta} \frac{C_n(z)}{z}. \tag{48}$$

The spurious poles β can be classified systematically in terms of the vanishing loci, $\Delta(z) = 0$, of shifted Gram determinants Δ associated with box, triangle and bubble functions. (In the massless case, the bubble Gram determinant does not generate a spurious pole.)

To illustrate this modified procedure, consider the five-gluon amplitude $A_5^{(1),s}(1^-, 2^-, 3^+, 4^+, 5^+)$, with a scalar in the loop. The construction of the rational terms in this amplitude, using on-shell recursion with cut completion, has already been discussed in some detail elsewhere [83, 132]. Here we describe the new approach for obtaining these terms.

The cut part of the amplitude [143] is

$$
\begin{aligned}
C_5 &= -\frac{i}{6} \frac{\langle 1\,2\rangle^3}{\langle 2\,3\rangle\langle 3\,4\rangle\langle 4\,5\rangle\langle 5\,1\rangle} \left[\ln\left(\frac{-s_{23}}{\mu^2}\right) + \ln\left(\frac{-s_{51}}{\mu^2}\right) \right] \\
&\quad -\frac{i}{3} \frac{[3\,4]\langle 4\,1\rangle\langle 2\,4\rangle[4\,5](\langle 2\,3\rangle[3\,4]\langle 4\,1\rangle + \langle 2\,4\rangle[4\,5]\langle 5\,1\rangle)}{\langle 3\,4\rangle\langle 4\,5\rangle} \frac{\ln\left(\frac{-s_{23}}{-s_{51}}\right)}{(s_{51} - s_{23})^3} + \cdots
\end{aligned}
\tag{49}
$$

where μ^2 is a scale and '$\cdots$' signifies that we are dropping terms not pertinent for our discussion. The spinor inner products and kinematic invariants are defined as,

$$\langle a\,b\rangle \equiv \langle a^- \,|\, b^+\rangle, \qquad [a\,b] \equiv \langle a^+ \,|\, b^-\rangle, \qquad s_{ab} \equiv (k_a + k_b)^2. \tag{50}$$

The rational terms are determined by evaluating the recursive diagrams, plus the rational residues of the cut terms at the spurious poles. Here we use the $[1, 2\rangle$ shift. (As discussed in ref. [83, 86], for this shift there are no additional contributions from either large z behavior or unreal poles.) With the $[1, 2\rangle$ shift, the non-vanishing recursive diagrams are depicted in fig. 9. A simple computation of these diagrams (see section 5.1 of ref. [132]) gives,

$$D_5^{(a)} = i \left(\frac{1}{3\epsilon} + \frac{8}{9} \right) \frac{\langle 1\,2 \rangle^3}{\langle 2\,3 \rangle \langle 3\,4 \rangle \langle 4\,5 \rangle \langle 5\,1 \rangle}, \qquad D_5^{(b)} = -\frac{i}{3} \frac{[2\,4][3\,5]^3}{\langle 3\,4 \rangle [1\,2][1\,5][2\,3]^2}, \qquad (51)$$

as the recursive contributions.

We still need to account for the residues at the spurious poles. In the present example with a $[1, 2\rangle$ shift, the only such pole comes from solving $s_{51}(z) - s_{23}(z) = 0$ (corresponding to a shifted two-mass triangle Gram determinant). The solution is,

$$z_s \equiv \frac{s_{51} - s_{23}}{\langle 1\,5 \rangle [5\,2] + \langle 1\,3 \rangle [3\,2]} = \frac{s_{51} - s_{23}}{\langle 1\,4 \rangle [2\,4]}. \qquad (52)$$

To obtain the residue, we start from the logarithmic terms of eq. (49), and perform the $[1, 2\rangle$ shift eq. (41), yielding,

$$\frac{C_5(z)}{z} = -\frac{i}{3} \frac{[3\,4]\langle 4\,1 \rangle (\langle 2\,4 \rangle + z\langle 1\,4 \rangle)[4\,5]((\langle 2\,3 \rangle + z\langle 1\,3 \rangle)[3\,4]\langle 4\,1 \rangle + (\langle 2\,4 \rangle + z\langle 1\,4 \rangle)[4\,5]\langle 5\,1 \rangle)}{\langle 3\,4 \rangle \langle 4\,5 \rangle}$$

$$\times \frac{\ln \left(\frac{(\langle 2\,3 \rangle + z\langle 1\,3 \rangle)[3\,2]}{\langle 5\,1 \rangle ([1\,5] - z[2\,5])} \right)}{z \left(s_{51} - s_{23} - z\langle 1\,4 \rangle [2\,4] \right)^3} + \cdots, \qquad (53)$$

where we have kept only the term contributing to the spurious residue at z_s.

The residue needed for eq. (48) can be extracted straightforwardly, by series expanding both the logarithm and its coefficient in eq. (53) around $z = z_s$. Cleaning up the result of this residue evaluation, we find,

$$\begin{aligned}
S_5^{(a)} &= \mathrm{Res}_{z=z_s} \frac{C_5(z)}{z} \\
&= -\frac{i}{6} \frac{\langle 1\,2 \rangle^2 \langle 1\,4 \rangle [3\,4]}{\langle 1\,5 \rangle \langle 2\,3 \rangle \langle 3\,4 \rangle \langle 4\,5 \rangle [2\,3]} + \frac{i}{6} \frac{\langle 1\,4 \rangle [3\,4][3\,5] \left(\langle 1\,4 \rangle [3\,4] - \langle 1\,5 \rangle [3\,5] \right)}{\langle 1\,5 \rangle \langle 3\,4 \rangle \langle 4\,5 \rangle [1\,5][2\,3]^2} \\
&\quad - \frac{i}{6} \frac{s_{51} + s_{23}}{s_{23} s_{51} (s_{51} - s_{23})^2} \frac{[3\,4]\langle 4\,1 \rangle \langle 2\,4 \rangle [4\,5] \left(\langle 2\,3 \rangle [3\,4]\langle 4\,1 \rangle + \langle 2\,4 \rangle [4\,5]\langle 5\,1 \rangle \right)}{\langle 3\,4 \rangle \langle 4\,5 \rangle}. \qquad (54)
\end{aligned}$$

The total rational part,

$$R_5 = R_5^D + R_5^S = D_5^{(a)} + D_5^{(b)} + S_5^{(a)}, \qquad (55)$$

matches the result obtained in refs. [83, 132] using a cut completion. The complete amplitude is obtained by summing the cut (49) and rational (55) contributions.

The modified construction described here is amenable to automation. In a numerical program, instead of obtaining the residues at spurious poles by series expansion, we may compute them by numerically evaluating the cut terms at several points around each pole. The automation and numerical implementation of on-shell recursion to amplitudes of interest for LHC phenomenology will be described elsewhere [142].

5. FOUR- AND D-DIMENSIONAL UNITARITY CUTS[10]

5.1 Four-dimensional unitary cuts

The application of unitarity as an on-shell method of calculation, as introduced in [74], is based on the principles that products of on-shell tree-level amplitudes produce functions with the correct branch cuts in all channels [144–147], and that any one-loop amplitude can be expressed as a linear combination of of scalar (i.e. trivial numerator) master integrals [148–153]. Given the independent knowledge of the master integrals, to compute any amplitude it is sufficient to evaluate the coefficients of such a decomposition.

For one-loop amplitudes, systematic techniques have been developed to extract the coefficients algebraically, preserving gauge invariance at every intermediate stage of the computation. The use of *four-dimensional* states and momenta in the cuts enables the construction of the polylogarithmic terms in the amplitudes, which are fixed by their branch cuts, but generically drops rational terms, which have to be recovered independently.

Some recent developments of unitarity-based methods apply generalized unitarity cuts to amplitudes and master integrals. The coefficients are then extracted by matching the generalized cuts. Generalized unitarity corresponds to requiring more than two internal particles to be on-shell, and the fulfillment of these constraints can only be realized through complex kinematics. Complex kinematics are the key for the exploration of singularities of amplitudes and the use of factorization information to reconstruct amplitudes recursively, since the singularities of a scattering amplitude are determined by lower-point amplitudes in the case of poles and by lower-loop ones in the case of cuts [49, 130, 133, 134].

A notable application of complex momenta within generalized unitarity is the quadruple cut, which allows for an immediate and purely algebraic determination of the coefficients of box functions [129]. Every box coefficient is simply determined by the product of the four tree-level amplitudes sitting at each corner, evaluated at the two particular values of the loop momentum which fulfill the four equations imposed by the vanishing of the cut denominators. Double and triple unitarity cuts have led to direct techniques for extracting triangle and bubble integral coefficients analytically [80, 89, 99]. In cases where fewer than four denominators are cut, the loop momentum is not frozen, so some explicit integration over the phase space is still required. In [80, 89, 99], double or triple cut phase-space integration has been reduced to extraction of residues in spinor variables, and, in the case of a triple cut, residues in a Feynman parameter. This approach has been used to compute analytically the final contributions to the cut-constructible part of the the six-gluon amplitude [80, 89], and the complete six-photon amplitudes [93, 94].

In general, one can compute n-point ($n \geq 4$) coefficients from quadruple cuts, three-point coefficients from triple-cuts, and two-point coefficients from double-cuts, by avoiding the conventional tensor reduction. As it turns out, given the decomposition of any amplitude in terms of master integrals, the coefficient of any n-point master integral can be recovered from the n-particle cut. Obviously, any n-particle cut may also detect higher-point master integrals, which appear with different analytic structures for they come from the Landau poles specific to each of the master integrals. This is indeed the case for the usual (double) unitarity cut, which can be used exclusively to derive box, triangle, and bubble coefficients. In cases with massive particles, it is useful to apply a generalized cut to find the coefficient of the 1-point (tadpole) master integral.

The algorithm of [80, 89] for evaluating any finite unitarity cut involves a change of coordinates that brings the loop momentum variable into the spinor formalism. The idea is that the final integrals always localize to some poles in the region of integration. Phase space integration is thus reduced to a sequence of algebraic manipulations, up to an integration over a single Feynman parameter, which is responsible for logarithms. Ultimately, even this integration does not need to be carried out, since it is possible to match integrands at an early stage of the calculation. The procedure naturally leads to a clean separation of the master integrals, allowing for an individual calculation of the corresponding

---

[10]Contributed by: R. Britto, P. Mastrolia

coefficients.

By now, explicit analytic formulas for the results of unitarity-based methods are available [100, 102, 104, 105, 129]. Coefficients of the master integrals are listed directly in terms of tree-level input data. All integration and reduction can now be avoided. Although it may not be a significant distinction in terms of the final results, we note that the derivations of [102, 105, 129] used generalized cuts, while those of [100, 104] used ordinary double cuts.

5.2 D-dimensional unitarity

Full one-loop amplitudes can be reconstructed from unitarity cuts in $D = 4 - 2\epsilon$ dimensions [135, 138]. In the D-dimensional unitarity method, there is no need to distinguish "rational" and "cut-constructible" parts of the amplitude. Contributions that might be called "rational" (after expanding around $\epsilon = 0$) appear here as ϵ-dependent terms in the coefficients of the master integrals (before expanding around $\epsilon = 0$).

A systematic D-dimensional unitarity double-cut method was proposed in [97, 98], reducing one-loop amplitudes to master integrals for arbitrary values of the dimension parameter. Coefficients of the master integrals can be extracted without fully carrying out the D-dimensional phase space integrals. Only a four dimensional (massive) integration is explicitly required. That can be performed by four-dimensional unitarity techniques or any other available alternative. The remaining integral, which gives rise to the ϵ-dependence of the cut-amplitude, is mapped to phase-space integrals in $4 + 2n - 2\epsilon$ dimensions, where n is a positive integer. With recursive dimensional shift identities, similar to the ones in loop integration, the cut-amplitude is reduced in terms of bubble, triangle, box and pentagon cut master integrals in $4 - 2\epsilon$ dimensions. The reduction is valid for an arbitrary number of dimensions. Expanding in ϵ gives both the (poly)logarithmic and rational part of the amplitude at $\mathcal{O}(\epsilon^0)$ and higher; these contributions are required in cross-sections beyond the next-to-leading order in the relevant coupling strength.

Generalized unitarity cuts are possible and useful in D dimensions as well [99, 154]. The benefits of the double-cut integration of [80, 89, 97, 98] have been extended to the evaluation of triple cuts [99], for the direct extraction of triangle and higher-point-function coefficients from any one-loop amplitude in arbitrary dimensions. Accordingly, the triple cut is treated as a difference of two double cuts with the same particle content, and the same propagator carrying respectively causal and anti-causal prescription in each of the two cuts. The triple cut phase space for a massless particle in D dimensions is written as a convolution of a four-dimensional triple cut of a massive particle, and an integration over the corresponding mass parameter, which plays the role of a (-2ϵ)-dimensional scale. Just as in the case of the double-cut [97, 98], to perform the four-dimensional integration, one combines the method of spinor integration of massive phase-space integrals, and an integration over the Feynman parameter. But, in the case of the triple-cut, after Feynman parametrization, by combining back the two double-cuts, the parametric integration is reduced to the extraction of residues to the branch points in correspondence of the zeroes of a standard quadratic function in the Feynman parameter. It is that standard quadratic function (or rather, its roots) that carry the analytic information characterizing each master integral, therefore determining its own generalized cuts. The final integration over the dimensional scale parameter is mapped directly to the triple cut of master integrals, possibly with shifted dimensions.

5.3 Mathematica package for spinor formalism

Recently, the package S@M (Spinors@Mathematica) was released [155]. It implements the spinor-helicity formalism in Mathematica. The package allows the use of complex-spinor algebra along with the multi-purpose features of Mathematica, and it is suitable for the algebraic manipulation and integration of products of tree amplitudes with complex spinors sewn in generalized unitarity cuts.

6.   COMMENTS ON UNITARITY BASED ONE-LOOP ALGORITHMS[11]

6.1   Introduction

At the LHC deviations from the Standard Model will likely show up in observables of complex multiparticle final states. It is important to understand the Standard Model predictions and uncertainties for these complicated final states. Leading-order Monte Carlo (LO-MC) programs give a first estimate. However, to understand the uncertainties we need at least a next-to-leading order Monte Carlo (NLO-MC).

The basic calculational framework for both tree-level amplitudes (needed for the LO-MC) and one-loop amplitudes (needed for NLO-MC) is the perturbative expansion in Feynman diagrams. This immediately gives us a straightforward algorithm suitable for numerical implementation. However, such implementations are not satisfactory from a numerical standpoint. The number of Feynman diagrams grows faster than factorial with the number of external particles involved in the scattering process. As a consequence the number of multiplications, and therefore the computer time needed to evaluate a phase space point, will grow at least as fast.

In computer science, algorithms with factorial growth are called exponential or factorial algorithms or simply E-algorithms [156]. Such algorithms are not considered optimal, i.e. the number of external particles we can calculate becomes quickly limited by computer resources. In contrast, the other class of algorithms with polynomial growth in the number of external legs are called P-algorithms. Such algorithms are highly desirable as the added computational effort needed to go from N to $(N+1)$ external particles is $\left(\frac{N+1}{N}\right)^{\alpha}$. This means the limiting factor for these types of algorithms in scattering amplitude calculations is often human resources instead of computer resources. In the subsequent sections we will argue that for numerical solutions, especially in the era of LHC physics, the complexity of the algorithms are an important consideration.

6.2   Tree-level algorithms of polynomial complexity

The number of Feynman graphs grows very fast with the number of external legs. For a tree-level N-gluon scattering the number of individual Feynman graphs is approximately $N^{(N-3)}$ (within 5% accuracy up to 16 gluons) [157]. This means that to extend the LO-MC from 2 gluon $\rightarrow$ 5 gluon to 2 gluon $\rightarrow$ 6 gluon, the number of multiplications increases by at least a factor of 13. Several LO-MC are available for the numerical evaluation of arbitrary tree-level processes in the Standard Model and some of its extensions. Most of these packages are based on simple Feynman diagram evaluations. We call these Numerically Implemented Exponential (NIE) algorithms. A prominent representative in this class of algorithms is MadGraph [158].

By using currents instead of amplitudes in Feynman diagram calculations one can construct recursion relations [159]. This method re-uses recurring groups of off-shell Feynman graphs in an optimal manner. Because this leads to a more factorized way of calculating the scattering amplitude one can immediately extend the analytic calculations to more complex processes such as vector boson production with up to 6 partons [160, 161] and 7 parton processes [162].

Another consequence of the recursion relations is the formulation of an algorithm of polynomial complexity. For a tree-level N-gluon process the number of multiplications grows as N^4 [157]. This means that to extend the LO-MC from 2 gluon $\rightarrow$ 5 gluon to 2 gluon $\rightarrow$ 6 gluon the increase in the number of multiplications is only 1.7 (compared to 13 for standard Feynman graph calculations). We will denote the LO-MC programs based on recursive type of evaluation Numerically Implemented Polynomial (or NIP) algorithms. A prominent representative is the ALPGEN program [163].

As is clear from the discussion we have reached a point for LO-MC where the problem of numerically calculating the scattering amplitudes can be considered solved.

---

[11]Contributed by: R.K. Ellis, W.T. Giele, Z. Kunszt

6.3 Toward one-loop algorithms of polynomial complexity

The LO-MC prediction at LHC type of energies for QCD and/or Electro-Weak processes are rather qualitative. One estimates the magnitude of the cross section and predicts the shape for an observables. The NLO-MC will give us a first real estimate of the expected normalization and will give an order α_S correction to the shape. Within the perturbative context this allows us to estimate the uncertainties on the predictions with some confidence.

The one-loop amplitude of the basic 2 gluon $\rightarrow$ 2 gluon was already calculated analytically in 1986 [164] using the standard Feynman diagram calculation. One can extend this method brute force with modern day computers. Using a combination of e.g. QGRAF [165] and FORM [166] one can generate and manipulate the Feynman graphs giving tensor coefficients times tensor integrals. The tensor integrals can be determined using Pasasarino-Veltman reduction [167] or other techniques. This then can be straightforwardly implemented in a numerical code for e.g. 2 gluon $\rightarrow$ 4 gluon [168]. The evaluation of a single phase space point for this process is of the order 9 second (10,000 times slower as the 2 gluon $\rightarrow$ 2 gluon one-loop amplitude generated using the same procedure). It is clear that such a direct approach using Feynman diagrams is severely affected by the factorial growth in complexity. One needs badly a polynomial complexity calculational approach.

It can be shown that any dimensional regulated multi-loop amplitude is fully reconstructible using unitarity cuts [169]. Because the unitarity cuts factorizes the one-loop amplitudes into a product of two tree-level amplitudes this proves the existence of a polynomial complexity algorithm for one-loop calculations. This was exploited in the analytic calculation of the $e^+e^- \rightarrow 4$ partons one-loop amplitude [139] [12]. The method applies four-dimensional unitarity cuts, thereby it only partly reconstructs the one-loop amplitude through unitarity, the so-called cut-constructible part. The missing part is referred to as the rational part and is determined by other methods. The applied 4-dimensional unitarity method has no direct numerical equivalent, but it is explicitly demonstrated that such methods of polynomial complexity work very well within the context of analytic multi-leg one-loop calculations.

The first numerically implementable method came from the so-called quadruple cut method [129]. While presented as an analytic method to calculate coefficients of the 4-point scalar master integrals for multi-gluon processes, it has a direct numerical implementation. The numerical procedure can be used to calculate the box coefficients for any multi-particle scattering process. By applying the quadruple cut the one-loop graph breaks down into four tree-level amplitudes. This is therefore instantly a NIP algorithm for calculating the coefficients of the 4-point master integrals. From the unitarity constraints, i.e. the four cut propagators have to be numerically zero, one gets only two complex solutions for the loop-momentum. By evaluating the product of the four tree-level graphs using the two complex loop momenta solutions, one gets the coefficient by simply averaging over the two solutions.

The numerical implementation of the method is extremely fast and simple, showing the potential of a full numerical implementable unitarity method. To achieve this one also has to calculate the coefficients of the other 3 master integrals (the 1-, 2- and 3-point scalar integrals). A direct generalization of the quadruple cut method becomes complicated because of overlapping contributions. By applying a triple cut to determine the 3-point coefficient one has to take into account that part of this contribution is also in the quadruple cut. Disentangling these overlapping contributions proves to be not that straightforward.

For a one-loop amplitude one can construct a general parametric form of the integrand and determine its coefficients by demanding different combinations of sets of propagators to be zero (i.e. cutting the lines) for both the parametric form of the amplitude and the expression obtained using Feynman graphs [95]. This method is purely algebraic as it works on the integrand level. When setting four propagators to zero this method is identical to the quadruple cut method. However, we now get in addition the full loop dependence of the integrand of the 4-point master functions through its parametric form. This allows one to simply determine the triple cut contribution of the parametric 4-point integrand and hence

---

[12]The 5 gluon one-loop was calculated using string inspired methods [143].

we know the subtraction term.

Using this method to construct the subtraction terms it is now straightforward to formulate a numerical implementable algorithm of polynomial complexity for the cut constructible part [126]. Because we determine the coefficients of the 2-, 3- and 4-point parametric form of integrands by the equivalent of unitarity cuts, the actual one-loop amplitude factorizes in a product of two, three or four tree-level amplitudes. That is, we can determine the full parametric form of the integrand from tree-level amplitudes. The final loop integration over the parametric form is straightforward and gives us the three scalar master integrals and their respective coefficients. This method now extends the polynomial complexity algorithm of the quadruple cut method to include also the triple and double cut contributions. As a demonstration we used this method to numerically evaluate multi-gluon scattering amplitudes. We found using a single standard processor the following results: the 2 gluon $\rightarrow$ 2 gluon at 9 seconds/10,000 events, the 2 gluon $\rightarrow$ 3 gluon at 35 seconds/10,000 events and the 2 gluon $\rightarrow$ 4 gluon at 107 seconds/10,000 events. This can be approximated by $N^6/450$ seconds/10,000 events, which by extrapolation would give around 260 seconds/10,000 events for 2 gluon $\rightarrow$ 5 gluon. These evaluation times are more than sufficient for use in NLO-MC generators, even on a modest single processor system.

6.4   Conclusions: the rational part

The final step is a numerical suitable algorithm for the rational part of the one-loop amplitude. This is the final hurdle in achieving a full solution of polynomial complexity for numerical one-loop amplitude evaluations. Three methods exist in the literature. The first method determines the rational part of the tensor integrals. These rational parts can then be contracted in with the tensor coefficients to give the full one-loop rational part [90, 93]. This method goes back to the Feynman diagram expansion and leads to an algorithm of factorial complexity. This negates all progress made with the determination of the cut constructible part using numerical unitarity techniques.

The other two methods are more analytic in concept, but should in principle be suitable for a numerical implementation. The so-called bootstrap method sets up a recursive procedure for the rational part [86] similar to the tree-level unitarity based recursion relations [51]. This makes the method of polynomial complexity. However, in its current formulation it is not suitable for numerical implementation. The reason is that both the rational and cut constructible part of the one-loop amplitude contain so-called spurious poles. When adding the two parts together these spurious poles cancel. This means that for the construction of an unitarity based recursion relation in the rational part these spurious poles have to be removed. This procedure is called cut-completion, i.e. make both cut-constructible and rational part free of spurious poles. Then the rational part contains only physical poles and a unitarity based tree-level like recurrence relation for the rational part is constructible. Unfortunately the cut-completion procedure requires analytic knowledge of the spurious terms, which up to now have only be determined by explicit analytic calculation of the cut-constructible part.

One can in principle retrieve the full one-loop amplitude by applying D-dimensional unitarity cuts [98, 135]. Such an implementation is per construction of polynomial complexity. It requires the calculation of the D-dimensional tree-level amplitudes. This can be implemented by restricting oneself to massive scalar internal particles where the mass in generated by the extra-dimensional length of the loop-momentum. In this manner the extra-dimensional part of the loop-momentum can be integrated out. After that one can read off the appropriate master integral coefficients and rational part. The required scalar internal particles restrict this method at the moment to purely gluonic scattering amplitudes. In its current implementation this method is restricted to analytic applications for purely gluonic one-loop scattering amplitudes.

It is clear from the discussions that a numerical algorithm of polynomial complexity is the only issue left in fully solving one-loop calculations in a similar way tree-level calculations have been solved. Achieving this final step would open the way to a multitude of NLO-MC generators for processes such as for example $PP \rightarrow t\bar{t} +2$ jets, $PP \rightarrow t\bar{t} + b\bar{b}$ and $PP \rightarrow$ Vector-Boson $+ 3, 4$ jets.

A NIP implementation for the rational part has to exist. Its construction in the near future is of great importance to make the first step towards more complicated NLO-MC programs relevant for the LHC phenomenology.

7. PHYSICAL APPLICATIONS OF THE OPP METHOD TO COMPUTE ONE-LOOP AMPLITUDES[13]

7.1 Introduction

In two recent papers [95, 96], we proposed a reduction technique (OPP) for arbitrary one-loop sub-amplitudes at *the integrand level* [121] by exploiting numerically the set of kinematical equations for the integration momentum, that extend the quadruple, triple and double cuts used in the unitarity-cut method [105, 126, 128, 129]. The method requires a minimal information about the form of the one-loop (sub-)amplitude and therefore it is well suited for a numerical implementation. The method works for any set of internal and/or external masses, so that one is able to study the full electroweak model, without being limited to massless theories.

In Section 7.2 we outline the basics features of the method. In Section 7.3 we describe a numerically stable implementation of the OPP algorithm, in a form of a `FORTRAN90` code, `CutTools` [103]. In the last section, we compute, as an application, the one-loop QCD corrections to the process $pp \rightarrow ZZZ$ at the LHC, also showing distributions for physically interesting quantities.

7.2 The OPP method

The starting point of the OPP reduction method is the general expression for the *integrand* of a generic m-point one-loop (sub-)amplitude

$$A(\bar{q}) = \frac{N(q)}{\bar{D}_0 \bar{D}_1 \cdots \bar{D}_{m-1}}, \quad \bar{D}_i = (\bar{q} + p_i)^2 - m_i^2, \quad p_0 \neq 0. \tag{56}$$

In the previous equation, we use a bar to denote objects living in $n = 4 + \epsilon$ dimensions, and $\bar{q}^2 = q^2 + \tilde{q}^2$, where $\tilde{q}^2$ is ϵ-dimensional and $(\tilde{q} \cdot q) = 0$. $N(q)$ is the 4-dimensional part of the numerator function of the amplitude. If needed, the ϵ-dimensional part of the numerator should be treated separately, as explained later. $N(q)$ depends on the 4-dimensional denominators $D_i = (q + p_i)^2 - m_i^2$ as follows

$$
\begin{aligned}
N(q) &= \sum_{i_0 < i_1 < i_2 < i_3}^{m-1} \left[d(i_0 i_1 i_2 i_3) + \tilde{d}(q; i_0 i_1 i_2 i_3) \right] \prod_{i \neq i_0, i_1, i_2, i_3}^{m-1} D_i \\
&+ \sum_{i_0 < i_1 < i_2}^{m-1} \left[c(i_0 i_1 i_2) + \tilde{c}(q; i_0 i_1 i_2) \right] \prod_{i \neq i_0, i_1, i_2}^{m-1} D_i \\
&+ \sum_{i_0 < i_1}^{m-1} \left[b(i_0 i_1) + \tilde{b}(q; i_0 i_1) \right] \prod_{i \neq i_0, i_1}^{m-1} D_i \\
&+ \sum_{i_0}^{m-1} \left[a(i_0) + \tilde{a}(q; i_0) \right] \prod_{i \neq i_0}^{m-1} D_i \\
&+ \tilde{P}(q) \prod_i^{m-1} D_i.
\end{aligned}
\tag{57}
$$

Inserted back in Eq. (56), this expression simply states the multi-pole nature of any m-point one-loop amplitude, that, clearly, contains a pole for any propagator in the loop, thus one has terms ranging from

---

[13]Contributed by: G. Ossola, C.G. Papadopoulos, R. Pittau

1 to m poles. Notice that the term with no poles, namely that one proportional to $\tilde{P}(q)$ is polynomial and vanishes upon integration in dimensional regularization; therefore does not contribute to the amplitude, as it should be. The coefficients of the poles can be further split in two pieces. A piece that still depend on q (the terms $\tilde{d}, \tilde{c}, \tilde{b}, \tilde{a}$), that vanishes upon integration, and a piece that do not depend on q (the terms d, c, b, a). Such a separation is always possible and the latter set of coefficients is immediately interpretable as the ensemble of the coefficients of all possible 4, 3, 2, 1-point one-loop functions contributing to the amplitude.

Once Eq. (57) is established, the task of computing the one-loop amplitude is then reduced to the algebraical problem of fitting the coefficients d, c, b, a by evaluating the function $N(q)$ a sufficient number of times, at different values of q, and then inverting the system. That can be achieved quite efficiently by singling out particular choices of q such that, systematically, 4, 3, 2 or 1 among all possible denominators D_i vanishes. Then the system of equations is solved iteratively. First one determines all possible 4-point functions, then the 3-point functions and so on. For example, calling $q_0^{\pm}$ the 2 (in general complex) solutions for which

$$D_0 = D_1 = D_2 = D_3 = 0,\tag{58}$$

(there are 2 solutions because of the quadratic nature of the propagators) and since the functional form of $\tilde{d}(q; 0123)$ is known, one directly finds the coefficient of the box diagram containing the above 4 denominators through the two simple equations

$$N(q_0^{\pm}) \quad = \quad [d(0123) + \tilde{d}(q_0^{\pm}; 0123)] \prod_{i \neq 0,1,2,3} D_i(q_0^{\pm}).\tag{59}$$

This algorithm also works in the case of complex denominators, namely with complex masses. Notice that the described procedure can be performed *at the amplitude level*. One does not need to repeat the work for all Feynman diagrams, provided their sum is known: we just suppose to be able to compute $N(q)$ numerically.

The described procedure works in 4 dimensions. However, even when starting from a perfectly finite tensor integral, the tensor reduction may eventually lead to integrals that need to be regularized (we use dimensional regularization). Such tensors are finite, but tensor reduction iteratively leads to rank m m-point tensors with $1 \leq m \leq 5$, that are ultraviolet divergent when $m \leq 4$. For this reason, we introduced, in Eq. (56), the d-dimensional denominators $\bar{D}_i$, that differs by an amount $\tilde{q}^2$ from their 4-dimensional counterparts

$$\bar{D}_i = D_i + \tilde{q}^2.\tag{60}$$

The result of this is a mismatch in the cancellation of the d-dimensional denominators of Eq. (56) with the 4-dimensional ones of Eq. (57). The rational part of the amplitude, called R_1 [170], comes from such a lack of cancellation. A different source of Rational Terms, called R_2, can also be generated from the ϵ-dimensional part of $N(q)$ (that is missing in Eq. (56)). For the time being, it should be added by hand by looking at the analytical structure of the Feynman Diagrams of via a dedicated set of Feynman Rules. Examples on how to compute R_2 are reported in [170] and [171, 172]. The Rational Terms R_1 are generated by the following extra integrals, introduced in [95, 96]

$$\int d^n \bar{q} \frac{\tilde{q}^2}{\bar{D}_i \bar{D}_j} \quad = \quad -\frac{i\pi^2}{2} \left[m_i^2 + m_j^2 - \frac{(p_i - p_j)^2}{3} \right] + \mathcal{O}(\epsilon),$$

$$\int d^n \bar{q} \frac{\tilde{q}^2}{\bar{D}_i \bar{D}_j \bar{D}_k} \quad = \quad -\frac{i\pi^2}{2} + \mathcal{O}(\epsilon), \quad \int d^n \bar{q} \frac{\tilde{q}^4}{\bar{D}_i \bar{D}_j \bar{D}_k \bar{D}_l} \quad = \quad -\frac{i\pi^2}{6} + \mathcal{O}(\epsilon).\tag{61}$$

The coefficients of the above integrals can be computed by looking at the implicit mass dependence (namely reconstructing the $\tilde{q}^2$ dependence) in the coefficients d, c, b of the one-loop functions, once $\tilde{q}^2$ is

reintroduced through the mass shift $m_i^2 \to m_i^2 - \tilde{q}^2$. One gets

$$b(ij; \tilde{q}^2) = b(ij) + \tilde{q}^2 b^{(2)}(ij), \quad c(ijk; \tilde{q}^2) = c(ijk) + \tilde{q}^2 c^{(2)}(ijk). \tag{62}$$

Furthermore, by defining

$$\mathcal{D}^{(m)}(q, \tilde{q}^2) \equiv \sum_{i_0 < i_1 < i_2 < i_3}^{m-1} \left[d(i_0 i_1 i_2 i_3; \tilde{q}^2) + \tilde{d}(q; i_0 i_1 i_2 i_3; \tilde{q}^2) \right] \prod_{i \neq i_0, i_1, i_2, i_3}^{m-1} \bar{D}_i, \tag{63}$$

the following expansion holds

$$\mathcal{D}^{(m)}(q, \tilde{q}^2) = \sum_{j=2}^{m} \tilde{q}^{(2j-4)} d^{(2j-4)}(q), \tag{64}$$

where the last coefficient is independent on q

$$d^{(2m-4)}(q) = d^{(2m-4)}. \tag{65}$$

In practice, once the 4-dimensional coefficients have been determined, one can redo the fits for different values of $\tilde{q}^2$, in order to determine $b^{(2)}(ij)$, $c^{(2)}(ijk)$ and $d^{(2m-4)}$. Such three quantities are the coefficients of the three extra scalar integrals listed in Eq. (61), respectively. Therefore, the OPP method allows an easy and purely numerical computation of the Rational Terms of type R_1.

7.3 `CutTools` and the problem of the Numerical Inaccuracies

A `FORTRAN90` program (`CutTools`) implementing the OPP method can be found in [103], to which we refer for more details. We just mention that the only information needed by the code is the number and type of contributing propagators and the numerator function $N(q)$ (and its maximum rank). A particularly interesting feature of the OPP technique, also implemented in `CutTools`, is that it allows a natural numerical check of the accuracy of the whole procedure. Given the paramount importance of this issue in practical calculations, we describe it here in some detail.

During the fitting procedure to determine the coefficients, numerical inaccuracies may occur due to

1) appearance of Gram determinants in the solutions for which 4, 3, 2 or 1 denominators vanish;
2) vanishing of some of the remaining denominators, when computed at a given solution;
3) instabilities occurring when solving systems of linear equations;

In principle, each of these three sources of instabilities can be cured by performing a proper expansion around the problematic (i.e. *exceptional*) Phase-Space point. However, this often results in a huge amount of work that, in addition, spoils the generality of the algorithm. Furthermore, one is anyway left with the problem of choosing a separation criterion to identify the region where applying the proper expansion rather than the general algorithm.

The solution implemented in `CutTools` is, instead, of a purely numerical nature and relies on a unique feature of the OPP method: the fact that the reduction is performed at the integral level. In detail, the OPP reduction is obtained when, as in Eq. (57), the numerator function $N(q)$ is rewritten in terms of denominators. Therefore $N(q)$ computed for some arbitrary value of q by using the l. h. s. of Eq. (57) should always be *numerically* equal to the result obtained by using the expansion in the r. h. s. This is a very stringent test that is applied in `CutTools` for any Phase-Space point. When, in an *exceptional* Phase-Space point, these two numbers differ more than a user defined quantity, the coefficients of the loop functions *for that particular point* are recomputed by using multi-precision routines (with up to 2000 digits) contained in `CutTools` [173, 174]. The only price to be payed by the user is writing, beside the normal ones (namely written in double-precision), a multi-precision version of the routines

computing $N(q)$. The described procedure ensures that the coefficients of the scalar loop functions are computed with a precision defined by the user. Finally, one should mention that, usually, only very few points are potentially dangerous, namely *exceptional*, so that a limited fraction of additional CPU time is used to cure the numerical instabilities, therefore compensating the fact that the multi-precision routines are by far much slower than the normal ones. This procedure has been shown to work rather well in practice, as we shall see in the next section.

7.4 $pp \to ZZZ$ at one-loop

The calculation is composed of two parts: the evaluation of virtual corrections, namely one-loop contributions obtained by adding a virtual particle to the tree-order diagrams, and corrections from the real emission of one additional massless particle from initial and final states, which is necessary in order to control and cancel infrared singularities. The virtual corrections are computed using the OPP reduction [95,96]. In particular, we make use of CutTools [103]. Concerning the contributions coming from real emission we used the dipole subtraction method [175] to isolate the soft and collinear divergences and checked the results using the phase space slicing method [176] with soft and collinear cutoffs, as outlined in [177].

These results have also been recently presented, following a very different approach, by Lazopoulos *et al* in Ref. [8]. A more complete study, that will also include the case of W^+W^-Z, $W^\pm ZZ$, and $W^+W^-W^\pm$ production, will be presented in a forthcoming publication [178].

Let us begin with the evaluation of the virtual QCD corrections to the process $q\bar{q} \to ZZZ$. We consider the process

$$q(p_1) + \bar{q}(p_2) \longrightarrow Z(p_3) + Z(p_4) + Z(p_5) \tag{66}$$

All momenta are chosen to be incoming, such that $\sum_i p_i = 0$.
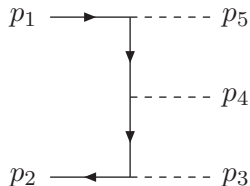

Fig. 10: Tree-level structure contributing to $q\bar{q} \to ZZZ$.

At the tree-level, there are six contributions to this process, obtained by the diagram illustrated in Fig. 10 by permuting the final legs in all possible ways. One-loop corrections are obtained by adding a virtual gluon to the tree-level structures, as depicted in Fig. 11. Each of the eight diagram of Fig. 11 should be evaluated for six permutations of the final particles: overall this calculation involves the reduction of 48 diagrams.

We perform a reduction to scalar integrals using the OPP reduction method [95,96]. As described in Section 7.2, we need to provide the numerical value of the numerator of the integrand in the loop integrals. The numerator function $N(q)$ can be expressed in terms of 4-dimensional denominators D_i according to the decomposition of Eq. (57). For the particular case of five denominators, that is the relevant case for the process studied in this paper, we have $m = 5$ and the indices range from 0 to 4. Next, simply by evaluating the numerator function $N(q)$ for a given set of values of q, we can extract all the coefficients in Eq. (57).

The coefficients determined in this manner should be multiplied by the corresponding scalar integrals. Since, in the process that we are studying, no q-dependent massive propagator appears, we will only need massless scalar integrals. They are computed using the package OneLOop written by A. van Hameren [122].
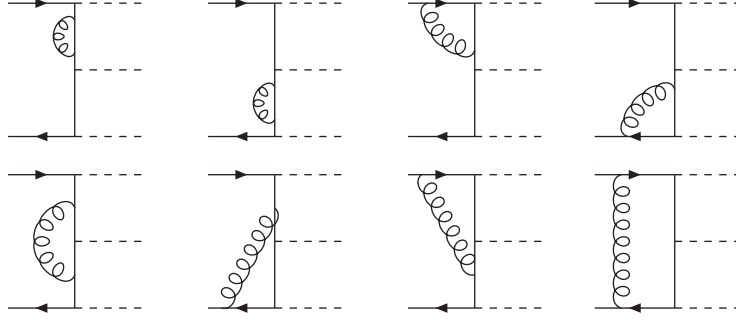
Fig. 11: Diagrams contributing to virtual QCD corrections to $q\bar{q} \rightarrow ZZZ$

As an example, let us consider the pentagon diagram (the last diagram of Fig. 11). In our notation, the integrand will read

$$A_5(q) = \frac{N_5(q)}{[q^2][(q+p_1)^2][(q+p_1+p_5)^2][(q-p_2-p_3)^2][(q-p_2)^2]} \tag{67}$$

with

$$N_5(q) = \left\{ \bar{u}(p_2)\, \gamma^\alpha\, P_{(q-p_2)}\, V_3^Z\, P_{(q-p_2-p_3)}\, V_4^Z\, P_{(q+p_1+p_5)}\, V_5^Z\, P_{(q+p_1)}\, \gamma^\alpha\, u(p_1) \right\} \tag{68}$$

The function $P(q)$ is the numerator of the quark propagator

$$P_{(q)} = \not{q} + m \,,$$

while $V_i^Z = V^Z \cdot \epsilon_i$, namely the contraction between he polarization vector of the *i-th* Z boson ϵ_i and the γ-matrix in the vertex $Zq\bar{q}$

$$V_\mu^Z = ie\gamma_\mu(g_f^- \omega_- + g_f^+ \omega_+) \tag{69}$$

where

$$g_f^+ = -\frac{s}{c}Q_f \;\;,\;\; g_f^- = \frac{I_{W,f}^3 - s^2 Q_f}{sc} \;\;,\;\; \omega_\pm = (1 \pm \gamma^5)/2\,. \tag{70}$$

For any fixed value q_0 of integration momentum, and for a given phase-space point, $N_5(q_0)$ is simply the trace of a string of known matrices. After choosing a representation for Dirac matrices and spinors, we evaluate $N(q)$ by performing a naive matrix multiplication. By providing this input to the reduction algorithm, we can compute all the coefficients of the scalar integrals (in other words, the "cut-constructible" part of the calculation).

The last step is the calculation of Rational Terms. As explained in Section 7.2, part of this contribution, that we call R_1, is automatically included by the to the reduction algorithm. The second term R_2, coming from the ϵ-dimensional part of $N_5(q)$, has been added by hand by looking at the Feynman Diagram and turns out to be proportional to the tree-order amplitude.

In the same fashion, we can repeat the calculation for the other seven diagrams. However, our method allows for a further simplification: for each fixed permutation of the final legs, only the q-dependent denominators of Eq. (67) will appear in the remaining diagrams. Therefore, we can combine all diagrams in a single numerator function and perform the reduction directly for the sum of such diagrams, allowing for a one-shot evaluation of the resulting scalar coefficients.

We checked that our results, both for poles and finite parts, agree with the results obtained by the authors of Ref. [8].

In what concerns the real emission, we only have to deal with initial state singularities, where we distinguish $q\bar{q}$ and qg initial states. For the qg initial state, no soft singularity is present because the

corresponding tree-level contribution vanishes. We recall that the structure of the NLO partonic cross sections is as follows:

$$\sigma_{q\bar{q}}^{NLO} = \int\limits_{VVV} \left[d\sigma_{q\bar{q}}^{B} + d\sigma_{q\bar{q}}^{V} + d\sigma_{q\bar{q}}^{C} + \int\limits_{g} d\sigma_{q\bar{q}}^{A}\right] + \int\limits_{VVVg} \left[d\sigma_{q\bar{q}}^{R} - d\sigma_{q\bar{q}}^{A}\right]$$

$$\sigma_{gq}^{NLO} = \int\limits_{VVV} \left[+d\sigma_{gq}^{C} \int\limits_{g} d\sigma_{gq}^{A}\right] + \int\limits_{VVVg} \left[d\sigma_{gq}^{R} - d\sigma_{gq}^{A}\right] , \tag{71}$$

where $d\sigma^{B}, d\sigma^{V}, d\sigma^{C}, d\sigma^{R}, d\sigma^{A}$ are respectively the Born cross section, the virtual, virtual counterterm, real and real-subtraction cross sections. For the $q\bar{q}$ initial state two dipoles are needed as subtraction terms. If p_6 is the momentum which can become soft or collinear, the dipole term for gluon emission off the quark is given by

$$\mathcal{D}^{q_1 g_6, \bar{q}_2} = \frac{8\pi\alpha_s C_F}{2\tilde{x}\, p_1 \cdot p_6} \left(\frac{1 + \tilde{x}^2}{1 - \tilde{x}}\right) |\mathcal{M}_{q\bar{q}}^{B}(\{\tilde{p}\})|^2 \tag{72}$$

$$\tilde{x} = \frac{p_1 \cdot p_2 - p_2 \cdot p_6 - p_1 \cdot p_6}{p_1 \cdot p_2}$$

where the $\{\tilde{p}\}$ are redefined momenta, $\{\tilde{p}_j\} = \{\tilde{p}_{16}, \tilde{p}_2, \tilde{p}_3, \tilde{p}_4, \tilde{p}_5\}$, which are again on-shell and go to $\{p_1, \ldots, p_5\}$ in the singular limit, e.g. $\tilde{p}_{16} = \tilde{x}\, p_1$. The regularised real emission part then reads

$$d\sigma_{q\bar{q}}^{R} - d\sigma_{q\bar{q}}^{A} = \frac{1}{6}\frac{1}{N}\frac{1}{2s_{12}}\left[C_F |\mathcal{M}_{q\bar{q}}^{R}(\{p_j\})|^2 - \mathcal{D}^{q_1 g_6, \bar{q}_2} - \mathcal{D}^{\bar{q}_2 g_6, q_1}\right] d\Phi_{VVVg} ,$$

where the factor $1/6$ accounts for the three identical bosons in the final state. More details can be found in [175, 178].

The hadronic differential cross section with hadron momenta P_1 and P_2 is the sum over all partonic initial states convoluted with the parton distribution functions

$$d\sigma(P_1, P_2) = \sum_{ab} \int dz_1 dz_2 f_a(z_1, \mu_F) f_b(z_2, \mu_F) d\sigma_{ab}(z_1 P_1, z_2 P_2) , \tag{73}$$

where the sum runs over the partonic configurations $q\bar{q}, \bar{q}q, gq, qg, g\bar{q}, \bar{q}g$.

7.4.1 *Numerical results*

As an explicit example we present the numerical results for the case $u\bar{u} \to ZZZ$ for $\sqrt{s} = 14$ TeV and using CTEQ6L1 [28]. The tree-order cross section has been evaluated using the HELAC event generator [179–181]. In the following table the results in fb are presented for the tree-order cross section σ_0, the ratio of the virtual to the tree-level cross section, and the real contribution, combining $5-$ and $6-$point contributions, as described above, for all channels, i.e., $u\bar{u}, ug, g\bar{u}$, for different values of the factorization(renormalization) scale ($\mu = \mu_F = \mu_R$).

scale	σ_0	σ_V/σ_0	σ_R	σ_{NLO}
$\mu = M_Z$	1.481(5)	0.536(1)	0.238(2)	2.512(2)
$\mu = 2M_Z$	1.487(5)	0.481(1)	0.232(2)	2.434(2)
$\mu = 3M_Z$	1.477(5)	0.452(1)	0.232(2)	2.376(2)
$\mu = 4M_Z$	1.479(5)	0.436(1)	0.232(2)	2.355(2)
$\mu = 5M_Z$	1.479(5)	0.424(1)	0.237(2)	2.343(2)

As it is evident from these results, the $K-$factor is quite sizable $(1.58 - 1.69)$, whereas the dependence on the scale μ is for both cases quite weak, due mainly to the electroweak character of the process.

7.5 Conclusions

We presented a new method for NLO processes (OPP), in which the reduction to known integrals is performed at the integrand level. The method has been successfully tested in a number of applications, the latest being the production of three Z bosons at the LHC.

The efficiency of the method is quite good. It can be further improved if the numerical evaluation of the integrand in the one-loop amplitude, by means of recursion relations, without relying on Feynman diagrams, is developed [67].

In general, the speed, the precision and the simplicity of the OPP method, make it a very good candidate for the construction of a universal NLO calculator/event-generator.

Part II
IMPROVEMENTS ON STANDARD TECHNIQUES

8. GOLEM: A SEMI-NUMERICAL APPROACH TO ONE-LOOP AMPLITUDES[14]

8.1 Introduction

The first collision data from the Large Hadron Collider (LHC) at CERN are expected in a couple of months, giving us the opportunity to explore unprecedented energies and luminosities. However, in order that a discovery of New Physics can be claimed, it is of crucial importance to have the Standard Model physics under control. This includes e.g. understanding of the detectors, the underlying event, the luminosity determination, the jet energy scale [182]. For most of these issues, an interplay between measurements and precise theory predictions is mandatory. In a hadron collider environment, multi-particle/jet final states will be produced in abundance. Therefore considerable effort needs to be spent to make predictions for multi-particle processes beyond the leading order. While the calculation of one-loop five-point amplitudes can be considered as the state of the art at the moment, the first complete cross section for six-point processes at hadron colliders still awaits its completion. Many different approaches to multi-particle production have been developed in the last few years, most of them being described in these proceedings. For other reviews and very recent developments, see e.g. [103, 132, 183].

Here we will focus on a method implemented in the program GOLEM (General One-Loop Evaluator of Matrix elements), which is based on a semi-numerical evaluation of building blocks stemming from the reduction of one-loop Feynman diagrams [184]. The main features of the formalism are the following:

- It is valid for massive and massless particles
- For $N > 5$ external legs, the reduction of rank R N-point integrals is done algebraically, reducing the rank and the number of propagators at the same time in each reduction step. For $N \leq 5$ we worked out form factor representations which allow to avoid inverse Gram determinants in exceptional kinematic regions.
- The infrared divergences are easily extracted analytically in terms of triangles.
- The rational parts of the amplitudes are obtained as by-products and can be projected out.
- The program has an analytic and a numerical branch: it can perform a complete reduction to scalar integrals, represented in terms of analytic functions: such a complete reduction introduces inverse Gram determinants, but this branch can be chosen safely in phase space regions where the Gram determinants are sufficiently large (which is the bulk of the phase space). As the evaluation

---

[14]Contributed by: C. Bernicot, T. Binoth, J.-Ph. Guillet, G. Heinrich, E. Pilon, T. Reiter

of analytic functions is fast, this speeds up the program considerably as compared to a purely numerical approach. Near exceptional phase space points, the program allows to stop the reduction *before* dangerous denominators are produced. The building blocks to evaluate in this case are finite three- and four-point functions with Feynman parameters in the numerator. As a brute-force numerical evaluation of the four-point functions is rather slow, we have worked out one-dimensional integral representations, whose numerical evaluation is extremely fast. Details will be given in the following section.

We have implemented the reduction in algebraic manipulation programs and have obtained fully analytical results for several amplitudes using these methods [2, 94, 185–188]. Without having efficient and automated simplification methods to reduce the size of big analytic expressions, the fully analytic approach based on form factors suffers from factorial complexity and therefore does not seem to be appropriate for 6-point processes. The semi-numerical reduction is preferable in this case. For the calculation of the rational terms alone the situation is different, as the form factor representations simplify considerably when restricted to terms which can generate rational parts [93].

8.2 Results

Below we will describe applications of our method to one-loop six-point amplitudes and explain in detail certain features which guarantee a fast and numerically robust evaluation in all phase space regions.

8.2.1 The GOLEM numerical library

In the GOLEM library, the strategy is to evaluate numerically higher dimensional three- and four-point functions in phase space regions where numerical instabilities arise due to spurious singularities. To be specific, these integrals are six- and eight-dimensional four-point functions I_4^{D+2}, I_4^{D+4}, and four- and six-dimensional three-point functions I_3^D, I_3^{D+2}, with or without Feynman parameters in the numerator. While the triangles are two-dimensional integrals in Feynman parameter space, the boxes a priori involve integration over three Feynman parameters. As numerical integrations in multi-dimensional parameter space are rather slow, we worked out one-dimensional integral representations for these integrals, whose evaluation is both fast and precise. In [184, 189] we have already presented other methods for the numerical evaluation of Feynman parameter integrals, but the one-dimensional representations discussed here are preferable, as they are much faster.

As an example, let us consider the case where two massive particles scatter into two light particles via a fermion loop. The two ingoing particles have a small velocity. In this kinematic region, the Gram determinant is small. In this case, we have to evaluate four-point functions with two adjacent massive legs, and with Feynman parameters in the numerator. In fig. 13 we plot the six-dimensional four-point function with two adjacent massive legs, $I_{4,\text{adj}}^6$, against the absolute value of the coefficient B which is proportional to the ratio $det(G)/det(S)$, for a trajectory of points with $10^{-15} \leq |B| \leq 10^{-3}$.

In the GOLEM library, there is a cut c which allows to split the phase space regions where the four-point function is evaluated analytically from those where it is evaluated numerically. The larger the cut, the longer the evaluation takes, as more calls of the numerical integration routine are made. On the other hand, if the cut is too small, the analytical evaluation causes a loss of precision of several digits.

As an illustration, we compute $I_4^6(z_1 z_2^2)$ and we plot the real and imaginary parts for different values of the cut c: $c = 10^{-1}$ (Fig. 13), $c = 10^{-3}$ (Fig. 14) and $c = 10^{-5}$ (Fig. 15).

In the case at hand, the CPU time does not vary very much with the cut, the evaluation time ranges from $0.14\,\text{s}$ (on an Intel Pentium M 1.3 GHz) for $c = 10^{-1}$ to $0.10\,\text{s}$ for $c = 10^{-5}$. However, this statement is hard to generalise to all possible situations occurring in a calculation of a complex multi-leg amplitude. In any case, the cut c allows to adjust the trade-off between speed and precision.

8.2.2 The $u\bar{u} \rightarrow d\bar{d}s\bar{s}$ amplitude

With our method we calculated the one-loop six-quark amplitude

$$\mathcal{A}(u(p_1, \lambda_1), \bar{u}(p_2, \lambda_2) \rightarrow d(p_3, \lambda_3), \bar{d}(p_4, \lambda_4), s(p_5, \lambda_5), \bar{s}(p_6, \lambda_6)) \tag{74}$$

in massless QCD. The calculation has been carried out using spinor helicity amplitudes in the 't Hooft-Veltman scheme. We have chosen a convenient colour basis, which allows to split the amplitude as follows

$$\sum_\lambda \sum_{i=1}^6 \mathbf{C}^i A_i^\lambda(p_1, \dots, p_6), \tag{75}$$

where A_c are the helicity and colour subamplitudes. In particular we chose the colour structures

$$(\mathbf{C}^1, \mathbf{C}^2, \mathbf{C}^3, \mathbf{C}^4, \mathbf{C}^5, \mathbf{C}^6) = (\delta_{c_1}^{c_2}\delta_{c_4}^{c_3}\delta_{c_6}^{c_5}, \delta_{c_1}^{c_2}\delta_{c_4}^{c_5}\delta_{c_6}^{c_3}, \delta_{c_1}^{c_5}\delta_{c_4}^{c_2}\delta_{c_6}^{c_3}, \delta_{c_1}^{c_5}\delta_{c_4}^{c_3}\delta_{c_6}^{c_2}, \delta_{c_1}^{c_3}\delta_{c_4}^{c_5}\delta_{c_6}^{c_2}, \delta_{c_1}^{c_3}\delta_{c_4}^{c_2}\delta_{c_6}^{c_5}). \tag{76}$$

In our notation λ is the vector $(\lambda_1, \dots, \lambda_6)$, and $\lambda_j = \pm 1$ is the helicity of the particle with momentum p_j of which the colour index is c_j. In the six-quark amplitude one can identify two independent helicites $\lambda^a = (+, +, +, +, +, +)$ and $\lambda^b = (+, +, +, +, -, -)$; all other helicities are either identically zero or related to λ^a or λ^b by parity invariance, which is exploited in our calculation.

We generated the Feynman diagrams for this process with *QGraf* [165] and reduced the tensor integrals using *FORM* [166, 190] to form factors as defined in [184]. We deal with the spinor algebra by completing spinor lines to traces, e.g. for an arbitrary product Γ of Dirac matrices we use

$$\langle p_i^+ | \Gamma | p_j^+ \rangle = \frac{1}{2[p_j q]\langle q p_i \rangle} \text{tr}\{(1 + \gamma_5)\not{p}_j \not{q} \not{p}_i \Gamma\}. \tag{77}$$

With the help of *FORM* and *Java* code the expressions for the diagrams are transformed into a *Fortran90* program. The Golem90 library is used for the numerical evaluation of the form factors. In this approach we found it advantageous to treat the spinor traces numerically as well, in order to keep the expressions more compact.

The code returns the subamplitudes in the form

$$A_i^\lambda(p_1, \dots, p_6) = \frac{g_s^6}{4\pi^2} \frac{1}{s} \left(\frac{A}{\varepsilon^2} + \frac{B}{\varepsilon} + C + \mathcal{O}(\varepsilon) \right) \tag{78}$$

for each of the six colour structures and for all non-zero helicities, where A, B and C are complex coefficients. As an example we plot in Figure 16 the quantity $s|A_c^\lambda|\alpha_s^{-3}$ for one colour structure $\mathbf{C}^1$ and the two helicity configurations λ^a and λ^b. The initial state momenta are chosen to be along the z-axis while the final state momenta have been rotated about the y-axis by an angle θ. For $\theta = 0$ the momenta are chosen as in Ref. [191]:

$$\begin{aligned}
\vec{p}_3 &= (33.5, 15.9, 25.0) \\
\vec{p}_4 &= (-12.5, 15.3, 0.3) \\
\vec{p}_5 &= (-10.0, -18.0, -3.3) \\
\vec{p}_6 &= (-11.0, -13.2, -22.0)
\end{aligned} \tag{79}$$

In the chosen units the renormalisation scale is $\mu = 1$. The amplitude has been evaluated at 50 successive points between $\theta = 0$ and $\theta = 2\pi$ ($\theta = 0, 0.126, 0.252, \dots$), which took 2.4 seconds per point and helicity on an Intel Pentium 4 CPU (3.2 GHz). Table 3 shows the numerical values of all coefficients for the point $\theta = 0$.

c	A	B	C
1	$-0.0029670 - 0.0036065i$	$0.0203701 + 0.0281510i$	$-0.0659100 - 0.1057940i$
2	$0.0042784 + 0.0049474i$	$-0.0191448 - 0.0420120i$	$0.0338141 + 0.1820798i$
3	$-0.0123663 - 0.0186981i$	$0.1171088 + 0.1401148i$	$-0.4902357 - 0.4754639i$
4	$0.0051836 + 0.0066459i$	$-0.0462621 - 0.0477458i$	$0.1803702 + 0.1706208i$
5	$-0.0143367 - 0.0137603i$	$0.1282264 + 0.1049820i$	$-0.5199953 - 0.3972433i$
6	$0.0083400 + 0.0100456i$	$-0.0745825 - 0.0730179i$	$0.2929410 + 0.2459317i$

Table 3: Six-quark amplitude. Numerical values of the virtual part $A_c^{\lambda^a}(\{p_j\}_{j=1\ldots6})\alpha_s^{-3}$ for the kinematics given in the text and $\theta = 0$.
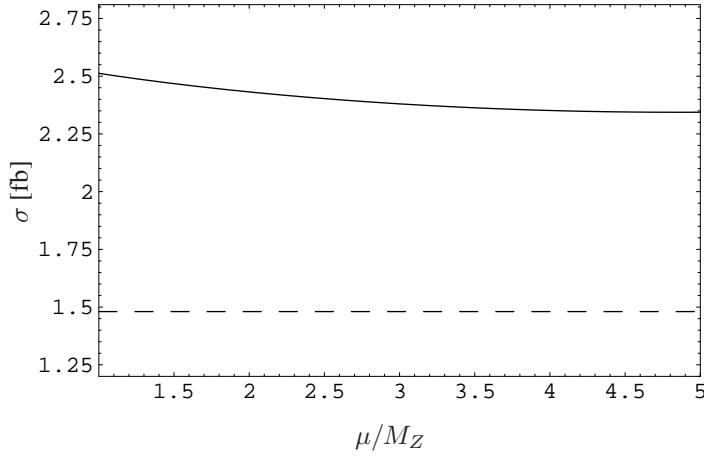

Fig. 12: Scale-dependence of the cross section σ_{NLO} (solid line) compared with the tree-level cross section σ_0 (dashed line). The scale is reported in the plot in units of M_Z, from $\mu = M_Z$ to $\mu = 5M_Z$.
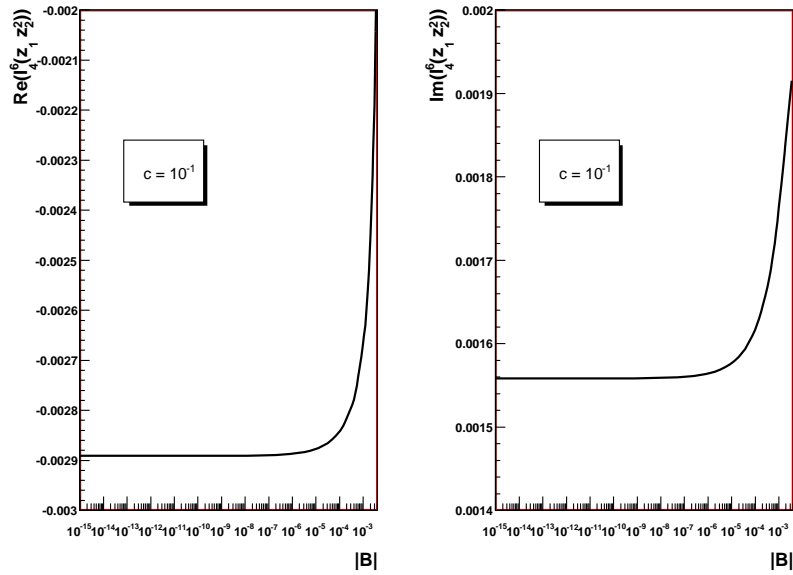

Fig. 13: *The six-dimensional four-point function with three Feynman parameters in the numerator, $I_4^6(z_1 z_2^2)$, with two adjacent massive legs and the cut $c = 10^{-1}$.*
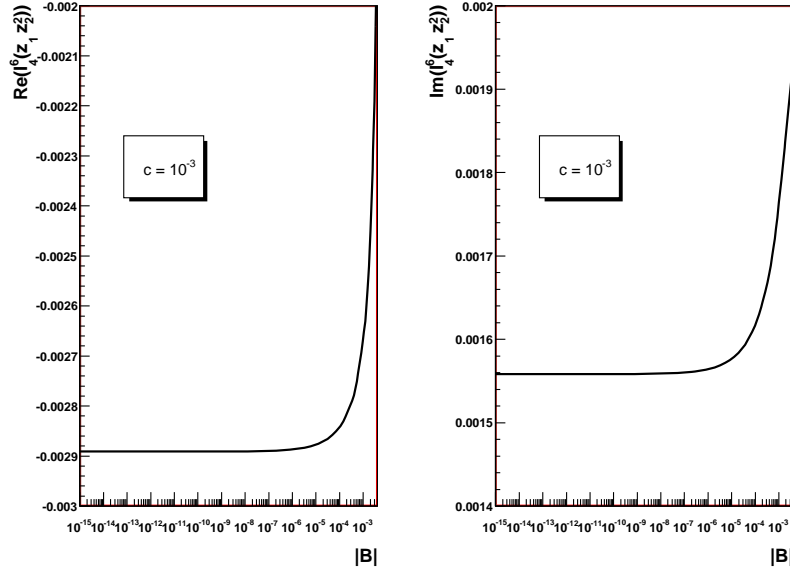
Fig. 14: *The six-dimensional four-point function with three Feynman parameters in the numerator, $I_4^6(z_1 z_2^2)$, with two adjacent massive legs and the cut $c = 10^{-3}$.*
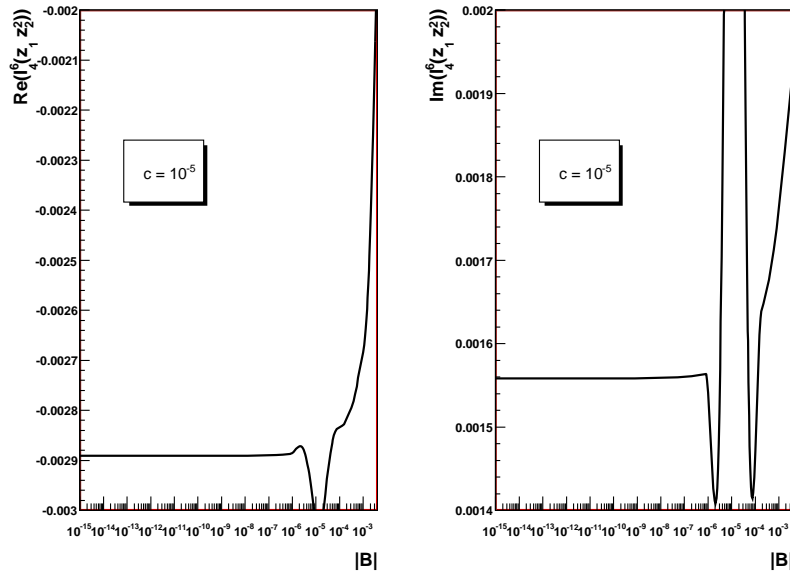

Fig. 15: *The six-dimensional four-point function with three Feynman parameters in the numerator, $I_4^6(z_1 z_2^2)$, with two adjacent massive legs and the cut $c = 10^{-5}$.*
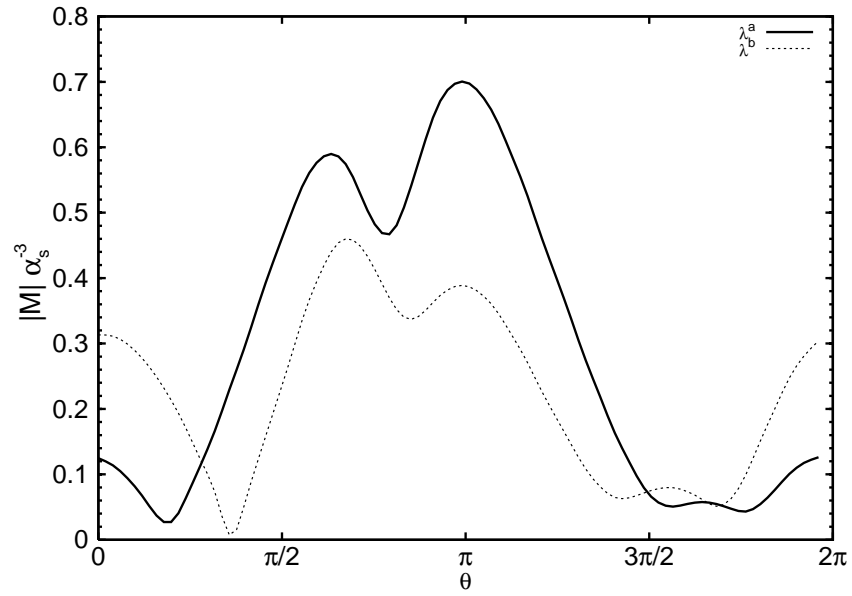
Fig. 16: The six-quark amplitude. The finite parts of the Laurent expansion in ε of $s|A_1^{\lambda^a}|\alpha_s^{-3}$ (solid) and $s|A_1^{\lambda^b}|\alpha_s^{-3}$ (dashed) are plotted for a kinematic point defined in the text, where the final state momenta have been rotated about the y-axis by an angle θ.

Acknowledgements

9. ISSUES WITH THE LANDAU SINGULARITIES[15]

9.1 Introduction

Cross sections involving a large number of external particles can contain numerical instabilities which must be carefully located and controlled. At tree-level one can mention integration over a t-channel pole if the integration variables are not properly chosen. The crossing of a resonance might also be problematic. Beside these physical situations there might be fake singularities specific to the way one has set up the amplitude; one example is the singularity brought about by an unlucky choice of a reference vector at the helicity amplitude level. These problems are exacerbated at the loop level since the loop integrals can also develop singularities. A prominent example is the occurrence of vanishing inverse Gram determinants: see for example the contribution of Denner and Dittmaier. The latter is a fake singularity that can be met for some special, and simple, kinematical conditions on the phase space of the external particles having to do with how one has chosen one's (independent) basis for the loop integrals and how one has subsequently expressed the other loop integrals in this basis. Loop integrals can also have *true* singularities that have an underlying physical origin. They depend on the dynamics of the problem. Thresholds are one example, though harmless and trivial to locate. These types of singularities belong to the general class of Landau singularities. The physical singularity can be revealed by studying the analytic properties of the scalar integral. Here we study the case of one-loop integrals. In particular we will review how the conditions for having such singularities can be derived, especially in a format that is conducive to an easy implementation in a computer code. When such a singularity is present it is important to inquire whether this singularity is integrable or not. We rederive here the singular part. We then consider two specific complementary examples taken from the recent literature. The first one, the electroweak corrections to $pp \rightarrow b\bar{b}H$, reveals a Landau singularity having to do with massive, indeed unstable, particles in the loop. In this case the singularity is smoothed out by the width of the unstable particles. The second is the 6-photon amplitude which involves massless states, both internally and externally. In this case the Landau determinant is a quadratic function whose square root is proportional to the Gram determinant.

9.2 Conditions for a Landau singularity and the nature of the singularity

Consider the one-loop process $F_1(p_1) + F_2(p_2) + \ldots + F_N(p_N) \rightarrow 0$, where F_i stands for either a scalar, fermion or vector field with momentum p_i as in the figure opposite. The internal momentum for each propagator is q_i with $i = 1, \ldots N$. Each momentum q_i is associated with one Feynman parameter x_i respectively. The scalar loop integral reads

$$
\begin{aligned}
T_0^N &\equiv \int \frac{d^D q}{(2\pi)^D i} \frac{1}{D_1 D_2 \cdots D_N}, \\
D_i &= q_i^2 - m_i^2 + i\epsilon, \quad q_i = q + r_i, \\
r_i &= \sum_{j=1}^{i} p_j, \quad i = 1, \ldots, N,
\end{aligned} \quad (80)
$$
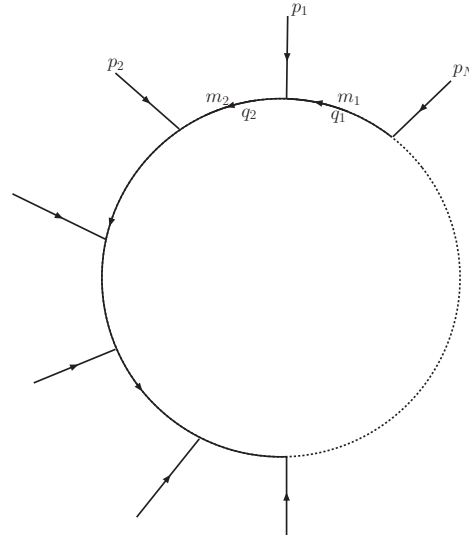
The Feynman parameter representation reads

$$T_0^N = \Gamma(N) \int_0^\infty dx_1 \cdots dx_N \delta(\sum_{i=1}^N x_i - 1) \int \frac{d^D q}{(2\pi)^D i} \frac{1}{(x_1 D_1 + x_2 D_2 + \cdots x_N D_N)^N}. \tag{81}$$

Because of the Dirac delta function, the integration boundary in the Feynman parameter space are $x_i = 0$, $i = 1, \ldots, N$. Thus the only important condition on x_i is that they are not negative. The singularities are given by the Landau conditions [123, 192]

$$\begin{cases} \forall i \;\; x_i(q_i^2 - m_i^2) = 0, \\ \sum_{i=1}^N x_i q_i = 0. \end{cases} \tag{82}$$

If eq. (82) has a solution $x_i > 0$ for every $i \in \{1, \ldots, N\}$, *i.e. all particles in the loop are simultaneously on-shell*, then the integral T_0^N has a leading Landau singularity (LLS). If a solution exists but with some $x_i = 0$ while the other x_i's are positive, the Landau condition corresponds to a lower-order Landau singularity (LOLS).

By introducing the matrix Q, under the condition $q_i^2 = m_i^2$,

$$Q_{ij} = 2 q_i . q_j = m_i^2 + m_j^2 - (q_i - q_j)^2 = m_i^2 + m_j^2 - (r_i - r_j)^2; \;\; i, j \in \{1, 2, \ldots, M\}, \tag{83}$$

the conditions to have a Landau singularity in the physical region are

$$\begin{cases} \det(Q) = 0, \\ x_i > 0, \;\; i = 1, \ldots, M. \end{cases} \tag{84}$$

For $M = N$ one has a leading singularity, otherwise if $M < N$ this is a subleading singularity. If some internal (external) particles are massless, as in the case of six-photon scattering, then some Q_{ij} are zero, and the above conditions can be easily checked. However, if the internal particles are massive then it is difficult to check these conditions explicitly, especially if M is large. In this case, we can rewrite the above conditions as follows

$$\begin{cases} \det(Q) = 0, \\ x_j = \det(\hat{Q}_{jM})/\det(\hat{Q}_{MM}) > 0, \;\; j = 1, \ldots, M - 1, \end{cases} \tag{85}$$

where $\hat{Q}_{ij}$ is obtained from Q by discarding row i and column j from Q. Note that $\det(\hat{Q}_{MM}) = d[\det(Q)]/dQ_{MM}$. If $\det(\hat{Q}_{MM}) = 0$ then the second condition in (85) becomes $\det(\hat{Q}_{jM}) = 0$ with $j = 1, \ldots, M - 1$. There may be cases, as we will encounter in section 9.4, where the Landau determinant $\det(Q)$ has a quadratic form. These special situations have to be handled with care.

The existence of a Landau singularity corresponds to an eigenvector of Q with zero eigenvalue. In general, Q has N real eigenvalues $\lambda_1, \ldots, \lambda_N$. Consider the case where Q has only one (non-degenerate) very small eigenvalue $\lambda_N \ll 1$. To leading order

$$\lambda_N = \frac{a_0}{a_1}, \qquad a_1 = \lambda_1 \lambda_2 \ldots \lambda_{N-1} \neq 0, \qquad a_0 = \det(Q). \tag{86}$$

With $V = \{x_1^0, x_2^0, \ldots, x_N^0\}$ the eigenvector corresponding to λ_N, we define $v^2 = V \cdot V$. We will assume that $\lambda_i > 0$ for $i = 1, \ldots, K$ and $\lambda_j < 0$ for $j = K + 1, \ldots, N - 1$ with $0 \leq K \leq N - 1$. It can then be shown that in D dimensions,

$$T_0^N = \frac{(-1)^N e^{i\pi(N-K-1)/2} v}{2^{3D/2-N} \sqrt{(-1)^{N-K-1} a_1}} \frac{\pi^{(N-D-1)/2} \Gamma((N-D+1)/2)}{(\lambda_N v^2 - i\varepsilon)^{(N-D+1)/2}}. \tag{87}$$

This result holds provided $a_1 \neq 0$ and $N - D + 1 > 0$. For the box, $N = 4$, $D = 4$, $a_0 \to 0$ and $a_1 \neq 0$ we get

$$(T_0^4)_{div} = \frac{e^{i\pi(3-K)/2}}{4\sqrt{(-1)^{3-K}\det(Q_4) - i\varepsilon}}. \tag{88}$$

This shows that $(T_0^4)_{div}$ is integrable but its square is not.

In the case $N = 3$ (the triangle), $D = 4$, it is possible to derive

$$T_0^3 = \frac{-e^{i\pi(2-K)/2}\upsilon}{8\pi\sqrt{(-1)^{2-K}\lambda_1\lambda_2}} \ln(\lambda_3\upsilon^2 - i\varepsilon) \tag{89}$$

T_0^3 and its square are therefore integrable.

9.3 $gg \to b\bar{b}H$

The first example we study is the electroweak corrections to $pp \to b\bar{b}H$ [193] where the one-loop amplitude squared, which is all that remains in the limit of vanishing bottom Yukawa coupling, develops a Landau singularity which represents the rescattering of the top pair and their decay into a W pair that produces the Higgs through WW fusion. As we will see, in this example, introducing the width of the internal top and W particles smoothes the singularity. There is a leading Landau singularity present in the box diagram shown in Fig. 17 that occurs for some specific values of the kinematic variables.
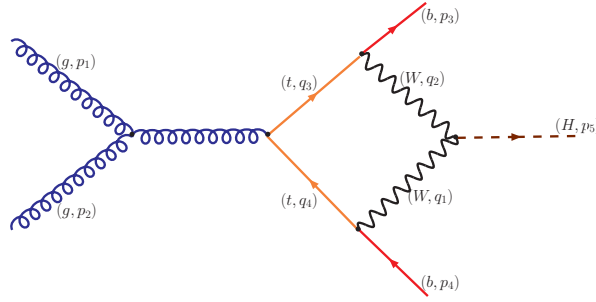

Fig. 17: *A box diagram contributing to $gg \to b\bar{b}H$ that can develop a Landau singularity for $M_H \geq 2M_W$ and $\sqrt{s} \geq 2m_t$, i.e. all the four particles in the loop can be simultaneously on-shell.*

With $g(p_1) + g(p_2) \to b(p_3) + \bar{b}(p_4) + H(p_5)$, $s = (p_1+p_2)^2$, $s_1 = (p_3+p_5)^2$, $s_2 = (p_4+p_5)^2$, and the on-shell conditions $p_1^2 = p_2^2 = 0$, $p_3^2 = p_4^2 = m_b^2 = 0$, $p_5^2 = M_H^2$, fixing s and M_H, the scalar box integral is a function of two variables $s_{1,2}$

$$T_0^4(s_1, s_2) = D_0(M_H^2, 0, s, 0, s_1, s_2, M_W^2, M_W^2, m_t^2, m_t^2). \tag{90}$$

The kinematically allowed region is

$$M_H^2 \leq s_1 \leq s, \quad M_H^2\frac{s}{s_1} \leq s_2 \leq M_H^2 + s - s_1. \tag{91}$$

The reduced matrix, $S^{(4)}$, which is equivalent in this case to the Q matrix for studying the Landau singularity, is given by

$$S_{ij}^{(4)} = \begin{pmatrix} 1 & \frac{2M_W^2-M_H^2}{2M_W^2} & \frac{m_t^2+M_W^2-s_1}{2M_Wm_t} & \frac{M_W^2+m_t^2}{2M_Wm_t} \\ \frac{2M_W^2-M_H^2}{2M_W^2} & 1 & \frac{M_W^2+m_t^2}{2M_Wm_t} & \frac{m_t^2+M_W^2-s_2}{2M_Wm_t} \\ \frac{m_t^2+M_W^2-s_1}{2M_Wm_t} & \frac{M_W^2+m_t^2}{2M_Wm_t} & 1 & \frac{2m_t^2-s}{2m_t^2} \\ \frac{M_W^2+m_t^2}{2M_Wm_t} & \frac{m_t^2+M_W^2-s_2}{2M_Wm_t} & \frac{2m_t^2-s}{2m_t^2} & 1 \end{pmatrix}, \quad S_{ij}^{(4)} = \frac{Q_{ij}}{2m_im_j}. \tag{92}$$

48

The singularity corresponds to $\det(S^{(4)}) = 0$. The determinant is a quadratic function of s_1, s_2 when s and all internal masses are fixed. The Landau determinant, the real and imaginary parts of T_0^4 are displayed in Fig. 18 for $\sqrt{s} = 353$ GeV, $M_H = 165$ GeV, $m_t = 174$ GeV, $M_W = 80.3766$ GeV. We clearly see that the Landau determinant vanishes inside the phase space and leads to regions of instability exhibiting leading and lower-order Landau singularities in the real and imaginary parts of the scalar integral. To investigate the structure of the singularities in more detail let us fix $\sqrt{s_1} =$
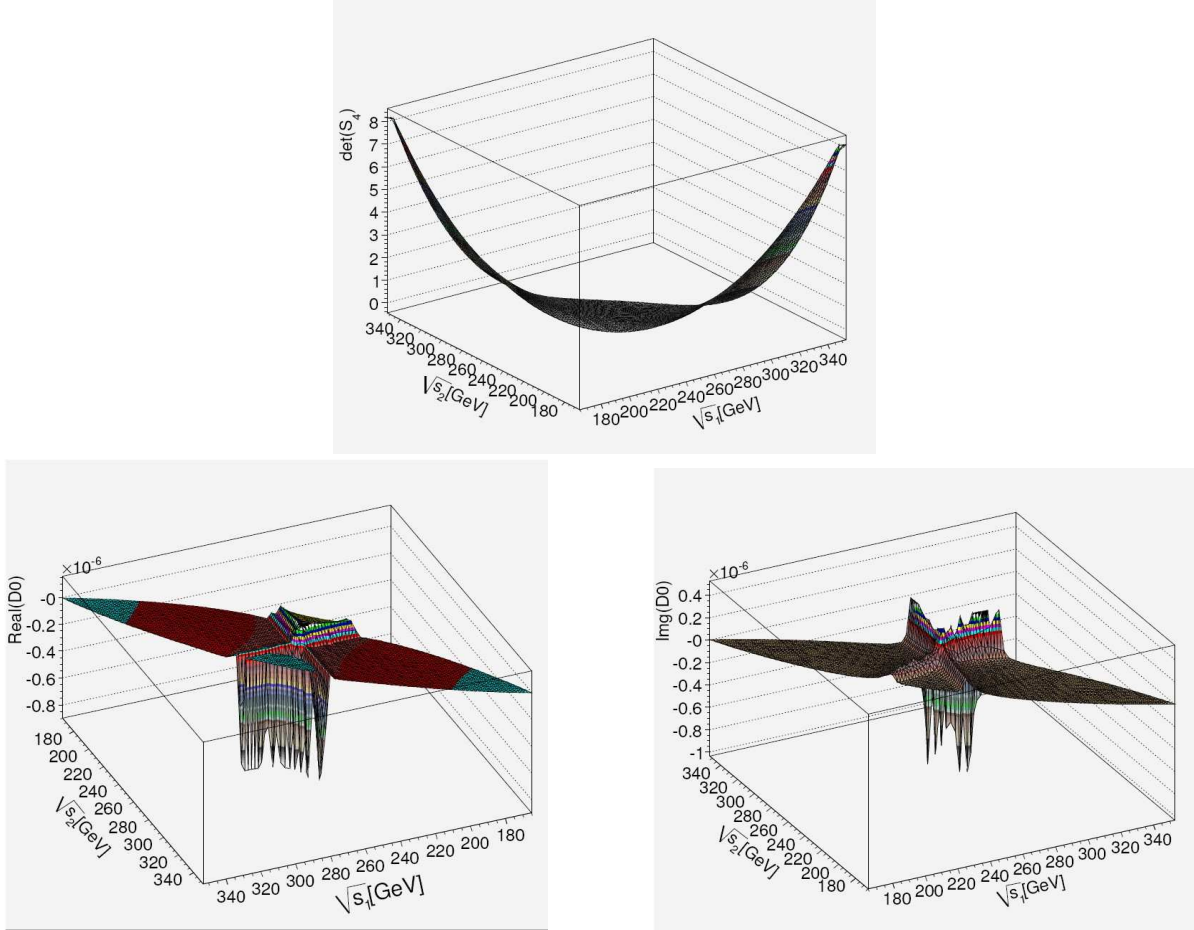

Fig. 18: *The Landau determinant as a function of s_1 and s_2 (upper figure). The real and imaginary parts of D_0 as a function of s_1 and s_2.*

$\sqrt{2(m_t^2 + M_W^2)} \approx 271.06$ GeV, so that the properties are studied for the single variable s_2. The results are shown in Fig. 19.

From Fig. 19 we see that there are four discontinuities in the function representing the real part of the scalar integral in the variable $\sqrt{s_2}$. As s_2 increases we first encounter a discontinuity at the normal threshold $\sqrt{s_2} = m_t + M_W = 254.38$ GeV. This corresponds to the solution (for the Feynman parameters) $x_{1,3} = 0$ and $x_{2,4} > 0$ of the Landau equations. The second discontinuity occurs at the anomalous threshold $\sqrt{s_2} = 257.09$ GeV of a reduced triangle diagram. This corresponds to the solution $x_3 = 0$ and $x_{1,2,4} > 0$ of the Landau equations. The condition of vanishing determinant $\det(S_3) = 0$ for this triangle has two solutions

$$s_2 = \frac{1}{2M_W^2}\left(M_H^2(m_t^2 + M_W^2) \mp M_H\sqrt{M_H^2 - 4M_W^2}(m_t^2 - M_W^2)\right) \tag{93}$$
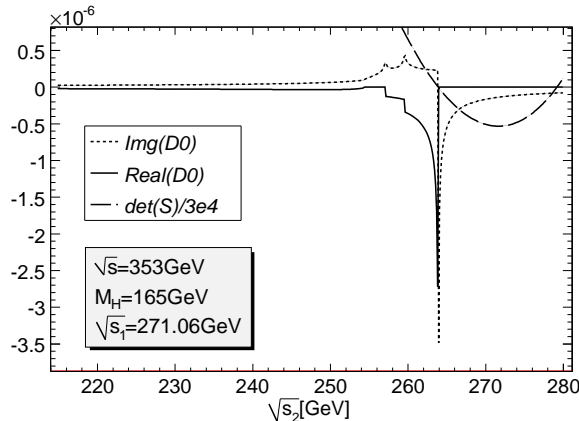
Fig. 19: *The imaginary, real parts of D_0 and the Landau determinant as functions of s_2.*

which gives $\sqrt{s_2} = 257.09$ GeV(inside of phase space) and 297.86 GeV(outside of phase space). We can also check that the former value satisfies the sign condition in (85) while the latter does not. Note that one of the conditions for this anomalous threshold to occur in the physical region is $M_H \geq 2M_W$, see Eq. (93). The same phenomenon happens for the third discontinuity at $\sqrt{s_2} = 259.58$ GeV which corresponds to the anomalous threshold of the reduced three point function obtained from the box diagram by contracting to a point the x_1 line. The last singular discontinuity is the leading Landau singularity. The condition $\det(S_4) = 0$ for the box has two solutions which numerically correspond to $\sqrt{s_2} = 263.88$ GeV or $\sqrt{s_2} = 279.18$ GeV. Both values are inside the phase space, see Fig. 19. However after inspection of the corresponding sign condition only $\sqrt{s_2} = 263.88$ GeV (with $x_1 \approx 0.533186, x_2 \approx 0.748618, x_3 \approx 0.774941$) qualifies as a Landau singularity. $\sqrt{s_2} = 279.18$ GeV has $x_1 \approx -0.742921, x_2 \approx -0.748618, x_3 \approx 1.06537$. The nature of the leading Landau singularity in Fig. 19 can be extracted by using the general formula (88). With the input parameters given above, the Landau matrix has only one positive eigenvalue at the leading singular point, *i.e.* $K = 1$. The leading singularity behaves as

$$D_0^{div} = -\frac{1}{16M_W^2 m_t^2 \sqrt{\det(S_4) - i\varepsilon}}. \tag{94}$$

When approaching the singularity from the left, $\det(S_4) > 0$, the real part turns singular. When we cross the leading singularity from the right, $\det(S_4) < 0$, the imaginary part of the singularity switches on, while the real part vanishes. In this example, both the real and imaginary parts are singular because $\det(S_4)$ changes sign when the leading singular point is crossed.

The instabilities of the integral and the singularities are due to the unstable internal particles. The problem can be remedied by introducing the finite width of the W and top. As seen from Fig. 20, introducing the finite width effect in the scalar box gives a smooth behaviour.

9.4 The six photon amplitude

The second example concerns a case with massless internal particles involving massless external particles: the 6-photon amplitude [194], see also [94, 96, 191]. Although the scalar integrals for the 6-photon amplitude have a potential Landau singularity that leads to some characteristic patterns of the amplitude, direct calculations of the helicity amplitudes show that the singularity is tamed by the dynamics of the gauge interaction in a somehow unexpected way. This is welcome since we would not able, in this case, to revert to the trick of introducing a width for the particles. This said, introducing non-zero (internal) masses, as would be fit for the couplings of the massless photons, would regulate a vanishing Landau
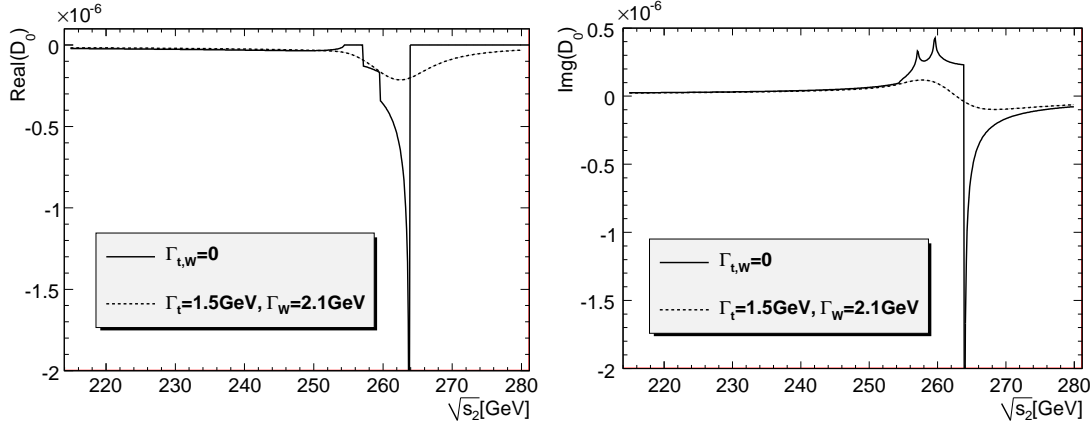
50

Fig. 20: *Effect of the combined width of the W, Γ_W and the top, $\Gamma - t$, to the real and imaginary part of the scalar function.*

determinant, but would of course still pose a considerable numerical problem if the singularity from the vanishing Landau determinant is not counterbalanced by the spin and gauge algebra.

To be able to see the cancellation at the level of the amplitude is only possible if one has very compact analytical expressions for these amplitudes. In our investigation the expressions for the amplitudes [194] are based on the unitarity-cut methods and are made particularly simple thanks to the fact that the six-photon amplitude has no IR/UV divergences and no rational terms. The six-photon amplitude was calculated in three models: i) scalar QED, A_6^{scalar}, ii) spinor QED: $A_6^{fermion}$ and iii) supersymmetric QED $\mathcal{N} = 1$: $A_6^{\mathcal{N}=1}$. The three amplitudes A_6^{scalar}, $A_6^{fermion}$ and $A_6^{\mathcal{N}=1}$ are in fact related through:

$$A_6^{fermion} = -2A_6^{scalar} + A_6^{\mathcal{N}=1} \tag{95}$$

Full compact expressions for the amplitudes can be found in [194]. The potential Landau singularity in the 6-photon amplitude reveals itself in the so-called double parton scattering configuration [191], see Fig. 21.
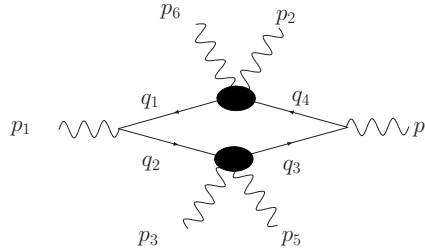
Fig. 21: *Double parton scattering configuration: p_1, p_4 are incoming photons with $\vec{p}_1 + \vec{p}_4 = \vec{0}$, each splits into a fermion pair which rescatters to give photon pairs (p_2, p_6); (p_3, p_5) at very small, vanishing, transverse momentum.*

The Landau conditions read

$$\det(Q) = (s_{135}s_{435} - s_{35}s_{26})^2 \to 0 \ , \quad s_{35}, s_{26} > 0 \ , \quad s_{135}, s_{435} < 0 \tag{96}$$

where $s_{ijk} = (p_i + p_j + p_k)^2$, all the p_i's are taken as incoming. Note the specific nature of $\det(Q)$ which has a quadratic form. This will lead to a double root (eigenvalue) at the singularity, or in other words the derivative of $\det(Q)$ at the singularity is also vanishing. In fact $\det(Q)$ is proportional to the square of the Gram determinant, $\det(G)$. To wit

$$\det(G) = -2s_{14}(s_{135}s_{435} - s_{35}s_{26}) \propto \sqrt{\det(Q)} \tag{97}$$

51

This property is due to the presence of many zeros, both from the kinematics of the external photons and the masslessness of the internal lines.

How does the singularity of the scalar integral transpire at the level of the amplitude? Let us turn to the NMHV $(---+++)$ six-photon helicity amplitude and specialise to the kinematics[16] of the Nagy and Soper configuration [191]. We start from a fixed point in phase space in the centre of mass frame $\vec{p}_1 + \vec{p}_4 = \vec{0}$ with $\vec{p}_4$ along the z-axis:

$$\begin{cases} \vec{p_2} = (-33.5, -15.9, -25.0) & \vec{p_3} = (11.0, 13.2, 22.0) \\ \vec{p_5} = (12.5, -15.3, -0.3) & \vec{p_6} = (10.0, 18.0, 3.3) \end{cases} \tag{98}$$

One can generate new configurations by rotating the final state about the y-axis by an arbitrary angle θ. We can then study the behaviour of the amplitude in this parameter. It is illuminating to rewrite $\det(Q)$ in terms of this parameter for this particular configuration:

$$\det(Q) = \left(s_{14}\, k_t^2\right)^2 \text{ with } k_t^2 = p_{35\,y}^2 + (p_{35\,x}\cos\theta + p_{35\,z}\sin\theta)^2 \tag{99}$$

where $p_{35\,i} = p_{3\,i} + p_{5\,i}$, $i = x, y, z$. The minimum value of k_t is given by $k_{t\,\min}^2 = p_{35\,y}^2$.

The behaviour of the amplitude as a function of θ for this particular configuration is shown in Fig. 22. The important conclusion to draw from Fig. 22 is that the structure of the amplitude, in particular
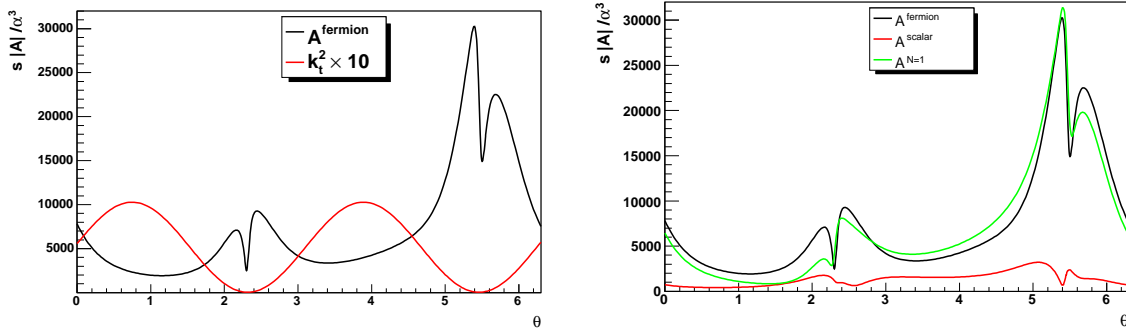

Fig. 22: *The NMHV amplitude as a function of θ in the Nagy-Soper configuration in the case of QED (left) as well as the scalar and $\mathcal{N} = 1$ SUSY(right). In the first panel we also show the dependence of k_t^2 which is a good measure of $\det(Q)$.*

the peculiar dips, is well tracked by $\det(Q)$. Indeed the dips that show in the amplitude occur exactly at the points where $\det(Q)$ is smallest. The dips occur at $\theta \simeq 2.32$ and $\theta \simeq 2.32 + \pi \simeq 5.46$. These values can be derived from Eq. (99) where $k_t = k_{t\,\min}$.

One can ask what would happen in a configuration where $k_{t\,\min}$ and consequently $\det(Q) \to 0$? One can arrive at this $\det(Q) \to 0$ configuration by perturbing the original kinematics in Eq. 98

$$\begin{cases} \vec{p_2} \to \vec{p_2'} = (-33.5, -15.9 - \Delta_y, -25.0) & \vec{p_3} \to \vec{p_3'} = (11.0, 13.2 + \Delta_y, 22.0) \\ \vec{p_5} \to \vec{p_5'} = (12.5, -15.3 + \Delta_y, -0.3) & \vec{p_6} \to \vec{p_6'} = (10.0, 18.0 - \Delta_y, 3.3) \end{cases} \tag{100}$$

The θ modulation is unchanged, such that the dips occur at the same location in θ. However now Δ_y can be chosen such that $k_{t\,\min} = 0$. This occurs for $\Delta_y = 1.05$.

Figs. 23 show how the pattern of the amplitude, as far as the dip around the singularity at $\theta = 5.46$ is concerned, evolves as Δ_y is varied from zero to 1.05 where $\det(Q)$ and $k_{t\,\min}$ vanish. It can be seen

---

[16]The correspondance between the kinematical conventions of Nagy and Soper and the one used here are the following: Nagy and Soper consider the reaction $\gamma^+(p_4) + \gamma^-(p_1) \to \gamma^-(-p_6) + \gamma^+(-p_2) + \gamma^+(-p_3) + \gamma^-(-p_5)$ i.e. their k_i's and our p_j are such that: $k_1 = p_4$, $k_2 = p_1$, $k_3 = -p_2$, $k_4 = -p_5$, $k_5 = -p_6$ and $k_6 = -p_3$ so that $k_1 + k_2 = k_3 + k_4 + k_5 + k_6$. See [194] for more details.
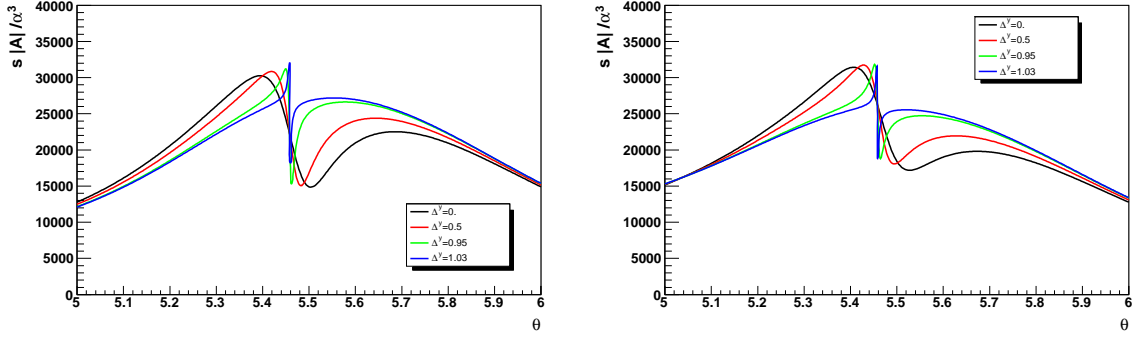
Fig. 23: *The six-photon amplitude around the Landau singularity characterised by θ around θ = 5.46 and for different values of the parameter Δ_y that gives a measure of $k_{t,\min}$ in spinor QED (left) and in $\mathcal{N} = 1$ susy QED (right).*

that as $\det(Q) \to 0$ with increasing Δ_y, the width of the dip decreases more and more so as to behave as a sudden jump, with the oscillation pattern disappearing completely for $\Delta_y = 1.05$. The numerators of the six-photon amplitudes, reflecting the dynamics of the gauge interaction, vanish fast enough as the Landau singularity is approached. Therefore the singularity seems to be *dynamically regulated* for the three cases of the scalar, the fermion and the SUSY-amplitude.

It is also revealing to investigate how the apparent Landau singularity is approached from different directions by considering a two-dimensional parameterisation of $\det(Q)$ and the kinematics.

We therefore modify the original Nagy-Soper parameterisation such as to generate a Landau singularity and add a k_t variable both along the x and y direction to follow the approach to the singularity:

$$
\begin{cases}
\overrightarrow{p_2} = (-33.5 - k_{t\,x}, -15.9 - k_{t\,y}, -25.0) & \overrightarrow{p_3} = (-12.5 + k_{t\,x}, 15.3 + k_{t\,y}, 22.0) \\
\overrightarrow{p_5} = (12.5 + k_{t\,x}, -15.3 + k_{t\,y}, -0.3) & \overrightarrow{p_6} = (33.5 - k_{t\,x}, 15.9 - k_{t\,y}, 3.3)
\end{cases}
\tag{101}
$$

Figs. 24 show the six-photon amplitudes $A_6^{fermion/\mathcal{N}=1}$ as functions of the two variables $k_{t\,x}$ and $k_{t\,y}$. Up to an overall rotation, the analytic structure of these amplitudes near the Landau singularity at $k_{t\,x} = k_{t\,y} = 0$ can be modelled as

$$
A_6 \sim \frac{k_{t\,x}\,k_{t\,y}}{k_{t\,x}^2 + k_{t\,y}^2} = \frac{1}{2}\sin(2\alpha)
\tag{102}
$$

where $k_{t\,x} = k_t \cos\alpha$, $k_{t\,y} = k_t \sin\alpha$, $k_t = (k_{t\,x}^2 + k_{t\,y}^2)^{1/2}$.

The amplitudes exhibit a valley and a ridge along mutually perpendicular axes crossing each other at $k_{t\,x} = k_{t\,y} = 0$. The various profiles shown in Fig. 23 are nothing but cross sections at fixed $k_{t\,y}$ of Fig 24. In particular, the profiles for $\Delta_y = 1.05$ correspond to $k_{t\,y} = 0$. More generally, when both $k_{t\,x}$ and $k_{t\,y}$ approach 0 simultaneously, A_6 remains finite: the Landau singularity of the double parton scattering type does not lead to a divergence $\sim 1/k_t^2$ as would have been naively expected from a general power counting argument [192, 195]. Yet the limiting value of A_6 depends on the direction α along which the origin $k_{t\,x} = k_{t\,y} = 0$ is approached.

9.5 Conclusions

We foresee that in the calculations of multi-leg one-loop processes the study of the Landau conditions will bring very useful, if not crucial, information. More investigations of the properties of these singularities need to be performed.
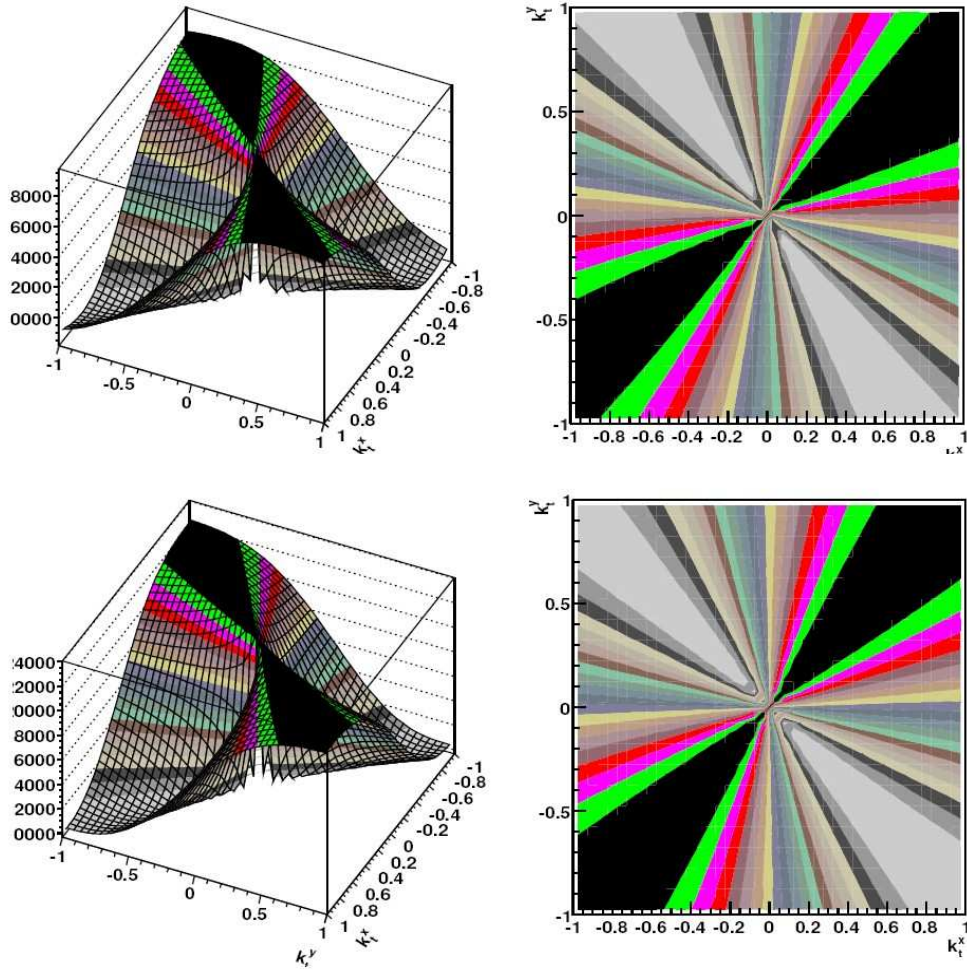
Fig. 24: *The six-photon amplitude in spinor QED (top) and in $\mathcal{N} = 1$ QED (bottom) around the Landau singularity*

10. TENSOR ONE-LOOP INTEGRALS IN EXCEPTIONAL PHASE-SPACE REGIONS[17]

10.1 Introduction

At the LHC and ILC, many interesting processes involve more than four external particles. A thorough description of such processes requires the evaluation of strong and electroweak radiative corrections at least in next-to-leading order (NLO). The most complicated part in such calculations concerns the numerically stable evaluation of the one-loop tensor integrals of the virtual corrections.

For processes with up to four external particles the classical Passarino–Veltman (PV) reduction [167], which recursively reduces tensor to scalar integrals, is sufficient in practically all cases. This scheme, however, involves Gram determinants in the denominator, which spoil the numerical stability if they become small. With up to four external particles this happens only near the edge of phase space (forward scattering, thresholds). With more than four external particles, Gram determinants also vanish within phase space, and methods are needed where Gram determinants can be small but still non-zero. In this context it should be noticed that the described problem of inverse Gram (and related) determinants occurs in *all* methods that reduce loop diagrams or amplitudes to the basis set of standard scalar integrals. This, in particular, also applies to unitarity-based or bootstrap approaches that work at the analytical (see e.g. Ref. [132] and references therein) or numerical [95,102,105,126,183] level. These methods certainly mitigate the problem of cancellations, but cannot avoid it completely.

---

[17]Contributed by: A. Denner, S. Dittmaier

In this article we inspect two benchmark phase-space points that are inspired from our calculation of electroweak (EW) $\mathcal{O}(\alpha)$ corrections to $e^+e^- \to 4$ fermions [196, 197].[18] One of the two points involves a small Gram determinant, the other involves both a small Gram and a small "modified Cayley determinant" at the same time. Although of course the real performance of proposed solutions can be only be found out in full applications, i.e. when integrating loop corrections to complicated processes over the whole phase space, a selection of such benchmark points is certainly a useful testground in the development of loop techniques.

Several solutions to the problem of numerical instabilities due to inverse Gram determinants have been proposed in recent years, but not many of them have proven their performance in complicated applications yet. For references and descriptions of some methods alternative to ours, we refer to Refs. [200, 201].

10.2 Tensor coefficients and their reduction

We consistently follow the notations and conventions for scalar and tensor one-loop integrals introduced in Refs. [200, 202]. Here we briefly repeat the conventions for 4-point integrals as required in the considered examples. Tensor 4-point integrals of rank P are defined as

$$D^{\mu_1\cdots\mu_P} = \frac{(2\pi\mu)^{4-D}}{i\pi^2} \int d^D q \frac{q^{\mu_1}\cdots q^{\mu_P}}{N_0 N_1 N_2 N_3}, \qquad N_k = (q+p_k)^2 - m_k^2 + i0, \quad p_0 = 0, \qquad (103)$$

where D is the number of space–time dimensions and μ the reference scale of dimensionional regularization. The tensor integrals are decomposed into covariants as follows,

$$D^\mu = \sum_{i_1=1}^{3} p_{i_1}^\mu D_{i_1}, \qquad D^{\mu\nu} = \sum_{i_1,i_2=1}^{3} p_{i_1}^\mu p_{i_2}^\nu D_{i_1 i_2} + g^{\mu\nu} D_{00},$$

$$D^{\mu\nu\rho} = \sum_{i_1,i_2,i_3=1}^{3} p_{i_1}^\mu p_{i_2}^\nu p_{i_3}^\rho D_{i_1 i_2 i_3} + \sum_{i_1=1}^{3} (g^{\mu\nu} p_{i_1}^\rho + g^{\nu\rho} p_{i_1}^\mu + g^{\rho\mu} p_{i_1}^\nu) D_{00 i_1}, \qquad (104)$$

and so on for higher rank. Up to rank 3, and only those are considered below, 4-point tensor integrals are UV finite. The kinematical arguments of the coefficients $D_{...}$, which comprise all scalar products $p_i p_j$ and internal masses m_k, are written as

$$D_{...} \equiv D_{...}(p_1^2, (p_2-p_1)^2, (p_3-p_2)^2, p_3^2, p_2^2, (p_3-p_1)^2, m_0^2, m_1^2, m_2^2, m_3^2). \qquad (105)$$

Conventional PV reduction [167] expresses the rank-P 4-point coefficients in terms of lower-rank 4- and 3-point coefficients. In each step $P \to (P-1)$ the inverse of the Gram matrix

$$Z = \begin{pmatrix} 2p_1p_1 & 2p_1p_2 & 2p_1p_3 \\ 2p_2p_1 & 2p_2p_2 & 2p_2p_3 \\ 2p_3p_1 & 2p_3p_2 & 2p_3p_3 \end{pmatrix} \qquad (106)$$

occurs, which causes the above-mentioned numerical problems if the determinant $|Z|$ becomes small. The highest negative power of $|Z|$ occurs in the calculation of tensor coefficients $D_{i_1 i_2 \dots}$ without "0" indices, rendering them numerically the most delicate. In the following we also need the matrix

$$X = \begin{pmatrix} 2m_0^2 & f_1 & f_2 & f_3 \\ f_1 & & & \\ f_2 & & Z & \\ f_3 & & & \end{pmatrix}, \qquad f_k = p_k^2 - m_k^2 + m_0^2. \qquad (107)$$

---

[18]Meanwhile the same methods have been successfully applied to NLO EW and QCD corrections to the Higgs decay H $\to$ WW/ZZ $\to 4f$ [198, 199] and to Higgs production via vector-boson fusion at the LHC [6, 7].

The vanishing of the modified Cayley determinant $|X|$ corresponds to necessary conditions for true (Landau) singularities in a Feynman diagram. The minors (i.e. determinants of submatrices where row i and column j are discarded) of the matrices Z and X, respectively, are called $\tilde{Z}_{ij}$ and $\tilde{X}_{ij}$ in the following.

10.3 The "DD" approach

One-loop tensor integrals can be naturally grouped into three categories, which we have treated in completely different ways:

(i) For *1- and 2-point integrals* of arbitrary tensor rank, numerically stable analytical expressions are presented in Ref. [200] (see also Ref. [167]).

(ii) For *3- and 4-point tensor integrals*, PV reduction [167] is applied for "regular" phase-space points where Gram determinants are not too small. For the remaining problematic cases special reduction techniques have been developed [200].

One of the techniques replaces the standard scalar integral by a specific tensor coefficient that can be safely evaluated numerically and reduces the remaining tensor coefficients as well as the standard scalar integral to the new basis integrals. In this scheme no dangerous inverse Gram determinants occur, but inverse modified Cayley determinants instead. We note that the procedure is related to the fully numerical method described in Ref. [203].

In a second class of techniques, the tensor coefficients are iteratively deduced up to terms that are systematically suppressed by small Gram or other kinematical determinants in specific kinematical configurations. The numerical accuracy can be systematically improved upon including higher tensor ranks. In our previous applications the highest relevant tensor rank was improved only by one additional iteration; in the results shown below we employ an new implementation of the methods where more than ten additional iterations are included if relevant. A similar idea, where tensor coefficients are iteratively determined from higher-rank tensors has been described in Ref. [204] for the massless case.

(iii) For *5- and 6-point integrals*, direct reductions to 5- and 4-point integrals, respectively, are possible owing to the four-dimensionality of space-time. For scalar integrals such a reduction was already derived in the 1960s [205]. In Refs. [200, 202] we follow basically the same strategy to reduce tensor integrals, which has the advantage that no inverse Gram determinants appear in the reduction. Instead modified Cayley determinants occur in the denominator, but we did not find numerical problems with these factors. A reduction similar to ours has been proposed in Ref. [184].

We would like to stress two important features of our approach.

(i) The methods are valid for massive and massless cases. The formulas given in Refs. [200, 202] are valid without modifications if IR divergences are regularized with mass parameters or dimensionally.[19] Finite masses can be either real or complex.

(ii) The in/out structure of the methods is the same as for conventional PV reduction, i.e. no specific algebraic manipulations are needed in applications. Therefore, the whole method can be (and in fact is) organized as a numerical library for scalar integrals and tensor coefficients.

We conclude this overview with some comments resulting from our experience collected in the treatment of a full $2 \to 4$ scattering reaction.

(i) For a specific point in a multi-particle (multi-parameter) phase space it is highly non-trivial to figure out which of the various methods is the most precise. It seems hopeless to split the phase space into regions that are dedicated to a given method. Therefore, we estimate the accuracy for the different methods at each phase-space point and take the variant promising the highest precision. The accuracy

---

[19]For the method of Ref. [202], this has been shown in Ref. [206].

of the PV method is valued by checking symmetries and PV relations, and by estimating cancellations. In the expansion approach, we estimate the number of valid digits based on the expected accuracy of the expansions and possible numerical cancellations before the evaluation of the coefficients. In the seminumerical approach, the integration error is propagated to the tensor coefficients, together with an estimate of possible cancellations.

(ii) In a complicated phase space it may happen that none of the various methods is perfect or good in some exceptional situations. Usually the corresponding events do not significantly contribute to cross sections. This issue can only be fathomed in actual applications. To be on the safe side, we employ the two independent "rescue systems" with different advantages and limitations.

(iii) In view of this, figures as shown below are nice illustrations, but should always be taken with a grain of salt. No matter how many of such figures are shown, they will never be exhaustive, so that no quantitative conclusions on the overall precision of methods can be drawn.

10.4   Two benchmark phase-space points

In the following two examples of exceptional phase-space configurations are considered:[20] one with small Gram determinant $|Z|$, another with both $|Z|$ and $|X|$ small. These two cases were already qualitatively illustrated in Ref. [207], but without providing explicit numbers. We also note that a complex Z-boson mass was used there. Here we switch to a real-valued Z mass to make it easier for other groups to compare with our numbers. For the sake of brevity, no results of the seminumerical method are included below; such results are illustrated in Ref. [207].

10.4.1   A case with a small Gram determinant

Figure 25 defines the first benchmark point for a 4-point function in which the Gram determinant $|Z|$ becomes small.   We compare results of PV reduction with results of the expansion in the small Gram determinant as described in Section 5.4 of Ref. [200]. In the upper half of the figure a hexagon diagram is shown that contains a box subdiagram with the considered kinematical configuration. The structural diagram illustrates the kinematical assignment with internal masses and squared external momenta given at the respective lines. The invariants near the arcs are the squares of the sum of momenta flowing into the two neighbouring external lines. The explicit values of the masses and invariants are given in the figure. As indicated there, the Gram determinant vanishes if the invariant $t_{\mathrm{e\bar{d}}}$ approaches the critical value t_{crit}, corresponding to an inner phase-space point. In the plots of Fig. 25 we show results on a few tensor coefficients when $t_{\mathrm{e\bar{d}}}$ is varied while keeping all other invariants fixed. The variation in $t_{\mathrm{e\bar{d}}}$ is translated into a variation of the dimensionless variable $x = t_{\mathrm{e\bar{d}}}/t_{\mathrm{crit}} - 1$ where the exceptional point with $|Z| = 0$ corresponds to $x = 0$.

It is clearly seen in the plot on the l.h.s. that the tensor coefficients calculated with PV reduction show numerical instabilities for small x, while the results of the expansion method behave smoothly. The PV instabilities increase with increasing tensor rank. The plot on the r.h.s. shows the relative difference between the PV results and the corresponding "best" predictions, which are either obtained with the PV or the expansion method. With decreasing x this difference rises because of the PV instabilities, and for a sufficiently high x the difference becomes zero (and falls out of the plot range), because PV reduction promises better accuracy there. It is essential to see a broad region in x where the difference is small for each tensor coefficient. This region corresponds to the overlap in which both PV reduction and the expansion method are trustworthy, the difference reflecting the uncertainty of the less precise result. The plot suggests that both methods should be precise within a relative accuracy of about 10^{-9} for the considered coefficients which go up to rank 3. As already mentioned for the x values of the shown points, the error estimate of the expansion promises better precision, otherwise (for larger x) PV

---

[20]We have to restrict the set of numerical results to a few selected tensor coefficients; more results can be found under http://wwwth.mppmu.mpg.de/members/dittmair/tensints/benchmarks.html.
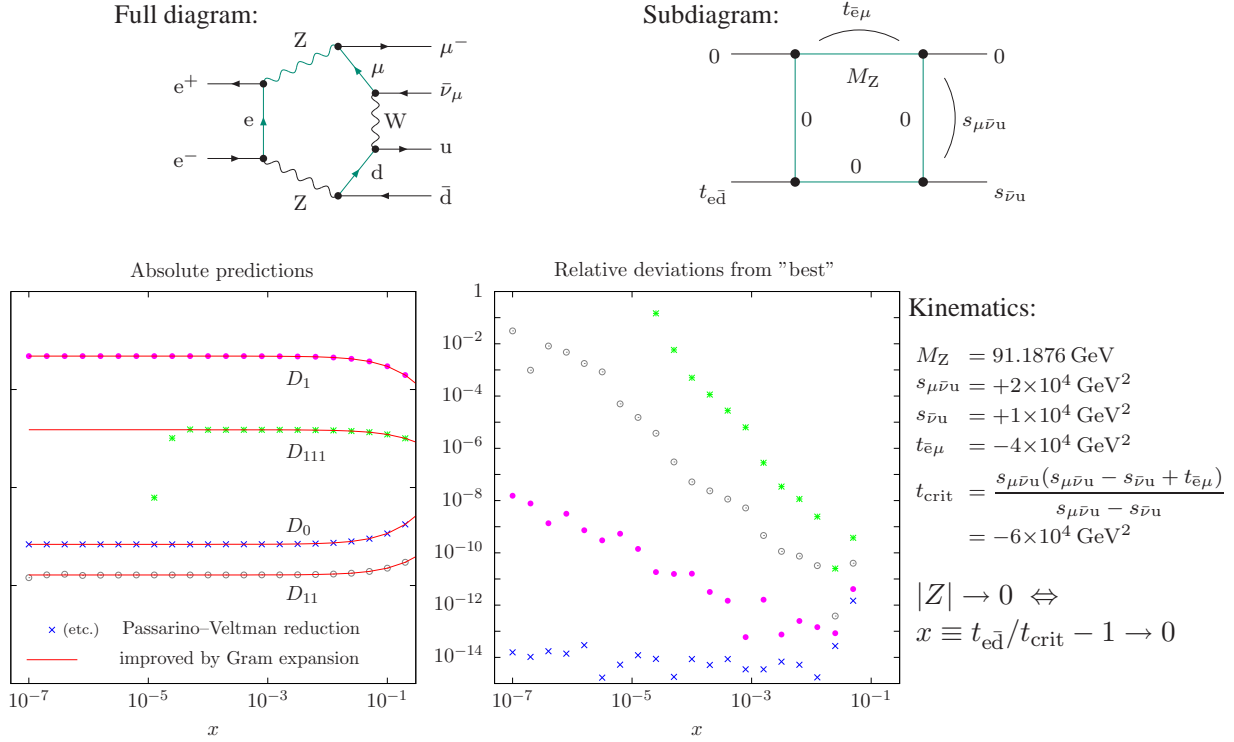
Fig. 25: A typical example for 4-point integrals with small $|Z|$ ($x \to 0$). The full diagram and the relevant subdiagram are given above; absolute predictions (in arbitrary units) for some tensor coefficients, relative deviations from PV reduction, and the kinematic specifications are shown below. The precise kinematical assignment is $D_{\ldots}(t_{\mathrm{e}\bar{\mathrm{d}}}, s_{\bar{\nu}\mathrm{u}}, 0, 0, t_{\bar{\mathrm{e}}\mu}, s_{\mu\bar{\nu}\mathrm{u}}, 0, 0, 0, M_Z^2)$.

	x	$D_0 [10^{-9}\,\mathrm{GeV}^{-4}]$	$D_1 [10^{-9}\,\mathrm{GeV}^{-4}]$
PV	10^{-1}	$-0.67882897158103 + \mathrm{i}\,6.0180488033754$	$1.7886414145138 - \mathrm{i}\,1.2549864424823$
GE		$-0.67882877418780 + \mathrm{i}\,6.0180477715020$	$1.7886420559893 - \mathrm{i}\,1.2549896774206$
PV	10^{-3}	$-0.83672359694266 + \mathrm{i}\,6.2756930854749$	$1.9379452063976 - \mathrm{i}\,1.3078118992970$
GE		$-0.83672359694268 + \mathrm{i}\,6.2756930854749$	$1.9379452063946 - \mathrm{i}\,1.3078118992992$
PV	10^{-5}	$-0.83844622485772 + \mathrm{i}\,6.2784151968393$	$1.9395624008169 - \mathrm{i}\,1.3083604510334$
GE		$-0.83844622485773 + \mathrm{i}\,6.2784151968392$	$1.9395624003839 - \mathrm{i}\,1.3083604516556$
PV	10^{-7}	$-0.83846346674121 + \mathrm{i}\,6.2784424334401$	$1.9395786154611 - \mathrm{i}\,1.3083659591802$
GE		$-0.83846346674123 + \mathrm{i}\,6.2784424334401$	$1.9395785857818 - \mathrm{i}\,1.3083659392409$

	x	$D_{11} [10^{-9}\,\mathrm{GeV}^{-4}]$	$D_{111} [10^{-9}\,\mathrm{GeV}^{-4}]$
PV	10^{-1}	$-1.1897035560343 + \mathrm{i}\,0.24556726948834$	$0.78386334534494 + \mathrm{i}\,0.015037069443873$
GE		$-1.1897015303789 + \mathrm{i}\,0.24555744219672$	$0.78386954016210 + \mathrm{i}\,0.015008250147071$
PV	10^{-3}	$-1.2896489514112 + \mathrm{i}\,0.24411794128315$	$0.85127803054027 + \mathrm{i}\,0.030174795680439$
GE		$-1.2896489629378 + \mathrm{i}\,0.24411794473416$	$0.85127066041158 + \mathrm{i}\,0.030177001227644$
PV	10^{-5}	$-1.2906894073746 + \mathrm{i}\,0.24417445247670$	$3.6185733047156 + \mathrm{i}\,5.5143276069563$
GE		$-1.2907326083248 + \mathrm{i}\,0.24408881850424$	$0.85200224111245 + \mathrm{i}\,0.030350914400978$
PV	10^{-7}	$-1.3307540613183 - \mathrm{i}\,0.18321620694255$	$-256227.63578209 - \mathrm{i}\,2736466.9255631$
GE		$-1.2907434539101 + \mathrm{i}\,0.24408852556218$	$0.85200956315901 + \mathrm{i}\,0.030352656048116$

Table 4: Numerical results corresponding to Fig. 25.

Full diagram:

e^+ γ u
e u W μ^-
d $\bar{\nu}_\mu$
e^- Z $\bar{d}$

Subdiagram:

$s_{\mu\bar\nu u}$
m_u^2 m_u $s_{\mu\bar\nu}$
0 0 $s_{\mu\bar\nu d}$
s M_Z 0

Absolute prediction

D_0

D_{11}

D_{111}

D_1

× (etc.) Passarino–Veltman reduction
——— improved by Gram/Cayley exp.

Relative deviations from "best"

Kinematics:

$m_u = 0.066\,\mathrm{GeV}$
$M_Z = 91.1876\,\mathrm{GeV}$
$s \quad = 4{\times}10^4\,\mathrm{GeV}^2$
$s_{\mu\bar\nu} = 64{\times}10^2\,\mathrm{GeV}^2$

$|Z|, |X| \to 0 \iff$
$s_{\mu\bar\nu d} \to s$ and $s_{\mu\bar\nu u} \to s_{\mu\bar\nu}$

Considered limit:
$x \equiv s_{\mu\bar\nu d}/s - 1$
$\equiv s_{\mu\bar\nu u}/s_{\mu\bar\nu} - 1 \to 0$
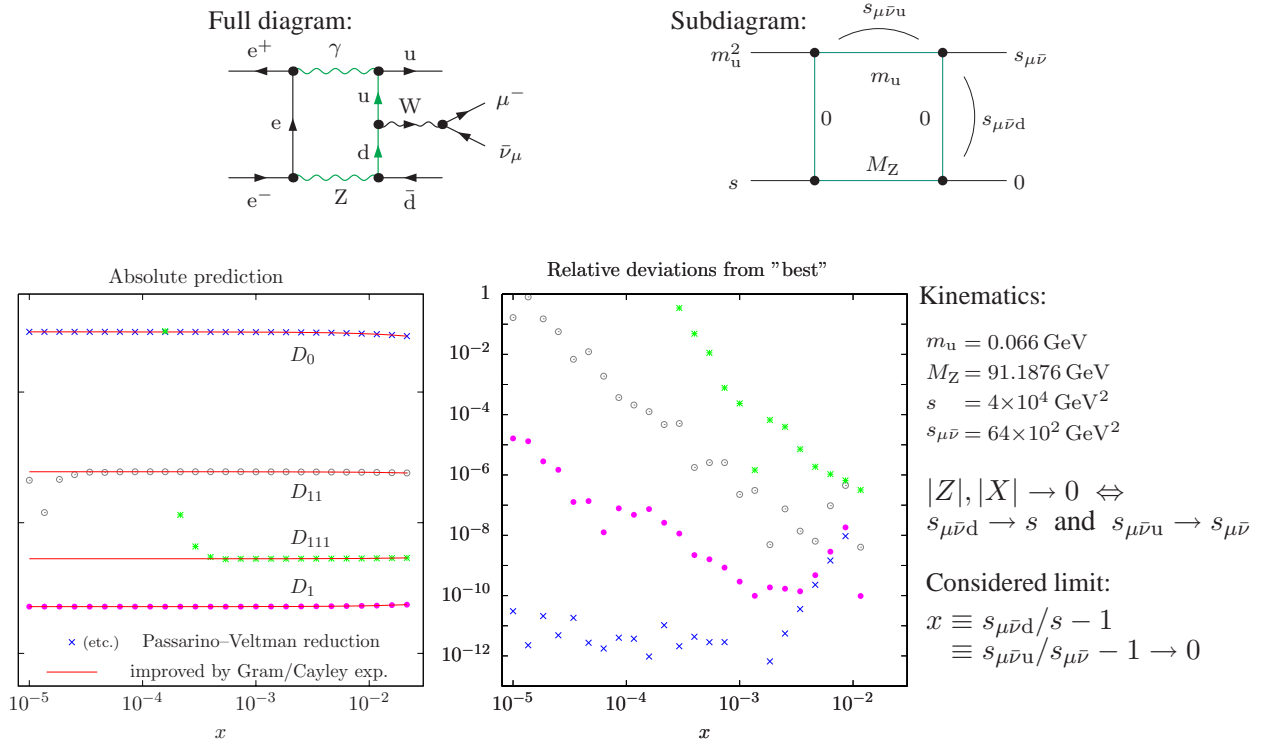
Fig. 26: An example for 4-point integrals with both $|Z|$ and $|X|$ small ($x \to 0$). Details as in Fig. 25. The precise kinematical assignment is $D_{...}(m_u^2, s_{\mu\bar\nu}, 0, s, s_{\mu\bar\nu u}, s_{\mu\bar\nu d}, 0, m_u^2, 0, M_Z^2)$.

	x	$D_0[10^{-8}\,\mathrm{GeV}^{-4}]$	$D_1[10^{-8}\,\mathrm{GeV}^{-4}]$
PV	10^{-2}	$8.3606217876308 - i\,3.0637590178519$	$-3.6746526331008 + i\,0.92370985809148$
GCE		$8.3605751148559 - i\,3.0637472109275$	$-3.6746146470383 + i\,0.92369999581248$
PV	10^{-3}	$8.4400974376543 - i\,3.0949777817064$	$-3.7124176130452 + i\,0.93444204630892$
GCE		$8.4400974331251 - i\,3.0949777805604$	$-3.7124176082911 + i\,0.93444204697694$
PV	10^{-4}	$8.4481162422241 - i\,3.0981290348801$	$-3.7162301181594 + i\,0.93552679201780$
GCE		$8.4481162422054 - i\,3.0981290348524$	$-3.7162304755308 + i\,0.93552678170043$
PV	10^{-5}	$8.4489188416187 - i\,3.0984444568680$	$-3.7165517842462 + i\,0.93563927582254$
GCE		$8.4489188413614 - i\,3.0984444566400$	$-3.7166121290025 + i\,0.93563537143079$

	x	$D_{11}[10^{-8}\,\mathrm{GeV}^{-4}]$	$D_{111}[10^{-8}\,\mathrm{GeV}^{-4}]$
PV	10^{-2}	$2.2302468112479 - i\,0.53202142768691$	$-1.5782872266397 + i\,0.38602980478054$
GCE		$2.2297642816234 - i\,0.53189620367287$	$-1.5778873843217 + i\,0.38592377802513$
PV	10^{-3}	$2.2539023067993 - i\,0.53805321575089$	$-1.5955732338585 + i\,0.38916806038788$
GCE		$2.2539023467387 - i\,0.53805185525506$	$-1.5951976445129 + i\,0.39030849156415$
PV	10^{-4}	$2.2578016118662 - i\,0.53856637974433$	$19.161260651686 + i\,1.6687070921546$
GCE		$2.2562925399069 - i\,0.53866164959083$	$-1.5969069247380 + i\,0.39074113712771$
PV	10^{-5}	$1.8810483898149 - i\,0.93548431089474$	$492069.51092499 + i\,67693.244541619$
GCE		$2.2565317562670 - i\,0.53872268382964$	$-1.5970779937221 + i\,0.39078443860164$

Table 5: Numerical results corresponding to Fig. 26.

reduction seems to be better. Table 4 provides explicit numbers for the considered tensor coefficients at some x values. These numbers could serve as a benchmark also for other methods.

We recall that the expansion for small $|Z|$ is limited to the case where $\tilde{X}_{0j}$ and $\tilde{Z}_{kl}$ are not too small for at least one set of indices j, k, l. If all $\tilde{X}_{0j}$ are small, then $|X|$ is small, too. Such a case is considered in the next subsection. The case in which all $\tilde{Z}_{kl}$ are small is elaborated in Section 5.6 of Ref. [200].

10.4.2 A case with small Gram and modified Cayley determinants

Figure 26 defines the second benchmark point for a 4-point function in which both determinants $|Z|$ and $|X|$ become small. Here we compare results of PV reduction with results of a simultaneous expansion in $|Z|$ and $|X|$ as described in Section 5.5 of Ref. [200]. In the upper half of the figure a pentagon diagram is shown that contains a box subdiagram with the considered kinematical configuration. The structural diagram again illustrates the kinematical situation as in the previous case and the explicit values of the masses and invariants are given in the figure. The u-quark mass m_{u} is kept only as regulator of the mass singularity, i.e. it is only kept non-zero in the logarithm $\ln m_{\mathrm{u}}$, but set to zero otherwise. The two determinants $|Z|$ and $|X|$ vanish if the two conditions $s_{\mu\bar{\nu}\mathrm{d}} = s$ and $s_{\mu\bar{\nu}\mathrm{u}} = s_{\mu\bar{\nu}}$ are fulfilled. We explore the neighbourhood of this exceptional configuration on the specific line parametrized by the dimensionless variable $x = s_{\mu\bar{\nu}\mathrm{d}}/s - 1 = s_{\mu\bar{\nu}\mathrm{u}}/s_{\mu\bar{\nu}} - 1$, while keeping the internal masses and the squares of the external momenta fixed.

The plot on the l.h.s. again illustrates the instabilities for small x in the PV reduction that become more serious for higher tensor ranks, while the results of the expansion method behave smoothly. The relative difference between the PV and the corresponding "best" prediction is shown on the r.h.s., revealing the expected increase for $x \to 0$. For a sufficiently high x the difference becomes zero, because PV reduction is more accurate than the expansion. In the overlap region both methods should be precise within a relative accuracy of about 10^{-6} for the considered coefficients. Table 5 provides explicit numbers for the considered tensor coefficients at some x values.

The expansion method fails if either all $\tilde{Z}_{ki}$ or all $\tilde{X}_{ij}$ are small. Possible treatments of these exceptional cases are also described in Ref. [200].

Acknowledgements

11. SINGULARITIES IN ONE-LOOP AMPLITUDES FROM THE POINT OF VIEW OF REDUCTION METHODS[21]

11.1 Introduction

Obtaining radiative corrections requires the evaluation of loop Feynman integrals. The simplest, but also the most important, loop integrals are one-loop Feynman integrals. Considerable progress has recently been made in developing various approaches for calculating one-loop integrals. Today, at least in principle, it is possible to calculate any of them to arbitrary precision no matter how many external legs the corresponding Feynman diagram has. Unfortunately, despite huge development, for a practitioner, the calculation of amplitudes up to one-loop contributions is still a difficult task. With the increasing complexity of the process under consideration, the number of Feynman diagrams whose contributions have to be obtained rises very quickly, as does the complexity of the corresponding one-loop Feynman integrals which have to be calculated. Therefore, we are forced to automatize our calculations. Use of available automatized algorithms helps tremendously, but the moment when calculations of physically relevant processes will demand for practical use unacceptable amounts of computer time and memory

---

[21]Contributed by: G. Duplančić

is not far away. To surpass this problem it is necessary to look for new approaches for calculating one-loop amplitudes, but also to implement algorithms in a more "computer friendly" way, which means less computer algebra and more numerics. Unfortunately, numerically oriented codes increase our chances to face numerical instabilities. This problem is usually connected with the presence of singularities in the functions under consideration. It is known that loop Feynamn integrals have rich singularity structures. For that reason, it is important to summarize all that is known about the problem as well as to share experience from previously performed calculations of amplitudes. Since reduction to the set of basic scalar Feynman integrals is at the heart of most methods for calculating Feynman integrals, here we discuss singularities from that point of view. Despite different approaches which can be taken, the final decomposition of the given Feynman integral, in terms of predefined set of basic integrals, should be unique. Therefore, any approach taken to discuss the singularity structure of the final decomposition is equally valid. Here the reduction method based on Refs. [151, 153, 208, 209] is used.

11.2 Definitions and reduction method

In order to obtain one-loop amplitudes, integrals of the following type are required,

$$I_{\mu_1\cdots\mu_P}^N(D;\{\nu_i\}) \equiv (\mu^2)^{2-D/2} \int \frac{\mathrm{d}^D l}{(2\pi)^D} \frac{l_{\mu_1}\cdots l_{\mu_P}}{\prod_{i=1}^N \left[(l+r_i)^2 - m_i^2 + \mathrm{i}\epsilon\right]^{\nu_i}}, \tag{108}$$

$$I_0^N(D;\{\nu_i\}) \equiv (\mu^2)^{2-D/2} \int \frac{\mathrm{d}^D l}{(2\pi)^D} \frac{1}{\prod_{i=1}^N \left[(l+r_i)^2 - m_i^2 + \mathrm{i}\epsilon\right]^{\nu_i}}. \tag{109}$$

The integral $I_{\mu_1\cdots\mu_P}^N$ (I_0^N) is a rank P tensor (scalar) one-loop N-point Feynman integral in D-dimensional space-time, where ν_i are powers of propagators and $l + r_i$ (m_i) is the momentum (mass) of particle propagating along the corresponding internal line. The momentum l is the loop momentum and the r_i are linear combinations of external momenta. The scale μ is the usual dimensional regularization scale and the quantity $\mathrm{i}\epsilon$ $(\epsilon > 0)$ represents an infinitesimal imaginary part which ensures causality and, after the integration, determines the correct sign of the imaginary part of the logarithms and dilogarithms. It is customary to choose the loop momentum in such a way that one of the momenta r_i vanishes. However, for general considerations, it is convenient to keep the symmetry of the integral with respect to the indices $1, \cdots, N$.

It can be shown that every tensor one-loop integral can be expressed as a linear combination of scalar one-loop integrals by the following equation,

$$I_{\mu_1\cdots\mu_P}^N(D;\{\nu_i\}) = \sum_{\substack{k,j_1,\cdots,j_N \geq 0 \\ 2k+\Sigma j_i = P}} \left\{[g]^k [r_1]^{j_1} \cdots [r_N]^{j_N}\right\}_{\mu_1\cdots\mu_P} \frac{(4\pi\mu^2)^{P-k}}{(-2)^k} \left[\prod_{i=1}^N \frac{\Gamma(\nu_i + j_i)}{\Gamma(\nu_i)}\right]$$

$$\times I_0^N(D + 2(P-k); \{\nu_i + j_i\}), \tag{110}$$

where $\{[g]^k [r_1]^{j_1} \cdots [r_N]^{j_N}\}_{\mu_1\cdots\mu_P}$ represents a symmetric (with respect to $\mu_1 \cdots \mu_P$) combination of tensors, each term of which is composed of k metric tensors and j_i momenta r_i. Therefore, the problem of calculating tensor integrals has been reduced to the calculation of the general scalar integral, which is the most convenient to evaluate from the following representation,

$$I_0^N(D;\{\nu_i\}) = \frac{\mathrm{i}}{(4\pi)^2}(4\pi\mu^2)^{2-D/2}\frac{\Gamma\left(\sum_{i=1}^N \nu_i - D/2\right)}{\prod_{i=1}^N \Gamma(\nu_i)}(-1)^{\Sigma_{i=1}^N \nu_i}$$

$$\times \int_0^1 \left(\prod_{i=1}^N \mathrm{d}y_i y_i^{\nu_i - 1}\right) \delta\left(\sum_{i=1}^N y_i - 1\right) \left[-\sum_{\substack{i,j=1 \\ i<j}}^N y_i y_j (r_i - r_j)^2 + \sum_{i=1}^N y_i m_i^2 - \mathrm{i}\epsilon\right]^{D/2 - \Sigma_{i=1}^N \nu_i}. \tag{111}$$

Direct evaluation of the general scalar integral represents a non-trivial problem. However, with the help of the recursion relations, the problem can be simplified in the sense that the calculation of the original scalar integral can be reduced to the calculation of a certain number of simpler basic integrals. All relevant recursion relations for scalar integrals can be written in matrix notation as

$$
\begin{pmatrix}
0 & 1 & 1 & \cdots & 1 \\
1 & R_{11} + 2i\epsilon & R_{12} + 2i\epsilon & \cdots & R_{1N} + 2i\epsilon \\
1 & R_{12} + 2i\epsilon & R_{22} + 2i\epsilon & \cdots & R_{2N} + 2i\epsilon \\
\vdots & \vdots & \vdots & \ddots & \vdots \\
1 & R_{1N} + 2i\epsilon & R_{2N} + 2i\epsilon & \cdots & R_{NN} + 2i\epsilon
\end{pmatrix}
\cdot
\begin{pmatrix}
(D - 1 - \sum_{j=1}^{N} \nu_j) I_0^N(D; \{\nu_i\}) \\
\nu_1\, I_0^N(D; \{\nu_i + \delta_{i1}\}) \\
\nu_2\, I_0^N(D; \{\nu_i + \delta_{i2}\}) \\
\vdots \\
\nu_N\, I_0^N(D; \{\nu_i + \delta_{iN}\})
\end{pmatrix}
=
$$

$$
=
\begin{pmatrix}
-(4\pi\mu^2)^{-1} I_0^N(D - 2; \{\nu_i\}) \\
-(4\pi\mu^2)^{-1}\, I_0^N(D - 2; \{\nu_i - \delta_{i1}\}) \\
-(4\pi\mu^2)^{-1}\, I_0^N(D - 2; \{\nu_i - \delta_{i2}\}) \\
\vdots \\
-(4\pi\mu^2)^{-1}\, I_0^N(D - 2; \{\nu_i - \delta_{iN}\})
\end{pmatrix}
,\tag{112}
$$

where $R_{ij} = (r_i - r_j)^2 - m_i^2 - m_j^2$. In the following we introduce the notation S_N for the $(N+1) \times (N+1)$ matrix in Eq. (112). Making use of relations which follow from Eq.(112), each scalar integral $I_0^N(D; \{\nu_i\})$ can be represented as a linear combination of integrals $I_0^N(D'; \{1\})$ and integrals with the number of propagators which is less than N (it has be understood that $I_0^N(D; \{\cdots \nu_{l-1}, 0, \nu_{l+1} \cdots \}) \equiv I_0^{N-1}(D; \{\cdots \nu_{l-1}, \nu_{l+1} \cdots \})$). For the dimension D', one usually chooses $4 + 2\varepsilon$, where ε is the infinitesimal parameter regulating the divergences. By successively applying the above mentioned procedure to the remaining less-than-N-point integrals it is at the end possible to express the integral $I_0^N(D; \{\nu_i\})$ as a linear combination of integrals $I_0^k(D'; \{1\})$, $k = 1, \ldots, N$. It is convenient to write these basic integrals as

$$
I_0^N(D'; \{1\}) = \frac{i}{(4\pi)^2} (4\pi\mu^2)^{2 - D'/2} \Gamma\left(N - D'/2\right) (-1)^N
$$

$$
\times \int_0^1 \prod_{i=1}^{N} dy_i\, \delta\left(\sum_{i=1}^{N} y_i - 1\right) \left[-\frac{1}{2} \sum_{i,j=1}^{N} y_i\, (R_{ij} + 2i\epsilon)\, y_j \right]^{D'/2 - N}, \tag{113}
$$

where the properties of the δ function were used.

11.3 Singularities

The necessary conditions for Feynman integrals to have singularities are given by the Landau equations. In the integral representations given by Eqs. (111) and (113), the singularity conditions [192] are given by

$$
\sum_{i,j=1}^{N} y_i\, (R_{ij} + 2i\epsilon)\, y_j = 0 \tag{114}
$$

and

$$
\textbf{either } y_i = 0 \textbf{ or } \sum_{j=1}^{N} (R_{ij} + 2i\epsilon)\, y_j = 0 \text{ for each } i. \tag{115}
$$

Notice that condition (114) is automatically satisfied when conditions (115) are. The singularity of the given Feynman integral corresponding to all $y_i \neq 0$ is called the *leading singularity* of the integral, while those corresponding to some $y_i = 0$ are called *lower-order singularities* of the integral. Lower-order singularities are leading singularities of integrals where all propagators associated with vanishing y_is

have been omitted. In the language of Feynman diagrams this translates as contraction to a point of all lines associated with $y_i = 0$.

Finding the general solution of the Landau equations is non-trivial task. Here we consider only real singularities. Real singularities are those occurring for real values of the invariants R_{ij} on the physical sheet. Notice that these real values of the invariants do not necessarily correspond to a physically possible kinematical configuration.

Due to presence of the iϵ, no singularity appears along the real contour of integration in the parametric space in Eqs. (111) and (113). It should be understood that singularities appear only in the limit i$\epsilon \to 0$.

In the previous section, it was described how to express an arbitrary Feynman integral as a linear combination of the basic scalar integrals. The question arises if all singularities of the starting integral correspond to singularities of the basic scalar integrals or some of them correspond to singularities of coefficients of the decomposition. To answer that question, it is enough to check if iϵ appears in denominators of the coefficients. That is, singularities appear only in the limit i$\epsilon \to 0$ and if some of the coefficients diverge independently of that limit, then the corresponding singularity is artificial in the sense that it is not a singularity of the starting Feynman integral. Consequently, such a divergence should cancel in sum of all terms in the decomposition.

The simplest way to see when iϵ appears in denominators is to invert Eq. (112) by multiplying it by inverse of S_N. The resulting equation is

$$
\begin{pmatrix} (D - 1 - \sum_{j=1}^N \nu_j) I_0^N(D; \{\nu_i\}) \\ \nu_1 \, I_0^N(D; \{\nu_i + \delta_{i1}\}) \\ \vdots \\ \nu_N \, I_0^N(D; \{\nu_i + \delta_{iN}\}) \end{pmatrix} = -\frac{(4\pi\mu^2)^{-1}}{\mathrm{Det}[S_N]} \times \tag{116}
$$

$$
\begin{pmatrix} \mathrm{Det}[R_N] - 2\mathrm{i}\epsilon \, \mathrm{Det}[S_N] & -S_N^{2\,1} & \cdots & (-1)^{N+2} S_N^{N+1\,1} \\ -S_N^{1\,2} & S_N^{2\,2} & \cdots & (-1)^{N+3} S_N^{N+1\,2} \\ \vdots & \vdots & \ddots & \vdots \\ (-1)^{N+2} S_N^{1\,N+1} & (-1)^{N+3} S_N^{2\,N+1} & \cdots & (-1)^{2N+2} S_N^{N+1\,N+1} \end{pmatrix} \begin{pmatrix} I_0^N(D-2; \{\nu_i\}) \\ I_0^N(D-2; \{\nu_i - \delta_{i1}\}) \\ \vdots \\ I_0^N(D-2; \{\nu_i - \delta_{iN}\}) \end{pmatrix},
$$

where $S_N^{i\,j}$ is minor of S_N obtained by removing ith row and jth column, and R_N is an $N \times N$ matrix with elements equal to R_{ij}. The matrix R_N is sometimes called modified Cayley matrix and its determinant the modified Cayley determinant. All minors appearing in Eq. (116) as well as $\mathrm{Det}[S_N]$ are iϵ independent. In all that determinants the first row or column can be simply used to remove completely the iϵ dependance. Therefore, only the recursion relation following from the first row of Eq. (116) will have an iϵ dependent coefficient. From the form of that relation it follows that real singularities can appear in the coefficients of decomposition only if relations of that type are used during reduction to increase dimension of integrals. In that case, a singularity can appear when $\mathrm{Det}[R_N] = 0$. As expected, the singularity is related to the same matrix which appears in Landau equations (114) and (115).

What happens if we calculate the integral exactly for kinematical variables and masses for which $\mathrm{Det}[R_N]$ vanishes? In that case the limit i$\epsilon \to 0$ should produce a divergence. But, from the beginning, dimensional regularization was introduced exactly to avoid explicit appearance of divergences. Hence, the limit i$\epsilon \to 0$ can be applied and divergences appear in the form of powers of $1/\varepsilon$. It follows that the term $\mathrm{Det}[R_N] - 2\mathrm{i}\epsilon \, \mathrm{Det}[S_N]$ vanishes and the first row from Eq. (116) can be used to reduce the N-point integral to a linear combination of $(N - 1)$-point integrals.

To complete the discussion, it is necessary to comment on how reduction works for vanishing $\mathrm{Det}[S_N]$. Let us first express $\mathrm{Det}[S_N]$ in a better known form. By subtracting the last column from the second, third, ..., and Nth column, and then the last row from the second, third, ..., and Nth row,

$\text{Det}[S_N]$ is given by

$$\text{Det}[S_N] = -\text{Det}\left[-2(r_i - r_N) \cdot (r_j - r_N)\right], \qquad i, j = 1, \ldots, N-1. \tag{117}$$

The determinant on the right hand side of Eq. (117) is known as the Gram determinant. If $\text{Det}[S_N]$, i.e. the Gram determinant, vanishes, then the rows (columns) of the matrix in Eq. (112) should be linearly dependent. That is, there are real constants $-C, z_1, \ldots, z_N$, not all of them equal zero, which satisfy the equation

$$\begin{pmatrix} 0 & 1 & 1 & \cdots & 1 \\ 1 & R_{11} + 2i\epsilon & R_{12} + 2i\epsilon & \cdots & R_{1N} + 2i\epsilon \\ 1 & R_{12} + 2i\epsilon & R_{22} + 2i\epsilon & \cdots & R_{2N} + 2i\epsilon \\ \vdots & \vdots & \vdots & \ddots & \vdots \\ 1 & R_{1N} + 2i\epsilon & R_{2N} + 2i\epsilon & \cdots & R_{NN} + 2i\epsilon \end{pmatrix} \cdot \begin{pmatrix} -C \\ z_1 \\ z_2 \\ \vdots \\ z_N \end{pmatrix} = \begin{pmatrix} 0 \\ 0 \\ 0 \\ \vdots \\ 0 \end{pmatrix}. \tag{118}$$

To see that the constants $-C, z_1, \ldots, z_N$ should be real, just remove the complete $i\epsilon$ dependance from the system in Eq. (118) by subtracting the equation from the first row multiplied by $2i\epsilon$ from equations in all other rows. After multiplying Eq. (112) by row $\begin{pmatrix} -C & z_1 & z_2 & \cdots & z_N \end{pmatrix}$, the following relation emerges,

$$C\, I_0^N(D - 2; \{\nu_i\}) = \sum_{j=1}^{N} z_j\, I_0^N(D - 2; \{\nu_i - \delta_{ij}\}). \tag{119}$$

It is easy to see that by using above relation it is always possible to reduce relevant N-point scalar integral to a linear combination of $N-1$-point scalar integrals. For details see [153].

From the considerations above, we can conclude that vanishing of the Gram determinant is not related to the singularities of Feynman integrals. It is important to point out that the situation is not so simple in the case of diagrams with more than one loop. There, Gram determinants are related to so-called *second-type singularities*.

11.4 Practice and problems

In practice we deal with 4-dimensional Minkowski space. An immediate consequence of this is that, for all integrals with $N > 5$, $\text{Det}[S_N]$ vanishes due to the linear dependence of the vectors r_i and all integrals with $N > 5$ can be reduced to the integrals with $N \leq 5$. In view of what has been said above, all one-loop integrals are expressible in terms of the integrals $I_0^k(4 + 2\varepsilon; \{1\})$ with nonvanishing $\text{Det}[S_k]$ and $\text{Det}[R_k]$, where $k = 1, \ldots, 5$. In fact, for practical calculations, also the 5-point basic scalar integral is reducible. That is because we are interested in calculations up to $\mathcal{O}(\varepsilon)$. Details can be found in the literature [150, 152, 209].

For most practical calculations the starting Feynman integrals obtained from Feynman diagrams by using Feynman rules are in $4 + 2\varepsilon$ dimensions and with $\nu_i = 1$. In the next step, tensor decomposition, Eq. (110), will produce scalar integrals with higher dimensions and powers of propagators. By successively using all recursion relations following from Eq. (116), except the one coming from the first row, in the cases of nonvanishing Gram determinants and recursion relations following from Eqs. (118) and (119) in the cases of vanishing Gram determinants, it is possible to express an arbitrary Feynman integral as a linear combination of integrals $I_0^k(2n + 2\varepsilon; \{1\})$ with nonvanishing $\text{Det}[S_k]$ and $\text{Det}[R_k]$, where $k = 1, \ldots, 5$. The possible values for parameter n depend on kinematics involved. If the kinematics is such that during reduction no case appears where the constant C in Eqs. (118) and (119) vanishes, the parameter n is an integer greater than 1. Now, the recursion from the first row of Eq. (116) can be successively used to lower all dimensions down to $4 + 2\varepsilon$. Since in the above procedure that relation was never used to increase dimension, from what has been said in the previous section, it follows that all singularities are in basic scalar integrals and divergences appearing in coefficients should cancel in

the sum. The cases with vanishing C appear regularly when dealing with diagrams containing collinear external lines, i.e. for exceptional kinematics.

Assuming the situation described in the previous paragraph, many Gram determinants to different powers will appear in denominators of the coefficients when an arbitrary Feynman integral is decomposed into the basic integrals. The real problem in practice is when one has to calculate in a kinematical region where some of those determinants are small. Since vanishing of the Gram determinant does not correspond to a singularity, one faces cancellation of big numbers and consequently numerical instabilities. In principle, if one is using methods where all Feynman integrals are expressed as linear combinations of basic integrals, this problem is unavoidable no matter in which framework coefficients are calculated. That is because the decomposition into the basic integrals is unique. However, there are some hints from experience as to where one should look to soften this problem. The main guideline is to try to avoid separate calculation of diagrams contributing to the process under consideration. Namely, powers of determinants in denominators tend to be smaller if a group of diagrams (for example, a gauge invariant group) is calculated together. Additionally, one has to use all symmetries of the basic integrals to reduce the basic set as much as possible. Of course, at the end, to get more precision, it is always necessary to make an expansion around a point where the Gram determinant vanishes. However, if calculating in the neighborhood of the point where both Gram and Cayley determinants vanish simultaneously, the expansion is problematic because the decomposition is not analytic at that point. One can hope that such regions will not give sizable contribution to calculated physical quantities.

11.5 Conclusion

Vanishing of various Gram and modified Cayley determinants will always produce numerical instabilities if reduction methods are used to perform the calculation. The instabilities can be softened by using various clever approaches but the question remains, will that work for all practical cases? One can also doubt if reduction to basic integrals is the optimal approach to perform calculations which, due to their complexity, become more and more numerically oriented. Maybe some kind of direct numerical integration of the Feynman integrals is more efficient. Surely this is a more natural approach for numerical calculations.

Acknowledgements

Part III

CROSS SECTIONS

12. TUNED COMPARISON OF QCD CORRECTIONS TO $pp \rightarrow WW+jet+X$ AT THE LHC[22]

12.1 Introduction

The complicated hadron collider environment of the LHC requires not only sufficiently precise predictions for the expected signals, but also reliable rates for complicated background reactions, especially for those that cannot be entirely measured from data. Among such background processes, several involve three, four, or even more particles in the final state, rendering the necessary next-to-leading-order (NLO) calculations in QCD technically challenging. At the previous Les Houches workshop this problem lead to the creation of a list of calculations that are a priority for LHC analyses, the so called "experimenters'

---

[22]Contributed by: T. Binoth, J. Campbell, S. Dittmaier, R.K. Ellis, J.-P. Guillet, S. Kallweit, S. Karg, N. Kauer, G. Sanguinetti, P. Uwer, G. Zanderighi

wishlist for NLO calculations" [16, 201]. The process $pp \rightarrow W^+W^- + jet + X$ made it to the top of this list.

The process of WW+jet production is an important source for background to the production of a Higgs boson that subsequently decays into a W-boson pair, where additional jet activity might arise from the production [210]. WW+jet production delivers also potential background to new-physics searches, such as the search for supersymmetric particles, because of leptons and missing transverse momentum from the W decays. Last, but not least, the process is interesting in its own right, since W-pair production processes enable a direct precise analysis of the non-abelian gauge-boson self-interactions, and a large fraction of W pairs will show up with additional jet activity at the LHC.

First results on the calculation of NLO QCD corrections to WW+jet production have been presented by two groups in Refs. [3, 4]. A third calculation is in progress [211]. In the following the key features of these three independent calculations are described and results of an ongoing tuned comparison are presented.

12.2 Descriptions of the various calculations

At leading order (LO), hadronic WW+jet production receives contributions from the partonic processes $q\bar{q} \rightarrow W^+W^-g$, $qg \rightarrow W^+W^-q$, and $\bar{q}g \rightarrow W^+W^-\bar{q}$, where q stands for up- or down-type quarks. All three channels are related by crossing symmetry.

The virtual corrections modify the partonic processes that are already present at LO. At NLO these corrections are induced by self-energy, vertex, box (4-point), and pentagon (5-point) corrections, the latter being the most complicated loop diagrams. Apart from an efficient handling of the huge amount of algebra, the most subtle point certainly is the numerically stable evaluation of the numerous tensor loop integrals, in particular in the vicinity of exceptional phase-space points. The three calculations described below employ completely different loop methods. Some of them are already briefly reviewed in Ref. [201], where more details on problems in multi-leg loop calculations and brief descriptions of proposed solutions can be found.

The real corrections are induced by the large variety of processes that result from crossing any pair of QCD partons in $0 \rightarrow W^+W^-q\bar{q}gg$ and $0 \rightarrow W^+W^-q\bar{q}q'\bar{q}'$ into the initial state. Here the main complication in the evaluation is connected to an efficient phase-space integration with a proper separation of soft and collinear singularities. For the separation of singularities the three calculations all employ the subtraction method [212] using the dipole subtraction formalism of Catani and Seymour [175].

The calculation of DKU [3]

This calculation is actually based on two completely independent evaluations of the virtual and real corrections. The W bosons are taken to be on shell, but the results on cross sections presented in Ref. [3] do not depend on the details of the W decays.

Both evaluations of loop diagrams start with an amplitude generation by *FeynArts*, using the two independent versions 1.0 [213] and 3.2 [214]. One of the calculations essentially follows the same strategy already applied to the related processes of t$\bar{t}$H [215] and t$\bar{t}$+jet [216] production. Here the amplitudes are further processed with in-house *Mathematica* routines, which automatically create an output in *Fortran*. The IR (soft and collinear) singularities are treated in dimensional regularization and analytically separated from the finite remainder as described in Refs. [206, 215]. The pentagon tensor integrals are directly reduced to box integrals following Ref. [202]. Box and lower-point integrals are reduced à la Passarino–Veltman [167] to scalar integrals, which are either calculated analytically or using the results of Refs. [148, 217, 218]. The second loop calculation is based on *FormCalc* 5.2 [14], which automatically produces *Fortran* code. The reduction of tensor to scalar integrals is done with the help of the *LoopTools* library [14], which also employs the method of Ref. [202] for the 5-point tensor integrals,

Passarino–Veltman [167] reduction for the lower-point tensors, and the *FF* package [219, 220] for the evaluation of regular scalar integrals. The dimensionally regularized soft or collinear singular 3- and 4-point integrals had to be added to this library.

One calculation of the real corrections employs analytical results for helicity amplitudes obtained in a spinor formalism. The phase-space integration is performed by a multi-channel Monte Carlo integrator [221] with weight optimization [222] written in *C++*. The results for cross sections with two resolved hard jets have been checked against results obtained with *Whizard* 1.50 [223] and *Sherpa* 1.0.8 [224]. Details on this part of the calculation can be found in Ref. [225]. The second evaluation of the real corrections is based on scattering amplitudes calculated with *Madgraph* [158] generated code. The code has been modified to allow for a non-diagonal quark mixing matrix and the extraction of the required colour and spin structure. The latter enter the evaluation of the dipoles in the Catani–Seymour subtraction method. The evaluation of the individual dipoles was performed using a *C++* library developed during the calculation of the NLO corrections for $t\bar{t}$+jet [216]. For the phase-space integration a simple mapping has been used where the phase space is generated from a sequential splitting.

The calculation of CEZ [4]

The method of choice for calculation of the virtual corrections of Ref. [4] is similar to the techniques adopted by the other groups and is based on the semi-numerical method of Ref. [226] augmented with a mechanism to handle exceptional configurations [227]. This method has already been used for the NLO calculation of Higgs plus dijet production via gluon-gluon fusion [5]. Tree-level matrix elements for real radiation have been checked against the results of *Madgraph* [228]. Soft and collinear singularities are handled using the dipole subtraction scheme [175]. As for the other authors, CEZ have performed several checks to test the reliability of their code. These include checks of Ward identities of the amplitudes containing external gluons.

The calculation of Ref. [4] is however different from the other two in that the decay of the W bosons is included from the outset. Rather than summing over the polarizations of a W boson of momentum k with

$$\sum \varepsilon^\mu \varepsilon^\nu = \left[-g^{\mu\nu} + \frac{k^\mu k^\nu}{M_W^2} \right], \tag{120}$$

the authors of this paper project out the combination of polarizations which occurs in the physical decay of the W boson, $W^-(k) \to e^-(l_1) + \bar{\nu}(l_2)$,

$$\sum \varepsilon^\mu \varepsilon^\nu \sim \frac{1}{2l_1.l_2} \text{Tr}[\slashed{l}_1 \gamma^\mu \slashed{l}_2 \gamma^\nu \gamma_L], \quad \gamma_L = (1 - \gamma_5)/2. \tag{121}$$

The inclusion of the decay is well-motivated from a physical point of view, because it allows phenomenological analyses which include cuts on the decay leptons.

For the purposes of the comparison of virtual matrix elements for a fixed phase-space point, the results including the decays can be used to extract the result for the amplitude squared summed over the polarization of the vector boson, as would be obtained using Eq. (120). This is achieved by performing 6×6=36 evaluations of the amplitude squared [229] in which each lepton is emitted along three orthogonal axes (in both positive and negative directions) in the corresponding vector-boson center-of-mass frame. The results of this comparison, with input parameters tuned for the comparison, will be given below.

The calculation of BGKKS [211]

This calculation is also done in two independent ways. The graph generation is based on *QGRAF* [165] and was cross checked by having two independent codes. All diagrams neglect the quarks of the 3rd generation.

Up to now the LO part and the virtual corrections are evaluated. By using the spinor helicity formalism, projectors on the different helicity amplitudes are defined. In this way all Lorentz indices can be saturated such that the complexity of the one-loop 5-point tensor reduction is such that at most rank-1 5-point integrals appear. For each helicity amplitude an algebraic representation in terms of certain basis functions is obtained by using the reduction methods developed in Refs. [152, 184]. The whole algebra is done in an automated way by using *FORM* [166] and *MAPLE*. In both approaches the IR divergent integrals are isolated by using 6-dimensional IR finite box functions such that IR poles are in 3-point functions only. One implementation uses the function set defined in Appendix C of Ref. [184], and uses the implementation of the *Fortran 90* code `golem90`. The other computation uses standard scalar 2- and 3-point functions as a basis. The complete algebraic reduction to d=6 scalar box and d=n scalar 2- and 3-point functions is largely equivalent to a standard Passarino–Veltman reduction. Only the 5-point functions are treated differently [184]. Tractable analytical expressions of the coefficients to the two sets of basis functions are obtained for each independent helicity amplitude.

Discrete symmetries (Bose,C,P) are used to check and relate helicity amplitudes with each other. The coefficients are exported to a *Fortran* code and used to evaluate the loop correction of the process.

For the treatment of γ_5 the 't Hooft–Veltman scheme is applied. The γ-algebra and the loop momenta are split into 4- and $(D-4)$-dimensional parts. Whereas the γ_5 anti-commutes with the $D=4$ matrices, it commutes with the gamma matrices defined in $d = D - 4$. As is well known the QCD corrections of an axial vector current are different from the vector part and a finite renormalisation has to be performed. The following gauge boson vertex which includes a finite counterterm for the axial part (see e.g. Refs. [230–232]) is used,

$$V^{\mu}_{Vq\bar{q}} \sim g_v \, \gamma^{\mu} + Z_5 \, g_a \, \gamma^{\mu}\gamma_5 \quad \text{with} \quad Z_5 = 1 - C_F \, \frac{\alpha_s}{\pi}, \tag{122}$$

to reinforce the correct chiral structure of the amplitudes. Note that the 't Hooft–Veltman scheme treats the observed particles in 4 dimensions but the soft/collinear gluons in D dimensions. This guarantees that for the IR subtractions the same Catani–Seymour dipole terms as for conventional dimensional regularisation can be used [233].

12.3 Tuned comparison of results

The following results essentially employ the setup of Ref. [3]. The CTEQ6 [28, 234] set of parton distribution functions (PDFs) is used throughout, i.e. CTEQ6L1 PDFs with a 1-loop running α_s are taken in LO and CTEQ6M PDFs with a 2-loop running α_s in NLO. Bottom quarks in the initial or final states are not included, because the bottom PDF is suppressed w.r.t. to the others. Quark mixing between the first two generations is introduced via a Cabibbo angle $\theta_C = 0.227$. In the strong coupling constant the number of active flavours is $N_F = 5$, and the respective QCD parameters are $\Lambda_5^{\text{LO}} = 165$ MeV and $\Lambda_5^{\overline{\text{MS}}} = 226$ MeV, leading to $\alpha_s^{\text{LO}}(M_W) = 0.13241687663294$ and $\alpha_s^{\text{NLO}}(M_W) = 0.12026290039064$. The top-quark loop in the gluon self-energy is subtracted at zero momentum. The running of α_s is, thus, generated solely by the contributions of the light quark and gluon loops. In all results shown in the following, the renormalization and factorization scales are set to M_W. The top-quark mass is $m_t = 174.3$ GeV, the masses of all other quarks are neglected. The weak boson masses are $M_W = 80.425$ GeV, $M_Z = 91.1876$ GeV, and $M_H = 150$ GeV. The weak mixing angle is set to its on-shell value, i.e. fixed by $c_w^2 = 1 - s_w^2 = M_W^2/M_Z^2$, and the electromagnetic coupling constant α is derived from Fermi's constant $G_\mu = 1.16637 \cdot 10^{-5}$ GeV^{-2} according to $\alpha = \sqrt{2} G_\mu M_W^2 s_w^2/\pi$.

We apply the jet algorithm of Ref. [235] with $R = 1$ for the definition of the tagged hard jet and restrict the transverse momentum of the hardest jet by $p_{T,jet} > 100$ GeV.

	$\lvert\mathcal{M}_{\mathrm{LO}}\rvert^2/e^4/g_{\mathrm{s}}^2[\mathrm{GeV}^{-2}]$
$u\bar{u} \to W^+W^-g$	$0.9963809154477200 \cdot 10^{-3}$
$d\bar{d} \to W^+W^-g$	$0.3676289952184384 \cdot 10^{-5}$
$ug \to W^+W^-u$	$0.1544340549124799 \cdot 10^{-3}$
$dg \to W^+W^-d$	$0.1537758419168101 \cdot 10^{-5}$
$g\bar{u} \to W^+W^-\bar{u}$	$0.7491333451663728 \cdot 10^{-4}$
$gd \to W^+W^-d$	$0.2776156068243590 \cdot 10^{-4}$

Table 6: Results for squared LO matrix elements at the phase-space point (123).

12.4 Results for a single phase-space point

For the comparison the following set of four-momenta is chosen,

$$
\begin{aligned}
p_1^\mu &= (7000, 0, 0, 7000), \qquad p_2^\mu = (7000, 0, 0, -7000), \\
p_3^\mu &= (6921.316234371218, 3840.577592920205, 0, 5757.439881432096), \\
p_4^\mu &= (772.3825553565997, -67.12960601170266, -279.4421082776151, -712.3990141151700), \\
p_5^\mu &= (6306.301210272182, -3773.447986908503, 279.4421082776151, -5045.040867316925),
\end{aligned}
\tag{123}
$$

where the momentum assignment is for $a(p_1)b(p_2) \to W^+(p_3)W^-(p_4)c(p_3)$.

Table 6 shows some results for the (spin- and colour-summed) squared LO matrix elements, as obtained with *Madgraph* [158]. The results of all three groups agree with these numbers within about 13 digits.

Because of the different treatment of the number of active flavours in the calculations of DKU and CEZ and in order to be independent of the subtraction scheme to cancel IR divergences, we found it useful to compare virtual results prior to any subtraction. The $\mathcal{O}(\alpha_s)$ contribution to the virtual, renormalized squared amplitude is given by the interference between tree-level and one-loop virtual amplitude, which we denote schematically as

$$
2\mathrm{Re}\{M_V^* \cdot M_{\mathrm{LO}}\} = e^4 g_s^2 f(\mu_{\mathrm{ren}}) \left(c_{-2}\frac{1}{\epsilon^2} + c_{-1}\frac{1}{\epsilon} + c_0 \right),
\tag{124}
$$

with[23] $f(\mu_{\mathrm{ren}}) = \Gamma(1+\epsilon)(4\pi\mu_{\mathrm{ren}}^2/M_W^2)^\epsilon$ and the number of space–time dimensions $D = 4 - 2\epsilon$. In the following we split the coefficients of the double and single pole and for the constant part, c_{-2}, c_{-1}, and c_0, into bosonic contributions ("bos") without closed fermion loops and the remaining fermionic parts. The fermionic corrections are further split into contributions from the first two generations ("ferm1+2") and from the third generation.

Table 7 shows the results for the bosonic parts of the coefficients c_{-2}, c_{-1}, and c_0 (c_{-2} does not receive fermion-loop corrections). The results on c_0 obtained by the different groups typically agree within $7-11$ digits; the ones on c_{-2} and c_{-1} agree much better, because they are much easier to calculate. The results for the fermionic contributions of the first two generations are given in Table 8. Compared to the bosonic corrections these contributions are suppressed by three orders of magnitude. Counting this suppression factor, which results from cancellations, as significant digits, the finite parts agree within $6-9$ digits. The agreement is somewhat better in the coefficients of the single pole, which entirely stems from the counterterm of the fermion-loop part of the gluon self-energy. The remaining contributions from closed loops of the third quark generation are not compared yet. For future reference we show the full corrections including all bosonic and fermionic contributions in Table 9.

---

[23]Note that this factor differs from the overall factor c_Γ extracted when quoting results for one phase-space point in the CEZ paper.

	$c_{-2}[\mathrm{GeV}^{-2}]$	$c_{-1}^{\mathrm{bos}}[\mathrm{GeV}^{-2}]$	$c_0^{\mathrm{bos}}[\mathrm{GeV}^{-2}]$
$u\bar{u} \to W^+W^-g$			
DKU	$-1.080699305508758 \cdot 10^{-4}$	$7.842861905263072 \cdot 10^{-4}$	$-3.382910915425372 \cdot 10^{-3}$
CEZ	$-1.080699305505865 \cdot 10^{-4}$	$7.842861905276719 \cdot 10^{-4}$	$-3.382910915464027 \cdot 10^{-3}$
BGKKS	$-1.080699305508814 \cdot 10^{-4}$	$7.842861905263293 \cdot 10^{-4}$	$-3.382910915616242 \cdot 10^{-3}$
$d\bar{d} \to W^+W^-g$			
DKU	$-3.987394716797222 \cdot 10^{-7}$	$2.893736116870099 \cdot 10^{-6}$	$-1.252531649334637 \cdot 10^{-5}$
CEZ	$-3.987394716665197 \cdot 10^{-7}$	$2.893736115389983 \cdot 10^{-6}$	$-1.252531614999332 \cdot 10^{-5}$
BGKKS	$-3.987394716798342 \cdot 10^{-7}$	$2.893736117550454 \cdot 10^{-6}$	$-1.252531647620369 \cdot 10^{-5}$
$ug \to W^+W^-u$			
DKU	$-1.675029833503229 \cdot 10^{-5}$	$1.236268430131559 \cdot 10^{-4}$	$-5.417120947927877 \cdot 10^{-4}$
CEZ	$-1.675029833501256 \cdot 10^{-5}$	$1.236268430124113 \cdot 10^{-4}$	$-5.417120948004078 \cdot 10^{-4}$
BGKKS	$-1.675029833503285 \cdot 10^{-5}$	$1.236268430131930 \cdot 10^{-4}$	$-5.417120948184518 \cdot 10^{-4}$
$dg \to W^+W^-d$			
DKU	$-1.667890693078443 \cdot 10^{-7}$	$1.231000679615805 \cdot 10^{-6}$	$-5.402644808236175 \cdot 10^{-6}$
CEZ	$-1.667890693268847 \cdot 10^{-7}$	$1.230999331981130 \cdot 10^{-6}$	$-5.402644353170802 \cdot 10^{-6}$
BGKKS	$-1.667890693077475 \cdot 10^{-7}$	$1.230999333576065 \cdot 10^{-6}$	$-5.402644211736123 \cdot 10^{-6}$
$g\bar{u} \to W^+W^-\bar{u}$			
DKU	$-8.125284951799448 \cdot 10^{-6}$	$7.047108864062224 \cdot 10^{-5}$	$-3.525581727244482 \cdot 10^{-4}$
CEZ	$-8.125284951286924 \cdot 10^{-6}$	$7.047108863931619 \cdot 10^{-5}$	$-3.525581728065669 \cdot 10^{-4}$
BGKKS	$-8.125284951799859 \cdot 10^{-6}$	$7.047108864102780 \cdot 10^{-5}$	$-3.525581727287365 \cdot 10^{-4}$
$g\bar{d} \to W^+W^-\bar{d}$			
DKU	$-3.011087314520321 \cdot 10^{-6}$	$2.611534269956032 \cdot 10^{-5}$	$-1.326197552139531 \cdot 10^{-4}$
CEZ	$-3.011087314528406 \cdot 10^{-6}$	$2.611534269870494 \cdot 10^{-5}$	$-1.326197549152728 \cdot 10^{-4}$
BGKKS	$-3.011087314520429 \cdot 10^{-6}$	$2.611534269951226 \cdot 10^{-5}$	$-1.326197552106838 \cdot 10^{-4}$

Table 7: Results for the bosonic virtual corrections at the phase-space point (123) with c_{-2}, c_{-1} and c_0 are defined in Eq. (124).

	$c_{-1}^{\text{ferm1+2}}[\text{GeV}^{-2}]$	$c_0^{\text{ferm1+2}}[\text{GeV}^{-2}]$
$u\bar{u} \to W^+W^-g$		
DKU	$2.542821895320379 \cdot 10^{-5}$	$4.372323372044527 \cdot 10^{-7}$
CEZ	$2.542821895311753 \cdot 10^{-5}$	$4.372790378087550 \cdot 10^{-7}$
BGKKS	$2.542821895314862 \cdot 10^{-5}$	$4.372324288356448 \cdot 10^{-7}$
$d\bar{d} \to W^+W^-g$		
DKU	$9.382105211529244 \cdot 10^{-8}$	$2.383985481697933 \cdot 10^{-8}$
CEZ	$9.382105220158816 \cdot 10^{-8}$	$2.381655056763332 \cdot 10^{-8}$
BGKKS	$9.382105215996126 \cdot 10^{-8}$	$2.383986138730693 \cdot 10^{-8}$
$ug \to W^+W^-u$		
DKU	$3.941246664484964 \cdot 10^{-6}$	$2.261655163318730 \cdot 10^{-7}$
CEZ	$3.941246667066658 \cdot 10^{-6}$	$2.261900862449825 \cdot 10^{-7}$
BGKKS	$3.941246667066566 \cdot 10^{-6}$	$2.261651778836927 \cdot 10^{-7}$
$dg \to W^+W^-d$		
DKU	$3.924449049876280 \cdot 10^{-8}$	$-3.340508442179341 \cdot 10^{-8}$
CEZ	$3.924448807787651 \cdot 10^{-8}$	$-3.341842650545260 \cdot 10^{-8}$
BGKKS	$3.924448689594072 \cdot 10^{-8}$	$-3.340505335889721 \cdot 10^{-8}$
$g\bar{u} \to W^+W^-\bar{u}$		
DKU	$1.911831753319591 \cdot 10^{-6}$	$-3.332688444715011 \cdot 10^{-7}$
CEZ	$1.911831753400357 \cdot 10^{-6}$	$-3.332770821153847 \cdot 10^{-7}$
BGKKS	$1.911831753364673 \cdot 10^{-6}$	$-3.332688443882355 \cdot 10^{-7}$
$g\bar{d} \to W^+W^-\bar{d}$		
DKU	$7.084911328500216 \cdot 10^{-7}$	$-3.420298601940541 \cdot 10^{-7}$
CEZ	$7.084911328417316 \cdot 10^{-7}$	$-3.419939732016338 \cdot 10^{-7}$
BGKKS	$7.084911328283340 \cdot 10^{-7}$	$-3.420298578631734 \cdot 10^{-7}$

Table 8: Results for the fermionic contributions of the first two quark generations to c_{-1} and c_0 at the phase-space point (123).

	$c_{-2}[\text{GeV}^{-2}]$	$c_{-1}[\text{GeV}^{-2}]$	$c_0[\text{GeV}^{-2}]$
$u\bar{u} \to W^+W^-g$			
DKU	$-1.080699305508778 \cdot 10^{-4}$	$8.160714642177893 \cdot 10^{-4}$	$-3.382201173786996 \cdot 10^{-3}$
$d\bar{d} \to W^+W^-g$			
DKU	$-3.987394716797186 \cdot 10^{-7}$	$3.011012432041691 \cdot 10^{-6}$	$-1.248828433702770 \cdot 10^{-5}$
$ug \to W^+W^-u$			
DKU	$-1.675029833503229 \cdot 10^{-5}$	$1.285534013444099 \cdot 10^{-4}$	$-5.413834847221341 \cdot 10^{-4}$
$dg \to W^+W^-d$			
DKU	$-1.667890693078551 \cdot 10^{-7}$	$1.280056291844283 \cdot 10^{-6}$	$-5.452219162448072 \cdot 10^{-6}$
$g\bar{u} \to W^+W^-\bar{u}$			
DKU	$-8.125284951799523 \cdot 10^{-6}$	$7.286087833227389 \cdot 10^{-5}$	$-3.528788476602400 \cdot 10^{-4}$
$g\bar{d} \to W^+W^-\bar{d}$			
DKU	$-3.011087314520238 \cdot 10^{-6}$	$2.700095661561590 \cdot 10^{-5}$	$-1.331943241722592 \cdot 10^{-4}$

Table 9: Results for the full bosonic+fermionic contributions to c_{-2}, c_{-1} and c_0 at the phase-space point (123).

$pp \rightarrow W^+W^- + jet + X$	σ_{LO}[fb]	σ_{NLO}[fb]	$\sigma_{\mathrm{virt+I}}$[fb]
DKU	10371.7(12)	14677.6(98)	$-881.5(42)$
CEZ	10372.26(97)		
BGKKS	10371.7(11)		

Table 10: Results for contributions to the integrated pp cross sections at the LHC in LO and NLO.

12.5 Results for integrated cross sections

A tuned comparison of integrated cross sections is still in progress. Table 10 illustrates the agreement in the LO cross section obtained by the different groups and provides the DKU result in NLO for future comparisons. The subcontribution $\sigma_{\mathrm{virt+I}}$ corresponds to the IR-finite sum of the virtual corrections and the contribution of the I operator that is extracted from the real corrections with the dipole subtraction formalism [175].

12.6 Conclusions

We have reported on an ongoing tuned comparison of NLO QCD calculations to WW+jet production at the LHC. For a fixed phase-space point, the virtual corrections obtained by three different groups using different calculational techniques agree within 6–9 digits. The comparison of full NLO cross sections, which involve the non-trivial integration of the virtual corrections over the phase space, is still in progress.

The agreement found so far gives us confidence in the conclusions drawn for physical quantities, which were reported in Refs. [3, 4].

13. FROM THE HIGH ENERGY LIMIT OF MASSIVE QCD AMPLITUDES TO THE FULL MASS DEPENDENCE[24]

13.1 Introduction

It is clear that the physics program of the LHC poses new challenges to the theory. In fact, the description of hadronic collisions involves several quantities, both non-perturbative and perturbative, the determination of which is a highly non-trivial task. As far as the perturbative part is concerned, we are still a long way of having the partonic cross sections predicted at a suitable level of accuracy. Whereas most processes will have to be known to next-to-leading order, there are some for which the experimental precision grants a study going one order higher in the strong coupling constant. Particularly interesting here is the top quark pair production cross section. With statistics going into millions of events, a systematics dominated error of under 10% is expected already in the first phase of the LHC. Despite years of efforts, the appropriate complete NNLO prediction is not yet available. The bottleneck, as in most such cases is the evaluation of the two-loop virtual corrections.

---

[24]Contributed by: M. Czakon

Recently, the high energy limit of the amplitudes in the quark annihilation and gluon fusion channels has been derived [236, 237] by a mixture of direct evaluation of Feynman graphs and an approach based on factorization properties of QCD (see A. Mitov's and S. Moch's contribution). The knowledge gained can already be used for the description of high p_T events and as a test of a future complete prediction. Clearly due to the behavior of the particle fluxes, what is needed is a calculation covering the whole range of variation of the kinematical parameters. It is interesting that one can actually use the high energy limit to deal with this problem. Unfortunately, it is not enough to have the whole amplitude, but it is rather necessary to know all of the master integrals. In the following, I describe the steps that lead to the complete result.

13.2 The high energy limit

By the high energy limit, I understand the limit where all the invariants are much larger than the mass. A direct approach to the evaluation of the amplitude under this assumption has been devised in [238, 239]. As a first step, one uses the Laporta algorithm to reduce all of the integrals occurring to a small set of masters. In the case at hand, the number of integrals is 145 and 422 for the quark annihilation and gluon fusion channels respectively.

Subsequently, Mellin-Barnes representations are constructed for all the integrals [240, 241]. This can be done by an automatic package, here by one written by the Author and G. Chachamis[25]. After analytic continuation in the dimension of space-time performed with the MB package [243], the integrals have the following general form

$$I = (m^2)^{n-2\epsilon} \int_{-i\infty}^{i\infty} dz \ \left(-\frac{m^2}{s} \right)^z f\left(\frac{t}{s}, z \right),$$

(125)

where the f function contains, amongst others, a product of Γ, or possibly ψ functions, which have poles in z. The desired expansion is obtained by closing the contour and taking residues. As a result, one obtains integrals which have lower dimension and a simpler structure. These still require evaluation. Due to the fact, that there is a relation between the massive and the massless cases, the result must have a similar structure. In particular, it has to be given by harmonic polylogarithms, and therefore it should be possible to resum the integrals by further closing contours and evaluating the resulting series. This can again be achieved automatically with the help of the XSummer package [244].

What remains at the end are integrals, which are pure numbers, but do not have a structure suggesting a solution in terms of harmonic series. The same argument as before shows, however, that this must be the case. Instead of working out specific methods for particular integrals, it turned out to be possible to evaluate them to very high precision and subsequently use the PSLQ algorithm to reconstruct the solution in terms of Riemann zeta values.

It has to be noted, that the procedure sketched above works for the majority of cases, but some remain at the end. For these, it is usually necessary to change the basis of integrals, in order to obtain expressions of suitable structure and/or size for evaluation. At present this program has been completed for the quark annihilation channel, and thus all the color structures given in [236] have been computed directly with agreement with the factorization approach. The gluon fusion channel is still under way.

13.3 Power corrections

As explained in the introduction, the high energy limit by itself is not enough for practical applications. To go one step further, it is possible to compute power corrections in the mass. These will then cover most of the range, apart from the threshold region and the small angle region, where the series is not convergent any more.

---

[25]There is a public package available [242] that constructs representations for planar graphs. In the present case, also non-planar graphs occur, however.
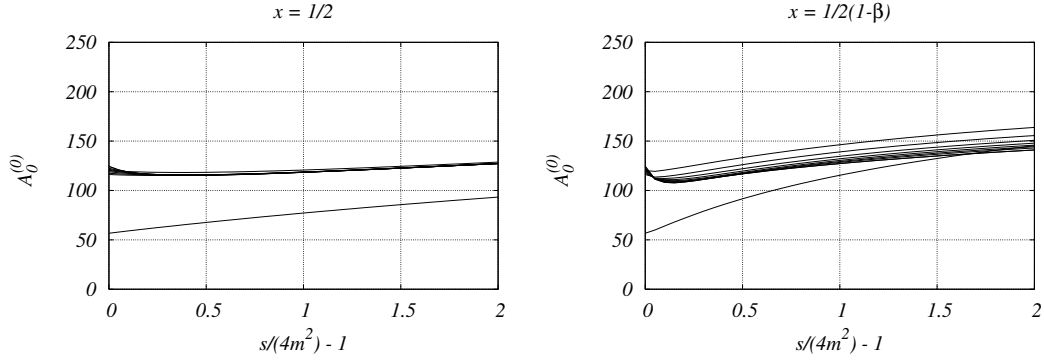
Fig. 27: Bare leading color amplitude for top quark pair production in the quark annihilation channel expanded in the mass. The more divergent terms at threshold (left of the plots) correspond to higher orders of expansion. The left panel corresponds to 90 degree scattering, whereas the right to forward scattering. The variables are defined in the text.

The main idea is as follows. The derivative of any Feynman integral with respect to any kinematical variable is again a Feynman integral with possibly higher powers of denominators or numerators. These can, however, be reduced to the same master integrals. This means that one can construct a partially triangular system of differential equations in the mass [245,246], which can subsequently be solved in the form of a power series.

In Fig. 27, I show the result of expansion for the leading color term. The kinematic variable x is

$$x = -\frac{t}{s}, \quad t = (p_3 - p_1)^2 - m_t^2, \tag{126}$$

and its variation within the range $[1/2(1 - \beta), 1/2(1 + \beta)]$, where $\beta = \sqrt{1 - 4m_t^2/s}$ is the velocity, corresponds to angular variation between the forward and backward scattering.

The series appears to be asymptotic at the boundaries. Unfortunately, the behavior is worse for the subleading color terms, as a consequence of the Coulomb singularity among others.

13.4 Numerical evaluation

Using the same system of differential equations one can obtain a full numerical solution to the problem. The only requirement is to have the boundary conditions to suitable accuracy. These are provided by the series expansions of the previous section. It is crucial to perform the numerical integration along a contour in the complex plane, since there are spurious singularities along the real axis. Here, I chose an ellipse, because of the improved control on the integration error that one gets from the software used (ODEPACK).

Fig. 28 shows the solution in the range, where the expansion of the previous section starts to diverge. The achievable precision, if double precision arithmetic is used, is about 10 digits for most points, with evaluation times of the order of a second. This is going to be substantially slower, when subleading color terms will be added. However, the method is fast and precise enough to be sufficient for practical applications. In particular it is possible to construct grids of solutions, which will be subsequently interpolated when implemented as part of a Monte Carlo program.

It is clear that the method is suitable for problems, which have a relatively small number of scales, and seems to be perfect for $2 \rightarrow 2$ QCD processes at the two-loop level. The main drawback is the size of the expressions, and the difficulties connected to the derivation of the boundary conditions.
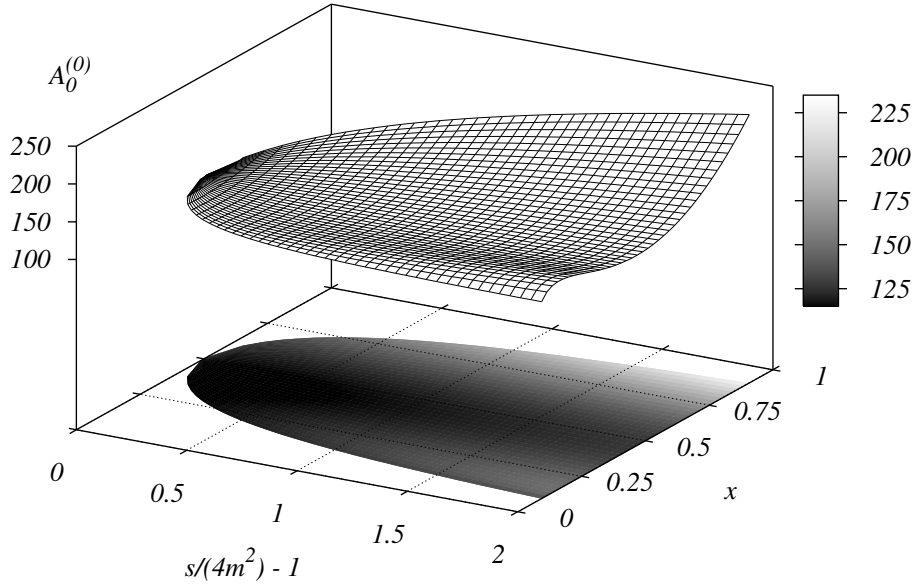
Fig. 28: Full mass dependence of the bare leading color amplitude in the quark annihilation channel.

13.5   Conclusions

I have described an approach for the evaluation of massive QCD amplitudes starting from the high energy limit and its application to the NNLO corrections to the top quark pair production cross section. Needless to say, the same procedure can be applied to other problems of interest. At present the Author, together with G. Chachamis and D. Eiras, is working on the corrections to gauge boson pair production.

Acknowledgements

14.   MUCH CAN BE SAID ABOUT MASSIVE AMPLITUDES JUST FROM KNOWING THEIR MASSLESS LIMIT[26]

14.1   The high-energy limit

For the precise evaluation of collider observables the knowledge of the pure virtual correction to the corresponding Born process is required. This is true at any order (NLO, NNLO, etc). In presence of heavy flavors, and especially at higher orders, the problem of their evaluation becomes acute.

There are very important applications awaiting such results. An example of central importance is top production at LHC which is one of the few eagerly awaited *precision* observables at this collider. One of the peculiar features of top production at LHC, and in contrast to the situation at the Tevatron, is that no specific kinematical region dominates the cross-section. This is due to the shape of the luminosity function for LHC kinematics.

Direct calculation of the amplitudes is certainly a very demanding task and it seems that one can hope that numerical results in some, hopefully easy to handle form, will become available soon (see the contribution by M. Czakon for progress in this direction). Here we consider an alternative approach which explores the special properties of the gauge theory amplitudes in the high-energy limit and easily provides (partial) results for the heavy flavor amplitudes even at higher perturbative orders.

---

[26]Contributed by: A. Mitov, S. Moch

In the following we start by introducing the concept of *high-energy limit* with the help of simple and physically motivated arguments. By high-energy limit one means a kinematical situation where the corresponding invariants are much larger than the masses of the heavy particles of interest. In the following we will consider the case of a single massive fermion with mass m in presence of a typical large kinematical invariant Q. Specific examples are detailed in section 14.3. If the quantity of interest (like total or differential cross-section, amplitude, etc.) is regular in the limit $m/Q \to 0$ then the high-energy limit is quite trivial: it is an m-independent function of the kinematical invariants which coincides with the one evaluated in the massless limit. Therefore it can be computed by setting the mass m to zero from the very beginning.

Such a situation is, however, relatively rare. In most quantities of interest, like the differential ones, the limit $m/Q \to 0$ is singular. The obvious manifestation of that singularity in the results is the presence of terms of the type $\sim \ln^n(m/Q)$. When such contributions appear (and in fact this is the typical situation) the high-energy limit is defined as the full result with all power corrections in the mass neglected, i.e. it contains all logarithms (not multiplied by powers of the mass) as well as the so-called "constant" or mass-independent terms. Clearly, in such cases the high-energy limit is different from the massless limit.

Before we detail the relation between these two limits, we would first like to clarify the origin and meaning of the logarithmic terms mentioned above. These terms are known as (quasi-) collinear logs since they originate from emissions of collinear radiation. To be precise, the role of the mass is to regulate small angle emissions that would otherwise diverge in a massless theory; see Ref. [247] for a detailed exposition. In this regard, a parton's mass gets dual significance, since one can take one of the following two viewpoints:

- small or large, the mass is nevertheless non-zero, therefore the result is always (collinearly) finite;

- the small mass is just a formal regulator for collinear singularities much like dimensional regularization in the purely massless case.

In this write-up we take the unifying viewpoint that both approaches are useful and do not have to be considered as alternatives to each other. One can think of the mass as a regulator which is helpful in deriving certain properties of the theory but it can also be thought of as an approximation to the full massive result which is surprisingly good in many physical applications.

The prominent role these logarithmic terms play in physical applications has been acknowledged long ago, and has been formalized in the so-called Perturbative Fragmentation Function approach [248] now known through two-loops [249, 250]; for a recent review see [251]. The idea behind this formalism is the fact that up to power corrections in the mass, a differential with respect to some kinematical parameter z cross-section for the production of a massive parton h, can be written as:

$$\frac{d\sigma_h}{dz}(z, Q, m) = \sum_a \frac{d\hat{\sigma}_a}{dz}(z, Q) \otimes D_{a \to h}(z, m) + \mathcal{O}(m) . \tag{127}$$

The function $D_{a \to h}(z, m)$ does not depend on the hard scale Q and is thus a process independent object that can be computed to any fixed order. It has the important property that it contains all the mass dependence within the approximation indicated in Eq. (127). On the other side the partonic cross-section $d\hat{\sigma}_a$ for the production of any parton a is intrinsically massless, i.e. it is obtained from a calculation where $m = 0$ is set from the very beginning. Of course, collinear singularities are still present in a massless calculation but they are regulated dimensionally, i.e. they appear as poles in ϵ, where $d = 4 - 2\epsilon$:

$$\frac{d\sigma_a}{dz}(z, Q, \epsilon) = \sum_b \frac{d\hat{\sigma}_b}{dz}(z, Q) \otimes \Gamma_{ba}(z, \epsilon) . \tag{128}$$

The explicit expression for the collinear counterterm Γ contains arbitrariness; the only condition on it is that it contains all poles in ϵ. It has become a standard practice in recent years to work in the $\overline{\text{MS}}$

scheme where Γ contains only poles. The choice of a subtraction scheme is of course also implicit in the definition of the function D in Eq. (127).

From Eqs. (127), (128) it is quite clear that one can obtain a massive cross-section in the small-mass (or high-energy) limit by performing a purely massless calculation. The calculational simplifications following from this can be enormous, especially at higher orders. The usefulness of such an approach has been appreciated in the past in many applications related to heavy quark production (typically b and c) at special kinematics like large P_T hadroproduction and e^+e^- annihilation at the Z-pole (see [252] for a review). In such kinematical configurations the neglected power corrections can be as low as a few percent effect and are often totally negligible.

A second virtue of Eq. (127), and one that cannot be matched in conventional perturbation theory, is that it allows resummation of large collinear logs $\ln(Q/m)$ to all perturbative orders. This feature is due to the fact that the function D satisfies the DGLAP evolution equation, or in other words one achieves exponentiation of the (remnants of) soft and collinear singularities.

As we will demonstrate in the next section, all these features of massive cross-sections in the small-mass limit can be translated to massive amplitudes in gauge theories where similar properties can be uncovered. Moreover, one can exploit these properties in much the same way; this is illustrated by the physical applications we consider in section 14.3.

14.2 Factorization in massive amplitudes

As was indicated above, in the following we will be concerned with the factorization properties of massive QCD amplitudes in the high-energy limit. Since one of our main objectives is to relate the small-mass limit of an amplitude with its massless limit, we start our discussion with a brief review of the well-known factorization properties of massless amplitudes [253, 254].

The scattering amplitude $\mathcal{M}_p$

$$|\mathcal{M}_p\rangle \equiv \mathcal{M}_p\left(\{k_i\},\{m_i\},\{c_i\},\frac{Q^2}{\mu^2},\alpha_s(\mu^2),\epsilon\right), \tag{129}$$

for a general $2 \to n$ scattering processes of on-shell partons p_i

$$\mathrm{p}: \qquad p_1 + p_2 \quad \to \quad p_3 + \cdots + p_{n+2}. \tag{130}$$

with a set of fixed external momenta $\{k_i\}$, masses $\{m_i\}$ and color quantum numbers $\{c_i\}$, can be written in the massless case $m_i = 0$ as a product of three functions $\mathcal{J}_p^{(m=0)}$, $\mathcal{S}_p^{(m=0)}$ and $\mathcal{H}^{[\mathrm{p}]}$,

$$|\mathcal{M}_p\rangle^{(m=0)} = \mathcal{J}_p^{(m=0)}\left(\frac{Q^2}{\mu^2},\alpha_s(\mu^2),\epsilon\right)\mathcal{S}_p^{(m=0)}\left(\{k_i\},\frac{Q^2}{\mu^2},\alpha_s(\mu^2),\epsilon\right)|\mathcal{H}_p\rangle, \tag{131}$$

The decomposition Eq. (131) can be understood with simple physical arguments. The jet function $\mathcal{J}_p^{(m=0)}$ contains all collinearly sensitive contributions, is color-diagonal and depends only on the external partons. On the other side the soft function $\mathcal{S}_p^{(m=0)}$ contains all soft radiation interferences and is therefore process specific. Finally, the short-distance dynamics of the hard scattering is described by the (infrared finite) hard function $\mathcal{H}_p$. To leading order this function is just proportional to the Born amplitude. More details about the above expressions can be found in the review [255].

As was explained in [254], the decomposition Eq. (131) contains arbitrariness related to subleading soft as well as finite contributions, which can be removed by fixing a prescription. A convenient and natural choice is to identify the jet function with the massless form factor for the flavor corresponding to any particular leg, i.e.:

$$\mathcal{J}_p^{(m=0)} = \prod_{i\in\,\{\text{all legs}\}} \mathcal{J}_{[i]}^{(m=0)} = \prod_{i\in\,\{\text{all legs}\}} \left(\mathcal{F}_{[i]}^{(m=0)}\right)^{\frac{1}{2}}, \tag{132}$$

where $i = q, g$ for quarks and gluons. $\mathcal{J}_{[i]}^{(m=0)}$ is the individual jet function of each external parton. The needed massless jet factors are known through three-loops and the soft functions through two-loops for any $2 \rightarrow n$ scattering process [256].

We are now ready to consider the massive case. Based on our discussion in the previous sections in the small-mass limit one should expect a decomposition of massive amplitudes similar to the one in Eq. (131). Let us be more specific: we know that in the massive case collinear logs do appear but we also know that they should be absorbed in a corresponding jet function. On the other side, up to power corrections, the soft and hard functions in the massive case should be the same as in the massless case since, by construction, they are not sensitive to collinear emissions. With the exception of contributions related to heavy quark loops (to be discussed below) in the presence of a hard scale Q we write for the massive amplitudes (130):

$$|\mathcal{M}_{\mathrm{p}}\rangle^{(m)} = \mathcal{J}_{\mathrm{p}}^{(m)} \left(\frac{Q^2}{\mu^2}, \{m_i\}, \alpha_{\mathrm{s}}(\mu^2), \epsilon \right) \mathcal{S}_{\mathrm{p}}^{(m=0)} \left(\{k_i\}, \frac{Q^2}{\mu^2}, \alpha_{\mathrm{s}}(\mu^2), \epsilon \right) |\mathcal{H}_{\mathrm{p}}\rangle + \mathcal{O}(m). \quad (133)$$

It is very easy to find out what the jet function in the massive case should be. Working in the prescription chosen for the massless case, one can apply the amplitude decomposition to the form factor itself; the latter has no nontrivial soft or hard functions. Therefore, in the massive case the jet function must be nothing but the massive form factor evaluated in the small-mass limit.

Combining Eqs. (131), (133) one gets the following very suggestive relation [257]:

$$\mathcal{M}_{\mathrm{p}}^{(m)} = \prod_{i \in \{\text{all legs}\}} \left(Z_{[i]}^{(m|0)} \right)^{\frac{1}{2}} \times \mathcal{M}_{\mathrm{p}}^{(m=0)} + \mathcal{O}(m, \dots), \quad (134)$$

where,

$$Z_{[i]}^{(m|0)} \left(\frac{m^2}{\mu^2}, \alpha_{\mathrm{s}}, \epsilon \right) = \mathcal{F}_{[i]}^{(m)} \left(\frac{Q^2}{\mu^2}, \frac{m^2}{\mu^2}, \alpha_{\mathrm{s}}, \epsilon \right) \left(\mathcal{F}_{[i]}^{(m=0)} \left(\frac{Q^2}{\mu^2}, \alpha_{\mathrm{s}}, \epsilon \right) \right)^{-1} + \dots, \quad (135)$$

is a universal, process independent factor. It is sensitive to the definition of the mass m as well as the coupling constant (see [257] for details). The process-independence in Eq. (135) is manifest because $Z_{[i]}^{(m|0)}$ is only a function of the process-independent ratio of scales μ^2/m^2. The process-dependent scale Q cancels completely between the massive and the massless form factors.

The last statement, however, requires one important clarification. From the explicit results for the massive and massless form factors one can easily see that starting from two loops the ratio indicated above contains also Q-dependent logarithmic terms originating from diagrams with the heavy parton in loops. It is these terms that we have indicated with dots in Eq. (135). Luckily, these terms are easy to recognize and to separate since in the color decomposition of the amplitudes they are proportional to the number of heavy flavors n_h. For that reason in the definition of Z-factor given originally in Ref. [257] contributions proportional to the number of heavy flavors have been excluded, as indicated by the dots in Eq. (134). A first step in the understanding of the loop contributions and their incorporation into the factorization approach was made in Ref. [258] in the context of Bhabha scattering. We discuss this process as well as other applications in the next section.

Comparing the results of this section with the ones in the previous section, we can clearly see the similarities offered by QCD factorization between small-mass limits of amplitudes and cross-sections. In both cases the small-mass results are proportional to the corresponding massless results. The proportionality factors are process independent and universal. The proportionality is in the sense of usual multiplication for amplitudes and convolution for cross-sections, as usual. Moreover, it was explained in Ref. [257] the so-called Z-factor in Eq. (135) seems in fact to equal the pure virtual contributions to the perturbative fragmentation function D in Eq. (127).

14.3 Applications

The results in the previous section have been cross-checked at the amplitude level with the general-mass predictions for the structure of the ϵ-poles and $\ln(m)$ terms of any one-loop amplitude [247]. Complete agreement was found. We have also checked that for the process $q\bar{q} \to h\bar{h}$ the prediction based on Eq. (134) completely agrees with the results from the one-loop calculation of Ref. [259]. We want to stress that we have compared not only the singular terms but also all terms that are finite in the limits $\epsilon \to 0$ and $m \to 0$. The agreement applies to all color structures of the amplitude as well as for both its real and imaginary parts.

In subsequent work [236, 237] a prediction for the small-mass limit of all two-loop heavy quark production squared amplitudes at hadron colliders has been made, while the terms proportional to n_h were obtained from a direct calculation. We will not go into details here (they can be found for example in the recent review [255]) but will only summarize the main features of the result: several of the color structures were calculated both directly as well as predicted and we observed full agreement between the two approaches. Therefore, this is a first two-loop check for the factorization approach and represents a direct confirmation of its validity.

Another obvious application where the small-mass limit plays important role is Bhabha scattering. The knowledge of the two-loop QED massive amplitudes in the small-mass limit there is needed for achieving the intended precision of the luminosity measurement; see for example [260]. Complete results for the photonic corrections to large-angle Bhabha scattering were first obtained by Penin [261] and later confirmed in Ref. [258] in the approach discussed in the previous section. Therefore, this is yet another example of its usefulness and power.

14.4 Conclusions

We have presented a newly developed relation between massive and massless QCD amplitudes. We have emphasized its relevance for physical applications and its ability to seamlessly produce results for processes that cannot be calculated currently by direct means.

The relation was introduced based on the idea for massless limit of a massive amplitude and was given in parallel to the much better known relation between massive and massless differential cross-sections.

The new relation between massive and massless amplitudes represents the proper generalization of the naive textbook replacement relation $1/\epsilon \to \ln(m) + \ldots$ to all perturbative orders and for any process. Moreover, with the obvious identification of the color factors, the relation is applicable to any $SU(N)$ gauge theory, QCD being a prominent example. QCD and QED applications like heavy quark production at hadron colliders at two loops and two-loop corrections to Bhabha scattering were briefly discussed.

15. NNLO PREDICTIONS FOR HADRONIC EVENT SHAPES IN e^+e^- ANNIHILATIONS[27]

15.1 Introduction

For more than a decade experiments at LEP (CERN) and SLC (SLAC) gathered a wealth of high precision high energy hadronic data from electron-positron annihilation at a range of centre-of-mass energies [262–278]. This data provides one of the cleanest ways of probing our quantitative understanding of QCD. This is particularly so because the strong interactions occur only in the final state and are not entangled with the parton density functions associated with beams of hadrons. As the understanding of the strong interaction, and the capability of making more precise theoretical predictions, develops, more and more stringent comparisons of theory and experiment are possible, leading to improved measurements of fundamental quantities such as the strong coupling constant [252, 279].

---

[27]Contributed by: G. Dissertori, A. Gehrmann–De Ridder, T. Gehrmann, E.W.N. Glover, G. Heinrich, H. Stenzel

In addition to measuring multi-jet production rates, more specific information about the topology of the events can be extracted. To this end, many variables have been introduced which characterise the hadronic structure of an event. With the precision data from LEP and SLC, experimental distributions for such event shape variables have been extensively studied and have been compared with theoretical calculations based on next-to-leading order (NLO) parton-level event generator programs [212, 280–285], improved by resumming kinematically-dominant leading and next-to-leading logarithms (NLO+NLL) [286–291] and by the inclusion of non-perturbative models of power-suppressed hadronisation effects [292–295].

Comparing the different sources of error in the extraction of α_s from hadronic data, one finds that the purely experimental error is negligible compared to the theoretical uncertainty. There are two sources of theoretical uncertainty: the theoretical description of the parton-to-hadron transition (hadronisation uncertainty) and the uncertainty stemming from the truncation of the perturbative series at a certain order, as estimated by scale variations (perturbative or scale uncertainty). Although the precise size of the hadronisation uncertainty is debatable and perhaps often underestimated, it is conventional to consider the scale uncertainty as the dominant source of theoretical error on the precise determination of α_s from three-jet observables. This scale uncertainty can be lowered only by including perturbative QCD corrections beyond NLO.

We report here on the computation of NNLO corrections to event shape distributions, and discuss the impact of these corrections on the extraction of α_s from LEP data.

15.2 Event shape variables

In order to characterise hadronic final states in electron-positron annihilation, a variety of event shape variables have been proposed in the literature, for a review see e.g. [291, 296]. These variables can be categorised into different classes, according to the minimal number of final-state particles required for them to be non-vanishing: In the following we shall only consider three particle final states which are thus closely related to three-jet final states.

Among those shape variables, six variables were studied in great detail: the thrust T [297, 298], the normalised heavy jet mass ρ [299], the wide and total jet broadenings B_W and B_T [300], the C-parameter [301, 302] and the transition from three-jet to two-jet final states in the Durham jet algorithm Y_3 [303–307].

The perturbative expansion for the distribution of a generic observable y up to NNLO at $\mathrm{e^+e^-}$ centre-of-mass energy $\sqrt{s}$, for a renormalisation scale μ^2, is given by

$$
\frac{1}{\sigma_{\mathrm{had}}} \frac{\mathrm{d}\sigma}{\mathrm{d}y}(s, \mu^2, y) = \left(\frac{\alpha_s(\mu^2)}{2\pi} \right) \frac{\mathrm{d}\bar{A}}{\mathrm{d}y} + \left(\frac{\alpha_s(\mu^2)}{2\pi} \right)^2 \left(\frac{\mathrm{d}\bar{B}}{\mathrm{d}y} + \frac{\mathrm{d}\bar{A}}{\mathrm{d}y} \beta_0 \log \frac{\mu^2}{s} \right)
$$
$$
+ \left(\frac{\alpha_s(\mu^2)}{2\pi} \right)^3 \left(\frac{\mathrm{d}\bar{C}}{\mathrm{d}y} + 2 \frac{\mathrm{d}\bar{B}}{\mathrm{d}y} \beta_0 \log \frac{\mu^2}{s} \right.
$$
$$
\left. + \frac{\mathrm{d}\bar{A}}{\mathrm{d}y} \left(\beta_0^2 \log^2 \frac{\mu^2}{s} + \beta_1 \log \frac{\mu^2}{s} \right) \right) + \mathcal{O}(\alpha_s^4) . \quad (136)
$$

The dimensionless perturbative coefficients $\bar{A}$, $\bar{B}$ and $\bar{C}$ depend only on the event shape variable y. They are computed by a fixed-order parton-level calculation, which includes final states with three partons at LO, up to four partons at NLO and up to five partons at NNLO. LO and NLO corrections to event shapes have been available already for a long time [212, 280–285].

The calculation of the NNLO corrections is carried out using a newly developed parton-level event generator programme EERAD3 which contains the relevant matrix elements with up to five external partons [139, 160, 308–315]. Besides explicit infrared divergences from the loop integrals, the four-parton and five-parton contributions yield infrared divergent contributions if one or two of the final state

partons become collinear or soft. In order to extract these infrared divergences and combine them with the virtual corrections, the antenna subtraction method [316–318] was extended to NNLO level [319–322] and implemented for $e^+e^- \to 3\,\mathrm{jets}$ and related event-shape variables [323]. The analytical cancellation of all infrared divergences serves as a very strong check on the implementation. EERAD3 yields the perturbative A, B and C coefficients[28] as histograms for all infrared-safe event-shape variables related to three-particle final states at leading order. As a cross check, the A and B coefficients have also been obtained from an independent integration [283–285] of the NLO matrix elements [212], showing excellent agreement.

For small values of the event shape variable y, the fixed-order expansion, eq. (136), fails to converge, because the fixed-order coefficients are enhanced by powers of $\ln(1/y)$. In order to obtain reliable predictions in the region of $y \ll 1$ it is necessary to resum entire sets of logarithmic terms at all orders in α_s. A detailed description of the predictions at next-to-leading-logarithmic approximation (NLLA) can be found in Ref. [325].

15.3 Generic features of the NNLO corrections

The precise size and shape of the NNLO corrections depend on the observable in question. Common to all observables is the divergent behaviour of the fixed-order prediction in the two-jet limit, where soft-gluon effects at all orders become important, and where resummation is needed. For several event shape variables (especially T and C) the full kinematical range is not yet covered for three partons, but attained only in the multi-jet limit. In this case, the fixed-order description is also not applicable since it is limited to a fixed multiplicity (five partons at NNLO). Consequently, the fixed-order description is expected to be reliable in a restricted interval bounded by the two-jet limit on one side and the multi-jet limit on the other side.

In this intermediate region, we observe that inclusion of NNLO corrections (evaluated at the Z-boson mass, and for a fixed value of the strong coupling constant) typically increases the previously available NLO prediction. The magnitude of this increase differs considerably between different observables [324, 326], it is substantial for T (18%), B_T (17%) and C (15%), moderate for ρ and B_W (both 10%) and small for Y_3 (6%). For all shape variables, we observe that the renormalisation scale uncertainty of the NNLO prediction is reduced by a factor of two or more compared to the NLO prediction. Inclusion of the NNLO corrections also modifies the shape of the event shape distributions. We observe that the NNLO prediction describes the shape of the measured event shape distributions over a wider kinematical range than the NLO prediction, both towards the two-jet and the multi-jet limit. To illustrate the impact of the NNLO corrections, we compare the fixed-order predictions for Y_3 to LEP2-data obtained by the ALPEH experiment in Figure 29, which illustrates especially the improvement when approaching the two-jet region, corresponding to large $-\ln(Y_3)$.

15.4 Determination of the strong coupling constant

Event shape data from LEP and LEP2 were used in the past for a precise determination of the strong coupling constant α_s. These studies were based on the previously available NLO results, improved by NLLA resummation; the resulting error on α_s was completely dominated by the renormalisation scale uncertainty inherent to the NLO calculation. Using the newly computed NNLO corrections to event shape variables, we performed a new extraction of α_s from data on the standard set of six event shape variables, measured by the ALEPH collaboration [263] at centre-of-mass energies of 91.2, 133, 161, 172, 183, 189, 200 and 206 GeV. The event-shape distributions were obtained using the reconstructed momenta and energies of charged and neutral particles. The measurements have been corrected for detector effects, ie., the final distributions correspond to a so-called particle (or hadron) level (stable hadrons and leptons after hadronisation).

---

[28]A, B and C differ from $\bar{A}$, $\bar{B}$ and $\bar{C}$ in their normalisation to σ_0 instead of σ_{had} [324].
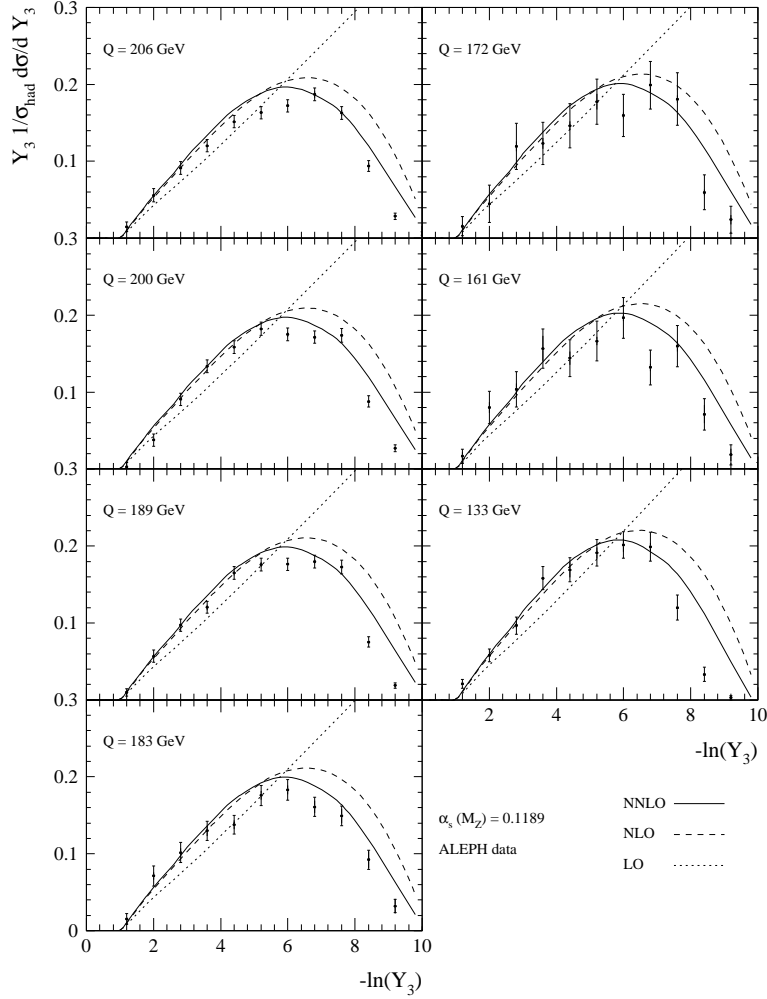
Fig. 29: Perturbative fixed-order predictions for the Y_3-distribution.

The coupling constant α_s is determined from a fit of the perturbative QCD predictions to measured event-shape distributions. The procedure adopted here follows closely the one described in Ref. [263]. Event-shape distributions are fitted in a central region of the three-jet production, where a good perturbative description is available. The fit range is placed inside the region where hadronisation and detector corrections are below 25% and the signal-to-background ratio at LEP2 is above one. At the higher LEP2 energies the good perturbative description extends further into the two-jet region, while in the four-jet region the background becomes large. Thus the fit range is selected as a result of an iterative procedure balancing theoretical, experimental and statistical uncertainties.

Here we concentrate on fits of NNLO predictions [327] and compare them to pure NLO and matched NLO+NLLA predictions as used in the analysis of Ref. [263]. Results from individual event shapes are displayed in Figure 30. The combination of all NNLO determinations from all shape variables yields

$$\alpha_s(M_Z^2) = 0.1240 \, \pm \, 0.0008\,(\text{stat}) \, \pm \, 0.0010\,(\text{exp}) \, \pm \, 0.0011\,(\text{had}) \, \pm \, 0.0029\,(\text{theo}), \quad (137)$$

which is indicated by the error band on Figure 30. We observe a clear improvement in the fit quality when going to NNLO accuracy. Compared to NLO the value of α_s is lowered by about 10%, but still higher than for NLO+NLLA [263], which shows the obvious need for a matching of NNLO+NLLA for a fully reliable result. The scatter among the α_s-values extracted from different shape variables is
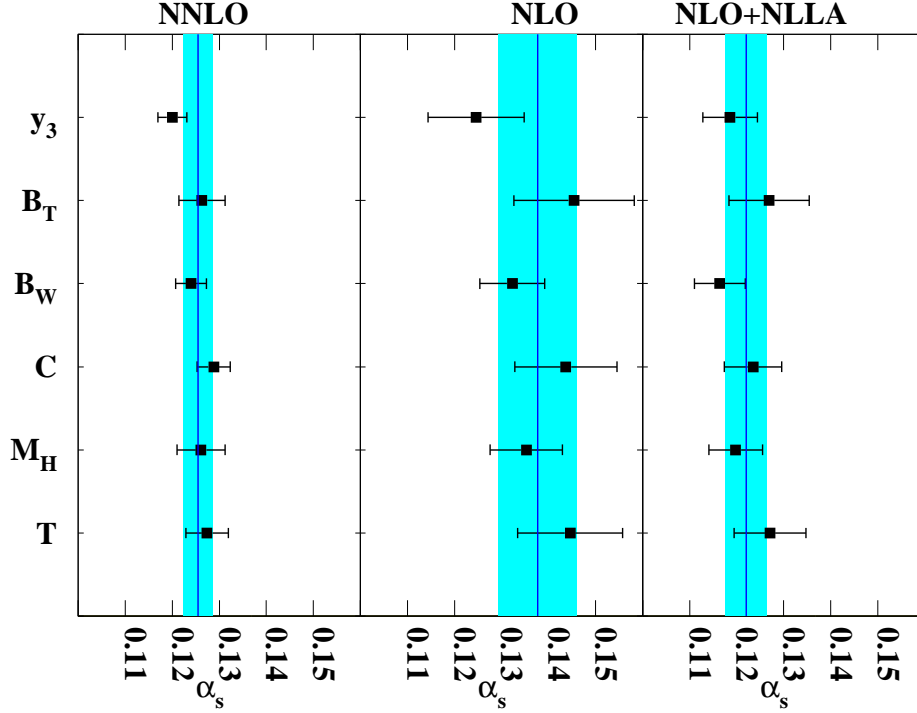
Fig. 30: The measurements of the strong coupling constant α_s for the six event shapes, at $\sqrt{s} = M_{\mathrm{Z}}$, when using QCD predictions at different approximations in perturbation theory.

lowered considerably, and the theoretical uncertainty is decreased by a factor 2 (1.3) compared to NLO (NLO+NLLA).

These observations visibly illustrate the improvements gained from the inclusion of the NNLO corrections, and highlight the need for further studies on the matching of NNLO+NLLA, and on the derivation of NNLLA resummation terms.

Acknowledgements

Part IV

PARTON SHOWERS

16. DEVELOPMENTS IN LEADING ORDER PARTON SHOWERS[29]

At the Les Houches workshop, there was lively discussion of parton showers as represented in Monte Carlo event generators. One of the main current issues in this field is the problem of matrix-element

---

[29]Contributed by: D.E. Soper, P.Z. Skands

/ parton-shower matching, and the workshop saw several reports on ways of (re-)formulating parton showers that could make this problem easier to deal with, a trend one might denote with a fancy word as "designer showers". In this section, we review the part of that discussion that relates to how a leading order parton shower can be organized. Despite the apparent differences, all the new approaches can be discussed at a common footing if we adopt a little bit of notation (adapted from [328]).

A typical parton shower algorithm for hadron-hadron collisions works with states with two initial state partons, a and b, and some number m of final state partons that we can label with integers $1, 2, \ldots, m$. The momenta of these partons can then be specified by giving $\{p\}_m = \{p_a, p_b, p_1, \ldots, p_m\}$. Each parton also carries a flavor $f \in \{g, u, \bar{u}, d, \bar{d}, \ldots\}$, so that the momenta and flavors can be specified with $\{p, f\}_m$. Typically, we also keep track of color connections (the labels of one or two partons to which parton i is connected in the leading-color limit). We may therefore denote the complete set of $m + 2$ partons by $\{p, f, c\}_m$, where c denotes the color connections.

We can now consider the states $\big|\{p, f, c\}_m\big)$ to form a basis for a vector space in the sense of statistical mechanics. After some amount of shower evolution starting from a basis state $\big|\{p, f, c\}_2\big)$ with two final state partons, one reaches a state $\big|\rho\big)$ that is a linear combination of basis states, so that $\big(\{p, f, c\}_m\big|\rho\big)$ represents the probability, in the shower model, for the state $\big|\rho\big)$ to consist of $m + 2$ partons with momenta, flavors, and colors $\{p, f, c\}_m$.

As the state develops, partons split. The evolution of the state is tracked with a shower "time" t which can be interpreted as (the logarithm of) a typical time for a quantum process such as a parton splitting. In most of the current algorithms, the shower time is the logarithm of the virtuality or transverse momentum in a splitting. (In HERWIG, the shower time represents the energy of the mother parton times the square of the splitting angle. In order to cast HERWIG into the form presented here, one also needs a cut on virtuality such that splittings with too small virtuality are not allowed. In other parton shower algorithms, there is also a smallest virtuality allowed, but that can be obtained by simply stopping the shower evolution at some point.)

The evolution starts with the hard process and works forward in physical time for final state evolution and backwards in physical time for the evolution of the initial state. Thus we take the shower time for a splitting $\{p, f, c\}_m \to \{\hat{p}, \hat{f}, \hat{c}\}_{m+1}$ to be $t = t(\{\hat{p}, \hat{f}, \hat{c}\}_{m+1})$ where, for instance if i and j are the daughter partons and Q represents the virtuality scale for the hard process that starts the shower,

$$t(\{\hat{p}, \hat{f}, \hat{c}\}_{m+1}) = \log\left(\frac{Q^2}{(\hat{p}_i + \hat{p}_j)^2}\right) \quad . \tag{138}$$

It can, and should, be debated whether there is a preferred choice for the shower evolution variable and, if so, what it is.

Using this notation, we can represent what a typical parton shower Monte Carlo does. This representation is an approximation to what real computer codes do. We assume that each stage of evolution is independent of what happened at previous stages, depending instead only on the shower time t and the partonic state at that stage. This is not the case if, for instance, we do not exactly conserve four-momentum at each stage and then adjust the parton four-momenta at the end.

If we start with a particular basis state $\big|\{p, f, c\}_m\big)$ at shower time t_0, then at a later time t' we get a state related to $\big|\{p, f, c\}_m\big)$ by an evolution operator $\mathcal{U}(t', t_0)$. In the notation of conventional parton showers, based on collinear DGLAP splitting kernels, the form of the evolution operator would be

$$\mathcal{U}(t', t_0)\big|\{p, f, c\}_m\big) = \Delta(t', t_0; \{p, f, c\}_m)\big|\{p, f, c\}_m\big)$$
$$+ \sum_{i,j,k} \int_{t_0}^{t'} dt_1 \, \Delta(t_1, t_0; \{p, f, c\}_m) \int_{z_{\min}(t_1)}^{z_{\max}(t_1)} dz \int \frac{d\phi}{2\pi} \frac{\alpha_s}{2\pi} \, P_{i \to jk}(z) \, \mathcal{U}(t', t_1)\big|\{\hat{p}, \hat{f}, \hat{c}\}_{m+1}\big) \quad , \tag{139}$$

where $dt_1 = dQ^2/Q^2$ is the differential of the evolution variable, z is an energy-momentum sharing fraction, $P(z)$ are the DGLAP splitting kernels, and we include an integral over angle that is usually uni-

formly distributed. Once the algorithm picks which parton splits, the flavors, and the splitting variables t, z, ϕ, the new state $\{\hat{p}, \hat{f}, \hat{c}\}_{m+1}$ is known. Reformulating Eq. (139) in the notation outlined above, the second term changes appearance slightly,

$$
\begin{aligned}
\mathcal{U}(t', t_0)\big|\{p, f, c\}_m) = {} & \Delta(t', t_0; \{p, f, c\}_m)\big|\{p, f, c\}_m) \\
& + \int_{t_0}^{t'} dt_1 \, \Delta(t_1, t_0; \{p, f, c\}_m) \\
& \times \int \frac{[d\{\hat{p}, \hat{f}, \hat{c}\}_{m+1}]}{(m+1)!} \left(\{\hat{p}, \hat{f}, \hat{c}\}_{m+1}\big|\mathcal{H}_I(t_1)\big|\{p, f, c\}_m\right) \mathcal{U}(t', t_1) \big|\{\hat{p}, \hat{f}, \hat{c}\}_{m+1}) \quad .
\end{aligned}
$$
(140)

In either notation, the second term represents that at a shower time $t_1 > t_0$, the first splitting occurs. This splitting time is determined on a probabilistic basis, so t_1 is integrated over. The probability to get a particular state $\{\hat{p}, \hat{f}, \hat{c}\}_{m+1}$ is given by

$$
\left(\{\hat{p}, \hat{f}, \hat{c}\}_{m+1}\big|\mathcal{H}_I(t_1)\big|\{p, f, c\}_m\right) \quad ,
$$
(141)

where $\mathcal{H}_I$ is the splitting operator, analogous to the interaction hamiltonian in quantum mechanics. There is an integration over the possible outcomes $\{\hat{p}, \hat{f}, \hat{c}\}_{m+1}$. The requirement that the splitting at shower time t_1 be the first after t_0 means that we must include the probability that there is no earlier splitting. This "no-branching" probability is given by a function (the Sudakov form factor)

$$
\Delta(t_1, t_0; \{p, f, c\}_m) \quad .
$$
(142)

In a lowest order shower, this function is fixed so that the probability not to split in shower time interval dt_1 is 1 minus the probability to split,

$$
\begin{aligned}
\Delta(t_1, t_0; \{p, f, c\}_m) = {} & \\
& \exp\left(-\int_{t_0}^{t_1} d\tau \, \frac{1}{(m+1)!} \int [d\{\hat{p}, \hat{f}, \hat{c}\}_{m+1}] \left(\{\hat{p}, \hat{f}, \hat{c}\}_{m+1}\big|\mathcal{H}_I(\tau)\big|\{p, f, c\}_m\right)\right) \quad .
\end{aligned}
$$
(143)

The last ingredient in line two of Eq. (140) is the evolution operator $\mathcal{U}(t', t_1)$. This says that further splittings can happen, in the same way, once the first splitting has occurred. It can also happen that there is *no* splitting generated between shower times t_0 and t_1. This is represented in the first term of Eq. (140).

Evidently, the main content of a parton shower resides in the generator $\mathcal{H}_I(t)$ of the evolution. This has two main parts: a splitting function and a momentum mapping.

Consider first the splitting functions, functions of the daughter parton momenta that give the probability to split. If a parton splits into two nearly collinear partons, then the splitting function must match the probability given by Feynman graphs in the collinear limit. For the moment, we discuss a spin averaged, leading color shower. Then the splitting function matches the result from Feynman graphs averaged over the mother parton spin and summed over the daughter spins in the approximation of neglecting contributions that are suppressed by $1/N_c^2$, where N_c is the number of colors. When the emitted parton is a soft gluon, the splitting function should match the probability given by Feynman graphs in the limit $p_{m+1} \to 0$. Away from the soft and collinear limits, however, one can choose what functional form to use and one can debate the merits of different choices.

This can be illustrated by the case of VINCIA [329], which represents a new development and is discussed in more detail later in this section. In a leading order shower in the leading color limit, the fundamental object that emits gluons is a color dipole, that is, two partons, say l and k, that are color-connected (i.e., adjoining on a color string). The basic idea here goes back to the Lund dipole [330], implemented in ARIADNE [331]. (We shall henceforth refer to such showers as *dipole-antenna* showers,

in order to disambiguate them from what we shall call *partitioned-dipole* showers below.) The relevant Feynman graphs in the amplitude are those in which the gluon $m+1$ is emitted from parton l and those in which it is emitted from parton k. In the squared amplitude, one has a contribution l-l, corresponding to the square of the graph for emission from l, a similar contribution k-k, and two interference contributions l-k and k-l. The approximation of keeping only the leading color contribution restricts us to the case that l and k are color-connected. In dipole-antenna showers, each dipole is treated as a unit, an antenna that radiates gluons, and the splitting functions can be chosen such as to match the perturbative result in all the relevant limits, i.e. gluon $m+1$ collinear to l, collinear to k, or soft. There are two main differences between VINCIA and ARIADNE (and also a recent SHERPA implementation [332]). The first is that an explicit possibility to vary the shower ambiguities away from the singular regions is retained in VINCIA, and the second is that it combines the original dipole shower with the antenna subtraction formalism of Refs. [316, 318, 319] to match to fixed-order matrix elements.

Another new development is what we can call the *partitioned-dipole* shower [333, 334], which is discussed in more detail later in this section. Here one partitions the splitting function into two parts. One part contains the singularity corresponding to parton $m+1$ being collinear with parton l and part of the soft singularity. The other part contains the singularity corresponding to parton $m+1$ being collinear with parton k, along with the remaining part of the soft singularity. Away from these singularities, one has a choice. A sensible choice (as suggested in Ref. [335]) is to take the splitting functions to be precisely those defined by the Catani-Seymour dipole subtraction scheme [175] that is widely used for next-to-leading order perturbative calculations. This has the advantage that it should be fairly straightforward to match these NLO calculations to a Catani-Seymour dipole shower. It has the disadvantage that the splitting of the emission probability from a dipole antenna into two parts is perhaps a bit artificial. There is more than one way to accomplish this splitting.

The second part of the generator $\mathcal{H}_{\mathrm{I}}(t)$ of shower evolution is the specification of the momentum mapping. In Eq. (140), there is a nominal integration over the momenta of all the partons after the splitting. However the matrix element of $\mathcal{H}_{\mathrm{I}}(t)$ contains delta functions that, for given starting momenta $\{p\}_m$, restrict the new momenta $\{\hat{p}\}_{m+1}$ to lie on a three dimensional surface. This surface could be parametrized by splitting variables t, z, ϕ, as in Eq. (139). In the case of the timelike dipole-antenna showers in ARIADNE, VINCIA, and SHERPA, the momenta of all of the partons not part of the dipole remain the same before and after the parton emission. For the partons l and k that form the dipole, the momenta p_l and p_k plus three splitting variables are mapped reversibly to the momenta of three daughter partons, $\hat{p}_l$, $\hat{p}_k$, and $\hat{p}_{m+1}$ after the splitting, with all of the parton momenta being on-shell. This mapping is symmetric under label interchange $l \leftrightarrow k$. In the special case that $\hat{p}_{m+1}$ is collinear with $\hat{p}_l$, we have $p_l = \hat{p}_l + \hat{p}_{m+1}$ and $p_k = \hat{p}_k$. Similarly, if $\hat{p}_{m+1}$ is collinear with $\hat{p}_k$, we have $p_k = \hat{p}_k + \hat{p}_{m+1}$ and $p_l = \hat{p}_l$. In the soft limit, $\hat{p}_{m+1} = 0$, we have $p_l = \hat{p}_l$ and $p_k = \hat{p}_k$. Away from these limits, the mapping is necessarily not so trivial, leading to a further non-singular ambiguity which VINCIA attempts to explore. For the partioned-dipole shower, there is a similar but simpler mapping, this time not symmetric under $l \leftrightarrow k$. The splitting function that includes the singularity for $\hat{p}_{m+1}$ collinear with p_l, comes with a momentum mapping for which $p_l = \hat{p}_l + \hat{p}_{m+1}$ and $p_k = \hat{p}_k$ when $\hat{p}_{m+1}$ is collinear with $\hat{p}_l$ or soft. Away from these limits, the mapping takes some momentum from parton k in order to keep momentum conserved and all partons on shell. The choice here is to use the same momentum mapping as was defined by Catani and Seymour for the subtractions in next-to-leading order calculations. In the case of splittings involving an initial state splitting (spacelike showers), the momentum mappings are a little more complicated than sketched here. We should mention that it is also possible to take the momentum needed to keep all partons on-shell from *all* of the final state partons in what might be called a democratic way [328].

We hope that this comparative discussion may be useful as a guide to the more detailed presentations later in this section. We may also mention the published work [328] that was discussed at Les Houches but is not separately presented in this document. The idea here is to extend the idea of a lead-

ing order parton shower so that one does *not* average over spins or take just the leading color limit. In this case, there is an evolution equation similar to Eq. (140) but with spin indices and a more detailed specification of the color state. The solution of the evolution equation yields integrals that could, in principle, be computed numerically. However, an algorithm that is likely to be usefully convergent with finite computer resources is still under development [336].

17. TIME-LIKE SHOWERS BASED ON DIPOLE-ANTENNA RADIATION FUNCTIONS [30]

17.1 Introduction

In this report we take the next step in the development of the VINCIA shower towards a full-fledged parton shower, embedded into the PYTHIA 8 generator [329, 337]. Previously, we included only the gluonic time-like shower [329]. By including massless quarks we can start making comparisons at LEP energies and make quantitative studies for future linear colliders. As the VINCIA shower is a dipole-antenna shower, we can make direct comparisons with the dipole-antenna functions used in ARIADNE [331].

We also make a phenomenological comparison with the PYTHIA 8 shower. For this purpose, we choose the evolution variable, the hadronization boundary and other parameters in VINCIA as close as possible to the default PYTHIA 8 settings. In this emulation mode we compare a few representative distributions, both infrared safe and infrared regulated observables, such as jet rates, thrust, and parton multiplicities for hadronic Z decays at $\sqrt{s} = m_Z$.

17.2 Dipole-antenna functions

The most general form for a leading-log antenna function for massless parton splitting, $\hat{a}\hat{b} \rightarrow arb$, can be represented by a double Laurent series in the two branching invariants,

$$a(y_{ar}, y_{rb}; s) = \frac{1}{s} \sum_{\alpha,\beta=-1}^{\infty} C_{\alpha,\beta}\, y_{ar}^{\alpha}\, y_{rb}^{\beta}\,, \tag{144}$$

where

$$s = s_{\hat{a}\hat{b}} = s_{arb} \quad \text{and} \quad y_{ij} = \frac{s_{ij}}{s} \leq 1 \tag{145}$$

are the invariant mass squared of the antenna and the scaled branching invariants, respectively. In principle, eq. (144) could also be multiplied by an overall phase space veto function, restricting the radiation to specific "sectors" of phase space, but we shall here use so-called "global" antenna functions which are summed together without such cuts. Note that we have here written the antenna function stripped of color factors, to emphasize that this part of the discussion is not limited to the leading-color limit.

The coefficient of the most singular term, $C_{-1,-1}$, controls the strength of the double (soft) singularity (the "double log" term) and the coefficients $C_{-1,j\geq0}$ and $C_{i\geq0,-1}$ govern the single (collinear) singularities ("single log" terms). These, in parton shower terminology collectively labeled "leading log" terms, are universal, whereas the polynomial coefficients $C_{i\geq0,j\geq0}$ are arbitrary, corresponding to beyond-leading-log ambiguities in the shower or, equivalently, different NLO subtraction terms in the fixed-order expansion.

We take the Gehrmann-de-Ridder-Glover ("GGG") antenna functions [319] as our starting point. The corresponding coefficients $C_{\alpha,\beta}$ for the the five antennae that occur in massless QCD at LL are collected in tab. 11. For reference, we also compare to the radiation functions [330, 338, 339] used in the ARIADNE dipole shower [331], which are also the ones used in a recent study by the SHERPA group [332]. Note that the single log terms have a slight ambiguity when gluons are involved, arising from the arbitrary choice of how to decompose the radiation off the gluon into the two antennae it participates in. Nominally, the ARIADNE single log coefficients therefore look different from the GGG

---

[30]Contributed by: R. Frederix, W.T. Giele, D.A. Kosower, P.Z. Skands

	$C_{-1,-1}$	$C_{-1,0}$	$C_{0,-1}$	$C_{-1,1}$	$C_{1,-1}$	$C_{-1,2}$	$C_{2,-1}$	$C_{0,0}$	$C_{1,0}$	$C_{0,1}$
GGG										
$q\bar{q} \to qg\bar{q}$	2	-2	-2	1	1	0	0	0	0	0
$qg \to qgg$	2	-2	-2	1	1	0	-1	$\frac{5}{2}$	-1	$\frac{3}{2}$
$gg \to ggg$	2	-2	-2	1	1	-1	-1	$\frac{8}{3}$	-1	-1
$qg \to q\bar{q}'q'$	0	0	$\frac{1}{2}$	0	-1	0	1	$-\frac{1}{2}$	1	0
$gg \to g\bar{q}q$	0	0	$\frac{1}{2}$	0	-1	0	1	-1	1	$\frac{1}{2}$
ARIADNE										
$q\bar{q} \to qg\bar{q}$	2	-2	-2	1	1	0	0	0	0	0
$qg \to qgg$	2	-2	-3	1	3	0	-1	0	0	0
$gg \to ggg$	2	-3	-3	3	3	-1	-1	0	0	0
$qg \to q\bar{q}'q'$	0	0	$\frac{1}{2}$	0	-1	0	1	-1	1	$\frac{1}{2}$
$gg \to g\bar{q}q$	0	0	$\frac{1}{2}$	0	-1	0	1	-1	1	$\frac{1}{2}$
ARIADNE2 (re-parameterization of ARIADNE functions à la GGG, for comparison)										
$q\bar{q} \to qg\bar{q}$	2	-2	-2	1	1	0	0	0	0	0
$qg \to qgg$	2	-2	-2	1	1	0	-1	-1	0	0
$gg \to ggg$	2	-2	-2	1	1	-1	-1	$-\frac{4}{3}$	-1	-1

Table 11: Laurent coefficients for massless LL QCD antennae ($\hat{a}\hat{b} \to arb$). The coefficients with at least one negative index are universal (apart from a re-parameterization ambiguity for gluons). For "GGG" (the defaults in VINCIA), the finite terms correspond to the specific matrix elements considered in [319]. In particular, the $q\bar{q}$ antenna absorbs the tree-level $Z \to qg\bar{q}$ matrix element [320] and the gg antennae absorb the tree-level $h^0 \to gg \to ggg$ and $h^0 \to gg \to g\bar{q}q$ matrix elements [322]. The qg antennae are derived from a neutralino decay process [321].

ones. However, a re-parameterization of the total gluon radiation, which we label ARIADNE2, reveals that the only real difference lies in the choice of finite terms. Interestingly, while all the ARIADNE radiation functions are positive definite, the equivalent ARIADNE2 one for $gg \to ggg$ is not and hence could not be used as a basis for a shower Monte Carlo.

In modern versions of ARIADNE, gluon splitting to quarks has an additional pre-factor $2/(1 + s_{\hat{a}\hat{b}}/s_{\hat{b}\hat{c}})$, where $\hat{c}$ is the neighbor on the other side of the splitting gluon. This is based on comparisons to $e^+e^- \to q\bar{q}'q'\bar{q}$ matrix elements and implies that the smaller dipole takes the larger part of the $g \to q\bar{q}$ branching. Such effects are not included in VINCIA at this point.

Our convention for color factors is that they count color degrees of freedom. Their normalization should therefore be such that, in the large-N_C limit, they tend to N_C raised to the power of the number of new color lines created in the splitting. In particular,

$$
\begin{aligned}
\hat{C}_F &= \frac{N_C^2-1}{N_C} &= \frac{8}{3}, \\
C_A &= N_C &= 3.
\end{aligned}
\tag{146}
$$

For gluon splitting to quarks, the antenna shower explicitly sums over each flavor separately, hence the relevant antenna functions should be normalized to one flavor, $\hat{T}_R = 1$. (We use the hatted symbols $\hat{C}_F$ and $\hat{T}_R$ to distinguish this normalization from the conventional parton-shower one in which $C_F = 4/3$ and $T_R = 1/2$.)

The complete antenna functions, in the notation of [329, eqs. (2) and (11)], are then

$$
\begin{aligned}
A(q\bar{q} \to qg\bar{q}) &= 4\pi\alpha_s\, \hat{C}_F\, a(q\bar{q} \to qg\bar{q}), \\
A(qg \to qgg) &= 4\pi\alpha_s\, \hat{C}_F\, a(qg \to qgg), \\
A(gg \to ggg) &= 4\pi\alpha_s\, N_C\, a(gg \to ggg), \\
A(qg \to q\bar{q}'q') &= 4\pi\alpha_s\, a(qg \to q\bar{q}'q'), \\
A(gg \to g\bar{q}q) &= 4\pi\alpha_s\, a(gg \to g\bar{q}q),
\end{aligned}
\tag{147}
$$

where $\alpha_s = \alpha_s(\mu_R)$ may depend on the branching kinematics. If so, we use a nominal $\hat{\alpha}_s = 1$ for generating trial branchings, which are then accepted with probability $\alpha_s(\mu_R)$ at the point when the full kinematics have been constructed (see below). The possibilities for μ_R currently implemented in VINCIA are

$$
\mu_R = \begin{cases} \text{type 0} & : & K_R\,2p_\perp \\ \text{type 1} & : & K_R\,Q_E \\ \text{type 2} & : & K_R\,\sqrt{s_{\hat{a}\hat{b}}}\,, \end{cases}
\tag{148}
$$

where K_R is an arbitrary constant, $p_\perp$ is defined as in ARIADNE with $p_\perp^2 = s_{ar}s_{rb}/s_{\hat{a}\hat{b}}$ [331], Q_E is the evolution variable, and $\sqrt{s_{\hat{a}\hat{b}}}$ is the invariant mass of the mother dipole-antenna. The default is a 1-loop running five-flavor α_s with $\mu_R = p_\perp$ (i.e., Type 0 above, with $K_R = \frac{1}{2}$) and $\alpha_s(m_Z) = 0.137$ (the default in PYTHIA 8, making comparisons simpler). Alternatively, both fixed and 2-loop running options are available as well [337]. For the pure shower, the dependence on the renormalization scheme of α_s is beyond the required precision and hence we do not insist on an $\overline{\text{MS}}$ definition here. Indeed, the default value of $\alpha_s(m_Z)$ in PYTHIA 8 is determined from tuning to LEP event shapes. Though beyond the scope of the present paper, we note that in the context of higher-order matching, one should settle on a specific scheme, and should then see the dependence on both the scheme and scale choices start to cancel as successive orders are included.

17.3 Shower implementation

Brief descriptions of the VINCIA switches and parameters are contained in the program's XML "manual", by default called `Vincia.xml`, which is included together with the code. This file also contains the default values and ranges for all adjustable parameters, which may subsequently be changed by the user in exactly the same way as for a standard PYTHIA 8 run [337].

The default antenna functions are contained in a separate XML file, `Antennae-GGG.xml`. Antennae that are related by charge conjugation to the ones listed tab. 11 are obtained by simple swapping of invariants (e.g., $g\bar{q}$ antennae are obtained from the qg ones). Similarly, antenna functions that are permutations of the ones in tab. 11, such as $gg \to \bar{q}qg$, are obtained by swapping. In view of the probabilistic nature of the shower, all antenna functions are checked for positivity during initialization. If negative regions are found, the constant term $C_{0,0}$ is increased to offset the difference and a warning is given, stating the new value of $C_{0,0}$.

We use the PYTHIA 8 event record [337], which includes Les Houches color tags [340, 341] for representing color connections. At every point during the event evolution, leading-color antennae are spanned between all pairs of (non-decayed) partons for which the color tag of one matches the anti-color tag of the other.

Shower generation proceeds largely as for the pure-gluon case described in [329], including the choice between two evolution variables

$$
y_E = \begin{cases} \text{type I ($p_\perp$-ordering)} & : & y_I^2 & = & \dfrac{Q_I^2}{s} & = & 4\dfrac{s_{ar}s_{rb}}{s^2} = 4y_{ar}y_{rb} \\[2ex] \text{type II (dipole-mass-ordering)} & : & y_{II}^2 & = & \dfrac{Q_{II}^2}{s} & = & 2\min(y_{ar}, y_{rb}) \end{cases}
\tag{149}
$$

Note that we do not include an "angular-ordering" option. In conventional parton showers, which use collinear splitting functions, angular ordering gives a good approximation of the coherent dipole radiation patterns we here describe by the antenna functions A. Since dipole-antenna showers use A directly, coherence is thus independent of the choice of evolution variable to first order in this formulation (see, e.g., [330]).

For the phase space map an optimal choice for the functional form of the "recoil angle" $\psi_{\hat{a}a}$ (see [329, 331]) away from the soft and collinear limit exists for $q\bar{q}$ antennae [342]. However, we have

not yet implemented this particular subtlety in the VINCIA code. The default choice for all antennae is thus currently the same as for the $gg \to ggg$ splitting in ARIADNE [331]

$$\psi_{\mathrm{ARIADNE}} = \frac{E_b^2}{E_a^2 + E_b^2}(\pi - \theta_{ab}) , \tag{150}$$

with alternative choices listed in [329].

Trial branchings are generated by numerically solving for y_{trial} in the equation $R = \widehat{\Delta}(y_{\mathrm{trial}})$, where R is a random number uniformly distributed between zero and one, and the trial Sudakov is [329, eq. (51)]

$$\widehat{\Delta}(y_{\mathrm{trial}}) = \exp\left[-\int_{y_{\mathrm{trial}}}^{1}\mathrm{d}y_E \int_0^1 \mathrm{d}y_{ar} \int_0^{1-y_{ar}} \mathrm{d}y_{rb}\, \delta(y_E - y_E(y_{ar}, y_{rb}))\frac{\hat{\mathcal{A}}(y_{ar}, y_{rb})}{16\pi^2} \right], \tag{151}$$

with $\mathcal{A}$ an overestimate of the "true" antenna function such that

$$\hat{\mathcal{A}}(y_{ar}, y_{rb}) \equiv s_{arb}\hat{A}(y_{ar}, y_{rb}; s_{arb}, 1) > s_{arb}A(y_{ar}, y_{rb}; s_{arb}, 1) \tag{152}$$

only depends on the rescaled invariants (for instance by using a fixed overestimate of $\hat{\alpha}_s = 1$ here). Once the full kinematics are known (see below) the trial branching can be vetoed with probability $1 - A/\hat{A}$, which by the veto algorithm changes the resulting distribution back to that of A, as desired.

During program execution, cubic splines of $\widehat{\Delta}$ and $\widehat{\Delta}^{-1}$ are used for the actual trial generation. These splines are constructed on the fly, with the 2-dimensional phase space integrals in eq. (151) carried out either by 2-dimensional adaptive Gaussian quadrature (AGQ) on $\hat{A}$ directly or (substantially faster) by 1-dimensional AGQ on the primitive function along a contour of fixed y_{ar}, defined by

$$
\begin{aligned}
I_a(y_{ar}, y_1, y_2) &= \int_{y_1}^{y_2}\mathrm{d}y_{rb}\, \frac{\hat{\mathcal{A}}(y_{ar}, y_{rb})}{16\pi^2} \\
&= \frac{\hat{\alpha}_s \mathcal{C}_i}{4\pi} \sum_{\alpha=-1}^{\infty} y_{ar}^{\alpha}\left[C_{\alpha,-1}\ln\left(\frac{y_2}{y_1}\right) + \sum_{\beta=0}^{\infty} C_{\alpha,\beta}\frac{y_2^{\beta+1} - y_1^{\beta+1}}{\beta+1} \right] ,
\end{aligned} \tag{153}
$$

where $\hat{\alpha}_s$ is the overestimate of α_s discussed earlier, $\mathcal{C}_i$ represents the color factors appearing in eq. (147), and the phase space limits $y_{1,2}$ depend on the choice of evolution variable, see below. During initialization, the program checks for consistency between the analytic and numeric integrals and a warning is issued if the numerical precision test fails.

The antenna with the largest trial scale is then selected for further inspection. A ϕ angle distributed uniformly in $[0, 2\pi]$ is generated, and a complementary phase space invariant, z, is chosen according to the probability distribution

$$I_z(y_E, z) = \int_{z_{\mathrm{min}}(y_E)}^{z}\mathrm{d}z'\,|J(y_E, z')|\frac{\hat{\mathcal{A}}(y_{ar}, y_{rb})}{16\pi^2} , \tag{154}$$

where $|J(y_E, z)|$ is the Jacobian arising from translating $\{y_{ar}, y_{rb}\}$ to $\{y_E, z\}$ and $z_{\mathrm{min}}(y_E)$ is the smallest value z attains inside the physical phase space for a given y_E. Depending on the type of evolution variable, as defined in eq. (149), we choose $\{y_E, z\}(y_{ar}, y_{rb})$ as

$$
\begin{aligned}
\text{type I} \quad &: \quad y_E = 4y_{ar}y_{rb} , \ z = y_{rb} \\
&\Rightarrow \ |J_{\mathrm{I}}| = 1/(4z) , \ z_{\mathrm{max,min}}(y_E) = \frac{1}{2}(1 \pm \sqrt{1 - y_E}) , \\
\text{type II} \quad &: \quad y_E = 2y_{ar} , \ z = y_{rb} \text{ for } z \leq 1 - \tfrac{1}{2}y_E \\
&\qquad y_E = 2y_{rb} , \ z = y_{ar} + (1 - 2y_{rb}) \text{ for } z > 1 - \tfrac{1}{2}y_E \\
&\Rightarrow \ |J_{\mathrm{II}}| = 1/2 , \ z_{\mathrm{min}}(y_E) = \frac{1}{2}y_E , \ z_{\mathrm{max}}(y_E) = 2 - \frac{3}{2}y_E
\end{aligned}
$$
$$\tag{155}$$
$$\tag{156}$$

where, for type II, we have arranged the two separate branches $y_{ar} < y_{rb}$ and $y_{rb} < y_{ar}$ one after the other by a trivial parallel displacement in the z coordinate. Using the Laurent representation of the antenna functions, the analytical forms of I_z become

$$\text{type I} \quad : \quad \frac{\hat{\alpha}_s \mathcal{C}_i}{16\pi} \sum_{\alpha=-1}^{\infty} \left(\frac{y_R}{4}\right)^\alpha \left[C_{\alpha,\alpha} \ln \frac{z}{z_{\min}(y_E)} + \sum_{\beta \neq \alpha} \frac{z^{\beta-\alpha} - z_{\min}(y_E)^{\beta-\alpha}}{\beta - \alpha} \right] \quad (157)$$

$$\text{type II} \quad : \quad \frac{\hat{\alpha}_s \mathcal{C}_i}{8\pi} \left[I_a \left(\frac{1}{2} y_E, z_{\min}(y_E), \min(z, 1 - z_{\min}(y_E)) \right) \right.$$
$$\left. + I_a^T \left(\frac{1}{2} y_E, 1 - z_{\min}(y_E), \max(z, 1 - z_{\min}(y_E)) \right) \right] , \quad (158)$$

where the I_a is defined in eq. (153) and I_a^T is the primitive along a direction of fixed y_{rb}

$$I_a^T(y_{rb}, y_1, y_2) = \sum_{\beta=-1}^{\infty} y_{rb}^\beta \left[C_{-1,\beta} \ln \left(\frac{y_2}{y_1} \right) + \sum_{\alpha=0}^{\infty} C_{\alpha,\beta} \frac{y_2^{\alpha+1} - y_1^{\alpha+1}}{\alpha + 1} \right] . \quad (159)$$

17.4 Numerical results

We now turn to a quantitative comparison between PYTHIA 8 and VINCIA for $e^+e^- \to Z \to q\bar{q}$ at $\sqrt{s} = m_Z$. We use a 1-loop running α_s with $\alpha_s(m_Z) = 0.137$ (the default in PYTHIA 8), with a 5-flavor running matched to 4 and 3 flavors at the b and c thresholds, but to eliminate the question of explicit quark mass effects we only allow d and u quarks in the Z decay and subsequent shower evolution. The evolution is terminated at $p_{\perp\text{had}} = 0.5\,\text{GeV}$, and we have switched off hadronization so as not to unintentionally obscure the differences between the partonic evolutions. Likewise, photon radiation is switched off in all cases, and in PYTHIA 8 we further switch off gluon polarization effects. For VINCIA, we use three different settings: transverse-momentum ordering with "GGG" antenna functions, dipole-mass ordering with "GGG" antenna functions, and transverse-momentum ordering with the "ARIADNE" antenna functions.

Fig. 31 shows the 3-, 4-, and 5-jet inclusive fractions as functions of the logarithm of Durham k_T, using the default PYTHIA 8 Durham clustering algorithm [337]. In PYTHIA 8, the 3-jet rate (the set of curves furthest to the right) is matched to the tree-level 3-parton matrix element, whereas the GGG and ARIADNE antenna functions in VINCIA reproduce it by construction. The general agreement on the 3-jet rate is therefore a basic validation of the $q\bar{q} \to qg\bar{q}$ antenna implementation. Higher-order effects appear to make the mass-ordered VINCIA slightly softer, which we tentatively conclude is due to this variable favoring soft wide-angle radiation over high-$p_\perp$ collinear radiation (as illustrated by fig. 2 in [329]).

Similarly, the 4-jet fractions (the middle set of curves in fig. 31) test the qg antennae in VINCIA, with the GGG showers here slightly higher and the ARIADNE one slightly lower, in agreement with the differences in qg antenna finite terms, cf. tab. 11. This trend becomes more pronounced in the 5-jet fraction, since also the $gg \to ggg$ function in ARIADNE is softer than GGG.

We may now study further distributions, as a representative example of which we take thrust, illustrated as $1 - T$ in the top row of fig. 32. The full distribution is shown to the left with a closeup of the region $1 - T < 0.1$ to the right. The region $0.1 < 1 - T < \frac{1}{3}$ is dominated by well-separated three-jet configurations. In the tail, $1 - T > \frac{1}{3}$, a matching to $e^+e^- \to 4$ jets would be required to improve the accuracy. In the region below $1 - T = 0.1$, however, this would not help. These are three-jet configurations which are "nearly two-jet". Here, the type and size of the Sudakov suppression is essential, the first fixed order of which could be accessed by 1-loop matching, but since the fixed-order expansion is poorly convergent in this region anyway, the disagreement is more likely to be cured by a systematic inclusion of higher-logarithmic effects in the showers (either implicitly, by "clever choices" of evolution, renormalization, and kinematic variables in the LL shower, or explicitly, by a systematic
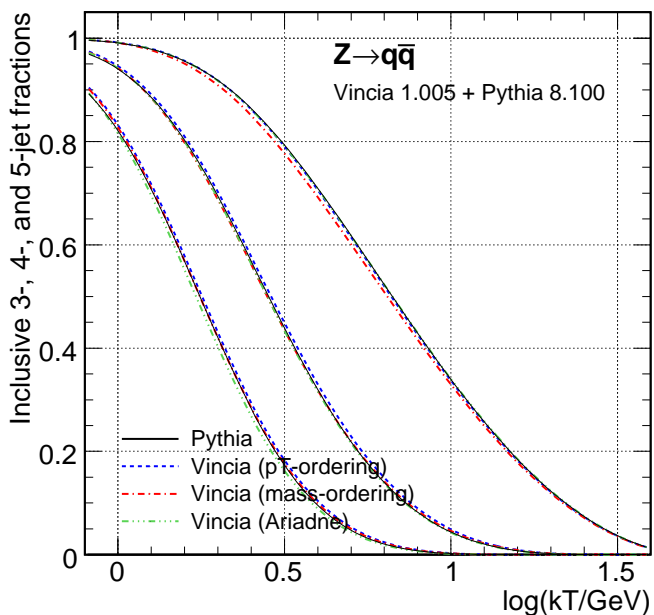
Fig. 31: Inclusive 3-, 4-, and 5-jet fractions.

inclusion of NLL splittings). It should be noted, however, that hadronization and hadron decay effects are important in the region below

$$1 - T \sim 1 - \max(x_k) = \min(y_{ij}) \lesssim \frac{(\text{A few GeV})^2}{m_Z^2} \lesssim 0.01 \,, \tag{160}$$

where the x and y fractions pertain to 3-jet configurations. This complicates the separation of genuine non-trivial higher-log effects from non-perturbative effects when comparing to experimental data at currently accessible collider energies.

Finally, as illustration of an infrared sensitive quantity, in the bottom row of fig. 32 we plot the probability distribution of the number of partons produced at the shower termination for each of the four models. The total number of partons is shown to the left and the number of quarks (not counting anti-quarks) to the right. The definitions of $p_\perp$ in PYTHIA and in VINCIA/ARIADNE, respectively, are not exactly identical, but they have the same infrared limiting behavior [343], and hence a comparison of the number of resolved partons with a cutoff at $p_{\perp\text{had}} = 0.5\,\text{GeV}$ should be meaningful. Since we have also chosen the same α_s values etc., the basic agreement between the models in the lower left-hand plot in fig. 32 reconfirms that there are no large differences between the showers, even at the infrared sensitive level. ARIADNE produces somewhat fewer partons, consistent with the ARIADNE radiation functions being slightly softer. On the right-hand plot, however, it is interesting to note the first substantial difference between PYTHIA 8 and the VINCIA showers. The PYTHIA shower produces significantly fewer quarks than any of the VINCIA showers, despite its being higher or comparable on the total number of partons (cf. the left-hand plot). A similar difference between parton and dipole-antenna showers was observed in an earlier ARIADNE study [339], in which a comparison was made to the virtuality-ordering of traditional parton showers. It is interesting that we here observe the same trend when comparing to the PYTHIA 8 shower which is ordered in $p_\perp$. Finally, we note that this difference will also have practical consequences; in the context of tuning of hadronization models, the VINCIA showers will presumably need a stronger suppression of non-perturbative strangeness production to make up for the larger perturbative production rate, as compared to PYTHIA 8.
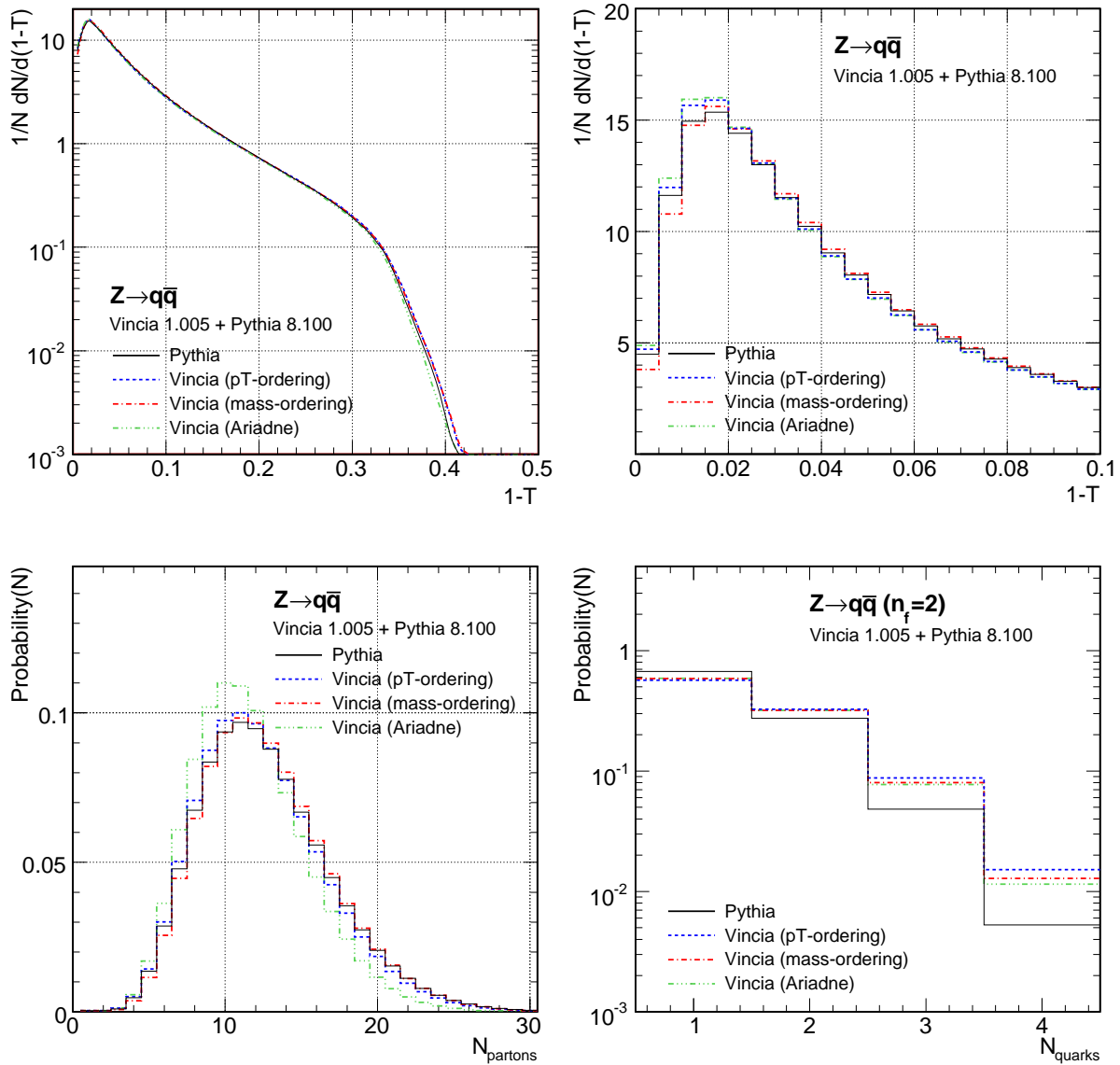
Fig. 32: Top row: Thrust, $1 - T$. Bottom row: Number of partons (left) and number of quarks (right) at shower termination, with 2 massless quark flavors.

17.5 Conclusions

We have presented the inclusion of massless quarks into the VINCIA shower algorithm, implemented as a plug-in to the PYTHIA 8 event generator. The dipole-antenna radiation functions are expressed as double Laurent series in the branching invariants, with user-specifiable coefficients. At the analytical level, we compare the coefficients of the "GGG" antenna functions [319] used by default in VINCIA to the ARIADNE ones [331]. Modulo a re-parameterization of emissions from gluons, we find the double and single log coefficients to be identical, as expected. The finite terms, however, are generally somewhat smaller for the ARIADNE functions. This represents a genuine shower ambiguity which can only be systematically addressed by matching to fixed-order matrix elements.

At the phenomenological level, we have also compared to the hybrid parton-dipole shower in PYTHIA 8 [337] for $e^+e^- \to Z \to q\bar{q}$ at $\sqrt{s} = m_Z$. We find a good overall agreement, even at the level of an infrared sensitive quantity such as the final number of partons. For the number of quarks produced, however, PYTHIA 8 is markedly lower than any of the VINCIA showers we have compared to here.
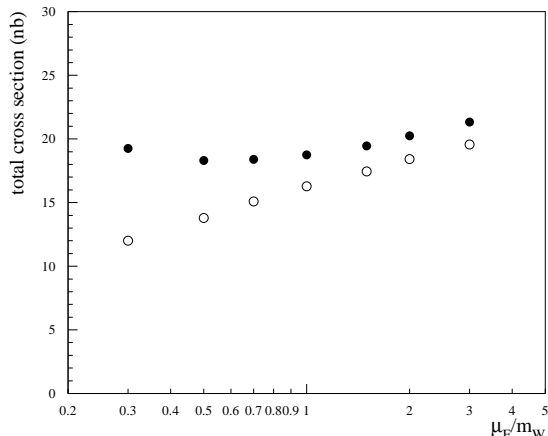
Fig. 33: Factorization-scale (μ_F) dependence of the total cross section for the W-boson production at LHC. An apparent μ_F dependence of the inclusive W ($W + 0$ jet) production cross section (open circles) is greatly reduced when we add the LLL-subtracted $W + 1$ jet production cross section. The summed cross sections are shown with filled circles.

Acknowledgements

18. LLL SUBTRACTION AND PS KINEMATICS[31]

18.1 Introduction

We are developing NLO event generators for hadron collision interactions based on GRACE [344], using the Limited Leading-Log (LLL) subtraction technique [345] for the parton radiation matching. The matching technique is crucial since the contributions of an additional QCD parton radiation in NLO are also involved in the evolution of Parton Distribution Functions (PDFs) in a collinear approximation. A naive application of a PDF to NLO calculations results in an apparent double-counting. We avoid the double-counting by subtracting Leading-Log (LL) collinear contributions from the matrix element (ME) of radiative processes. The subtraction is stopped ("limited") at the factorization scale (μ_F) since PDFs do not involve any radiation harder than this energy scale. The LL contribution of the radiation is easy to calculate [346], though an appropriate care is necessary in the kinematical mapping to non-radiative processes [345]. The subtracted LL terms are formally moved to non-radiative processes and to be cancelled with divergences in virtual corrections.

Figure 33 shows the sum of the total cross sections for inclusive W-boson production and LLL-subtracted $W + 1$ jet production evaluated for the LHC condition (proton-proton collisions at $\sqrt{s} = 14$ TeV). Here, "jet" denotes a gluon or a light quark in the final state. The cross sections are calculated using the tree-level MEs for W production and $W + 1$ jet production, respectively, convoluted with the CTEQ5L PDF [347]. Results are shown as a function of the factorization scale (μ_F). We can see a strong μ_F dependence of the inclusive W production cross section (open circles) is greatly reduced by adding the LLL-subtracted radiative cross section. This shows a good matching between the ME and PDF; *i.e.*, the LL contents in ME and PDF are nearly the same.

---

[31]Contributed by: S. Odaka

The virtual corrections are yet to be included in the results shown in Fig. 33. They can also be evaluated automatically in the framework of GRACE [346]. Divergent terms in these corrections are to be cancelled with those moved from radiative processes. Remaining finite terms will alter the normalization of non-radiative processes, and will result in a substantial mismatch since there is no such correction in radiative processes. However, this mismatch is at the level of NNLO. It will be possible to restore the matching within the accuracy of NLO. The simplest way would be to change the normalization of LL components of the hard radiation remaining in radiative processes by the same amount as applied to non-radiative processes. This is actually a modification at the NNLO (α_s^2) level.

So far we have discussed the matching in the integrated cross section. We have to achieve a good matching in differential cross sections, as well, in order to construct practical event generators. The QCD evolution evaluated in PDFs is simulated by means of a parton shower (PS) in event generators for hadron collisions. PS and PDF are based on the same factorization theory. However, since theoretical arguments are given only at the collinear limit, the theory gives us predictions only at the first-order approximation for the transverse behavior. It is necessary to introduce a model of 3-dimensional kinematics in order to construct a practical PS conserving the energy and momenta. The introduction of a suitable model is crucial for achieving a good matching in differential cross sections. We discuss about such models in the following sections.

18.2   Initial-state PS kinematics

We have constructed an initial-state Leading-Log (LL) PS program for the use in NLO event generation. The program is based on the simplest expression of the LL Sudakov form factor employing Q^2 as the evolving parameter,

$$S(Q_1^2, Q_2^2) = \exp\left[-\int_{Q_1^2}^{Q_2^2} \frac{dQ^2}{Q^2} \int_\epsilon^{1-\epsilon} dz \, \frac{\alpha_s(Q^2)}{2\pi} \, P(z) \right].$$

(161)

The details are described in our paper [345]. We stay in a naive LL implementation without introducing corrections partially incorporating higher order effects, such as the angular ordering, because we plan to extend our PS to a true Next-to-Leading-Log (NLL) approximation [348].

We first tested the kinematics model employed in the "old" PYHTIA-PS [349, 350], since the theoretical bases is nearly the same. We found this model gives a very soft transverse activity. It results in an apparent mismatch in the transverse momentum (p_T) distribution of W bosons, when we tried to merge the inclusive W production with the LLL-subtracted $W + 1$ jet production by applying this PS to both processes. The starting assumptions of the "old" PYHTIA-PS kinematics are that the z parameter of a branch is the ratio of squared cm energies after and before each branch instead of the fraction of light-cone momenta, and that the Q^2 is identical to the virtuality of the evolving partons. The first assumption requires the definition of a "target" parton; thus, it is model dependent. However, this z definition ensures a simple relation between squared cm energies of a hard interaction and the beam collision; $s_\text{hard} = x_1 x_2 s_\text{beam}$ where x_1 and x_2 are given by the product of all z values in each beam. From a simple kinematical argument we found this model gives a relation,

$$p_T^2 = (1 - z)^2 Q^2,$$

(162)

for each branch at the soft limit [345].

On the other hand, ordinary arguments based on the massless approximation give a slightly different relation,

$$p_T^2 = (1 - z)Q^2$$

(163)

at the soft limit. Apparently Eq. (162) gives a smaller p_T value than Eq. (163) for a given set of Q^2 and z. The relation (163) must be better for the matching since external partons are nearly massless in ME
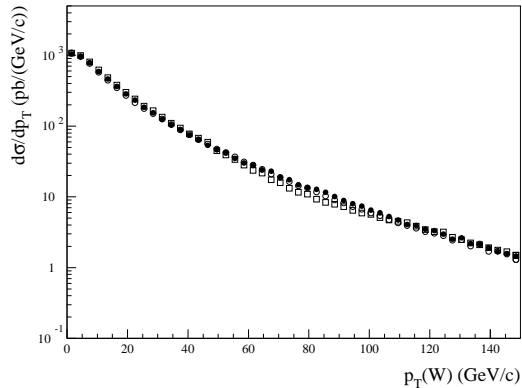
Fig. 34: Sum of the simulated p_T spectra of W bosons for the inclusive W production and the LLL-subtracted $W + 1$ jet production at LHC. The new p_T-prefixed PS described in the text is applied to both processes. Results are plotted for three different choices of μ_F: $\mu_F/m_W = 0.5$ (open circles), 1.0 (filled circles) and 1.5 (open squares).

calculations. We have introduced a new kinematics model where p_T of each branch is given ("prefixed") by Eq. (163). We keep the definition of the z parameter. The momenta of evolving partons are calculated from this p_T value and the z value. Thus, the virtuality is not necessarily equal to the Q^2 of a branch. This new PS gives a harder W-boson p_T spectrum than the "old" PYTHIA-PS in the inclusive W production simulation, showing a better matching to the LLL-subtracted $W + 1$ jet simulation. The sum of the two simulations gives a smooth p_T spectrum stable against a variation of the factorization scale (μ_F) [345].

After the submission of the paper [345] we tried another definition of the "prefixed" p_T,

$$p_T^2 = (1 - z - Q^2/\hat{s})Q^2. \tag{164}$$

The parameter $\hat{s}$ is the squared cm energy before the branch. This is the result of the massless approximation of branching kinematics before taking the soft limit ($Q^2/\hat{s} \to 0$). This definition is ugly in some sense since $\hat{s}$ is model dependent, but gives us a better matching than Eq. (163). We plot the summed p_T spectra of W-bosons for three different μ_F values ($\mu_F/m_W = 0.5$, 1.0 and 1.5) in Fig. 34. We can see almost no variation of the spectrum except for a small difference around $p_T = m_W$ in this μ_F range.

18.3 Prospects for the final-state PS matching

It is enough to consider the initial-state matching if we consentrate ourselves to NLO corrections for color singlet or heavy particle productions. However, once we go to NLO for those processes having a gluon or a light quark ("jet") in the final state, we also need to consider the matching in the final state.

We plan to use a simple LL parton shower employing Q^2 as the evolving parameter also for the final state. We need to introduce an appropriate kinematics model to this PS, too. In the initial-state PS, models in which the definition of p_T precedes that of Q^2 give us a better matching as we have discussed in the previous section. This is because p_T is in principle an observable quantity while Q^2 is not physically well-defined for initial-state partons. Similar arguments should be done also for the final state.

In the final state, the virtuality is in principle an observable as an invariant mass of particles even after the hadronization and decays. Therefore, it must be natural to identify Q^2 as the virtuality of the evolving partons. The transverse momentum (p_T) is also an observable in principle. Thus, z should be treated as an unphysical parameter. It should be used as a hidden parameter only to give p_T values according to the relation,

$$p_T^2 = z(1 - z)Q^2. \tag{165}$$

In this kinematics model, PS is a process to give final-state partons additional masses equal to the Q^2 of their first branches. The invariant mass of the hard interaction system should be unchanged even after the application of PS, since it is a very fundamental parameter for the evaluation of matrix elements. We also want to keep the production angles in the cm frame unchanged. These requirements can be fulfilled by introducing a common multiplication factor to the momenta of all final-state particles.

We need to apply a proper mapping of non-radiative subsystem in a radiative event to an on-shell non-radiative event in the LL subtraction. A mapping using momenta of the branched parton and the target parton works well for the initial-state radiation [345]. The subsystem is boosted and rotated to its cm frame where the momenta of two incoming partons are aligned along the z axis. This is the process exactly reversing the kinematical rearrangement in our initial-state PS.

The mapping should be done in the same concept also in the final state, exactly reversing the rearrangement in PS. It can be done as follows: pick up an arbitrary pair of final-state partons. If they can be considered as products of a PS branch, replace them with the parent parton having the invariant mass of the pair as its virtuality (Q^2). If not, skip this pair. Rescale the momenta of all particles in the cm frame with a common factor to make the replaced parent parton become on-shell. Evaluate the matrix element of the non-radiative process based on these rearranged momenta, multiply it with the LL radiation factor proportional to $1/Q^2$, then we get an LL approximation of a final-state radiation. This procedure should be applied to all possible combinations if we have more than two partons in the final state.

We expect that the LL contribution can be evaluated in such a systematic way, including the initial-state contributions, as well. All contributions should be summed to evaluate the total LL contribution. A program is under development based on these concepts.

18.4   Conclusions

We have achieved a good matching between PDF and matrix-element (ME) evaluations for the parton radiation in NLO QCD corrections, by using the Limited Leading-Log (LLL) subtraction technique. It has been demonstrated as a good stability of the W production cross section against a variation of the factorization scale (μ_F), where the total cross section is evaluated by the sum of the cross sections for inclusive W production and the LLL-subtracted $W + 1$ jet production.

We have to achieve a good matching between the parton shower (PS) and ME, as well, in order to construct practical NLO event generators. The transverse activity of PS depends on the applied kinematics model of parton branches. We have successfully built a suitable model for our Leading-Log (LL) initial-state PS, where p_T is prefixed according to the relation in the massless approximation of branching kinematics. The simulation employing this PS shows a good matching between the inclusive W production and the LLL-subtracted $W + 1$ jet production in the p_T spectrum of W bosons. The spectrum is stable against the variation of μ_F in a wide range.

It is necessary to achieve a good PS-ME matching for the final-state radiation, as well, when we construct NLO event generators for those processes including "jet(s)" in the final state. A study is in progress for the final state based on the experience on the initial-state radiation.

19. A PARTON-SHOWER MODEL BASED ON CATANI–SEYMOUR DIPOLE FACTORISATION[32]

19.1 Introduction

Parton-shower models form an indispensable building block of Monte Carlo event generators, such as Herwig [351], Pythia [352] and Sherpa [224], that aim at the realistic description of multi-particle final states as they are observed in high-energy collider experiments. By accounting for QCD bremsstrahlung processes, parton showers relate a small number of partons emerging from a hard interaction, defined at scale Q_{hard} and theoretically described through a fixed order calculation, to a larger set of partons at scales $Q_o \ll Q_{\mathrm{hard}}$. The parton-shower approach relies on the universal pattern of QCD emission processes once soft or collinear parton kinematics are considered. The soft and collinear phase-space regions are singular and obtain large corrections order by order in perturbation theory what makes an all-orders resummation of the associated kinematical logarithms essential. Most shower algorithms rely on collinear factorisation of QCD matrix elements and are accurate to the leading-logarithmic level. The Ariadne approach, however, is based around the soft limits [331].

The parton-shower approach being perturbative it cannot be extended to arbitrary small scales but has to be stopped at some infrared cut-off scale $Q_o \geq \Lambda_{\mathrm{QCD}}$. Below that scale event generators model the transition of QCD partons into the experimentally observed hadrons through non-perturbative hadronisation models. In fact, only through the incorporation of parton showers these hadronisation models can be made universal or independent of the underlying hard process. This, however, assumes that perturbative QCD between scales Q_{hard} and Q_o is appropriately described by the parton-shower model used.

In the past few years there have been lots of major improvements related to parton-shower Monte Carlos. This includes the incorporation of exact multi-leg tree-level matrix elements for the description of the first few hardest emissions from a given hard process, know as "matrix element parton shower merging", see e.g. [353, 354], or the consistent matching of next-to-leading order calculations with parton showers, know as "Monte Carlo at NLO", see for instance [45, 355]. In addition the available shower algorithms of Herwig and Pythia have been revised and improved [343, 356].

Only very recently new shower algorithms emerged that are based on formalisms used to construct subtraction terms that allow for a numerical cancellation of infrared singularities in NLO QCD calculations [329, 332–335, 357]. There exist now implementations of such shower algorithms for two commonly used subtraction schemes, the antenna subtraction method [316] and the Catani–Seymour dipole formalism [175, 358]. Besides incorporating the last knowledge on the infrared behaviour of QCD matrix elements, these models should largely facilitate the matching with NLO calculations carried out in the respective scheme. In this note we briefly report on the construction of a parton-shower algorithm relying on Catani–Seymour subtraction that has more extensively been presented in [333].

19.2 The shower model

The Catani–Seymour formalism provides all the ingredients to construct a local approximation to the real-correction matrix element in *any* QCD NLO calculation. These subtraction terms, that can be constructed in a process-independent way, possess exactly the same infrared divergences as the real-emission correction, such that the difference of the two is infrared finite and can safely be (numerically) integrated in four dimensions. In addition, the subtraction terms are chosen such, that they can be analytically integrated in $d = 4 - 2\epsilon$ dimensions over the phase space of the produced soft or collinear parton that causes the divergences. The occurring $1/\epsilon^2$ and $1/\epsilon$ poles exactly cancel the ones from the loop integration in the virtual part when adding the two pieces. Such, the Catani–Seymour method provides a way to construct a parton-level Monte Carlo program for a NLO calculations once the one-loop and real-emission corrections to the Born process are known.

---

[32]Contributed by: S. Schumann, F. Krauss

In the Catani–Seymour approach the additional soft or collinear parton is emitted from an emitter-spectator pair (called dipole). Considering both the emitter and the spectator to be either in the final or initial state, four configurations have to be considered, representing the singularities associated to emissions from the final or initial state. Labelling final-state particles by i, j and k and initial-state partons by a and b the real-emission matrix element can always be approximated by the sum over all the possible dipoles,

$$|\mathcal{M}_{m+1}|^2 = \sum_{i,j} \sum_{k \neq i,j} \mathcal{D}_{ij,k} + \left[\sum_{i,j} \mathcal{D}_{ij}^a + \sum_i \sum_{k \neq i} \mathcal{D}_k^{ai} + \sum_i \mathcal{D}^{ai,b} + (a \leftrightarrow b) \right]. \qquad (166)$$

Hereby, $\mathcal{D}_{ij,k}$ describe splittings of a final-state parton $\widetilde{ij}$ into the pair i, j accompanied by a spectator k. Due to the presence of the spectator, four-momentum conservation and on-shell momenta can be accomplished locally for each individual splitting. The terms $\mathcal{D}_{ij}^a$ represent final-state splittings with an initial-state spectator, while $\mathcal{D}_k^{ai}$ and $\mathcal{D}^{ai,b}$ correspond to a splitting initial-state line accompanied by a final- and initial-state parton, respectively. The individual dipole terms are constructed from the Born matrix element by inserting colour- and spin-dependent operators that describe the actual splitting. For massless final-state emitters and final-state spectators, for instance, the dipole contributions read

$$\mathcal{D}_{ij,k} = -\frac{1}{2p_i p_j} \; {}_m\langle 1, \ldots, \widetilde{ij} \ldots, \tilde{k}, \ldots | \frac{\mathbf{T}_k \cdot \mathbf{T}_{ij}}{\mathbf{T}_{ij}^2} \mathbf{V}_{ij,k} | 1, \ldots, \widetilde{ij} \ldots, \tilde{k}, \ldots \rangle_m. \qquad (167)$$

The $\mathbf{T}_{ij}$ and $\mathbf{T}_k$ thereby denote the colour charge operators of the emitter and spectator, respectively, they lead to colour correlations in the full amplitude. The $\mathbf{V}_{ij,k}$ are d-dimensional matrices in the emitter's spin space that induce spin correlations.

For the construction of a parton-shower algorithm from the dipole formula Eq. (166) certain approximations are needed that finally allow for an exponentiation of the splitting operators to derive the Sudakov form factors central for a shower implementation. In addition, the splitting kinematics, choices on scale settings and the actual shower-ordering parameter have to be fixed.

19.2.1 Shower construction criteria

The full colour correlations present in the $|\mathcal{M}_{m+1}|^2$ matrix element have to be discarded in the shower picture, instead the leading terms in $1/N_c$ are considered only [33]. In this approximation a colour flow can be assigned to each parton configuration. Motivated by considerations on the colour dynamics for soft emissions, we choose the emitter and spectator to be colour connected in the shower formalism. The colour-charge operators simplify to

$$-\frac{\mathbf{T_k} \cdot \mathbf{T_{ij}}}{\mathbf{T_{ij}^2}} \rightarrow \frac{1}{\mathcal{N}_{ij}^{spec}}, \qquad (168)$$

with $\mathcal{N}_{ij}^{spec} = 1, 2$ in case the emitter has one ($SU(3)$ (anti-)triplet) or two ($SU(3)$ octet) possible spectators. The four-dimensional dipole functions $\mathbf{V}$ are used as the shower splitting functions. Furthermore, we neglect spin correlations by using spin-averaged splitting functions $\langle \mathbf{V} \rangle$ [34].

As shower evolution variable we choose the transverse momentum between the splitting products for branching final-state partons and the transverse momentum with respect to the beam for emissions from the initial state, collectively denoted by $\mathbf{k}_\perp$. This scale is also employed as the scale of the running coupling and the parton distributions, once initial-state partons are present.

---

[33]Although formally subleading, we consider splittings of the type $g \rightarrow q\bar{q}$ as well

[34]Some of the dipole functions can become negative in non-singular phase-space region, prohibiting a simple probabilistic interpretation. We choose to set them to zero in these cases.

Based on the above approximations and choices Sudakov form factors corresponding to the different types of Catani–Seymour dipoles can be derived, that determine the probability for a certain branching not to occur for a given range of the evolution variable. The four generic cases are briefly reviewed in the following. For simplicity, here we consider massless partons only, the massive case is discussed in [333].

19.2.2 Final-state emitter – final-state spectator

Consider the final-state splitting $\{\widetilde{ij}, \tilde{k}\} \rightarrow \{i, j, k\}$ with the four-momentum constraint $\tilde{p}_{ij} + \tilde{p}_k = p_i + p_j + p_k \equiv Q$ and all momenta being on their mass-shell. The branching can be characterised by the Lorentz invariant variables

$$y_{ij,k} = \frac{p_i p_j}{p_i p_j + p_i p_k + p_j p_k}, \quad \tilde{z}_i = 1 - \tilde{z}_j = \frac{p_i p_k}{p_i p_k + p_j p_k}. \tag{169}$$

The factorised form of the fully differential $(m + 1)$-parton cross section that exactly reproduces the corresponding soft and collinear divergences of the real-emission process reads

$$d\hat{\sigma}_{m+1} = d\hat{\sigma}_m \sum_{ij} \sum_{k \neq ij} \frac{dy_{ij,k}}{y_{ij,k}} d\tilde{z}_i \frac{d\phi}{2\pi} \frac{\alpha_s}{2\pi} \frac{1}{\mathcal{N}_{ij}^{spec}} (1 - y_{ij,k}) \langle \mathbf{V}_{ij,k}(\tilde{z}_i, y_{ij,k}) \rangle. \tag{170}$$

The spin-averaged splitting kernels $\langle \mathbf{V}_{ij,k} \rangle$ for the branchings $q \rightarrow qg$, $g \rightarrow gg$ and $g \rightarrow q\bar{q}$ read

$$\langle \mathbf{V}_{q_i g_j, k}(\tilde{z}_i, y_{ij,k}) \rangle = C_F \left\{ \frac{2}{1 - \tilde{z}_i + \tilde{z}_i y_{ij,k}} - (1 + \tilde{z}_i) \right\}, \tag{171}$$

$$\langle \mathbf{V}_{g_i g_j, k}(\tilde{z}_i, y_{ij,k}) \rangle = 2C_A \left\{ \frac{1}{1 - \tilde{z}_i + \tilde{z}_i y_{ij,k}} + \frac{1}{\tilde{z}_i + y_{ij,k} - \tilde{z}_i y_{ij,k}} - 2 + \tilde{z}_i (1 - \tilde{z}_i) \right\}, \tag{172}$$

$$\langle \mathbf{V}_{q_i q_j, k}(\tilde{z}_i) \rangle = T_R \left\{ 1 - 2\tilde{z}_i (1 - \tilde{z}_i) \right\}. \tag{173}$$

In terms of the splitting variables the transverse momentum between the splitting products i and j (our shower evolution variable) can then be written as

$$\mathbf{k}_\perp^2 = 2\tilde{p}_{ij}\tilde{p}_k \, y_{ij,k} \, \tilde{z}_i (1 - \tilde{z}_i), \tag{174}$$

and accordingly

$$\frac{dy_{ij,k}}{y_{ij,k}} = \frac{d\mathbf{k}_\perp^2}{\mathbf{k}_\perp^2}. \tag{175}$$

Setting the infrared shower cut-off equal to $\mathbf{k}_{\perp,0}^2$ and the upper limit to $\mathbf{k}_{\perp,\max}^2$ the $\tilde{z}_i$ integration is constrained to

$$z_\mp(\mathbf{k}_{\perp,\max}^2, \mathbf{k}_{\perp,0}^2) = \frac{1}{2} \left(1 \mp \sqrt{1 - \frac{\mathbf{k}_{\perp,0}^2}{\mathbf{k}_{\perp,\max}^2}} \right). \tag{176}$$

The kinematics of the splitting are fixed through

$$p_i = \tilde{z}_i \tilde{p}_{ij} + \frac{\mathbf{k}_\perp^2}{\tilde{z}_i \, 2\tilde{p}_{ij}\tilde{p}_k} \tilde{p}_k + k_\perp, \tag{177}$$

$$p_j = (1 - \tilde{z}_i) \tilde{p}_{ij} + \frac{\mathbf{k}_\perp^2}{(1 - \tilde{z}_i) \, 2\tilde{p}_{ij}\tilde{p}_k} \tilde{p}_k - k_\perp, \tag{178}$$

$$p_k = (1 - y_{ij,k}) \tilde{p}_k, \tag{179}$$

with $k_\perp$ the spacelike transverse-momentum vector perpendicular to $\tilde{p}_{ij}$ and $\tilde{p}_k$ and $k_\perp \cdot k_\perp = -\mathbf{k}_\perp^2$. The Sudakov form factor for having no final-state splitting with a final-state spectator between $\mathbf{k}_{\perp,\mathrm{max}}^2$ and $\mathbf{k}_{\perp,0}^2$ reads

$$
\begin{aligned}
&\Delta_{\mathrm{FF}}(\mathbf{k}_{\perp,\mathrm{max}}^2, \mathbf{k}_{\perp,0}^2) \\
&= \ \exp\left(-\sum_{ij}\sum_{k \neq ij} \frac{1}{\mathcal{N}_{ij}^{spec}} \int_{\mathbf{k}_{\perp,0}^2}^{\mathbf{k}_{\perp,\mathrm{max}}^2} \frac{\mathrm{d}\mathbf{k}_\perp^2}{\mathbf{k}_\perp^2} \int_{z_-}^{z_+} \mathrm{d}\tilde{z}_i \frac{\alpha_\mathrm{s}(\mathbf{k}_\perp^2)}{2\pi} (1 - y_{ij,k}) \langle \mathbf{V}_{ij,k}(\tilde{z}_i, y_{ij,k}) \rangle \right) .
\end{aligned}
\tag{180}
$$

19.2.3 Final-state emitter – initial-state spectator

In the presence of initial-state partons a final-state splitter may be colour connected to one of the incoming lines. We consider the splitting $\{\widetilde{ij}, \tilde{a}\} \to \{i, j, a\}$, with $\tilde{p}_{ij} - \tilde{p}_a = p_i + p_j - p_a \equiv Q$. This time the branching is parameterised by the quantities

$$
x_{ij,a} = \frac{p_i p_a + p_j p_a - p_i p_j}{p_i p_a + p_j p_a}, \quad \tilde{z}_i = 1 - \tilde{z}_j = \frac{p_i p_a}{p_i p_a + p_j p_a}.
\tag{181}
$$

The relative transverse momentum of the new emerging final-state partons is given by

$$
\mathbf{k}_\perp^2 = 2\tilde{p}_a \tilde{p}_{ij} \frac{1 - x_{ij,a}}{x_{ij,a}} \tilde{z}_i (1 - \tilde{z}_i).
\tag{182}
$$

The derived Sudakov form factor for this splitting type reads

$$
\begin{aligned}
&\Delta_{\mathrm{FI}}(\mathbf{k}_{\perp,\mathrm{max}}^2, \mathbf{k}_{\perp,0}^2) \\
&= \ \exp\left(-\sum_{ij}\sum_{a} \frac{1}{\mathcal{N}_{ij}^{spec}} \int_{\mathbf{k}_{\perp,0}^2}^{\mathbf{k}_{\perp,\mathrm{max}}^2} \frac{\mathrm{d}\mathbf{k}_\perp^2}{\mathbf{k}_\perp^2} \int_{z_-}^{z_+} \mathrm{d}\tilde{z}_i \frac{\alpha_\mathrm{s}(\mathbf{k}_\perp^2)}{2\pi} \frac{f_a(\eta_a/x_{ij,a}, \mathbf{k}_\perp^2)}{f_a(\eta_a, \mathbf{k}_\perp^2)} \langle \mathbf{V}_{ij}^a(\tilde{z}_i, x_{ij,a}) \rangle \right) .
\end{aligned}
\tag{183}
$$

Here, η_a is the momentum fraction of the spectator parton a and $f_a(\eta_a, \mathbf{k}_\perp^2)$ the corresponding hadronic PDF evaluated at some scale $\mu_F^2 = \mathbf{k}_\perp^2$. The parton-distribution function $f_a(\eta_a/x_{ij,a}, \mathbf{k}_\perp^2)$ accounts for the new incoming momentum. The $\tilde{z}_i$ integration boundaries are given by Eq. (176) and the concrete splitting functions, $\langle \mathbf{V}_{ij}^a(\tilde{z}_i, x_{ij,a}) \rangle$, can be found in Ref. [333]. The branching kinematics are fixed to

$$
p_i \ = \ \tilde{z}_i\, \tilde{p}_{ij} + \frac{\mathbf{k}_\perp^2}{\tilde{z}_i\, 2\tilde{p}_{ij}\tilde{p}_a} \tilde{p}_a + k_\perp,
\tag{184}
$$

$$
p_j \ = \ (1 - \tilde{z}_i)\, \tilde{p}_{ij} + \frac{\mathbf{k}_\perp^2}{(1 - \tilde{z}_i)\, 2\tilde{p}_{ij}\tilde{p}_a} \tilde{p}_a - k_\perp,
\tag{185}
$$

with $k_\perp$ perpendicular to both the emitter and the spectator momentum. The new spectator momentum is given by

$$
p_a \ = \ \frac{1}{x_{ij,a}} \tilde{p}_a.
\tag{186}
$$

19.2.4 Initial-state emitter – final-state spectator

Once a final-state line is colour connected to the initial state, besides the situation discussed in Sec. 19.2.3, the reversed case occurs as well. Namely, the initial-state line can split and emit a new

final-state parton while the spectator is in the final state. The momentum-conservation condition for such a branching $\{\widetilde{ai}, \tilde{k}\} \rightarrow \{a, i, k\}$ reads $\tilde{p}_k - \tilde{p}_{ai} = p_i + p_k - p_a \equiv Q$. The splitting variables are defined as

$$x_{ik,a} = \frac{p_i p_a + p_k p_a - p_i p_k}{p_i p_a + p_k p_a} , \quad u_i = \frac{p_i p_a}{p_i p_a + p_k p_a} , \tag{187}$$

and the transverse-momentum squared of parton i with respect to the beam becomes

$$\mathbf{k}_\perp^2 = 2\tilde{p}_{ai}\tilde{p}_k \frac{1 - x_{ik,a}}{x_{ik,a}} u_i(1 - u_i) . \tag{188}$$

The Sudakov form factor associated with this splitting type reads

$$\Delta_{\mathrm{IF}}(\mathbf{k}_{\perp,\mathrm{max}}^2, \mathbf{k}_{\perp,0}^2)$$
$$= \exp\left(-\sum_{ai}\sum_k \frac{1}{\mathcal{N}_{ai}^{spec}} \int\limits_{\mathbf{k}_{\perp,0}^2}^{\mathbf{k}_{\perp,\mathrm{max}}^2} \frac{\mathrm{d}\mathbf{k}_\perp^2}{\mathbf{k}_\perp^2} \int\limits_{x_-}^{x_+} \mathrm{d}x_{ik,a} \frac{\alpha_\mathrm{s}(\mathbf{k}_\perp^2/4)}{2\pi} \tilde{J}(x_{ik,a}, u_i; \mathbf{k}_\perp^2) \langle \mathbf{V}_k^{ai}(x_{ik,a}, u_i) \rangle \right) , \tag{189}$$

with $x_- = \eta_{ai}$ and $x_+ = Q^2/(Q^2 + 4\mathbf{k}_{\perp,0}^2)$ and

$$\tilde{J}(x_{ik,a}, u_i; \mathbf{k}_\perp^2) = \frac{1 - u_i}{1 - 2u_i} \frac{1}{x_{ik,a}} \frac{f_a(\eta_{ai}/x_{ik,a}, \mathbf{k}_\perp^2)}{f_{ai}(\eta_{ai}, \mathbf{k}_\perp^2)} , \tag{190}$$

accounting for a possible flavour change of the incoming line through the backward-evolution step. The complete list of splitting kernels can again be found in Ref. [333]. The branching kinematics are given by

$$p_a = \frac{1}{x_{ik,a}} \tilde{p}_{ai} , \tag{191}$$

$$p_i = (1 - u_i)\frac{1 - x_{ik,a}}{x_{ik,a}} \tilde{p}_{ai} + u_i \tilde{p}_k + k_\perp , \tag{192}$$

$$p_k = u_i \frac{1 - x_{ik,a}}{x_{ik,a}} \tilde{p}_{ai} + (1 - u_i) \tilde{p}_k - k_\perp . \tag{193}$$

19.2.5 Initial-state emitter – initial-state spectator

The last case to be considered is the splitting of an initial-state line that is colour connected to the second incoming parton. The branching is parametrised through

$$x_{i,ab} = \frac{p_a p_b - p_i p_a - p_i p_b}{p_a p_b} , \quad \tilde{v}_i = \frac{p_i p_a}{p_a p_b} , \tag{194}$$

such that the transverse-momentum squared of the new final-state parton becomes

$$\mathbf{k}_\perp^2 = 2\tilde{p}_{ai}p_b \tilde{v}_i \frac{1 - x_{i,ab} - \tilde{v}_i}{x_{i,ab}} . \tag{195}$$

The Sudakov form factor of this configuration reads

$$\Delta_{\mathrm{II}}(\mathbf{k}_{\perp,\mathrm{max}}^2, \mathbf{k}_{\perp,0}^2)$$
$$= \exp\left(-\sum_{ai}\sum_{b \neq ai} \frac{1}{\mathcal{N}_{ai}^{spec}} \int\limits_{\mathbf{k}_{\perp,0}^2}^{\mathbf{k}_{\perp,\mathrm{max}}^2} \frac{\mathrm{d}\mathbf{k}_\perp^2}{\mathbf{k}_\perp^2} \int\limits_{x_-}^{x_+} \mathrm{d}x_{i,ab} \frac{\alpha_\mathrm{s}(\mathbf{k}_\perp^2/4)}{2\pi} \tilde{J}(x_{i,ab}, \tilde{v}_i; \mathbf{k}_\perp^2) \langle \mathbf{V}^{ai,b}(x_{i,ab}) \rangle \right) , \tag{196}$$

with

$$\tilde{J}(x_{i,ab}, \tilde{v}_i; \mathbf{k}_\perp^2) = \frac{1 - x_{i,ab} - \tilde{v}_i}{1 - x_{i,ab} - 2\tilde{v}_i} \frac{1}{x_{i,ab}} \frac{f_a(\eta_{ai}/x_{i,ab}, \mathbf{k}_\perp^2)}{f_{ai}(\eta_{ai}, \mathbf{k}_\perp^2)}, \tag{197}$$

and $x_- = \eta_{ai}$ and $x_+ = 2\tilde{p}_a p_b / (2\tilde{p}_a p_b + 4\mathbf{k}_{\perp,0}^2)$. For the kinematics of the emission process it is convenient to keep the spectator momentum fixed and to align the new incoming parton a with the old incoming momentum according to $p_a = 1/x_{i,ab} \cdot \tilde{p}_{ai}$. The momentum of the newly emerged final-state parton i, is given by

$$p_i = \frac{1 - x_{i,ab} - \tilde{v}_i}{x_{i,ab}} \tilde{p}_{ai} + \tilde{v}_i \, p_b + k_\perp. \tag{198}$$

Its transverse momentum has to be balanced by the entire set of final-state particles of the m-parton process (including all non-QCD particles).

19.2.6 The algorithm

Having at hand factorised expressions for all possible emission processes and corresponding Sudakov form factors a probabilistic shower algorithm of independent emissions can be formulated. The start seed forms a $2 \to 2$ core event with fixed colour flow and a process dependent shower start scale $\mathbf{k}_{\perp,\mathrm{max}}^2$.

1. The scale of the next emission is chosen according to the Sudakov form factors of all contributing emitter–spectator pairs. The dipole that yields the highest transverse momentum is picked to split.
2. The value of the second splitting variable is chosen according to the splitting kernel.
3. The splitting kinematics are determined, the new particle is inserted and the colour flow gets adapted.
4. Start from step 1 as long as $\mathbf{k}_\perp^2 > \mathbf{k}_{\perp,0}^2$ and replace $\mathbf{k}_{\perp,\mathrm{max}}^2$ by the transverse momentum of the last splitting.

This yields a chain of subsequent emissions strictly ordered in transverse momenta. There is no formal subdivision of initial and final state evolution, instead, all dipoles are treated on equal footing.

19.3 Comparison with experimental data

The ultimate test of a theoretical model is a direct comparison with experimental measurements. Here we compare the newly developed and implemented parton-shower algorithm (called CS shower in the following) with some experimental data on hadron production in e^+e^- annihilation, and Drell-Yan and jet production in $p\bar{p}$ collisions. Therefore the shower simulation has been supplemented with the string fragmentation routines of Pythia-6.2 [359] to account for hadronisation.

We begin with some of the most precisely measured quantities, event-shape observables in e^+e^- annihilation at the Z^0 pole. Fig. 19.3 contains a comparison for the normalised 1-Thrust $(1 - T)$ and C-parameter (C) distributions with LEP1 Delphi data [360]. Both observables obtain large higher-order corrections for two-jet like events that appear as $1 - T \approx 0$ and $C \approx 0$. In addition, there is a singularity in the C-parameter also in the region $C \approx 0.75$ that requires a resummation of large kinematical logarithms [324, 361]. The CS shower yields a good agreement with the experimental data. Only very pencil like events, that are sensitive to hadronisation corrections, are overestimated in the Monte Carlo. We believe that this can be improved through a more detailed tuning of the hadronisation model parameters.

In Fig. 19.3 we present the predictions of our model for the lepton-pair transverse-momentum distribution in Drell-Yan production and for the azimuthal decorrelation of inclusive dijet events in $p\bar{p}$ collisions. Both observables are nontrivial only if additional QCD radiation is produced and thereby test the emission pattern of the shower ansatz. We observe a good agreement with data for both observables in phase-space regions dominated by rather soft or collinear emissions but the agreement outside this range, i.e. large p_T^Z or small $\Delta\phi_{\mathrm{dijet}}$, is also very satisfactory.
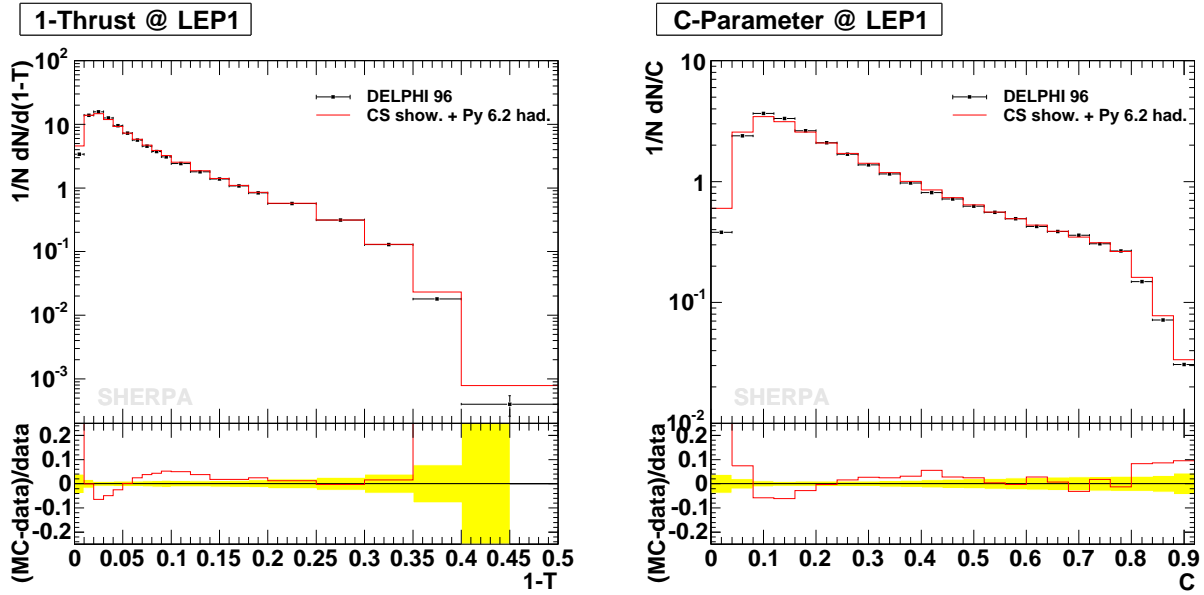
Fig. 35: The event-shape variables 1-Thrust $(1 - T)$ and C-parameter (C) in comparison with Delphi LEP1 data [360].
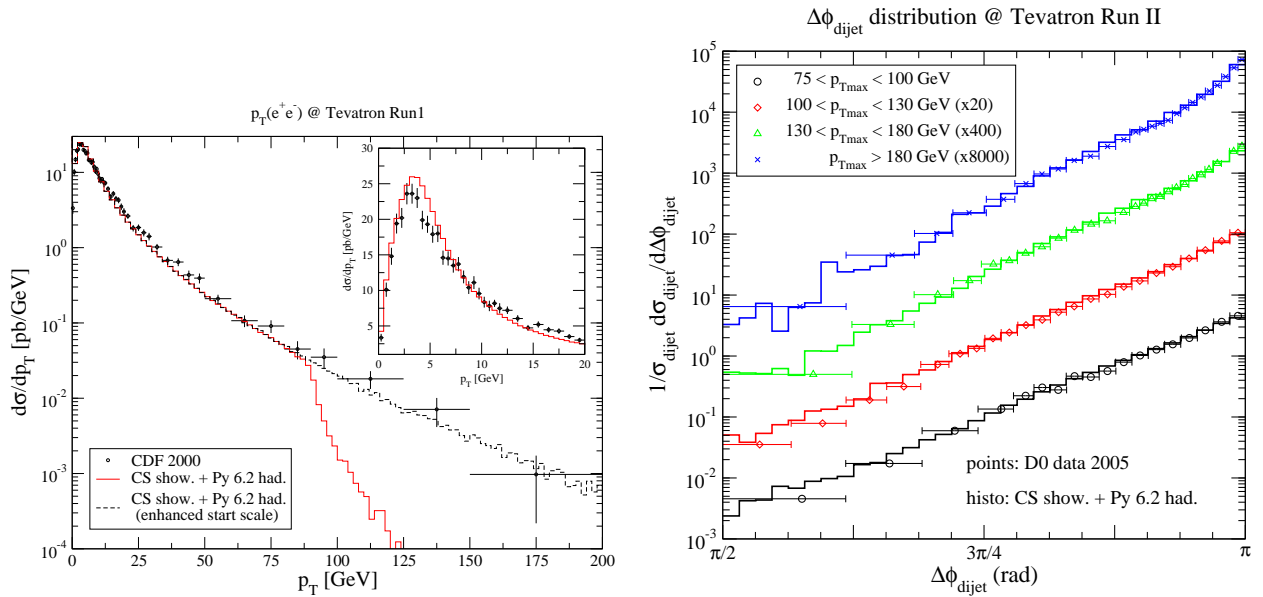

Fig. 36: The transverse-momentum distribution of e^+e^- Drell-Yan pairs compared with CDF Run I data [362] (left panel) and the Dijet Azimuthal decorrelation measured by DØ at Tevatron Run II [363] (right panel).

19.4 Conclusions

We have presented a new parton-shower algorithm that uses fully factorised versions of the Catani–Seymour dipole functions to describe multi-parton production processes in a probabilistic manner. The model encodes exact four-momentum conservation on the level of each individual splitting due to the notion of splitting emitter–spectator pairs. Subsequent emissions are ordered in transverse momenta and the evolution of initial- and final-state partons is done in a unified way. Comparison with experimental data yields very encouraging results. In a next step we will combine this new shower approach with exact multi-leg tree-level matrix elements. Moreover, this model should facilitate a matching with exact NLO QCD calculations.

References

[1] A. Bredenstein, K. Hagiwara, and B. Jager, arXiv:0801.4231 [hep-ph].

[2] J. R. Andersen, T. Binoth, G. Heinrich, and J. M. Smillie, arXiv:0709.3513 [hep-ph].

[3] S. Dittmaier, S. Kallweit, and P. Uwer, *Phys. Rev. Lett.* **100** (2008) 062003, [arXiv:0710.1577 [hep-ph]].

[4] J. M. Campbell, R. K. Ellis, and G. Zanderighi, *JHEP* **12** (2007) 056, [arXiv:0710.1832 [hep-ph]].

[5] J. M. Campbell, R. K. Ellis, and G. Zanderighi, *JHEP* **10** (2006) 028, [hep-ph/0608194].

[6] M. Ciccolini, A. Denner, and S. Dittmaier, *Phys. Rev. Lett.* **99** (2007) 161803, [arXiv:0707.0381 [hep-ph]].

[7] M. Ciccolini, A. Denner, and S. Dittmaier, *Phys. Rev.* **D77** (2008) 013002, [arXiv:0710.4749 [hep-ph]].

[8] A. Lazopoulos, K. Melnikov, and F. Petriello, *Phys. Rev.* **D76** (2007) 014001, [hep-ph/0703273].

[9] V. Hankele and D. Zeppenfeld, arXiv:0712.3544 [hep-ph].

[10] B. Jager, C. Oleari, and D. Zeppenfeld, *JHEP* **07** (2006) 015, [hep-ph/0603177].

[11] B. Jager, C. Oleari, and D. Zeppenfeld, *Phys. Rev.* **D73** (2006) 113006, [hep-ph/0604200].

[12] G. Bozzi, B. Jager, C. Oleari, and D. Zeppenfeld, *Phys. Rev.* **D75** (2007) 073004, [hep-ph/0701105].

[13] G. J. van Oldenborgh, *Comput. Phys. Commun.* **66** (1991) 1–15.

[14] T. Hahn and M. Perez-Victoria, *Comput. Phys. Commun.* **118** (1999) 153–165, [hep-ph/9807565].

[15] R. K. Ellis and G. Zanderighi, arXiv:0712.1851 [hep-ph].

[16] J. M. Campbell, J. W. Huston, and W. J. Stirling, *Rept. Prog. Phys.* **70** (2007) 89, [hep-ph/0611148].

[17] G. L. Bayatian *et. al.*,, **CMS** Collaboration. CERN-LHCC-2006-001.

[18] D. Froidevaux and P. Sphicas, *Ann. Rev. Nucl. Part. Sci.* **56** (2006) 375–440.

[19] F. Gianotti and M. L. Mangano, hep-ph/0504221.

[20] ATLAS Collaboration,. CERN-LHCC-99-14/15, 1999.

[21] G. L. Bayatian *et. al.*,, **CMS** Collaboration *J. Phys.* **G34** (2007) 995–1579.

[22] G. Dissertori, *PoS* **HEP2005** (2006) 401, [hep-ex/0512007].

[23] M. Dittmar, in proceedings of the 21st Les Rencontres De Physique De La Vallee D'Aoste, Italy, 2007.

[24] P. Sphicas, *Nucl. Phys. Proc. Suppl.* **117** (2003) 298–317.

[25] G. P. Salam and G. Soyez, *JHEP* **05** (2007) 086, [`arXiv:0704.0292 [hep-ph]`].

[26] G. P. Salam, `arXiv:0801.0070 [hep-ph]`.

[27] S. D. Ellis, J. Huston, K. Hatakeyama, P. Loch, and M. Toennesmann, `arXiv:0712.2447 [hep-ph]`.

[28] J. Pumplin *et. al.*, *JHEP* **07** (2002) 012, [`hep-ph/0201195`].

[29] **CMS** Collaboration. CMS PAS SBM-07-001.

[30] A. Bhatti *et. al.*, *Nucl. Instrum. Meth.* **A566** (2006) 375–412, [`hep-ex/0510047`].

[31] B. Abbott *et. al.*,, **D0** Collaboration *Nucl. Instrum. Meth.* **A424** (1999) 352–394, [`hep-ex/9805009`].

[32] R. M. Harris, private communication, 2007.

[33] F. Behner and M. Dittmar, contributed paper at the Europhysics Conference on High-Energy Physics (HEP 97), Jerusalem, Israel, 19-26 Aug 1997.

[34] M. Dittmar, F. Pauss, and D. Zurcher, *Phys. Rev.* **D56** (1997) 7284–7290, [`hep-ex/9705004`].

[35] K. Melnikov and F. Petriello, *Phys. Rev.* **D74** (2006) 114017, [`hep-ph/0609070`].

[36] M. Dittmar *et. al.*, `hep-ph/0511119`.

[37] W.-K. Tung, H. L. Lai, J. Pumplin, P. Nadolsky, and C. P. Yuan, `arXiv:0707.0275 [hep-ph]`.

[38] S. Dittmaier and M. Kramer, *Phys. Rev.* **D65** (2002) 073007, [`hep-ph/0109062`].

[39] U. Baur, S. Keller, and D. Wackeroth, *Phys. Rev.* **D59** (1999) 013002, [`hep-ph/9807417`].

[40] J. H. Kuhn, A. Kulesza, S. Pozzorini, and M. Schulze, *Phys. Lett.* **B651** (2007) 160–165, [`hep-ph/0703283`].

[41] C. Anastasiou, L. J. Dixon, K. Melnikov, and F. Petriello, *Phys. Rev.* **D69** (2004) 094008, [`hep-ph/0312266`].

[42] J. D'Hondt, `arXiv:0707.1247 [hep-ph]`.

[43] N. Kauer, *Phys. Rev.* **D70** (2004) 014020, [`hep-ph/0404045`].

[44] G. Davatz, A. S. Giolo-Nicollerat, and M. Zanetti, *PoS* **TOP2006** (2006) 027, [`hep-ex/0604041`].

[45] S. Frixione and B. R. Webber, *JHEP* **06** (2002) 029, [`hep-ph/0204244`].

[46] S. Frixione, P. Nason, and B. R. Webber, *JHEP* **08** (2003) 007, [`hep-ph/0305252`].

[47] E. Witten, *Commun. Math. Phys.* **252** (2004) 189–258, [`hep-th/0312171`].

[48] F. Cachazo, P. Svrcek, and E. Witten, *JHEP* **09** (2004) 006, [`hep-th/0403047`].

[49] S. J. Parke and T. R. Taylor, *Phys. Rev. Lett.* **56** (1986) 2459.

[50] R. Britto, F. Cachazo, and B. Feng, *Nucl. Phys.* **B715** (2005) 499–522, [`hep-th/0412308`].

[51] F. Britto, R.and Cachazo, B. Feng, and E. Witten, *Phys. Rev. Lett.* **94** (2005) 181602, [hep-th/0501052].

[52] M.-x. Luo and C.-k. Wen, *JHEP* **03** (2005) 004, [hep-th/0501121].

[53] M.-x. Luo and C.-k. Wen, *Phys. Rev.* **D71** (2005) 091501, [hep-th/0502009].

[54] R. Britto, B. Feng, R. Roiban, M. Spradlin, and A. Volovich, *Phys. Rev.* **D71** (2005) 105017, [hep-th/0503198].

[55] S. D. Badger, E. W. N. Glover, V. V. Khoze, and P. Svrcek, *JHEP* **07** (2005) 025, [hep-th/0504159].

[56] S. D. Badger, E. W. N. Glover, and V. V. Khoze, *JHEP* **01** (2006) 066, [hep-th/0507161].

[57] D. Forde and D. A. Kosower, *Phys. Rev.* **D73** (2006) 065007, [hep-th/0507292].

[58] C. Quigley and M. Rozali, *JHEP* **03** (2006) 004, [hep-ph/0510148].

[59] K. Risager, *JHEP* **12** (2005) 003, [hep-th/0508206].

[60] P. D. Draggiotis, R. H. P. Kleiss, A. Lazopoulos, and C. G. Papadopoulos, *Eur. Phys. J.* **C46** (2006) 741, [hep-ph/0511288].

[61] D. Vaman and Y.-P. Yao, *JHEP* **04** (2006) 030, [hep-th/0512031].

[62] K. J. Ozeren and W. J. Stirling, *Eur. Phys. J.* **C48** (2006) 159–168, [hep-ph/0603071].

[63] C. Schwinn and S. Weinzierl, *JHEP* **05** (2005) 006, [hep-th/0503015].

[64] C. Schwinn and S. Weinzierl, *JHEP* **03** (2006) 030, [hep-th/0602012].

[65] M. Dinsdale, M. Ternick, and S. Weinzierl, *JHEP* **03** (2006) 056, [hep-ph/0602204].

[66] C. Duhr, S. Hoche, and F. Maltoni, *JHEP* **08** (2006) 062, [hep-ph/0607057].

[67] P. Draggiotis *et. al.*, *Nucl. Phys. Proc. Suppl.* **160** (2006) 255–260, [hep-ph/0607034].

[68] D. de Florian and J. Zurita, *JHEP* **05** (2006) 073, [hep-ph/0605291].

[69] D. de Florian and J. Zurita, *JHEP* **11** (2006) 080, [hep-ph/0609099].

[70] G. Rodrigo, *JHEP* **09** (2005) 079, [hep-ph/0508138].

[71] P. Ferrario, G. Rodrigo, and P. Talavera, *Phys. Rev. Lett.* **96** (2006) 182001, [hep-th/0602043].

[72] C. Schwinn and S. Weinzierl, *JHEP* **04** (2007) 072, [hep-ph/0703021].

[73] A. Hall, arXiv:0710.1300 [hep-ph].

[74] Z. Bern, L. J. Dixon, D. C. Dunbar, and D. A. Kosower, *Nucl. Phys.* **B425** (1994) 217–260, [hep-ph/9403226].

[75] Z. Bern, L. Dixon, D. C. Dunbar, and D. A. Kosower, *Nucl. Phys.* **B435** (1995) 59–101, [hep-ph/9409265].

[76] S. J. Bidder, N. E. J. Bjerrum-Bohr, L. J. Dixon, and D. C. Dunbar, *Phys. Lett.* **B606** (2005) 189–201, [hep-th/0410296].

[77] S. J. Bidder, N. E. J. Bjerrum-Bohr, D. C. Dunbar, and W. B. Perkins, *Phys. Lett.* **B608** (2005) 151–163, [`hep-th/0412023`].

[78] S. J. Bidder, N. E. J. Bjerrum-Bohr, D. C. Dunbar, and W. B. Perkins, *Phys. Lett.* **B612** (2005) 75–88, [`hep-th/0502028`].

[79] J. Bedford, A. Brandhuber, B. J. Spence, and G. Travaglini, *Nucl. Phys.* **B712** (2005) 59–85, [`hep-th/0412108`].

[80] R. Britto, E. Buchbinder, F. Cachazo, and B. Feng, *Phys. Rev.* **D72** (2005) 065012, [`hep-ph/0503132`].

[81] Z. Bern, L. J. Dixon, and D. A. Kosower, *Phys. Rev.* **D71** (2005) 105013, [`hep-th/0501240`].

[82] Z. Bern, L. J. Dixon, and D. A. Kosower, *Phys. Rev.* **D72** (2005) 125003, [`hep-ph/0505055`].

[83] Z. Bern, L. J. Dixon, and D. A. Kosower, *Phys. Rev.* **D73** (2006) 065013, [`hep-ph/0507005`].

[84] Z. Bern, N. E. J. Bjerrum-Bohr, D. C. Dunbar, and H. Ita, *JHEP* **11** (2005) 027, [`hep-ph/0507019`].

[85] D. Forde and D. A. Kosower, *Phys. Rev.* **D73** (2006) 061701, [`hep-ph/0509358`].

[86] C. F. Berger, Z. Bern, L. J. Dixon, D. Forde, and D. A. Kosower, *Phys. Rev.* **D74** (2006) 036009, [`hep-ph/0604195`].

[87] C. F. Berger, Z. Bern, L. J. Dixon, D. Forde, and D. A. Kosower, *Phys. Rev.* **D75** (2007) 016006, [`hep-ph/0607014`].

[88] C. F. Berger, V. Del Duca, and L. J. Dixon, *Phys. Rev.* **D74** (2006) 094021, [`hep-ph/0608180`].

[89] R. Britto, B. Feng, and P. Mastrolia, *Phys. Rev.* **D73** (2006) 105004, [`hep-ph/0602178`].

[90] Z. Xiao, G. Yang, and C.-J. Zhu, *Nucl. Phys.* **B758** (2006) 1–34, [`hep-ph/0607015`].

[91] X. Su, Z. Xiao, G. Yang, and C.-J. Zhu, *Nucl. Phys.* **B758** (2006) 35–52, [`hep-ph/0607016`].

[92] Z. Xiao, G. Yang, and C.-J. Zhu, *Nucl. Phys.* **B758** (2006) 53–89, [`hep-ph/0607017`].

[93] T. Binoth, J. P. Guillet, and G. Heinrich, *JHEP* **02** (2007) 013, [`hep-ph/0609054`].

[94] T. Binoth, G. Heinrich, T. Gehrmann, and P. Mastrolia, *Phys. Lett.* **B649** (2007) 422–426, [`hep-ph/0703311`].

[95] G. Ossola, C. G. Papadopoulos, and R. Pittau, *Nucl. Phys.* **B763** (2007) 147–169, [`hep-ph/0609007`].

[96] G. Ossola, C. G. Papadopoulos, and R. Pittau, *JHEP* **07** (2007) 085, [`arXiv:0704.1271 [hep-ph]`].

[97] C. Anastasiou, R. Britto, B. Feng, Z. Kunszt, and P. Mastrolia, *Phys. Lett.* **B645** (2007) 213–216, [`hep-ph/0609191`].

[98] C. Anastasiou, R. Britto, B. Feng, Z. Kunszt, and P. Mastrolia, *JHEP* **03** (2007) 111, [`hep-ph/0612277`].

[99] P. Mastrolia, *Phys. Lett.* **B644** (2007) 272–283, [`hep-th/0611091`].

[100] R. Britto and B. Feng, *Phys. Rev.* **D75** (2007) 105006, [hep-ph/0612089].

[101] S. D. Badger, E. W. N. Glover, and K. Risager, *JHEP* **07** (2007) 066, [arXiv:0704.3914 [hep-ph]].

[102] D. Forde, *Phys. Rev.* **D75** (2007) 125019, [arXiv:0704.1835 [hep-ph]].

[103] G. Ossola, C. G. Papadopoulos, and R. Pittau, arXiv:0711.3596 [hep-ph].

[104] R. Britto and B. Feng, arXiv:0711.4284 [hep-ph].

[105] W. B. Kilgore, arXiv:0711.5015 [hep-ph].

[106] F. A. Berends, R. Kleiss, P. De Causmaecker, R. Gastmans, and T. T. Wu, *Phys. Lett.* **B103** (1981) 124.

[107] P. De Causmaecker, R. Gastmans, W. Troost, and T. T. Wu, *Nucl. Phys.* **B206** (1982) 53.

[108] J. F. Gunion and Z. Kunszt, *Phys. Lett.* **B161** (1985) 333.

[109] R. Kleiss and W. J. Stirling, *Nucl. Phys.* **B262** (1985) 235–262.

[110] R. Kleiss and W. J. Stirling, *Phys. Lett.* **B179** (1986) 159.

[111] Z. Xu, D.-H. Zhang, and L. Chang, *Nucl. Phys.* **B291** (1987) 392.

[112] R. Gastmans and T. T. Wu,. Oxford, UK: Clarendon (1990) 648 p. (International series of monographs on physics, 80).

[113] P. Cvitanovic, P. G. Lauwers, and P. N. Scharbach, *Nucl. Phys.* **B186** (1981) 165.

[114] F. A. Berends and W. Giele, *Nucl. Phys.* **B294** (1987) 700.

[115] M. L. Mangano, S. J. Parke, and Z. Xu, *Nucl. Phys.* **B298** (1988) 653.

[116] D. Kosower, B.-H. Lee, and V. P. Nair, *Phys. Lett.* **B201** (1988) 85.

[117] Z. Bern and D. A. Kosower, *Nucl. Phys.* **B362** (1991) 389–448.

[118] V. Del Duca, L. J. Dixon, and F. Maltoni, *Nucl. Phys.* **B571** (2000) 51–70, [hep-ph/9910563].

[119] F. Maltoni, K. Paul, T. Stelzer, and S. Willenbrock, *Phys. Rev.* **D67** (2003) 014026, [hep-ph/0209271].

[120] S. Weinzierl, *Eur. Phys. J.* **C45** (2006) 745–757, [hep-ph/0510157].

[121] F. del Aguila and R. Pittau, *JHEP* **07** (2004) 017, [hep-ph/0404120].

[122] A. van Hameren, J. Vollinga, and S. Weinzierl, *Eur. Phys. J.* **C41** (2005) 361–375, [hep-ph/0502165].

[123] L. D. Landau, *Nucl. Phys.* **13** (1959) 181–192.

[124] R. E. Cutkosky, *J. Math. Phys.* **1** (1960) 429–433.

[125] A. Brandhuber, B. Spence, G. Travaglini, and K. Zoubos, *JHEP* **07** (2007) 002, [arXiv:0704.0245 [hep-th]].

[126] R. K. Ellis, W. T. Giele, and Z. Kunszt, arXiv:0708.2398 [hep-ph].

[127] N. E. J. Bjerrum-Bohr, D. C. Dunbar, and W. B. Perkins, arXiv:0709.2086 [hep-ph].

[128] Z. Bern, L. J. Dixon, D. C. Dunbar, and D. A. Kosower, *Nucl. Phys.* **B435** (1995) 59–101, [hep-ph/9409265].

[129] R. Britto, F. Cachazo, and B. Feng, *Nucl. Phys.* **B725** (2005) 275–305, [hep-th/0412103].

[130] Z. Bern, L. J. Dixon, and D. A. Kosower, *Ann. Rev. Nucl. Part. Sci.* **46** (1996) 109–148, [hep-ph/9602280].

[131] F. Cachazo and P. Svrcek, *PoS* **RTN2005** (2005) 004, [hep-th/0504194].

[132] Z. Bern, L. J. Dixon, and D. A. Kosower, *Annals Phys.* **322** (2007) 1587–1634, [arXiv:0704.2798 [hep-ph]].

[133] M. L. Mangano and S. J. Parke, *Phys. Rept.* **200** (1991) 301–367, [hep-th/0509223].

[134] L. J. Dixon, hep-ph/9601359.

[135] Z. Bern and A. G. Morgan, *Nucl. Phys.* **B467** (1996) 479–509, [hep-ph/9511336].

[136] S. Mandelstam, *Phys. Rev.* **112** (1958) 1344–1360.

[137] S. Mandelstam, *Phys. Rev.* **115** (1959) 1741–1751.

[138] W. L. van Neerven, *Nucl. Phys.* **B268** (1986) 453.

[139] Z. Bern, L. J. Dixon, and D. A. Kosower, *Nucl. Phys.* **B513** (1998) 3–86, [hep-ph/9708239].

[140] Z. Bern and G. Chalmers, *Nucl. Phys.* **B447** (1995) 465–518, [hep-ph/9503236].

[141] J. M. Campbell, E. W. N. Glover, and D. J. Miller, *Nucl. Phys.* **B498** (1997) 397–442, [hep-ph/9612413].

[142] C. F. Berger et al., *to appear*.

[143] Z. Bern, L. J. Dixon, and D. A. Kosower, *Phys. Rev. Lett.* **70** (1993) 2677–2680, [hep-ph/9302280].

[144] L. D. Landau, *Nucl. Phys.* **13** (1959) 181.

[145] S. Mandelstam, *Phys. Rev.* **115** (1959) 1741.

[146] R. E. Cutkosky, *J. Math. Phys.* **1** (1960) 429.

[147] R. J. Eden, P. V. Landshoff, D. I. Olive, and J. C. Polkinghorne, *Cambridge University Press* (1966).

[148] G. 't Hooft and M. J. G. Veltman, *Nucl. Phys.* **B153** (1979) 365–401.

[149] Z. Bern, L. J. Dixon, and D. A. Kosower, *Phys. Lett.* **B302** (1993) 299–308, [hep-ph/9212308].

[150] Z. Bern, L. J. Dixon, and D. A. Kosower, *Nucl. Phys.* **B412** (1994) 751–816, [hep-ph/9306240].

[151] O. V. Tarasov, *Phys. Rev.* **D54** (1996) 6479–6490, [hep-th/9606018].

[152] T. Binoth, J. P. Guillet, and G. Heinrich, *Nucl. Phys.* **B572** (2000) 361–386, [hep-ph/9911342].

[153] G. Duplancic and B. Nizic, *Eur. Phys. J.* **C35** (2004) 105–118, [hep-ph/0303184].

[154] A. Brandhuber, S. McNamara, B. J. Spence, and G. Travaglini, *JHEP* **10** (2005) 011, [hep-th/0506068].

[155] D. Maitre and P. Mastrolia, arXiv:0710.5559 [hep-ph].

[156] M. Sipser,, *Introduction to the theory of computation*. Thomson Course Technology, 2006.

[157] R. Kleiss and H. Kuijf, *Nucl. Phys.* **B312** (1989) 616.

[158] T. Stelzer and W. F. Long, *Comput. Phys. Commun.* **81** (1994) 357–371, [hep-ph/9401258].

[159] F. A. Berends and W. T. Giele, *Nucl. Phys.* **B306** (1988) 759.

[160] F. A. Berends, W. T. Giele, and H. Kuijf, *Nucl. Phys.* **B321** (1989) 39.

[161] F. A. Berends, H. Kuijf, B. Tausk, and W. T. Giele, *Nucl. Phys.* **B357** (1991) 32–64.

[162] F. A. Berends, W. T. Giele, and H. Kuijf, *Nucl. Phys.* **B333** (1990) 120.

[163] M. L. Mangano, M. Moretti, F. Piccinini, R. Pittau, and A. D. Polosa, *JHEP* **07** (2003) 001, [hep-ph/0206293].

[164] R. K. Ellis and J. C. Sexton, *Nucl. Phys.* **B269** (1986) 445.

[165] P. Nogueira, *J. Comput. Phys.* **105** (1993) 279–289.

[166] J. A. M. Vermaseren, math-ph/0010025.

[167] G. Passarino and M. J. G. Veltman, *Nucl. Phys.* **B160** (1979) 151.

[168] R. K. Ellis, W. T. Giele, and G. Zanderighi, *JHEP* **05** (2006) 027, [hep-ph/0602185].

[169] W. L. van Neerven, *Nucl. Phys.* **B268** (1986) 453.

[170] G. Ossola, C. G. Papadopoulos, and R. Pittau, arXiv:0802.1876 [hep-ph].

[171] R. Pittau, *Comput. Phys. Commun.* **111** (1998) 48–52, [hep-ph/9712418].

[172] R. Pittau, *Comput. Phys. Commun.* **104** (1997) 23–36, [hep-ph/9607309].

[173] D. H. Bailey, ARPREC (C++/Fortran-90 arbitrary precision package), http://crd.lbl.gov/∼dhbailey/mpdist/.

[174] D. H. Bailey, A Fortran-90 Based Multiprecision System, ACM Transactions on Mathematical Software, vol. 21, no. 4 (Dec 1995), pg. 379-387.

[175] S. Catani and M. H. Seymour, *Nucl. Phys.* **B485** (1997) 291–419, [hep-ph/9605323].

[176] W. T. Giele, E. W. N. Glover, and D. A. Kosower, *Nucl. Phys.* **B403** (1993) 633–670, [hep-ph/9302225].

[177] B. W. Harris and J. F. Owens, *Phys. Rev.* **D65** (2002) 094032, [hep-ph/0102128].

[178] G. Ossola, C. G. Papadopoulos, R. Pittau, T. Binoth, and G. Heinrich, in preparation.

[179] A. Kanaki and C. G. Papadopoulos, *Comput. Phys. Commun.* **132** (2000) 306–315, [hep-ph/0002082].

[180] A. Kanaki and C. G. Papadopoulos, hep-ph/0012004.

[181] A. Cafarella, C. G. Papadopoulos, and M. Worek, arXiv:0710.2427 [hep-ph].

[182] G. Dissertori, these proceedings.

[183] W. T. Giele, Z. Kunszt, and K. Melnikov, arXiv:0801.2237 [hep-ph].

[184] T. Binoth, J. P. Guillet, G. Heinrich, E. Pilon, and C. Schubert, *JHEP* **10** (2005) 015, [hep-ph/0504267].

[185] T. Binoth, M. Ciccolini, N. Kauer, and M. Kramer, *JHEP* **12** (2006) 046, [hep-ph/0611170].

[186] T. Binoth, S. Karg, N. Kauer, and R. Ruckl, *Phys. Rev.* **D74** (2006) 113008, [hep-ph/0608057].

[187] T. Binoth, J. P. Guillet, and F. Mahmoudi, *JHEP* **02** (2004) 057, [hep-ph/0312334].

[188] T. Binoth, J. P. Guillet, G. Heinrich, and C. Schubert, *Nucl. Phys.* **B615** (2001) 385–401, [hep-ph/0106243].

[189] T. Binoth, G. Heinrich, and N. Kauer, *Nucl. Phys.* **B654** (2003) 277–300, [hep-ph/0210023].

[190] J. A. M. Vermaseren and M. Tentyukov, *Nucl. Phys. Proc. Suppl.* **160** (2006) 38–43.

[191] Z. Nagy and D. E. Soper, *Phys. Rev.* **D74** (2006) 093006, [hep-ph/0610028].

[192] R. Eden, P. Landshoff, D. Olive, and J. Polkinghorne, The Analytic S-matrix, *Cambridge University Press* (1966).

[193] F. Boudjema and L. D. Ninh, arXiv:0711.2005 [hep-ph], Phys. Rev. D, in Press.

[194] C. Bernicot and J. P. Guillet, *JHEP* **01** (2008) 059, [arXiv:0711.4713 [hep-ph]].

[195] C. Itzykson and J. B. Zuber, Quantum Field Theory, *New York, USA Mcgraw-Hill (1980) 705 P.(International Series In Pure and Applied Physics)*.

[196] A. Denner, S. Dittmaier, M. Roth, and L. H. Wieders, *Phys. Lett.* **B612** (2005) 223–232, [hep-ph/0502063].

[197] A. Denner, S. Dittmaier, M. Roth, and L. H. Wieders, *Nucl. Phys.* **B724** (2005) 247–294, [hep-ph/0505042].

[198] A. Bredenstein, A. Denner, S. Dittmaier, and M. M. Weber, *Phys. Rev.* **D74** (2006) 013004, [hep-ph/0604011].

[199] A. Bredenstein, A. Denner, S. Dittmaier, and M. M. Weber, *JHEP* **02** (2007) 080, [hep-ph/0611234].

[200] A. Denner and S. Dittmaier, *Nucl. Phys.* **B734** (2006) 62–115, [hep-ph/0509141].

[201] C. Buttar *et. al.*, hep-ph/0604120.

[202] A. Denner and S. Dittmaier, *Nucl. Phys.* **B658** (2003) 175–202, [hep-ph/0212259].

[203] A. Ferroglia, M. Passera, G. Passarino, and S. Uccirati, *Nucl. Phys.* **B650** (2003) 162–228, [hep-ph/0209219].

[204] W. Giele, E. W. N. Glover, and G. Zanderighi, *Nucl. Phys. Proc. Suppl.* **135** (2004) 275–279, [hep-ph/0407016].

[205] D. B. Melrose, *Nuovo Cim.* **40** (1965) 181–213.

[206] S. Dittmaier, *Nucl. Phys.* **B675** (2003) 447–466, [hep-ph/0308246].

[207] A. Denner and S. Dittmaier, *Nucl. Phys. Proc. Suppl.* **157** (2006) 53–57, [hep-ph/0601085].

[208] A. I. Davydychev, *Phys. Lett.* **B263** (1991) 107–111.

[209] J. Fleischer, F. Jegerlehner, and O. V. Tarasov, *Nucl. Phys.* **B566** (2000) 423–440, [hep-ph/9907327].

[210] B. Mellado, W. Quayle, and S. L. Wu, *Phys. Rev.* **D76** (2007) 093007, [arXiv:0708.2507 [hep-ph]].

[211] T. Binoth, J.-P. Guillet, S. Karg, N. Kauer, and G. Sanguinetti, in preparation.

[212] R. K. Ellis, D. A. Ross, and A. E. Terrano, *Nucl. Phys.* **B178** (1981) 421.

[213] J. Küblbeck, M. Böhm, and A. Denner, *Comput. Phys. Commun.* **60** (1990) 165–180.

[214] T. Hahn, *Comput. Phys. Commun.* **140** (2001) 418–431, [hep-ph/0012260].

[215] W. Beenakker *et. al.*, *Nucl. Phys.* **B653** (2003) 151–203, [hep-ph/0211352].

[216] S. Dittmaier, P. Uwer, and S. Weinzierl, *Phys. Rev. Lett.* **98** (2007) 262002, [hep-ph/0703120].

[217] W. Beenakker and A. Denner, *Nucl. Phys.* **B338** (1990) 349–370.

[218] A. Denner, U. Nierste, and R. Scharf, *Nucl. Phys.* **B367** (1991) 637–656.

[219] G. J. van Oldenborgh and J. A. M. Vermaseren, *Z. Phys.* **C46** (1990) 425–438.

[220] G. J. van Oldenborgh, *Comput. Phys. Commun.* **66** (1991) 1–15.

[221] F. A. Berends, R. Pittau, and R. Kleiss, *Nucl. Phys.* **B424** (1994) 308–342, [hep-ph/9404313].

[222] R. Kleiss and R. Pittau, *Comput. Phys. Commun.* **83** (1994) 141–146, [hep-ph/9405257].

[223] W. Kilian, T. Ohl, and J. Reuter, arXiv:0708.4233 [hep-ph].

[224] T. Gleisberg *et. al.*, *JHEP* **02** (2004) 056, [hep-ph/0311263].

[225] S. Kallweit, *diploma thesis (in German), LMU Munich* (2006).

[226] W. T. Giele and E. W. N. Glover, *JHEP* **04** (2004) 029, [hep-ph/0402152].

[227] R. K. Ellis, W. T. Giele, and G. Zanderighi, *Phys. Rev.* **D73** (2006) 014027, [hep-ph/0508308].

[228] F. Maltoni and T. Stelzer, *JHEP* **02** (2003) 027, [hep-ph/0208156].

[229] L. J. Dixon, Z. Kunszt, and A. Signer, *Nucl. Phys.* **B531** (1998) 3–23, [hep-ph/9803250].

[230] S. A. Larin, *Phys. Lett.* **B303** (1993) 113–118, [hep-ph/9302240].

[231] T. L. Trueman, *Z. Phys.* **C69** (1996) 525–536, [hep-ph/9504315].

[232] B. W. Harris, E. Laenen, L. Phaf, Z. Sullivan, and S. Weinzierl, *Phys. Rev.* **D66** (2002) 054024, [hep-ph/0207055].

[233] S. Catani, M. H. Seymour, and Z. Trocsanyi, *Phys. Rev.* **D55** (1997) 6819–6829, [hep-ph/9610553].

[234] D. Stump *et. al.*, *JHEP* **10** (2003) 046, [hep-ph/0303013].

[235] S. D. Ellis and D. E. Soper, *Phys. Rev.* **D48** (1993) 3160–3166, [hep-ph/9305266].

[236] M. Czakon, A. Mitov, and S. Moch, *Phys. Lett.* **B651** (2007) 147–159, [arXiv:0705.1975 [hep-ph]].

[237] M. Czakon, A. Mitov, and S. Moch, arXiv:0707.4139 [hep-ph].

[238] M. Czakon, J. Gluza, and T. Riemann, *Phys. Rev.* **D71** (2005) 073009, [hep-ph/0412164].

[239] M. Czakon, J. Gluza, and T. Riemann, *Nucl. Phys.* **B751** (2006) 1–17, [hep-ph/0604101].

[240] V. A. Smirnov, *Phys. Lett.* **B460** (1999) 397–404, [hep-ph/9905323].

[241] J. B. Tausk, *Phys. Lett.* **B469** (1999) 225–234, [hep-ph/9909506].

[242] J. Gluza, K. Kajda, and T. Riemann, *Comput. Phys. Commun.* **177** (2007) 879–893, [arXiv:0704.2423 [hep-ph]].

[243] M. Czakon, *Comput. Phys. Commun.* **175** (2006) 559–571, [hep-ph/0511200].

[244] S. Moch and P. Uwer, *Comput. Phys. Commun.* **174** (2006) 759–770, [math-ph/0508008].

[245] A. V. Kotikov, *Phys. Lett.* **B254** (1991) 158–164.

[246] E. Remiddi, *Nuovo Cim.* **A110** (1997) 1435–1452, [hep-th/9711188].

[247] S. Catani, S. Dittmaier, and Z. Trocsanyi, *Phys. Lett.* **B500** (2001) 149–160, [hep-ph/0011222].

[248] B. Mele and P. Nason, *Nucl. Phys.* **B361** (1991) 626–644.

[249] K. Melnikov and A. Mitov, *Phys. Rev.* **D70** (2004) 034027, [hep-ph/0404143].

[250] A. Mitov, *Phys. Rev.* **D71** (2005) 054021, [hep-ph/0410205].

[251] A. Mitov, *ECONF* **C050318** (2005) 0608, [hep-ph/0510263].

[252] S. Kluth, *Rept. Prog. Phys.* **69** (2006) 1771–1846, [hep-ex/0603011].

[253] S. Catani, *Phys. Lett.* **B427** (1998) 161–171, [hep-ph/9802439].

[254] G. Sterman and M. E. Tejeda-Yeomans, *Phys. Lett.* **B552** (2003) 48–56, [hep-ph/0210130].

[255] S. Moch and A. Mitov, *Acta Phys. Polon.* **B38** (2007) 3507–3515, [arXiv:0711.1121 [hep-ph]].

[256] S. Mert Aybat, L. J. Dixon, and G. Sterman, *Phys. Rev.* **D74** (2006) 074004, [hep-ph/0607309].

[257] A. Mitov and S. Moch, *JHEP* **05** (2007) 001, [hep-ph/0612149].

[258] T. Becher and K. Melnikov, *JHEP* **06** (2007) 084, [arXiv:0704.3582 [hep-ph]].

[259] J. G. Korner and Z. Merebashvili, *Phys. Rev.* **D66** (2002) 054023, [hep-ph/0207054].

[260] G. Balossini, C. M. Carloni Calame, G. Montagna, O. Nicrosini, and F. Piccinini, *Nucl. Phys. Proc. Suppl.* **162** (2006) 59–62, [hep-ph/0610022].

[261] A. A. Penin, *Phys. Rev. Lett.* **95** (2005) 010408, [hep-ph/0501120].

[262] D. Buskulic *et. al.*,, **ALEPH** Collaboration *Z. Phys.* **C73** (1997) 409–420.

[263] A. Heister *et. al.*,, **ALEPH** Collaboration *Eur. Phys. J.* **C35** (2004) 457–486.

[264] P. D. Acton *et. al.*,, **OPAL** Collaboration *Z. Phys.* **C59** (1993) 1–20.

[265] G. Alexander *et. al.*,, **OPAL** Collaboration *Z. Phys.* **C72** (1996) 191–206.

[266] K. Ackerstaff *et. al.*,, **OPAL** Collaboration *Z. Phys.* **C75** (1997) 193–207.

[267] G. Abbiendi *et. al.*,, **OPAL** Collaboration *Eur. Phys. J.* **C16** (2000) 185–210, [hep-ex/0002012].

[268] G. Abbiendi *et. al.*,, **OPAL** Collaboration *Eur. Phys. J.* **C40** (2005) 287–316, [hep-ex/0503051].

[269] M. Acciarri *et. al.*,, **L3** Collaboration *Phys. Lett.* **B371** (1996) 137–148.

[270] M. Acciarri *et. al.*,, **L3** Collaboration *Phys. Lett.* **B404** (1997) 390–402.

[271] M. Acciarri *et. al.*,, **L3** Collaboration *Phys. Lett.* **B444** (1998) 569–582.

[272] M. Acciarri *et. al.*,, **L3** Collaboration *Phys. Lett.* **B489** (2000) 65–80, [hep-ex/0005045].

[273] P. Achard *et. al.*,, **L3** Collaboration *Phys. Lett.* **B536** (2002) 217–228, [hep-ex/0206052].

[274] P. Achard *et. al.*,, **L3** Collaboration *Phys. Rept.* **399** (2004) 71–174, [hep-ex/0406049].

[275] P. Abreu *et. al.*,, **DELPHI** Collaboration *Phys. Lett.* **B456** (1999) 322–340.

[276] J. Abdallah *et. al.*,, **DELPHI** Collaboration *Eur. Phys. J.* **C29** (2003) 285–312, [hep-ex/0307048].

[277] J. Abdallah *et. al.*,, **DELPHI** Collaboration *Eur. Phys. J.* **C37** (2004) 1–23, [hep-ex/0406011].

[278] K. Abe *et. al.*,, **SLD** Collaboration *Phys. Rev.* **D51** (1995) 962–984, [hep-ex/9501003].

[279] O. Biebel, *Phys. Rept.* **340** (2001) 165–289.

[280] Z. Kunszt, *Phys. Lett.* **B99** (1981) 429.

[281] J. A. M. Vermaseren, K. J. F. Gaemers, and S. J. Oldham, *Nucl. Phys.* **B187** (1981) 301.

[282] K. Fabricius, I. Schmitt, G. Kramer, and G. Schierholz, *Zeit. Phys.* **C11** (1981) 315.

[283] Z. Kunszt and P. Nason,. Z Physics at LEP 1, CERN Yellow Report 89-08, Vol. 1, p. 373.

[284] W. T. Giele and E. W. N. Glover, *Phys. Rev.* **D46** (1992) 1980–2010.

[285] S. Catani and M. H. Seymour, *Phys. Lett.* **B378** (1996) 287–301, [hep-ph/9602277].

[286] S. Catani, L. Trentadue, G. Turnock, and B. R. Webber, *Nucl. Phys.* **B407** (1993) 3–42.

[287] S. Catani, G. Turnock, B. R. Webber, and L. Trentadue, *Phys. Lett.* **B263** (1991) 491–497.

[288] S. Catani, G. Turnock, and B. R. Webber, *Phys. Lett.* **B295** (1992) 269–276.

[289] Y. L. Dokshitzer, A. Lucenti, G. Marchesini, and G. P. Salam, *JHEP* **01** (1998) 011, [hep-ph/9801324].

[290] A. Banfi, G. P. Salam, and G. Zanderighi, *JHEP* **01** (2002) 018, [hep-ph/0112156].

[291] G. Dissertori, I. G. Knowles, and M. Schmelling,. Oxford, UK: Clarendon (2003) 538 p.

[292] G. P. Korchemsky and G. Sterman, *Nucl. Phys.* **B437** (1995) 415–432, [hep-ph/9411211].

[293] Y. L. Dokshitzer and B. R. Webber, *Phys. Lett.* **B404** (1997) 321–327, [hep-ph/9704298].

[294] Y. L. Dokshitzer and B. R. Webber, *Phys. Lett.* **B352** (1995) 451–455, [hep-ph/9504219].

[295] Y. L. Dokshitzer, A. Lucenti, G. Marchesini, and G. P. Salam, *JHEP* **05** (1998) 003, [hep-ph/9802381].

[296] R. K. Ellis, W. J. Stirling, and B. R. Webber, *Camb. Monogr. Part. Phys. Nucl. Phys. Cosmol.* **8** (1996) 1–435.

[297] S. Brandt, C. Peyrou, R. Sosnowski, and A. Wroblewski, *Phys. Lett.* **12** (1964) 57–61.

[298] E. Farhi, *Phys. Rev. Lett.* **39** (1977) 1587–1588.

[299] L. Clavelli and D. Wyler, *Phys. Lett.* **B103** (1981) 383.

[300] P. E. L. Rakow and B. R. Webber, *Nucl. Phys.* **B191** (1981) 63.

[301] G. Parisi, *Phys. Lett.* **B74** (1978) 65.

[302] J. F. Donoghue, F. E. Low, and S.-Y. Pi, *Phys. Rev.* **D20** (1979) 2759.

[303] S. Catani, Y. L. Dokshitzer, M. Olsson, G. Turnock, and B. R. Webber, *Phys. Lett.* **B269** (1991) 432–438.

[304] N. Brown and W. J. Stirling, *Phys. Lett.* **B252** (1990) 657–662.

[305] W. J. Stirling, *J. Phys.* **G17** (1991) 1567–1574.

[306] S. Bethke, Z. Kunszt, D. E. Soper, and W. J. Stirling, *Nucl. Phys.* **B370** (1992) 310–334.

[307] S. Bethke, Z. Kunszt, D. E. Soper, and W. J. Stirling, hep-ph/9803267.

[308] L. W. Garland, T. Gehrmann, E. W. N. Glover, A. Koukoutsakis, and E. Remiddi, *Nucl. Phys.* **B642** (2002) 227–262, [hep-ph/0206067].

[309] L. W. Garland, T. Gehrmann, E. W. N. Glover, A. Koukoutsakis, and E. Remiddi, *Nucl. Phys.* **B627** (2002) 107–188, [hep-ph/0112081].

[310] S. Moch, P. Uwer, and S. Weinzierl, *Phys. Rev.* **D66** (2002) 114001, [`hep-ph/0207043`].

[311] E. W. N. Glover and D. J. Miller, *Phys. Lett.* **B396** (1997) 257–263, [`hep-ph/9609474`].

[312] Z. Bern, L. J. Dixon, D. A. Kosower, and S. Weinzierl, *Nucl. Phys.* **B489** (1997) 3–23, [`hep-ph/9610370`].

[313] J. M. Campbell, E. W. N. Glover, and D. J. Miller, *Phys. Lett.* **B409** (1997) 503–508, [`hep-ph/9706297`].

[314] K. Hagiwara and D. Zeppenfeld, *Nucl. Phys.* **B313** (1989) 560.

[315] N. K. Falck, D. Graudenz, and G. Kramer, *Nucl. Phys.* **B328** (1989) 317.

[316] D. A. Kosower, *Phys. Rev.* **D57** (1998) 5410–5416, [`hep-ph/9710213`].

[317] D. A. Kosower, *Phys. Rev.* **D71** (2005) 045016, [`hep-ph/0311272`].

[318] J. M. Campbell, M. A. Cullen, and E. W. N. Glover, *Eur. Phys. J.* **C9** (1999) 245–265, [`hep-ph/9809429`].

[319] A. Gehrmann-De Ridder, T. Gehrmann, and E. W. N. Glover, *JHEP* **09** (2005) 056, [`hep-ph/0505111`].

[320] A. Gehrmann-De Ridder, T. Gehrmann, and E. W. N. Glover, *Nucl. Phys.* **B691** (2004) 195–222, [`hep-ph/0403057`].

[321] A. Gehrmann-De Ridder, T. Gehrmann, and E. W. N. Glover, *Phys. Lett.* **B612** (2005) 36–48, [`hep-ph/0501291`].

[322] A. Gehrmann-De Ridder, T. Gehrmann, and E. W. N. Glover, *Phys. Lett.* **B612** (2005) 49–60, [`hep-ph/0502110`].

[323] A. Gehrmann-De Ridder, T. Gehrmann, E. W. N. Glover, and G. Heinrich, *JHEP* **11** (2007) 058, [`arXiv:0710.0346 [hep-ph]`].

[324] A. Gehrmann-De Ridder, T. Gehrmann, E. W. N. Glover, and G. Heinrich, `arXiv:0711.4711 [hep-ph]`.

[325] R. W. L. Jones, M. Ford, G. P. Salam, H. Stenzel, and D. Wicke, *JHEP* **12** (2003) 007, [`hep-ph/0312016`].

[326] A. Gehrmann-De Ridder, T. Gehrmann, E. W. N. Glover, and G. Heinrich, *Phys. Rev. Lett.* **99** (2007) 132002, [`arXiv:0707.1285 [hep-ph]`].

[327] G. Dissertori *et. al.*, `arXiv:0712.0327 [hep-ph]`.

[328] Z. Nagy and D. E. Soper, *JHEP* **09** (2007) 114, [`arXiv:0706.0017 [hep-ph]`].

[329] W. T. Giele, D. A. Kosower, and P. Z. Skands, `arXiv:0707.3652 [hep-ph]`.

[330] G. Gustafson, *Phys. Lett.* **B175** (1986) 453.

[331] L. Lonnblad, *Comput. Phys. Commun.* **71** (1992) 15–31.

[332] J.-C. Winter and F. Krauss, `arXiv:0712.3913 [hep-ph]`.

[333] S. Schumann and F. Krauss, `arXiv:0709.1027 [hep-ph]`.

[334] M. Dinsdale, M. Ternick, and S. Weinzierl, *Phys. Rev.* **D76** (2007) 094003, [arXiv:0709.1026 [hep-ph]].

[335] Z. Nagy and D. E. Soper, hep-ph/0601021.

[336] Z. Nagy and D. E. Soper, arXiv:0801.1917 [hep-ph].

[337] T. Sjöstrand, S. Mrenna, and P. Skands, arXiv:0710.3820 [hep-ph].

[338] G. Gustafson and U. Pettersson, *Nucl. Phys.* **B306** (1988) 746.

[339] B. Andersson, G. Gustafson, and L. Lönnblad, *Nucl. Phys.* **B339** (1990) 393–406.

[340] E. Boos *et. al.*, hep-ph/0109068.

[341] J. Alwall *et. al.*, *Comput. Phys. Commun.* **176** (2007) 300–304, [hep-ph/0609017].

[342] R. Kleiss, *Phys. Lett.* **B180** (1986) 400.

[343] T. Sjostrand and P. Z. Skands, *Eur. Phys. J.* **C39** (2005) 129–154, [hep-ph/0408302].

[344] T. Ishikawa *et. al.*,, **MINAMI-TATEYA group** Collaboration. KEK-92-19.

[345] S. Odaka and Y. Kurihara, *Eur. Phys. J.* **C51** (2007) 867–873, [hep-ph/0702138].

[346] Y. Kurihara *et. al.*, *Nucl. Phys. Proc. Suppl.* **157** (2006) 231–235.

[347] H. L. Lai *et. al.*,, **CTEQ** Collaboration *Eur. Phys. J.* **C12** (2000) 375–392, [hep-ph/9903282].

[348] H. Tanaka, *Prog. Theor. Phys.* **110** (2003) 963–973.

[349] T. Sjostrand, *Phys. Lett.* **B157** (1985) 321.

[350] M. Bengtsson, T. Sjostrand, and M. van Zijl, *Z. Phys.* **C32** (1986) 67.

[351] G. Corcella *et. al.*, *JHEP* **01** (2001) 010, [hep-ph/0011363].

[352] T. Sjostrand *et. al.*, *Comput. Phys. Commun* **135** (2001) 238–259, [hep-ph/0010017].

[353] S. Catani, F. Krauss, R. Kuhn, and B. R. Webber, *JHEP* **11** (2001) 063, [hep-ph/0109231].

[354] J. Alwall *et. al.*, arXiv:0706.2569 [hep-ph].

[355] S. Frixione, P. Nason, and C. Oleari, *JHEP* **11** (2007) 070, [arXiv:0709.2092 [hep-ph]].

[356] S. Gieseke, P. Stephens, and B. Webber, *JHEP* **12** (2003) 045, [hep-ph/0310083].

[357] Z. Nagy and D. E. Soper, *JHEP* **10** (2005) 024, [hep-ph/0503053].

[358] S. Catani, S. Dittmaier, M. H. Seymour, and Z. Trocsanyi, *Nucl. Phys.* **B627** (2002) 189–265, [hep-ph/0201036].

[359] T. Sjostrand, L. Lonnblad, and S. Mrenna, hep-ph/0108264.

[360] P. Abreu *et. al.*,, **DELPHI** Collaboration *Z. Phys.* **C73** (1996) 11–60.

[361] S. Catani and B. R. Webber, *JHEP* **10** (1997) 005, [hep-ph/9710333].

[362] A. A. Affolder *et. al.*,, **CDF** Collaboration *Phys. Rev. Lett.* **84** (2000) 845–850, [hep-ex/0001021].

[363] V. M. Abazov *et. al.*,, **D0** Collaboration *Phys. Rev. Lett.* **94** (2005) 221801, [hep-ex/0409040].